Investigation of Point Defects in AlGaN/GaN High Electron Mobility Transistor Heterostructures Grown on Si Wafers

by

Burcu Ozden

A dissertation submitted to the Graduate Faculty of
Auburn University
in partial fulfillment of the
requirements for the Degree of
Doctor of Philosophy

Auburn, Alabama
August 6, 2016

Keywords: AlGaN/GaN, Heterostructure, Defect, Spectroscopy, Photocurrent

Approved by

Minseo Park, Chair, J T Walter Professor of Physics
Sarit Dhar, Associate Professor of Physics
Marcelo Kuroda, Assistant Professor of Physics
Michael C. Hamilton, Associate Professor of Electrical & Computer Engineering
Dong-Joo Kim, Alumni Professor of Materials Research & Education Center

Abstract

This PhD dissertation focuses on the investigation of surface/interface defects in AlGaN/GaN high electron mobility transistors (HEMTs) on Si wafers for power electronic applications. Recently, significant attention has been paid to gallium nitride (GaN) for application in power electronics due to its desired materials characteristics. Among the power electronic devices based on GaN and its alloys, AlGaN/GaN high electron mobility transistors (HEMTs) are considered promising.

Nevertheless, deleterious effects of high concentration of point defects on the performance of AlGaN/GaN high electron mobility transistors (HEMTs) cannot be disregarded. It is of great importance to analyze deep level defects in the AlGaN/GaN HEMTs structure since it is recognized that deep level defects are the main source for causing current collapse phenomena leading to reduced device reliability. Raman spectroscopy, photoluminescence (PL), and spectroscopic photo current-voltage measurements were performed to characterize point defects at surface/interface and bulk in AlGaN/GaN HEMTs wafer.

Recently, a simple and novel spectroscopic photo I–V method of diagnosing the homogeneity of electrically-active defect distribution in the large area AlGaN/GaN HEMTs epi-structure grown on 6-inch silicon wafers has been developed. The spectroscopic photo current-voltage (I-V) measurements with sub-bandgap illumination exhibited the presence of sub-bandgap defects with different activation energies for each sample. The depth-resolved ultra-violet (UV) spectroscopic photo current-voltage (I-V) (DR-UV-SPIV) measurements revealed that the depth dependent distribution of the defects for these samples are

different. Time resolved photocurrent spectroscopy (TRPC) was used to distinguish between the traps that have the same de-trapping energy but have the different physical origins. It was demonstrated that even though electrically active defects for two devices on the same pieces of AlGaN/GaN HEMTs heterostructures cannot be distinguished in Raman spectroscopy and PL measurements, they can be differentiated by using the spectroscopic photo I-V with sub-bandgap illumination and DR-UV-SPIV measurements.

Acknowledgements

My Ph.D. at Auburn University was certainly one of the most fruitful experiences in my life. This was only possible because of the very nice administration and faculty at Auburn University. I had the opportunity to work with many skillful scientists and at the same time many nice people. Therefore, I would like to thank them all, as each of them contributed, in one way or another, to my growth from both a professional and a human points of view. I would like to acknowledge all those who participated and assisted me in this work.

My biggest and deepest thanks are for my supervisor Dr. Minseo Park, for giving me the opportunity to work in this exciting field of research. He showed great faith and encouragement in me throughout the entirety of the project and for that I am sincerely grateful. He provided invaluable experiences, guidance, and support. I strongly appreciated his help in this stage of my work, his excellent point of view, and his capacity to pose with me challenges to improve our scientific publication record in international journals. Without his guidance, this dissertation work and related publications would not have been possible.

My gratitude also goes to other supervisory committee members Dr. Sarit Dhar who also helped me on AFM measurements, Dr. Michael Hamilton, and Dr. Marcelo Kuroda. In addition, I am extremely grateful to Dr. Dong-Joo Kim for serving as my external committee member.

I am grateful to Dr. Claud Ayayi for developing the software program for my experiments, and for his patience in answering my endless questions, his insight on my research, all the useful scientific discussions, and his help in the laboratories I have used. His comments have been much appreciated.

I would also like to express my gratitude to Ms. Tamara Isaacs-Smith for training me in microelectronics fabrication, helping all the laboratories that I have used during my research, proof-reading my articles and dissertation, and last but not the least for her endless patience towards my mistakes.

I am also deeply thankful to Dr. Naci Balkan who encourage me to pursue a PhD in physics and become a professor. I deeply appreciate our department chair Dr. Hanson's support on the opportunities to travel to present at conferences. I also would like to thank Dr. Goufu Niu for his interest to my project and his help in the very beginning of this work. I really appreciate Dr. Michael Bolzack's and Dr. Michael E. Miller's help on XPS and SEM measurements. I also thank to Dr. Jianjun Dong for teaching me how to draw the crystal structure of GaN by using a software program.

I greatly appreciate the time of different people that I involve in this dissertation work, such as Mr. Max Chip Cichon and Mr. Patrick Stringer for technical support. I am very grateful to the Dow Corning and IMEC for the support provided during my dissertation work, namely Dr. Yoga Saripalli, Dr. Ming Zhao, Dr. Hu Liang, Dr. Prem Kumar Kandaswamy, Dr. David Ewoldt, and Dr. Gil Chung.

I would also like to thank to former and current members of the research group; Vahid Mirkhani for his endless patience, kindness, support and the most importantly friendship, Min P Khanal for helping me on my fabrication and characterization process, Kosala Yapabandara for the constructive research discussions we made, Chungman Yang for helping me in the cleanroom, Muhammad Shehzad Sultan for his support and prayers, Dr. Fei Tong for helping in the construction of experimental setup, and Chunkun Jiao for checking all my calculations, Suhyeon Youn and Sangjong Ko helping me to plot my graphs, and Dr. Mobbassar Hasan Sk for his advices. Their help, time, useful discussions, and friendships are well appreciated. A special thanks to my friends, Eleanor Williamson, Erica Snipes, Spencer LeBlanc, and Maggie Abeyta for proof reading my dissertation and providing support.

I thank my husband soon to be Dr. Sabahattin Gokhan Ozden, who has constantly been an encouraging influence and source of inspiration with his love, patience and kindness. Thank you very much for making this journey possible. I also would like to thank my husband's parents Ahmet and Emel Ozden, and Nurgul Ozalp for their endless support and prayers.

Most importantly, I wish to convey my deep appreciation and gratitude to my parents Ismail Rasik and Havva Ozkulhanci, and my brother Enver Ozkulhanci, for their sacrifice and commitment. I owe all of my successes to their unconditional support and love in all aspects of my education and life. I would like to thank my grandparents as well as my uncle Mehmet and aunt Hikmet Bayrakoglu for their support and prayers during my academic life.

Table of Contents

List of Tables

List of Figures

List of Abbreviations

2DEG	2 Dimensional Electron Gas
AC	Alternating Current
AX	Deep Acceptor Levels
BFOM	Baligia's Figure of Merit
BL	Blue Luminescence
CCD	Charged Coupled Detector
C-V	Capacitance Voltage
CVD	Chemical Vapor Deposition
DAP	Donor Acceptor Pair
DARS	Disorder Activated Raman Scattering
DC	Direct Current
DI	Deionized
DIBL	Drain Induced Barrier Lowering
DLTS	Deep Level Transient Spectroscopy
DR-UV-SPIV	Depth Resolved Ultra-Violet Spectroscopic Photo Current-Voltage
DX	Deep Donor Levels
EHP	Electron Hole Pair
EV	Electric Vehicles
FE	Field Emission
FET	Field Effect Transistor
FOM	Figure of Merit
FWHM	Full Width at Half Maximum
HB	High Brightness
HBT	Heterojunction Bipolar Transistor
HFET	Heterojunction Field Effect Transistor
HEMT	High Electron Mobility Transistor
HEV	Hybrid Electric Vehicles
HVPE	Hydride Vapor Phase Epitaxy
IC	Integrated Circuit
I-V	Current-Voltage
IR	Image Reversal/ Infrared
JFOM	Johnson's Figure of Merit
KFOM	Keyes' Figure of Merit
LED	Light Emitting Diode
LO	Longitudinal
LPP	Longitudinal Phonon Plasma

LVM	Local Vibrational Mode
MBE	Molecular Beam Epitaxy
MFS	Minimum Feature Size
MOSFET	Metal Oxide Semiconductor Field Effect Transistor
MODFET	Modulation Doped Field Effect Transistor
MOCVD	Metal-Organic Chemical Vapor Deposition
MOVPE	Metal Organic Vapor Phase Epitaxy
NA	Numerical Aperture
NBE	Near Band Edge
PAB	Post Apply Bake
PAC	Photoactive Compound
PC	Photo Current/ Photo Conductivity
PCE	Power Conversion Efficiency
PDCR	Photo to Dark Current Ratio
PEB	Post Exposure Bake
PD	Penetration Depth
PL	Photoluminescence
PPC	Persistent Photoconductivity
PV	Photovoltaic
Q-DLTS	Charge-based Deep Level Transient Spectroscopy
RF	Radio Frequency
RT	Room Temperature
RTA	Rapid Thermal Annealing
SBH	Schottky Barrier Height
SEM	Scanning Electron Microscopy
TCE	Trichloroethylene Current Spectroscopy
TE	Thermionic Emission
TFE	Thermionic Field Emission
TLM	Transmission Line Model / Transfer Length Method
TO	Transverse
TRPC	Time Resolved
UV	Ultra-Violet
YL	Yellow Luminescence
WBG	Wide Band Gap
XPS	X-ray Photoelectron Spectroscopy

Chapter 1

1 Introduction

Since its appearance in the early 1930s, gallium nitride (GaN) and its alloys has attracted a significant attention as highly promising material systems for both high power and high frequency applications due to its high desirable material characteristics. Over the last eighty years researchers all around the world have made great efforts in order to redeem these promises. GaN is typically seen as a channel material in field effect transistors (FETs) and as base material in AlGaN/GaN heterojunction bipolar transistors (HBTs).[1]

The value of the world wide GaN device market was estimated at US$481.8 million in 2014 and is estimated to be US$1,315.0 million by 2021.[2] Demand for GaN industrial devices rises with the increase in demand from the defense sector for enhanced battlefield performance. The key application of GaN in armed forces is its utilization in HEMT (high electron mobility transistor), which is a necessity in high-frequency operations.

Gallium Nitride (GaN) was first synthesized by Johnson *et al*.,[3] and Juza and Hahn in the 1930s by passing ammonia (NH_3) over liquid gallium (Ga) at elevated temperatures.[4] In 1969, Maruska obtained the first single crystalline GaN film.[5] In 1986, a milestone was achieved when highly improved surface morphology, as well as optical and electrical properties of GaN films grown by metal organic chemical vapor deposition (MOCVD) on sapphire substrates is reported by Amono *et al.*[6] First, a way to produce conducting p-type GaN films was discovered by Akasaki in 1989. In 1992, activation of p-type GaN by annealing was discovered by Nakamura *et al.*[7] In 1993, Nakamura *et al.*[8] demonstrated the first high-brightness (HB) blue double-heterostructure (DH) GaN LEDs. First evidence for two-dimensional electron gas (2DEG) formation at an $Al_xGa_{1-x}N$/GaN heterojunction grown by MOCVD on sapphire was reported by Khan *et al.* in 1991.[9]

Since then, GaN technology has rapidly diffused into optoelectronic applications.[10]Although rapid progress has been made, the growth and device fabrication were still primitive compared to Si and GaAs. However, with the improvement in the growth technology on Si substrates, such as availability of silicon substrates in 150mm and 200mm, and GaN on 200mm silicon substrate growth, GaN-on-Si technology has become the best alternative to the well-established but aged Si technology[11]. GaN-on-Si technology is introduced to high voltage power switching applications with the development of RF power amplifier to primarily target applications, such as wireless communication as early as 2009.[12,13] Ever since, many manufacturers, have announced their intention to manufacture and develop GaN transistors for the power conversion market. In 2014, larger GaN on silicon epitaxial wafers 8" were demonstrated by Ravkowski *et al.*[14].

Despite the fact that the GaN technology has broken into the market, it is still behind its theoretical performance. In order to compete with the current state-of-the-art Si devices improving the starting material quality and yield, increasing the wafer diameter, reducing wafer cost, and developing normally OFF devices are required.

When this Ph.D. work started, there were still problems in the reliability of device with the widespread application of AlGaN/GaN HEMTs. In AlGaN/GaN HEMTs, the so-called “current collapse” occurs as a result of entrapment of charge carriers at the surface/interface and bulk trap sites and is known to reduce the drain current.[15] This necessitates minimization of the undesired trap sites for achieving a high performance, long life and a reliable HEMT device.

This work is the detailed study of the investigation of surface/interface defects in AlGaN/GaN HEMTs heterostructures grown on Si wafers.

In this chapter, I will first focus on the main performance requirements of high voltage switching devices. Next, I discuss the advantages of using GaN compared to other materials in terms of material properties and figures of merit. Later, I will give an overview of the application areas. Finally, I will describe the organization of this dissertation.

1.1 Performance required for switching devices

In power electronic circuits, rectifiers and power switches are required to control the direction of current flow and to regulate the duration of current flow, respectively. It is known that transistors behave as ideal switches in the field of electric power conversion. An ideal transistor conducts current in the on-state with zero voltage drop and blocks voltage in the off-state with zero leakage current.[16] Low leakage current is required to decrease the conduction losses. In addition, operation with high current and voltage in the active region is also observed in an ideal transistor with the saturated forward current in this mode controlled by the applied gate bias[16].

In well-designed field effect transistors (FETs), carrier transient time from source to drain under the applied voltage through gate affects the speed. In these transistors, delays in transient time result from passive elements, such as capacitors, resistors, inductors, and filters. Operating a FET at a higher switching frequency enables the use of smaller passive components. In summary, power electronic devices are expected to have a high stand-off voltage, absolute current levels, frequency switching operation, operation temperature, and low forward voltage drop, specific on resistance, and capacitance[17]. These needs are summarized in the Table 1.1-1.

Table 1.1-1: *Summary of performance needs for power electronic devices.*

Need	Enabling Feature	Performance Advantage
High Power/Unit Width	Wide Bandgap, High Field	Compact, Ease of Matching
High Voltage Operation	High Breakdown Field	Eliminate/Reduce Step Down
High Linearity	HEMT Topology	Optimum Band Allocation
High Frequency	High Electron Velocity	Bandwidth, μ-Wave/mm-Wave
High Efficiency	High Operating Voltage	Power Saving, Reduced Cooling
Low Noise	High gain, high velocity	High dynamic range receivers
High Temperature Operation	Wide Bandgap	Rugged, Reliable, Reduced Cooling
Thermal Management	SiC Substrate	High power devices with reduced cooling needs
Technology Leverage	Direct Bandgap: Enabler for Lighting	Driving Force for Technology: Low Cost

Increased switching speed and conversion capabilities of III-V FETs, and their efficient transmission and distribution of electric power properties makes these devices an attractive technology for power conversion systems. Although GaN devices do not have a higher breakdown voltage, they do have a smaller switching energy at the same breakdown voltages. In general, more efficient power distribution at higher power levels and more compact device sizes are allowed due to high power handling capabilities of GaN devices.

1.2 Advantages of AlGaN/GaN HEMTs as switching devices

1.2.1 Comparison of GaN Material Properties with other WBG semiconductors

The GaN wide bandgap semiconductor has attracted much attention since the early 1990s due to its advanced material characteristics, such as high electrical field, high electron mobility, high saturation, and drift velocity compared to Si, SiC, and GaAs shown in the Table 1.2-1.[18] Having stronger chemical bonds causes wider band gap in GaN since the band gap of a semiconductor is related to the strength of the

chemical bonds between the atoms in the lattice.[19] These stronger bonds mean that it is harder for an electron to jump from one site to the next. This property provides lower intrinsic leakage currents and higher operating temperatures for higher band gap semiconductors.

Table 1.2-1: *Physical characteristics of GaN and other main wide bandgap semiconductors at room temperature.*[20,21,22]

Property	GaN AlGaN/GaN	SiC	Diamond	Si	GaAs AlGaAs/InGaAs
Bandgap Energy, E_g (eV)	**3.44**	3.26	5.45	1.12	1.43
Electric breakdown field, E_c (MV/cm)	**3**	3	10	0.3	0.4
Saturated electron velocity, ϑ_{sat}($\times 10^7$ cm/s)	**2.5**	2.0	2.7	1.0	1.0
Electron mobility, μ_s (cm^2/V.s)	**900** **2000**	700	4800	1500	8500 10.000
2DEG density, n_s ($\times 10^{13} cm^{-2}$)	**1.0**	N.A	N.A	N.A	<0.2
Thermal conductivity (κ (W/cm.K)	**1.3-2.1**	3.7-4.5	22	1.5	0.5
Melting Temperature, T (K)	**>1700**	>2100	3800	1690	1510

Furthermore the application in high supply voltages is enabled *via* high electric breakdown fields (E_c), which results from a large bandgap energy (E_g). Another advantages of having a high E_c is having higher doping levels; thus device layers can be made thinner at the same breakdown voltage.[23] It is known that wide band gap (WBG) materials have high electric breakdown fields compared to conventional semiconductors.[17]

The voltage, at which a device breaks down can be approximated with the formula in equation [1.2-1].

$$V_{BR} = \frac{1}{2} w_{drift} E_C \qquad [\ 1.2\text{-}1]$$

where V_{BR} is the breakdown voltage, and w_{drift} is the width of the drift region.

SiC and GaN both have a drift region 10 times smaller than of Si devices for the same breakdown voltage. It is known that, there needs to be carriers in the drift region that are depleted away at the point where the devices reaches the critical field in order to support high electric field. This is why there is a huge power gain in devices with high electrical fields. The number of electrons (assuming an N-type semiconductor) between the two terminals can be calculated using Poisson's equation:

$$qN_D = \varepsilon_0 \varepsilon_r E_{crit} / w_{drift} \qquad [\ 1.2\text{-}2\ ]$$

where q is the charge of the electron (1.6×10^{-19} coulombs), N_D is the total number of electrons in the volume, ε_o is the permittivity of a vacuum measured in farads per meter (8.854×10^{-12} F/m), and ε_r being the relative permittivity of the crystal compared to a vacuum.

Usually, high charge carrier mobility (μ) and high saturation velocity (v_{sat}) are desirable to achieve high currents and high frequency operation. Even though bulk GaN has relatively low electron mobility at around 900 cm^2/Vs, this value is sufficient for a transistor to operate at high power. The ability of III-nitride materials to create a two dimensional electron gas (2DEG) at the heterointerface of an AlGaN/GaN device with high charge density and very high mobility compared to the value of the bulk GaN is the most important property of these materials. In general, WBG semiconductors have a relatively low mobility but very high values for the saturation velocity, which is reached at high electric fields that can easily be supported.

The theoretical on-resistance $R_{DS(on)}$ of this majority-carrier device can be obtained from equation [1.2-3].

$$R_{DS(on)} = w_{drift}/q\mu_n N_D \qquad [\ 1.2\text{-}3\ ]$$

where μ_n is the mobility of electrons.

Combining equations [1.2-1], [1.2-2], and [1.2-3] produces the following relationship between the breakdown voltage and the on-resistance;

$$R_{DS(on)} = 4V_{BR}^2/E_{crit}^3\varepsilon_0\varepsilon_r \qquad [\ 1.2\text{-}4\ ]$$

Figure 1.2-1 indicates the theoretical limitation of the trade-off characteristics between the specific R_{on} and the V_{BR} in Si, SiC, and GaN devices. According to Figure 1.2-1 GaN has greater potential in high voltage and high power density applications compared to SiC and Si since it has lower R_{on} compared to SiC and Si.

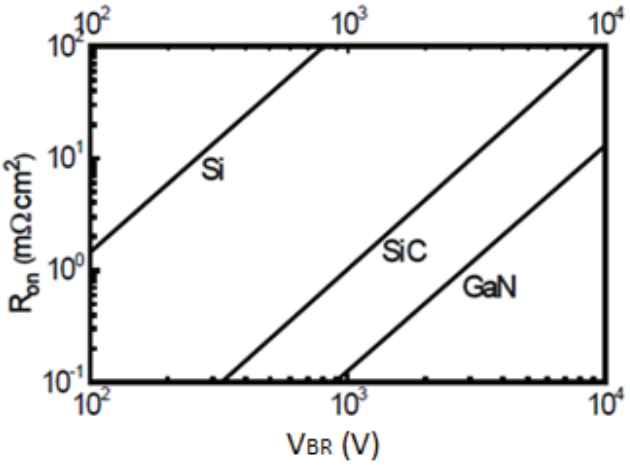

Figure 1.2-1: *The theoretical trade-off characteristics between specific on resistance (R_{on}) and off state breakdown voltage (V_{BR}) of Si, SiC, and GaN devices.* [24]

The burden of thermal management is important for power applications in operational capability at high temperatures. Figure 1.2-2 shows the intrinsic carrier density as a function of temperature and indicates that GaN requires higher temperature to reach the density of 10^{14} cm^{-3}, in which material can no longer behave as semiconductor.

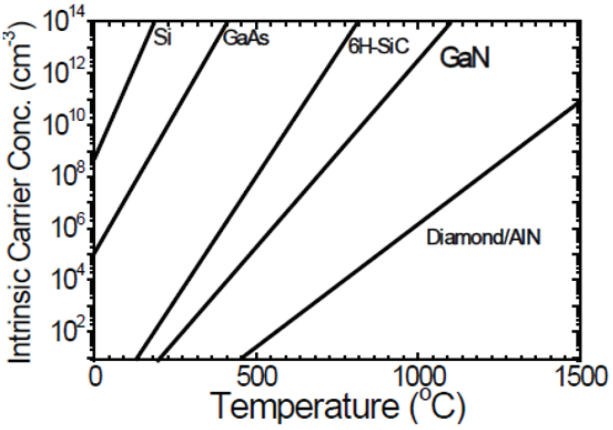

Figure 1.2-2: *The temperature dependence of intrinsic carrier concentration profiles for Si, GaAs, 6H-SiC, GaN and Diamond.*[24]

Moreover, the thermal conductivity (κ) of a semiconductor material is an extremely important parameter to determine dissipation power. Poor thermal conductivity results in degradation in device operation at elevated temperatures. GaN has comparable thermal conductivity with Si, even though it is not as high as diamond or SiC. The relative permittivity (ϵ_r) is an indication of the capacitive loading of a transistor and affects the device terminal impedance. The values for WBG semiconductors are much lower than those for conventional semiconductors. GaN has 20% lower ϵ_r values compared to conventional semiconductors, which permits 20% larger area for a given impedance, and results in larger current and higher microwave output power.

All these advantages makes AlGaN/GaN heterostructures favored candidates for fabricating power electronic devices among the other power electronic devices based on GaN and its alloys. $Al_xGa_{1-x}N$ alloys cover bandgap energies from 1.9eV to 6.2eV, which corresponds to wavelengths ranging from red to deep UV. Having a wide bandgap allows the material to withstand high operating temperatures up to 300^{o}C -

500ºC. Moreover, 2-dimensional electron gas (2DEG) sheet charge density (n_s) up to 1 x 10^{13} cm^{-2} is created at the AlGaN/GaN interface. As a result, the mobility of the electrons in the transistor channel become as high as 2000 cm^2 V^{-1} s^{-1}.[25,26] Hence, the large drain currents (> 1 A/mm), which are the second requirement for a power device, can be achieved. The mobility and saturation velocity of the 2DEG at the $Al_xGa_{1-x}N$/GaN heterojunction is very suitable for high-power, high-frequency device applications. Drastic reductions in the gate width, chip area, and in power loss are the main advantages of AlGaN/GaN heterostructure devices. Increase in the power density of GaN FETs causes a rise in the thermal dissipation and requires an improvement via packaging technique.

1.2.2. Figure of Merit

There are many predictions to determine promising III-V semiconductors. A calculated number called figure of merits (FOM) is suggested in order to quantify the ultimate performance of semiconductor devices. FOM combines the most relevant material properties shown in the Table 1.2-1 with respect to high-power and high-frequency applications into one number that represents a rough measure of the relative strengths of the alternative materials. Johnson's FOM is utilized from breakdown voltage and saturated electron drift velocity to define a value for the high frequency handling capacity of a certain semiconductor and calculates an FOM of GaN 215 times higher than Si.[27] Baligia's FOM take the relative permittivity, electron mobility, and electric breakdown field into account to measure high-power handling capability and calculates an FOM of GaN 1507 times higher than Si.[28,20] Keyes' FOM uses saturated electron drift velocity, and relative permittivity for the measurement of high-temperature handling capability. Figure 1.2-4 displays the comparison of John's and Keyes' FOM for the semiconductors GaN, GaAs, 4H-SiC and Si.[29] Comparison of Baliga's and Johnson's FOM for the semiconductors GaN, GaAs, 4H-SiC, and Si normalized to Si is given at Figure 1.2-3[29]. From these figures it is very clear that GaN offers much better high-power/high-frequency performance possibilities.

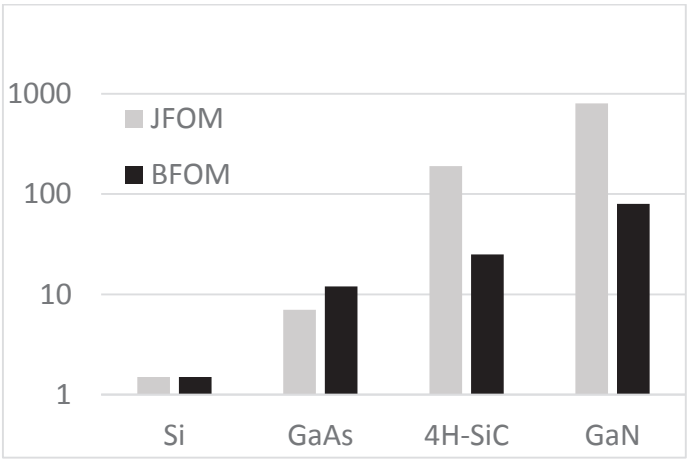

Figure 1.2-3: *Comparison of Baliga's and Johnson's figure of merit for semiconductors GaN, GaAs, 4H-SiC, and Si normalized to Si.*[30]

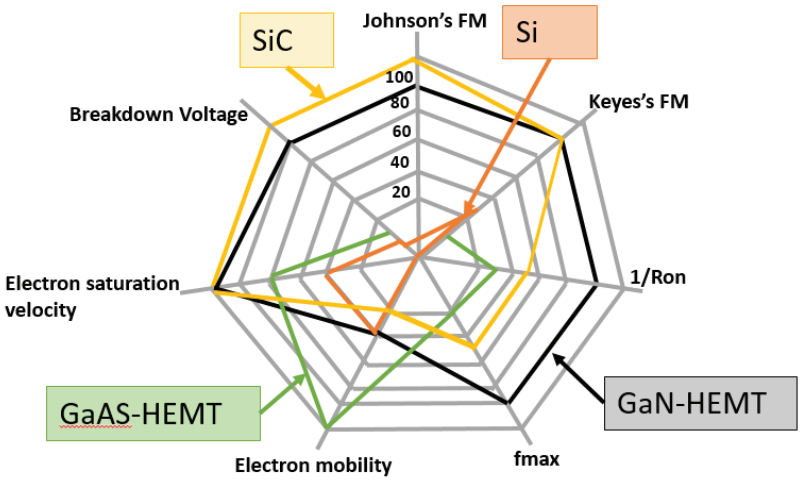

Figure 1.2-4: *Comparison of Keyes's and Johnson's figure of merit for semiconductors GaN, GaAs, 4H-SiC, and Si.*[29]

Table 1.2-2 shows the FOM normalized to Si for the most common semiconducting materials.[31,32,33] In this table, E_B is the electrical field for breakdown in semiconducting material, v_s is the electron saturation velocity, κ is the thermal conductivity, c is the speed of light, ε_S is the dielectric constant of the semiconductor, μ is the mobility of the charge carrier, and E_g is the bandgap energy (in eV). Among the

common semiconducting materials, GaN has the highest figure of merit making it suitable for the high power, high temperature, and high frequency applications.

Table 1.2-2: *Main figures of merit for wide bandgap semiconductors compared with Si.*[34,21]

Figure of Merits	Expression	Si	GaAs	SiC-4H	GaN	Associated
Johnson (JFOM)	$\frac{E_B^2 v_s^2}{4\pi^2}$	1	1.8	215.1	215.1	High Power
Baliga (BFOM)	$\varepsilon_s \mu E_B^3 \sqrt{\frac{V_G}{4V_G^3}}$	1	13.3	548	1507	High Frequency
Keyes (KFOM)	$K(\sqrt{\frac{cv_s}{4\pi\varepsilon_s}})$	1	0.41	4.61	1.6	High Temperature

1.3 Applications of AlGaN/GaN switching HEMTs

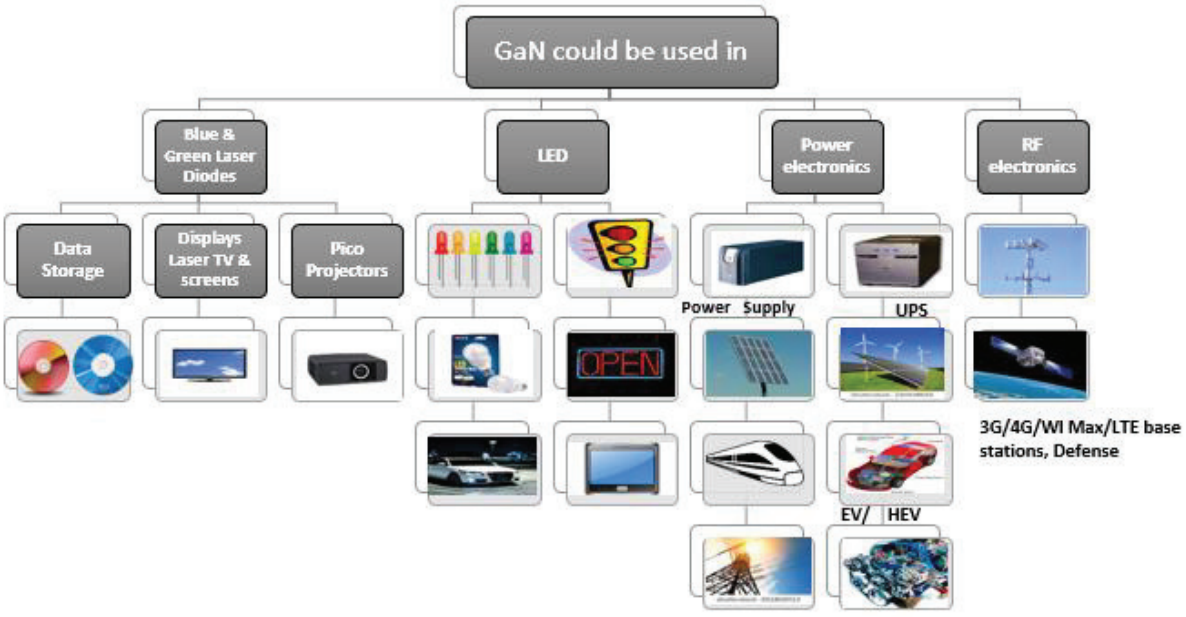

Figure 1.3-1: *Different applications of GaN devices in the semiconductor market.*[35]

Recent massive increases in the GaN devices application have been observed due to the technology advancements, such as the availability of native and GaN-on-silicon substrates, development of normally-off gate structures, suppression of the current collapse phenomenon as well as the demonstration of high-

voltage blocking capability.[36] Figure 1.3-1 displays different applications of GaN devices in the semiconductor market. Nowadays, GaN technology offers transistors, diodes, and even IC`s compatible with power electronic expectations, FET have many potential application at high frequency and/or high temperature operation devices.[37]

In this dissertation, mainly we will focus on power electronic applications because AlGaN/GaN HEMTs are power switching devices. Figure 1.3-2 presents applications of GaN devices in power electronics. GaN power devices are known as the next generation power devices because of their advanced properties, such as achieving “very low resistance of the device current loop” and "high-speed switching". These properties could be used effectively for high-efficiency power supplies, hybrid electric vehicles (HEV)/ electric vehicles (EVs), or photovoltaic (PV) inverters. The most popular power switch application of GaN devices is for the HEV. HEV’s motor drive is a power-electronics component which converts stored energy into an alternating current (AC) source. Currently HEV use silicon (Si) based power-electronic components. However, Si based system has encountered challenges, such as over size, over weight, and low temperature limit. Therefore, it is believed that GaN can be good alternative to Si. Besides the great opportunities that GaN-based high-temperature electronics present to HEVs, they also offer important capabilities to aerospace, energy production, and other industrial systems that will affect modern everyday life.

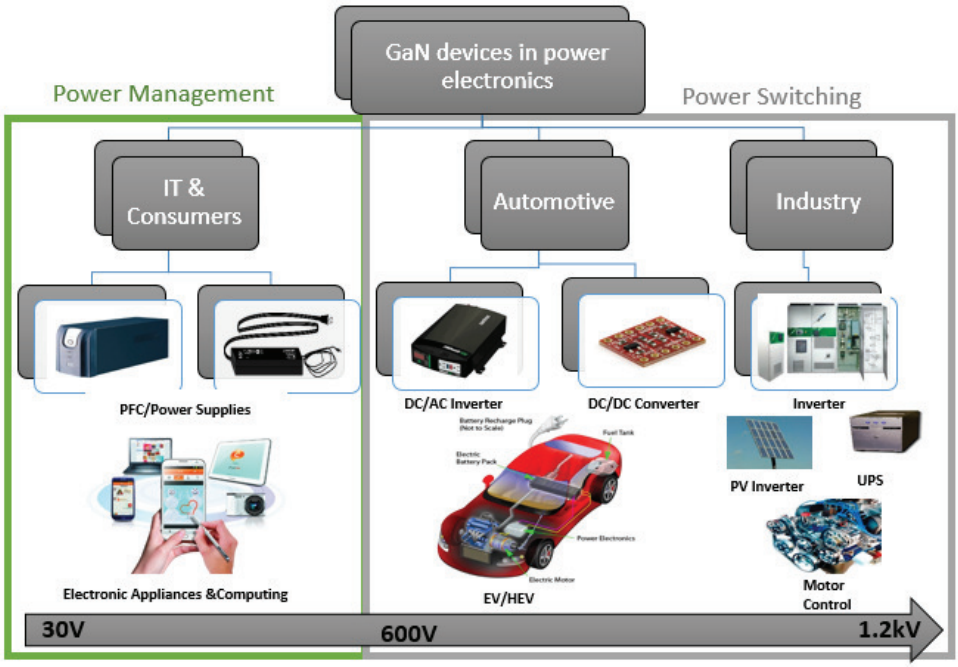

Figure 1.3-2: *Application of GaN devices in power electronics.*[38]

1.4 Motivation

Despite the remarkable advances in optoelectronic and electronic device performances, and growth methods for AlGaN/GaN HEMTs epi-structures, there still remain technical issues to be understood and resolved.[39] With regards to reliability and the stability of AlGaN/GaN HEMTs, one of the major issues that remain unresolved is the deleterious effect of the deep level defects present in the heterostructures on the device performance.[40] GaN technology has rapidly diffused in the optoelectronic applications. However, to be a more commercially viable technology, it will be great if the substrate cost can be further reduced. This is only possible by growing GaN on top of a large diameter Si substrate.

Due to the lack of inexpensive large area GaN substrates, AlGaN/GaN HEMTs epi-layers are usually grown heteroepitaxially on foreign substrates, such as Si, SiC, and sapphire.[41,42,43] As a result of the lattice/thermal expansion mismatches between the epi-layers and the foreign substrates, a high concentration of material defects is expected in AlGaN/GaN HEMTs epi-structures. These deep level

defects can be point defects, such as Ga[44,45] or N vacancies.[45] The deep level defects create localized levels inside the bandgap and can potentially act as charge carrier traps, causing the current collapse phenomena that lead to a substantial degradation in device performance.[44] The impact of deep level defects is significant in all device applications and these defects degrade the device performance. Therefore, it is very important to elucidate the nature of the defects and their distribution across the wafer.

1.5 Synopsis of the dissertation

This dissertation focuses on the investigation of point defects in AlGaN/ GaN HEMTs on Si wafer for power electronic applications. This dissertation is organized in the following way:

Chapter 2 describes the device physics of AlGaN/GaN heterostructures.

Chapter 3 summarizes surface, bulk, and interface defects.

Chapter 4 focuses on device processing techniques.

Chapter 5 studies Raman Spectroscopy and Photoluminescence.

Chapter 6 discuss in detail the characterization of AlGaN/GaN HEMTs *via* various spectroscopic techniques.

Finally, chapter 7 provides retrospection of the conclusion which can be drawn from the investigation of surface/interface defects *via* spectroscopic techniques and an outlook for future research.

References

[1] C. Monier, F. Ren, J. Han, P. Chang, R. Shul, K. Lee, A. Zhang, A. Baca, and S. Pearton, "Simulation of npn and pnp AlGaN/GaN heterojunction bipolar transistors performances: limiting factors and optimum design", IEEE Trans. Electron Devices, **48**, 427 (2001).

[2] Available online: "www.transparencymarketresearch.com/article/gan-industrial-devices-market.htm", June (2015).

[3] W. C. Johnson, J. B. Parson, M. C. Crew, J. Phys. Chem. **234**. 2651 (1930).

[4] R. Juza and H. Hahn, "Über die kristallstrukturen von Cu3N, GaN und InN metallamide und metallnitride," Zeitschrift für anorganische und allgemeine Chemie, **239**, 282 (1938).

[5] H. P. Maruska and J. J. Tietjen, "The preparation and properties of vapor-deposited single-crystalline GaN," Appl. Phys. Lett. **15**, 327 (1969).

[6] H. Amano, N. Sawaki, I. Akasaki, and Y. Toyoda, "Metalorganic vapor phase epitaxial growth of a high quality GaN film using AlN buffer layer", Appl. Phys. Lett. **48**, 353 (1986).

[7] S. Nakamura, N. Iwasa, M. Senoh, and T.Mukai, "Hole compensation mechanism of p-type GaN films", Jpn. J. Appl. Phys. **31**, 1258 (1992).

[8] S. Nakamura, M. Senoh, and T. Mukai, "p-GaN/n-InGaN/n-GaN double-heterostructure bluelight-emitting diodes", Jpn. J. Appl. Phys. **32**, L8 (1993).

[9] M. Khan, J. Van Hoven, J. Kuznia, and D. Olson, "High electron mobility GaN/AlGaN heterostructures grown by low-pressure metalorganic chemical vapor deposition", Appl. Phys. Lett. **58**, 2408 (1991).

[10] Available on line: "www.coumpondsemiconductor.net", September (2009).

[11] P. L. Hower, S. Pendharkar, and T. Efland, "Current status and future trends in silicon power devices", Proc. International Electron Device Meeting, San Fransisco 13.1.1, (2010).

[12] Available online: "www.nitronex.com", June (2011).

[13] Available online: "www.epc-co.com", August (2011).

[14] J. Ravkowski, D. Peftitsis, and H.-P. Nee, "Recent advances in power semiconductor technology, in H. Abu-Rub, M. Malinowski, & K. Al-Haddad (Eds.), Power electronics for renewable energy systems, transportation and industrial applications", John Wiley & Sons, Ltd. Chichester, UK, (2014).

[15] S. C. Binari, W. Kruppa, H. B. Dietrich, G. Kelner, A. E. Wickenden, and J. A. Freitas, Jr., "Fabrication and characterization of GaN FETs", Solid State Electron. **41**, 1549 (1997).

[16] B. J. Baliga, "Fundamentals of power semiconductor devices", Springer Science, Berlin (2008).

[17] R. Quay, "Gallium nitride electronics", Springer-Verlag, Berlin, (2008).

[18] J. I. Pankove and T. D. Moustakas, "Gallium nitride (I & II)", Academic Press, San Diego (1998 & 1999).

[19] A. Lidow, J. Strydom, M. de Rooji, D. Reusch, "GaN transistors for efficient power conversion", Efficient Wiley, El Segundo, USA (2015).

[20] R. T. Kemerley, H. B. Wallace, and M. N. Yoder, "Impact of wide bandgap microwave devices on systems", Proceedings of the IEEE, **90**, 1059 (2002).

[21] L. M. Tolbert, B. Ozpineci, S. K. Islam, and M. S. Chinthavali, "Wide bandgap semiconductors for utility applications", in Proc. Power and Energy Systems. ACTA Press, USA (2003).

[22] R. J. Trew, "SiC and GaN transistors - Is there one winner for microwave power applications?", Proceedings of the IEEE, **90**, 1032 (2002).

[23] B. Ozpineci, and L. M. Tolbert "Comparison of wide bandgap semiconductors for power electronic applications", Oakridge National Laboratory, ORNL/TM-20003/257 available online: http://web.ornl.gov/~webworks/cppr/y2001/rpt/118817.pdf (2003).

[24] J. I. Pankove and T. D. Moustakas, "Gallium nitride (I & II)", Academic Press, San Diego (1998 & 1999).

[25] A. D. Bykhovski, B. L. Gelmont, and M. S. Shur, "Elastic strain relaxation and piezoeffect in GaN-AlN, GaN-AlGaN and GaN-InGaN superlattices", J. Appl. Phys. **81**, 6332 (1997).

[26] E. T. Yu, G. J. Sullivan, P. M. Asbeck, C. D. Wang, D. Qiao, and S. S. Lau, "Measurement of piezoelectrically induced charge in GaN/AlGaN heterostructure field-effect transistors", Appl. Phys. Lett. **71**, 2794 (1997).

[27] E. Johnson, "Physical limitations on frequency and power parameters of transistors", RCA Rev. **26**, 165 (1965).

[28] R. Borges, "Gallium nitride electronic devices for high-power wireless applications," Application Notes, RF Design, pp. 72, (2001).

[29] Available online: "www.slideshare.net/Yole_Developpement/rf-gan-technology-market-analysis-applications-players-devices", RF GaN technology & market analysis: applications, players, devices & substrates" Report by Yole Development (2014).

[30] T. P. Chow, V. Khemka, J. Fedison, N. Ramungul, K. Matocha, Y. Tang, and R. J. Gutmann, “SiC and GaN bipolar power devices”, Solid-State Electron. **44**, 277 (2000).

[31] R. W. Keyes, "Figure of merit for semiconductors for high speed switches”, Proc. IEEE, **60**, 225 (1972).

[32] B. J. Baliga, "Semiconductors for high-voltage, vertical channel field-effect transistors", J. Appl. Phys. **53**, 1759 (1982).

[33] B. J. Baliga, “Power semiconductor device figure of merit for high frequency applications”, IEEE Electron Device Lett. **10**, 455 (1989).

[34] H. Morkoç, “Nitride semiconductors and devices: Fundamentals and applications”, Wiley-VCH, Weinheim, (2013).

[35] Available online: “www.pradeepchakraborty.com/2014/06/is-gan-on-si-disruptive-technology.html”, December (2015).

[36] M. Su, C. Chen, and S. Rajan “Prospects for the application of GaN power devices in hybrid electric vehicle drive systems”, Semicond. Sci. Technol. **28**, 074012 (2013).

[37] A. Ozgur, W. Kim, Z. Fan, S .N. Muhammad, A. Botchkarev, A. Salvador, B. Sverdlov, and H. Morkoc, “High transconductance normally-off GaN MODFETs” Electon. Lett. **31**, 1389 (1995).

[38] Available online: http://www.prlog.org/11043182-power-gan-market-technology-analysis-report-from-yole-dveloppement.htm”, December (2015).

[39] J. Z. Li, J. Y. Lin, H. X. Jiang, and M. A. Khan, “Effects of persistent photoconductivity on the characteristic performance of an AlGaN/GaN heterostructure ultraviolet detector”, Appl. Phys. Lett. **72**, 2868 (1998).

[40] O. Mitrofanov and M. Manfra, “Mechanisms of gate lag in GaN/AlGaN/GaN high electron mobility transistors”, Superlattices and Microstruct. **34**, 33 (2003).

[41] E. A. Douglas, S. J. Peatron, B. Poling, G. D. Via, L. Liu, and F. Ren, “Effect of drain bias on degradation of AlGaN/GaN high electron mobility transistors under X-Band operation”, Electrochem. Solid-State Lett. **14**, H464 (2011).

[42] B. Ozden, C. Yang, F. Tong, M. P. Khanal, V. Mirkhani, M. H. Sk, A. C. Ahyi, and M. Park, “Depth-resolved ultra-violet spectroscopic photo current-voltage measurements for the analysis of AlGaN/GaN high electron mobility transistor epilayer deposited on Si”, Appl. Phys. Lett. **105**, 172105 (2014).

[43] M. Wolter, P. Javorka, M. Marso, A. Fox, R. Carius, A. Alam, M. Heuken, P. Kordoš, and H. Lüth, “Photoionization spectroscopy of traps in doped and undoped AlGaN/GaN HEMTs”, Phys. Stat. Sol. (c) **0**, 82 (2002).

[44] Z. Q. Fang, D. C. Look, D. H. Kim, and I. Adesida, “Traps in AlGaN⁄GaN⁄SiC heterostructures studied by deep level transient spectroscopy”, Appl. Phys. Lett. **87**, 182115 (2005).

[45] M. A. Reshchikov and H. Morkoç, "Luminescence properties of defects in GaN", J. Appl. Phys. **97**, 061301 (2005).

Chapter 2

2 Theoretical Background

2.1 Crystal Structure of GaN

Wurtzite, zincblende, and rock salt are the three most known crystal structure types in the group III nitrides. Usually bulk GaN is found in wurtzite (hexagonal) structure since it is thermodynamically stable at ambient conditions. Stability of wurtzite structure depends on ionic contribution of bulk GaN to the bond due to the large difference in electronegativity of Ga and N atoms. On the other hand, growth of zincblende (cubic) structures for bulk GaN has been achieved on {001} crystal planes of cubic substrates, such as Si[1], MgO[2] GaAs[3], and SiC[4]. Contrary to zincblende structure, wurtzite structure is commonly found in bulk GaN because the lowest energy state for bulk GaN does not exist in cubic phase.[5] The rock salt structure can also be observed in bulk GaN under high pressure by tuning interatomic distances in the bulk material.[6] However, the rock salt structure phase does not have a significant contribution in electronic device applications.[7] In this dissertation, we will focus on wurtzite crystal structures, since the materials used have the wurtzite crystal structure.

The unit cell of wurtzite structure is hexagonal with two lattice constants, as equilibrium basal length "a_0" and equilibrium unit cell height "c_0" along the [0001] direction equilibrium cation-anion bond length ratio (the nearest neighbor distance) u_0 in unit of c_0. The ratio of c_0/a_0 is calculated as 1.633 when the value of u_0 is equal to 0,375 for an ideal wurtzite crystal.[8] GaN wurtzite structure has four atoms in the unit cell with two of each kind. Each atom belongs to one of two interpenetrating hexagonal closed packed sub-lattices which are distorted along the c axis by 5/8 of the equilibrium unit cell height. It falls into the (C_{6v}^4) space grouping category under the translational symmetry of a unit cell. The stacking sequence of (0001) plane for wurtzite structure is …*AaBbAaBbAaBb*… in the [0001] direction. Small and big letters represent two different constituents. Changes in stack sequence cause the free energy difference between the wurtzite

and the zincblende structures. When there is low energy difference between these phases, high density of structural defects are estimated in III nitrides.[8] In bulk GaN, the conventional [0001] direction occurs from the N-plane (Ga atoms) to the Ga-plane (N atoms) without inversion symmetry.

The inversion symmetry operation takes an atom with coordinates (x,y,z) and transform it to the inverted position (-x,-y,-z) around the inversion center. Inversion is denoted $\bar{1}$ in international notation. In the case of lack of inversion symmetry in GaN, while Ga atoms bind to only N-plane, N atoms bind only Ga atoms bound. As a result, wurtzite GaN structure can be found in two different polarity directions as [0001] and [000$\bar{1}$]. The [0001] polarity direction is generally known as Ga polarity and the direction of bonds are from Ga (cation) atoms to N atoms (anion) along the c direction. Whereas, in the [000$\bar{1}$] the direction the bonds along the c direction are from N atoms (anion) to Ga atoms (cation) and the polarity is known as N polarity. A schematic representation of Ga and N polarity of a model GaN crystal is shown in the Figure 2.1-1. In the Table 2.1-1, basic properties of GaN wurtzite structure at room temperature are summarized.[7,8,9,10]

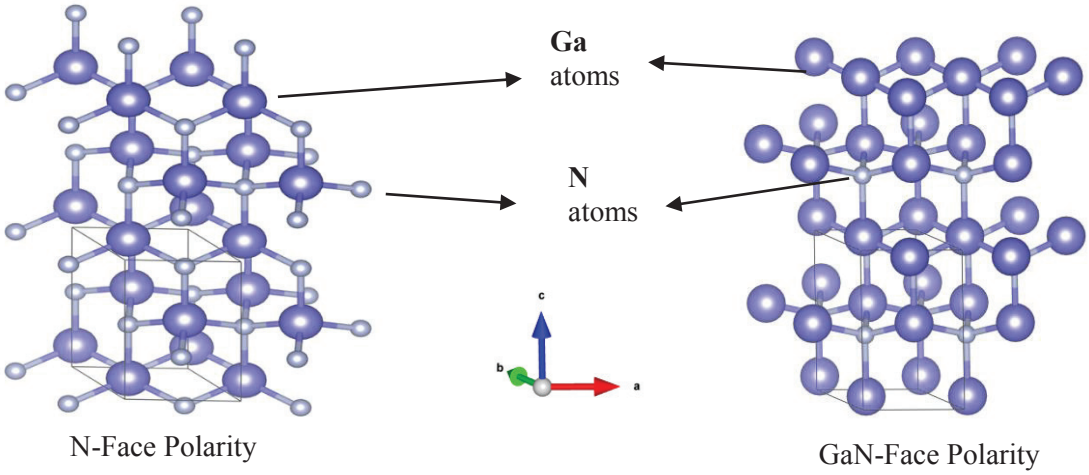

Figure 2.1-1: *GaN crystal structure (a) N-Face and (b) Ga-Face.*

Table 2.1-1: *Optoelectronic properties of wurtzite GaN crystal structure.*

Properties	GaN Wurtzite Structure
Lattice Constant	$a_0 = 3.1892 \pm 0.0009\ (\dot{A})$
	$c_0 = 5.1850 \pm 0.0005\ (\dot{A})$
Thermal Conductivity	$1.3\ (W\ cm^{-1}K^{-1})$
Number of atoms in 1 cm^3	$8.9 * 10^{22}$
Coefficients of thermal expansion (CTE)	$\alpha_a = 3.1 * 10^{-6}\ (K^{-1})$
	$\alpha_C = 2.8 * 10^{-6}\ (K^{-1})$
Dielectric Constants	$\epsilon_{r_{\parallel}} = 10.4$
	$\epsilon_{r_{\perp}} = 9.5$
	$\epsilon_r^{inf} = 5.5$
Low –field mobility	(n type) $\mu = 990\ (cm^2V^{-1}s^{-1})$
	(p type) $\mu = 150\ (cm^2V^{-1}s^{-1})$
Effective Mass	$m_n = 0.2\ m_e$
	$m_n(\Gamma - K) = 0.26\ m_e$
	$m_n(\Gamma - A) = 0.27\ m_e$
	$m_n(\Gamma - M) = 0.33\ m_e$
	$m_{p,h} = 1.4\ m_e$
	$m_{p,l} = 0.3\ m_e$
	$m_{p,so} = 0.6\ m_e$
Band Gap	$E_{g,\Gamma_1} = 3.43\ (eV)$
	$E_{g,\Gamma_3} = 5.29\ (eV)$
	$E_{g,L-M} = 5.49\ (eV)$
Mass Density	6.1 (g cm^{-3})
Molecular Weight	83.728 (g/mol)
Electron affinity	$4.1\ (eV)$

2.2 Polarization Effects in GaN

Polarization effects take place with the distortion of the negative cloud of electrons around the positive atom nuclei in the opposite direction of applied electric field. This causes the accumulation of the charges with an amount of "q" in different sides of the atom within a distance "d" with a dipole moment of "$\vec{p}$". Polarization density or polarization of the material is equal to the average electric dipole moment "<p>" divided by the unit volume "V" of a polarized material.

$$\vec{p} = q\vec{d} \qquad [\ 2.2\text{-}1\ ]$$

$$P = \frac{< p >}{V} \qquad [\ 2.2\text{-}2\ ]$$

More generally, the i^{th} type of atom in the vicinity of "r" with the average number of N_i per unit volume and average dipole moment of $< p_i >$ polarization is defined as ;

$$P(r) = \sum N_i < p_i > \qquad [\ 2.2\text{-}3\ ]$$

Significant polarization effects have been observed in group III-V nitride semiconductors as a consequence of high electronegativity in the noncentrosymmetric nitride crystals. Larger piezoelectric coefficients were stated in nitrides compared to the other best known group III-V semiconductors.[11] Semiconductor nitrides exhibit piezoelectric polarization in the presence of strain along [0001] direction, due to the absence of a center of inversion as stated in section Crystal Structure of GaN. Lattice mismatch strain and thermal strain, which is attributable to the dissimilarity of thermal expansion coefficients among the substrate and epitaxial layers, are known as two main causes of piezoelectric effect.[12]

Piezoelectric polarization produced by strained can be lowered by reducing the strain through the increase of defect related relaxations. Even in the lack of strain wurtzite GaN has the ability to exhibit a polarization called spontaneous polarization due to its distinctive crystal structure properties. For the ideal wurtzite crystal structure, the nonvanishing spontaneous polarization is permitted.[13] In the presence of heterojunctions with different electronegativity, significance of spontaneous polarization increases. An example would be the existence of spontaneous polarization between AlGaN and GaN in different amounts and piezoelectric polarization in AlGaN/GaN heterostructures cause the increase of the polarization charges. It is known that the presence of polarization charges has a huge effect on device performance of all nitride based devices, especially HFETs.[12] Moreover, both spontaneous and piezoelectric polarizations has an effect on the band structure of the heterojunctions. Therefore, it is of great importance to take polarization effect in consideration in device designs.

2.2.1 Piezoelectric Polarization

Piezoelectric polarization is caused by the shifts of the unit cells with respect to each other due to the external stress. Piezoelectricity only occurs in the absence of center of inversion. As a result of the change in lattice parameters of a_0 and c_0 due to the applied stress, the polarization strength will be changed. In the case of the compressive biaxial stress while a_0 values will increase, c_0 will decrease. This will lead to an increase in the c_0/a_0 ratio and hence, a decrease in the total polarization strength since piezoelectric and spontaneous polarizations will through in opposite directions. Based on the same logic, piezo and spontaneous polarizations will act in the same direction and increase the total polarization when a tensile biaxial stress is applied. For better understanding of piezoelectric polarization calculations, one should consider the strains by the tensor of e_{ijk} of piezoelectric coefficient.

$$P_i^{PZ} = \sum_j e_{ijk}\varepsilon_{jk} \; ; i = 1,2,3 \ldots . and \; j = 1, \ldots ,6 \qquad [\text{ 2.2-4 }]$$

here P_i , e_{ijk}, and ε_{jk} denotes the i^{th} component of piezoelectric polarization, electric piezoelectric coefficient, and strain, respectively.[14] In the presence of only biaxial strain, without shear;

$$\varepsilon_{xx} = \varepsilon_{yy} = \frac{a - a_0}{a_0} \qquad [\text{ 2.2-5 }]$$

$$\varepsilon_{zz} = \frac{c - c_0}{c_0} \qquad [\text{ 2.2-6 }]$$

$$\varepsilon_{yz} = \varepsilon_{zx} = \varepsilon_{xy} = 0 \qquad [\text{ 2.2-7 }]$$

where $\vec{x}\ and\ \vec{y}$ are basal (in) plane direction, $\vec{z}$ is in the [0001] growth direction out of the plane, and a and c are basal length and unit cell height lattice constants of strained structure, respectively. Subscribe "0" under the lattice constants represents the relaxed (unstrained) structures. ε_{xx} and ε_{yy} are the symbols for the representation of the basal plain strain along $\vec{x}\ and\ \vec{y}$ directions, and ε_{zz} denotes the strain along the growth direction.[12,9]

In the case of a structure with [0001] growth direction along the z axis when setting the value of "i" to "3", piezoelectric polarization can be acquired as follows; [9,12]

$$P_{PZ} = 2e_{31}\varepsilon_{xx} + e_{33}\varepsilon_{zz} \qquad [\ 2.2\text{-}8\ ]$$

One can express the strain in the z direction in terms of the x component of the basal length strain through use of the elastic coefficients C_{ij} as;

$$\varepsilon_{zz} = -2(\frac{C_{13}}{C_{33}})\varepsilon_{xx} \qquad [\ 2.2\text{-}9\ ]$$

Combining equations [2.2-5] and [2.2-8]with [2.2-9] strain induced piezoelectric polarization along the z axis of wurtzite III-V semiconductors can be calculated as follows;

$$\vec{P}_{PZ} = 2(e_{31} - e_{33}\frac{C_{13}}{C_{33}})(\frac{a - a_0}{a_0})\vec{z} \qquad [\ 2.2\text{-}10\ ]$$

In the wurtzite nitride structures, the value of the e_{31} is always negative as opposed to positive values of $e_{33}, C_{13}, and\ C_{33}$, and this makes the result of $(e_{31} - e_{33}\frac{C_{13}}{C_{33}})$ always negative. Therefore, one can conclude that under tensile stress ($a>a_0$), the piezoelectric polarization of III nitrites is always negative, whereas it becomes positive when a compressive stress ($a<a_0$) is applied.

Piezoelectric parameters of end binary points of GaN and AlN, which are given in the table 2.2-1 are used to derive parameters of $Al_xGa1_{-x}N$ here after indicated as AlGaN up to first order. Using the Vegard's law the piezoelectric polarization of AlGaN can be expressed as follows;

$$\vec{P}_{PZ} = [x\overleftrightarrow{e}\,AlN + (1-x)\overleftrightarrow{e}\,GaN]\vec{\varepsilon}(\mathrm{x}) \qquad [\ 2.2\text{-}11\ ]$$

Table 2.2-1: *Piezoelectric constants e_{ij}, dielectric constants ε_{ijk}, elastic coefficients C_{ij} and their ratios R and lattice parameter a_i, c_i of binary wurtzite GaN and AlN materials.*

Parameter	GaN	AlN	Ref
e_{33} (C m^{-2})	0.73	1.46	[11]
	1	_	[15]
	_	1.55	[16]
e_{31} (C m^{-2})	-0.49	-0.6	[11]
	-0.36	_	[15]
	_	-0.58	[16]
e_{15} (C m^{-2})	-0.3	_	[15]
	_	-0.48	[16]
ε_{11} (-)	9.5	9	[11,17]
ε_{33} (-)	10.4	10.7	[11,17]
C_{33}(GPa)	415	384	[18](LDA)
		373	
C_{31}(GPa)	83	111	[18](LDA)
		108	
$R = -2\frac{C_{31}}{C_{33}}$	-0.4	-0.578	[18](LDA)
		-0.579	
a_0 ($\dot{A}$)	3.189	3.112	[19]
	6.040	5.814	[11]
	3.1890	3.1106	[13](Calculated)
	3.1986	3.1095	[13](Experimental)
c_o ($\dot{A}$)	5.185	4.982	[19]
$\frac{a_0}{c_0}$	1.633	1.6010	[11]
	1.6259		

2.2.2 Spontaneous Polarization

The wurtzite GaN exhibits strong spontaneous polarization, even in the lack of applied strain due to the presence of robust ionicity of the covalent bonds. In the wurtzite GaN, spontaneous polarization is observed along the growth axis and results in a strong electric field of 3 MVcm^{-2}.[16] Strength of the spontaneous polarization is also affected by the non-ideality of the crystal lattice as well as the ionicity of the covalent bonds. In wurtzite nitride structures, the direction of the covalent bonds which are primarily responsible from spontaneous polarization, is along the growth direction. The other three covalent bonds

are equally ionic and they produce a resultant polarization in the opposite direction. With the increase of a_0 and decrease of c_0, the ratio of c_0/a_0 decreases hence, the resultant polarization decreases since the angle between these three covalent bonds and the growth axis gets wider. As a consequence, an increase in the macroscopic spontaneous polarization happens. The value of the ratio of c_0/a_0 for GaN and AlN was given in the Table 2.2-2.

As we stated in section 2.1 the GaN wurtzite structures have two growth layer as Ga face up or N face up. Both in the Ga face up and N face up wurtzite structures, the direction of polarization appears different. An example would be, while the polarization direction towards to the substrate for Ga face interface, the polarization direction towards to the surface of the layer in N face interface. Based on the growth condition two different situations can be observed for an AlGaN layer grow on top of a GaN layer. Under tensile stress, an electron GaN channel at the interface is formed in the Ga- face up case because of parallel alignment of the spontaneous and piezoelectric polarizations. In the case of change in the both polarization orientations directions, where the growth layer is N-face up, there is no electron channel formed at the AlGaN/GaN interface. As in piezoelectric polarization, spontaneous polarization of AlGaN quaternary alloys can be calculated by using a linear combination of the binary end points with regard to the mole fraction. Consequently, according to Vegard's law spontaneous polarization of $Al_xGa_{1-x}N$ can be express as;

$$\overrightarrow{P^{SP}_{AlGaN}}(x) = x\overrightarrow{P^{SP}_{AlN}} + (1-x)\overrightarrow{P^{SP}_{GaN}} \qquad [\ 2.2\text{-}12\ ]$$

Linear interpolation of spontaneous polarization in $Al_xGa_{1-x}N$ ternaries by using generalized gradient approximation (GGA) and local density approximation (LDA) are given as;[9]

$$\overrightarrow{P^{SP}_{AlGaN}}(x) = -0.09x - 0.034(1-x) \text{ for GGA} \qquad [\ 2.2\text{-}13\ ]$$

$$\overrightarrow{P^{SP}_{AlGaN}}(x) = -0.1x - 0.032(1-x) \text{ for LDA} \qquad [\ 2.2\text{-}14\ ]$$

Table 2.2-2: *Spontaneous polarization of GaN and AlN in generalized gradient approximation (GGA) and in local density approximation (LDA).*[9,11,20]

Spontaneous Polarization	GaN	AlN
LDA (C m^{-2})	-0.032	-0.1
GGA (C m^{-2})	-0.034	-0.09

For the total polarization of AlGaN/GaN heterostructures total polarization is given as follows;

$$\vec{P}^{total} = \vec{P}^{SP} + \vec{P}^{PE} \qquad [\ 2.2\text{-}15\ ]$$

2.3 AlGaN/GaN Heterostructures

The term heterostructure is used to explain a structure that is formed with two or more different semiconducting layers with different optoelectronic properties and yet similar crystal structures. Heterojunction or heterointerface generally refers to the interface between these layers. For a heterojunction device, device concepts will depend on the type of the heterostuctures. For that reason, it is great of importance to study band alignment of heterojunction. Different semiconductor layers, which compose the heterojunctions result in band discontinuity because of the misalignment of conduction and valance bands. Since the bandgap of these heterojunctions is not identical, there will be band discontinuities in the alignment of two structures. These alignment discontinuities result in band bending of a real heterostructure under thermodynamic equilibrium to match the Fermi levels E_f of two semiconductors.

Heterostructures are referred to as *type I, type II,* and *broken* depending on their alignments. Straddle of conduction and valance bands of larger bandgap semiconductor with smaller bandgap semiconductor is known as *type I* and this the most common one. In *type II*, conduction and valance bands are staggered; their bandgap is overlap but do not completely enclose the other's bandgap. When the staggering between the conduction and valance bands turn out to be bigger and the band gaps do not overlap, the resulting heterostructure is referred to as *broken*. Types of heterostructure energy band alignments are shown in the Figure 2.3-1. In this figure, ΔE_c and ΔE_v stands for conduction and valance band offsets indicating the

difference between the conduction band and valance band edge at the interface relatively. The ΔE_g is a measure of band discontinuity and calculated with the addition of these band offset as follows;

$$\Delta E_g = \Delta E_c + \Delta E_g \qquad [\ 2.3\text{-}1\ ]$$

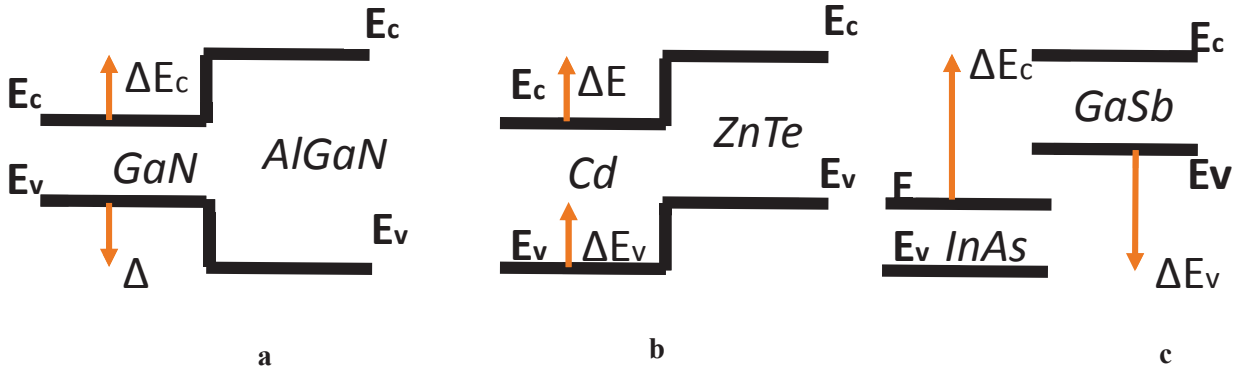

Figure 2.3-1: *Types of heterostructure energy band alignments: (a) Type I or straddled structure (b) Type II or staggered structure (c) Type III or broken structure.*

As shown in the Figure 2.3-1 AlGaN/ GaN heterojunctions are known as type I structures and created with the growth of wide band gap AlGaN barrier layer (doped or undoped) on top of a narrow band gap non-intentionally doped relaxed GaN layer. Figure 2.3-2 (a) shows a schematic cross-section of a basic Ga-face doped AlGaN/GaN heterostructure and the corresponding energy band diagram. When AlGaN and GaN are brought together to form a heterostructure, a triangular quantum potential well will be formed with the highly mobile two dimensional electron gas (2DEG), which will be described in detail later, as shown in the Figure 2.3-2 (b).

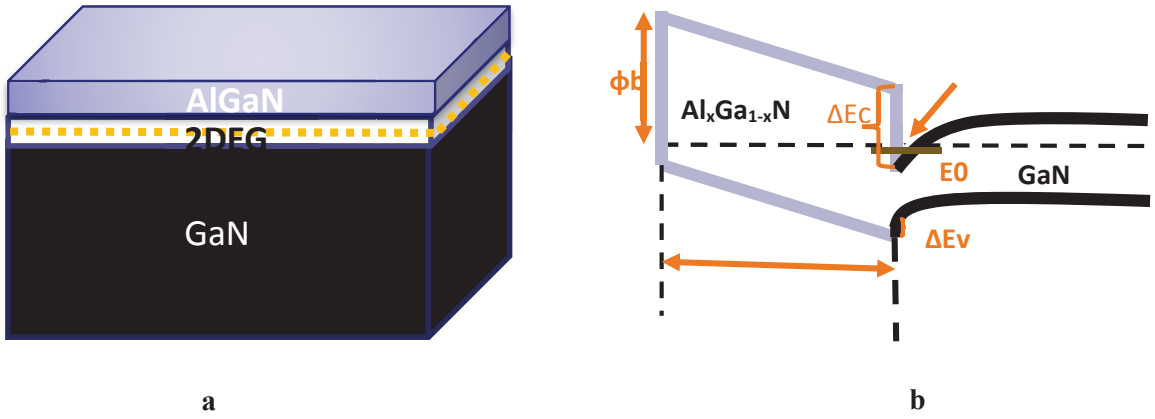

Figure 2.3-2:(a) S*chematic cross-section of a basic Ga-face doped AlGaN/GaN heterostructure and (b) the corresponding energy band diagram.*

Since specially quantized electrons in one direction are confined to move in the other two directions parallel to interface, they are referred to as 2DEG. The presence of the 2DEG is one of the biggest advantages of AlGaN/ GaN heterostructures and allows for the fabrication of an innovative device called High Electron Mobility Transistor (HEMT) that will be discussed in the following paragraphs. Moreover, the availability of the AlGaN/GaN heterostructure with simultaneously achieved high voltage, high current, and low on-resistance, results in high-power high-efficiency operation, which provides technological advantages.

2.3.1 Formation of 2DEG in AlGaN/GaN

The wurtzite AlGaN/GaN based transistor structures have a piezoelectric polarization of the strained top layer five times larger than that of the AlGaAs/GaAs heterostructures.[21] The spontaneous and piezoelectric polarization in wurtzite GaN is ten times stronger than that of conventional III-V semiconductor materials.[16] At undoped AlGaN/GaN interfaces, these very high polarizations and resulting electric fields are mainly the cause of accumulation of high interface charges densities along the heterojunction in the high bandgap AlGaN side.[22] Availability of undoped AlGaN/GaN layers results in

enhanced electron mobility in the 2DEG by further reducing the Coulomb scattering. It is known that enhanced mobility future of HEMTs differentiate these devices from other FETs devices. The origin of the 2DEG at the AlGaN/GaN heterostructures has been a controversial issue since the layers are not doped.

Some researchers suggested that the AlGaN barrier or the surface could be the source of the electrons.[23,24] The observations of variations in thickness and alloy composition of the AlGaN barrier layer with the change of 2DEG density, made positive surface charge states or donor-like surface states contenders for the source of the 2DEG.[25,26,27] The donor-like states are also called positive surface charge states because they are positively charged when they are emptied and neutral when they are occupied. There are different claims about the origin of these surface defects. Some researchers believe that oxygen impurities, due to the oxidation of the gallium terminated layers, inside the conduction band, are the reason for these surface donors.[28,29] The nitrogen atoms can dissociate from AlN or GaN bonds due to the high annealing and can form volatile molecules, such as NO with O atoms.[30] Other researchers have claimed that these surface donors are nitrogen vacancies.[31,32]

The surface states with an energy level E_d lie below the conduction band for a thin AlGaN barrier layer. In the case of the deep level surface defect, 2DEG is not observed. However, the donor levels reaches the Fermi level at a certain critical thickness t_{cr} with decrease of $E_d - E_f$ due to the increase of the barrier thickness. As a result, electrons inside the occupied surface states become available to be transferred to empty conduction band states at the interface. Moreover, they leave positive surface charges behind and create 2DEG. The number of transferred electrons increases with the increase of the AlGaN barrier thickness of t higher than the one of t_{cr}. The expression for the critical thickness t_{cr} can be given as follows;

$$t_{cr} = (E_d - \Delta E_c)(\frac{\varepsilon}{q\sigma_{pol}}) \qquad [\ 2.3\text{-}2\ ]$$

where ε is the AlGaN dielectric constant, ΔE_c is the conduction band offset of AlGaN as shown in equations below;

$$\varepsilon(x) = 9.5 - 0.5x \qquad [\ 2.3\text{-}3\ ]$$

$$\Delta E_c = 0.7\left(E_g(x) - E_g(0)\right) eV \qquad [\ 2.3\text{-}4\ ]$$

here $E_g(x)$ is the bandgap energy of $Al_XGa_{1-x}N$ and given as;

$$Eg(x) = x \cdot\ Eg^{AlN} + (1-x) \cdot\ Eg^{GaN} - bx(1-x) \qquad [\ 2.3\text{-}5\ ]$$

where "x" is the Al mole fraction (0.25), $Eg\,(x)$ is the band-gap of the $Al_xGa_{1-x}N$, Eg^{AlN} is the band-gap energy of the AlN (6.2 eV)[7,33] Eg^{GaN} is the band-gap energy of the GaN (3.43eV)[34] , and b is the band-gap bowing parameter (curvature correction in the calculation of bandgap energies), 1 in this case.[35,36,37]

In the case of critical thickness determined by the band gap energy of AlGaN, E_{AlGaN} is used instead of the surface state energy E_d and where E_d=1/2 E_{AlGaN}, the only available occupied states will be in the valance band. The only way for 2DEG to exist is for the barrier thickness of AlGaN layer to be high enough to bring the valance band to the Fermi level. Consequently, a surface hole gas can be produced with the transfer of electrons from the AlGaN valance band to the GaN conduction band.

The 2DEG density as a function of the barrier thickness is given as follows when $t>t_c$;

$$qn_S = \rho_P(1 - \frac{t_{cr}}{t}) \qquad [\ 2.3\text{-}6\ ]$$

here ρ_P is the polarization induced charges at the heterointerface due to the discontinuity of the total polarization $\vec{P}$ and is given as follows;

$$\rho_p = -\nabla.\vec{P} \qquad [\ 2.3\text{-}7\ ]$$

A polarization sheet charge density σ due the total polarization in the presence of an abrupt interface AlGaN/GaN or GaN/AlGaN (top/bottom) can be defined as follows;

$$\sigma = P_{TOP} - P_{BOTTOM} \qquad [\ 2.3\text{-}8\ ]$$

$$\sigma = \left(P_{SP_{TOP}} + P_{PZ_{TOP}}\right) - \left(P_{SP_{BOTTOM}} + P_{PZ_{BOTTOM}}\right) \qquad [\ 2.3\text{-}9\ ]$$

To explain the formation of the surface charges and 2DEG an undoped Ga-face wurtzite AlGaN/GaN heterostructure will be considered. N-face polarity AlGaN/GaN heterostructure will follow the general rules as well but detail can be found in Ambacher *et al*.'s research[16]. In the case of AlGaN/GaN heterostructure grown in the (0001) direction, there will be a positive charge at the interface of AlGaN, and a negative charge at the surface of AlGaN. This is because of the difference in the polarization between the positive and the negative charges due to the sheet electron charge density of n_s at the 2DEG, charges due to the ionized donors in the AlGaN layer ($+\sigma_{AlGaN}$), $\sigma_{surface}$ charges due to the ionized surface states, and buffer charges of σ_{buffer} originating from the GaN buffer layer. A schematic illustration of the various space charge components in Ga-face polarity AlGaN/GaN heterostructure can be seen in the Figure 2.3-3. The net charge of various space charge components at the surface must be zero to retain the surface charge neutrality. Therefore, one get the following equation by solving space charge neutrality;

$$+\sigma - \sigma + \sigma_{AlGaN} + \sigma_{surface} - \sigma_{buffer} = qn_s \qquad [\ 2.3\text{-}10\ ]$$

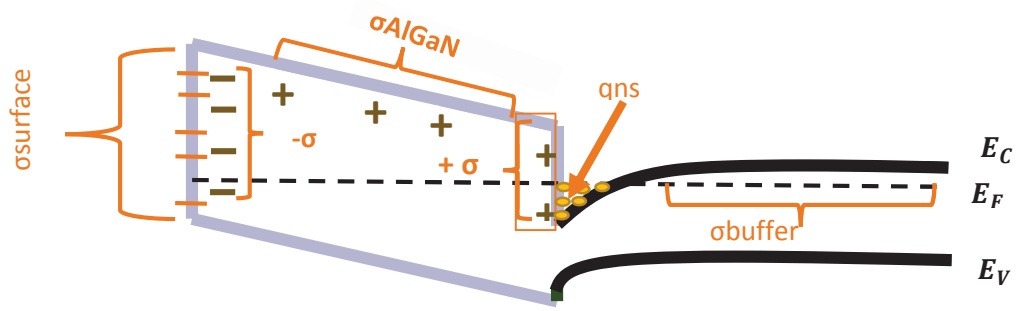

Figure 2.3-3: *Schematic illustration of the conduction band diagram of the AlGaN/GaN heterostructure showing various space charge components.*

In the above equation, induced bound charges of positive and negative σ cancels each other and do not contribute to 2DEG. In the case of undoped AlGaN as we stated above, there will be no ionized donors and σ_{AlGaN} will be equal to zero. From the condition of charge neutrality, it is obvious that, σ_{buffer} charges are forced to be negative to keep the 2DEG at the interface. As a result, equation [2.3-10] can be written as follows;

$$\sigma_{surface} = qn_s \qquad [\ 2.3\text{-}11\ ]$$

A semi-classical electrostatic model based on overall charge neutrality can be used to calculate the theoretical sheet carrier concentration n_s of 2DEG for an undoped $Al_xGa_{1-x}N$/GaN HFET structure with a Schottky contact as follows;[16]

$$n_s(x) = \frac{\sigma(x)}{e} - \left(\frac{\epsilon_0\ \epsilon_r(x)}{de^2}\right)(e\varphi_B(x) + E_f(x) - \Delta E_c(x)) \qquad [\ 2.3\text{-}12\ ]$$

here x is the aluminum alloy composition of the $Al_xGa_{1-x}N$ barrier layer, $\sigma(x)$ is the polarization induced bound sheet charge density at the AlGaN/GaN heterojunction, ϵ_0 is the permittivity of the free space, $\epsilon_r(x)$ is the relative dielectric constant of the $Al_xGa_{1-x}N$ layer, e is the charge of an electron, d is the thickness of $Al_XGa_{1-x}N$, $e\varphi_B$ is the Schottky barrier height of the gate contact on top of the $AlxGa_{1-x}N$ layer, $E_f(x)$ is the position of the Fermi level with respect to the GaN conduction band edge, and $\Delta E_c(x)$ is the conduction band offset at the AlGaN/GaN interface.

The Fermi level $E_f(x)$ is derived as follows; [38]

$$E_f(x) = E_0(x) + \left(\frac{\pi\hbar^2}{m^*(x)}\right)n_s(x) \qquad [\ 2.3\text{-}13\ ]$$

where $m^*(x)$ is the effective electron mass with the value equal to $0.22m_e$, and $E_0(x)$ is the ground state sub band level of the 2DEG density and is given by equation [2.3-14];

$$E_0(x) = \left[\left(\frac{9\pi\hbar^2}{8\ \epsilon_0\ \sqrt{8m^*(x)}}\right)\left(\frac{n_s(x)}{\varepsilon(x)}\right)\right]^{\frac{2}{3}} \qquad [\ 2.3\text{-}14\ ]$$

2.4 Semiconductor Contacts

Connection between the devices and the outside world is provided by contacts with the deposition of the required metal on the semiconductor. When a semiconductor and metal are brought together, if no barrier exists to carrier flow in either from metal to semiconductor or from semiconductor to metal, then the contact is known as ideal contact. There are two kinds of contacts known as Schottky contacts or rectifying contacts and non-rectifying ohmic contacts with a very small resistivity.

2.4.1 Ohmic Contact

Ohmic contact is a metal-semiconductor contact that has virtually no barrier between the metal and the conduction band of the semiconductor. A contact is defined as ohmic when the ratio of the potential drop "*V*" across the contact versus the current "*I*" following through the contact is linear with a constant R_c. The contact resistance for metal-semiconductor contacts with a high doping level in the semiconductor can be calculated by the tunneling process as follows;[39]

$$R_c = \exp[\frac{2\sqrt{\varepsilon_s m^*}}{h}\left(\frac{\varphi_{Bn}}{\sqrt{N_D}}\right)] \qquad [\ 2.4\text{-}1\ ]$$

where φ_{Bn} is the barrier height and N_D is the doping concentration, ε_s is the dielectric constant of the semiconductor, m^* is the effective mass for electrons, and *h* is the Planck's constant. It is important for ideal ohmic contacts to have a low contact resistance compared to the bulk resistance of the device in order to reduce the on-state voltage drop and power dissipation during current conduction. For a typical power device structure, a specific contact resistance less than $1x10^{-5}\Omega cm^2$ is required.[40]

A metal-semiconductor contact with high doping concentration, low barrier height and narrow barrier width can be utilized to obtain the low contact resistance. The use of a thin layer of small bandgap material can also help to lower contact resistance. Barrier height of the contact can be lowered with the suitable choose of the metal and thermal annealing method. Moreover, in AlGaN/GaN heterostructures,

highly doped GaN layer is placed at the top to lower the barrier. Contact resistance minimization is required to obtain max drain current (I_D), to minimize the power dissipated and to achieve higher frequencies (f_{max}) and extrinsic transconductance (g_{mext}).

In addition, a high density of states near the interface to bring the Fermi level in the semiconductor close to the conduction band is required for the formation of ohmic contacts at the surface of the semiconductor. In the wide bandgap III-V semiconductors, this can be achieved with super lattice engineering in the cap layers.[41] Moreover, ideal ohmic contact must be mechanically stable not to be scratched away during testing or bonding and to prevent degradation during high temperature annealing.[9] It should also have a smooth surface morphology to prevent alignment problems for further lithography steps.[9]

It is difficult to make ohmic contact on a wide-gap III-V semiconductor because the lack of the metal with low work function yields a high barrier. Typically Ti/Al/blocking layer/Au multilayer metallization scheme is used in AlGaN/GaN heterostructures.[42] The most common blocking layers are the metals Ni, Ti, Mo or Pt.[43,44,45,46] These barrier layers are used to prevent penetration of Au. Extraction of nitrogen out of the AlGaN/GaN and forming titanium nitride (TiN) *via* thermal annealing is known as the basic mechanism behind the formation of the ohmic contact.[47] Removal of the N creates high density of N vacancies, which causes donor states near the metal interface or in the AlGaN layer. [42,48] These donor states pin the Fermi level and result in a tunnel junction and the facilitation of the electron transport mechanism. Nitrogen vacancies in AlGaN causes the AlGaN material underneath the contact to become highly doped enabling electrons which can tunnel through the remaining thin potential barrier that separates them from the 2DEG.[49]

Using Ti/Al sequence, rather than a single Ti layer provides optimum Ti/Al thickness on AlGaN/GaN.[42] Since this sequence has lower resistivity and work function compared to Ti, it also reduces the contact resistance.[50] Al might diffuse into the contact interface and form AlN, which causes an increase in the contact resistance.[50] Every metal used in the ohmic contact has their own specific roles. The first, metal layer deposited on the AlGaN is the titanium (Ti) and it is used as an adhesion layer to provide good

mechanical stability.[51] It also dissolves the native oxide on the AlGaN surface.[52] More importantly, as mentioned above, it creates nitrogen vacancies (V_N) in the AlGaN barrier layer. Aluminum reacts with Ti and forms Al_3Ti layer to prevent the oxidation under the Ti layer.[51] It also serves as a diffusion barrier for the Ni and Au layers since they might form high Schottky barriers with the AlGaN barrier layer.[52] Finally, it is responsible for improving contact resistance. [42]

2.4.2 Schottky Contact

The Fermi level position of a metal and semiconductor generally lies in different energy levels when they are not in contact. In this case, a metal is defined by its work function φ_m as given equation [2.4-5] and a semiconductor is characterized by its electron affinity χ_{sc} given in equation [2.4-4]. The metal work function is defined as the energy required moving an electron from the Fermi level position in the metal to a rest state in free space outside the surface of the metal. Similarly, electron affinity is the energy required to move an electron from the bottom of the conduction band in the semiconductor to a rest state in free space outside the surface of the semiconductor.

When a semiconductor and a metal with no surface states are brought together, Fermi levels of the metal and semiconductor will align and cause a charge motion from the higher energy side to the lower one. Moreover, alignment of Fermi levels forms a positively charged depletion region or space-charge layer in the semiconductor as given in equation [2.4-2] and a potential barrier at the interface. The depletion region with a depletion width of W_D as in equation [2.4-2] gives rise to a built-in potential (Vbi) and electric field (E_0) at the interface between the metal and the semiconductor.

$$W_D = \sqrt{(V_{bi} - V_{ext} - \frac{kT}{q})\frac{2\varepsilon_s}{qN_D}} \qquad [\ 2.4\text{-}2\ ]$$

where V_{ext} is the applied voltage and ε_s is the permittivity of the semiconductor. The built in potential which is necessary for electrons in the conduction band to overcome to move into the metal is given by equation [2.4-3];

$$V_{bi} = \varphi_{Bn} - V_n \qquad [\ 2.4\text{-}3\ ]$$

The potential barrier prevents charge carriers from following one to another. The Schottky barrier height φ_{Bn} between the metal and the n-type semiconductor is given as the difference between the work function of the metal and the affinity of the semiconductor.

$$\varphi_{Bn} = \varphi_m - \chi_{SC} \qquad [\ 2.4\text{-}4\ ]$$

$$-e\varphi_m = E_{vac} - E_F \qquad [\ 2.4\text{-}5\ ]$$

$$-e\chi_{sc} = E_{vac} - E_C \qquad [\ 2.4\text{-}6\ ]$$

When a negative voltage is applied to the n-type semiconductor with respect to metal, (a forward bias) the barrier height is lowered. Whereas the semiconductor to metal barrier potential increases with the applied positive voltage in the n-type semiconductor with respect to metal (a reverse bias). In the case of applied bias, there will be current flow, if there is sufficient energy provided for the carriers in metal or semiconductor to transport.

It is known that metal work function and semiconductor electron affinity are important to determine Schottky barrier height. Higher barrier height can be obtain through metals with high work function, such as Palladium (Pd=5, 12 eV), Gold (Au=5.10eV), Nickel (Ni=5.15eV), and Platinum (Pt=5.65eV).[53] Ni/Au is the most frequently used metallization for Schottky diode in AlGaN/GaN HEMTs.[7,54] It is also recognized that high reverse gate leakage current is one of the key issues in AlGaN/GaN HEMTs.[54] The excess leakage current not only contributes to low frequency noise[55] but also deteriorates the breakdown voltage.[56] Therefore, it reduces the efficiency and reliability of the transistors for power electronic applications. It is believed that effective barrier thinning through unintentional surface-defect donors leads to this effect.[7,57] Consequently, it is of great importance to investigate the Schottky contacts in AlGaN/GaN HEMTs structures.

2.4.3 Electrical Measurement of Contacts

2.4.3.1 Transmission Line Model / Transfer Length Method

The transmission line model (TLM) is one of the most commonly used methods to evaluate the specific contact resistivity and other related parameters of ohmic contact.[9] For this measurement, an array of identical ohmic contacts are metalized on the semiconductor with increasing spaces, "*l*", between the contacts. Figure 2.4-1displays a schematic representation of circular (a) and rectangular (b) contact designs for the TLM measurement. The total resistance R_T *(Ω)* can be found from the resistance R versus l measurements by using a linear regression as described in the following equation;[9]

$$R_T = 2R_C + \frac{lR_S}{Z} \qquad [\ 2.4\text{-}7\ ]$$

where R_C is the contact resistance and l is the spacing between the contacts, Z is the width of the contact and R_S is the sheet resistance of the semiconductor layer. R_C is multiplied by two because the resistance is measured between the two contacts and the value of it can be found from the intercept of the R versus l measurements. The value of R_S can be derived from the slope of R versus l line. The value of specific contact resistivity ρ_S is given by equation [2.4-8].

$$\rho_S = \frac{R_C^2}{R_S} \qquad [\ 2.4\text{-}8\ ]$$

The current flowing in (or out) at the edge of the contact is important because the current drops off until at the far edge when moving away from that edge. This is known as "current crowding" which shows the current drop from the edge of the contact and approximated as follows;

$$I(x) \sim \exp(-\frac{x}{L_T}) \qquad [\ 2.4\text{-}9\ ]$$

here L_T is the average distance that an electron (or hole) travels in the semiconductor beneath the contact before it flows up into the contact and given by equation [2.4-10];

$$L_T = \sqrt{\frac{\rho_C}{R_S}} \qquad [\ 2.4\text{-}10\ ]$$

L_T is also determined at the intercept of R versus l graph when R is equal to zero.

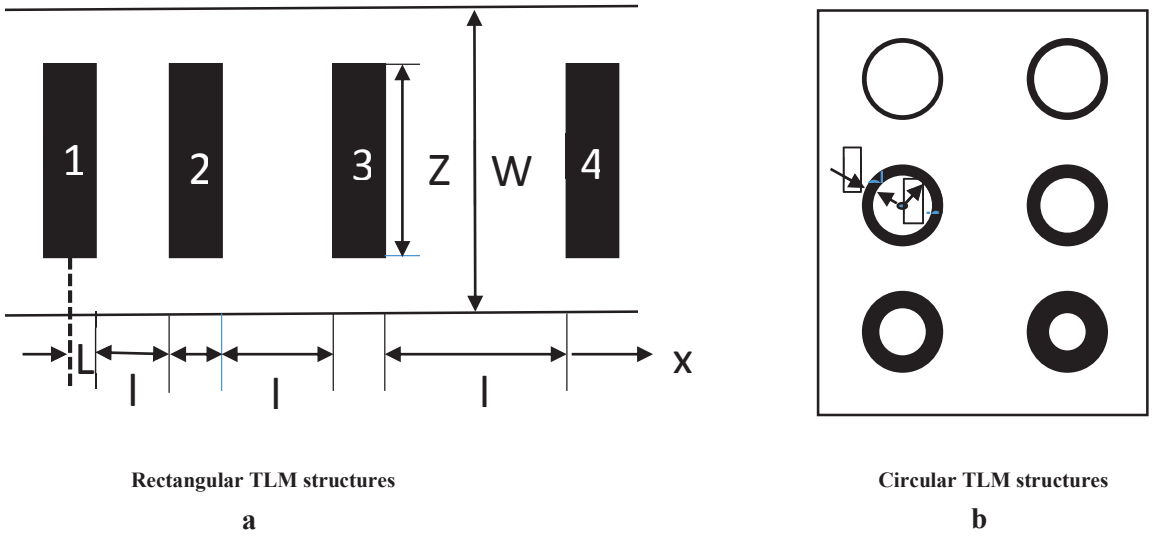

Figure 2.4-1: *Schematic representation of (a) circular and (b) rectangular contact designs for the TLM measurement.*

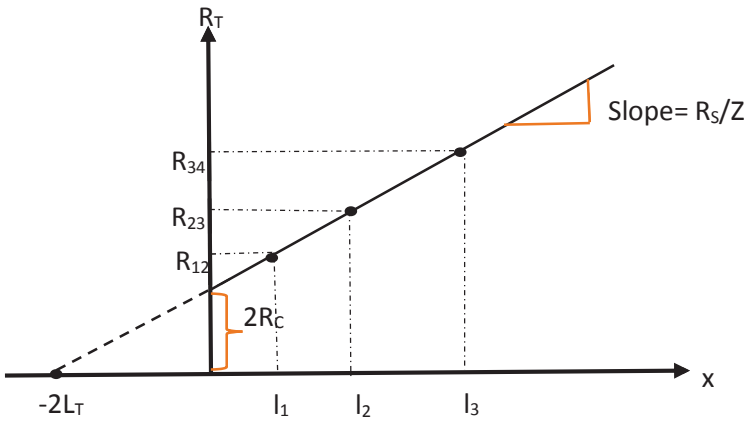

Figure 2.4-2: *A representative graph of the variation of resistance with respect to the gap distance for TLM measurements.*

A representative graph of the variation of resistance with respect to the gap distance is shown in the Figure 2.4-2. The current flow at the contact edge significantly affects the results of the contact resistance for the rectangular contacts. Therefore, to avoid unwanted current flow mesa island fabrication is required. In the case of circular contacts, there is no unwanted current flow even without mesa etching. In the TLM method, to prevent the edge effects the spacing between the contacts must be much smaller than the contact width. To avoid from edge effect circular transmission line method (CTLM), where the contacts are circular, can be used. To obtain R_C and R_S values from CTLM following relation is used;[58]

$$R_T = R_C \frac{1}{2\pi}\left(\frac{1}{r} + \frac{1}{r-d}\right) + R_S \frac{1}{2\pi} \ln \frac{r}{r-d} \qquad [\ 2.4\text{-}11\ ]$$

2.4.3.2 Current-Voltage Characteristics

The majority charge carriers i.e., electrons (holes) in the case of an n-type (p-type) semiconductor, respectively, are the main sources for the current transport through a metal-semiconductor junction. There are several ways for the carriers overcome the barrier across a metal-semiconductor junction. In the case of *thermionic emission* (*TE*), electrons can be transported over the top of the barrier which is lowered with respect to Fermi level in the semiconductor by an amount equal to the applied bias.[9] Electrons can be also transport by tunneling through a thinner barrier with some energy gained from the bias in a process known as *thermionic field emission (TFE).*[9] Direct electron tunneling occurs from the conduction band or Fermi level of the semiconductor to the metal in the *field emission (FE)* process.[9] This kind of current transport is more seen in ohmic contacts.

For a typical Schottky diode with moderately doped (low N_D, doping concentration) semiconductors thermionic emission is the dominant process for the current transport under moderate temperature. Thermionic field emission and/or field emission process will become dominant in the case of highly doped semiconductors and the tunneling probability of the electrons will increase. Figure 2.4-3 displays an energy diagram and current flow mechanisms for TE, TFE, and FE processes. A corresponding current versus voltage graph for these processes is shown in the Figure 2.4-4.

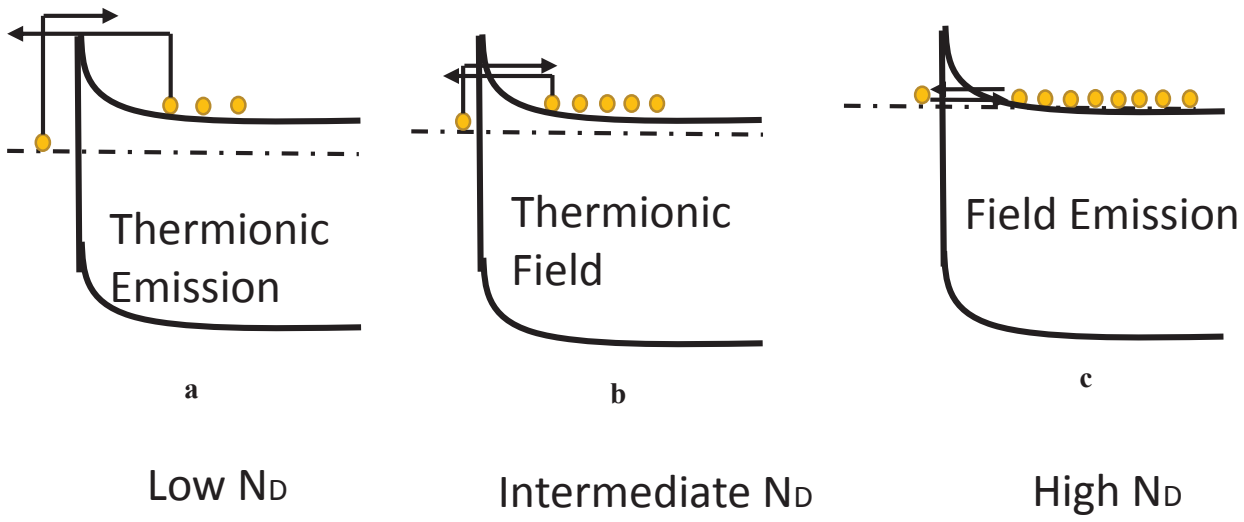

Figure 2.4-3: *Energy diagram and current flow mechanism for (a) TE process (b) TFE process (c) FE process.*

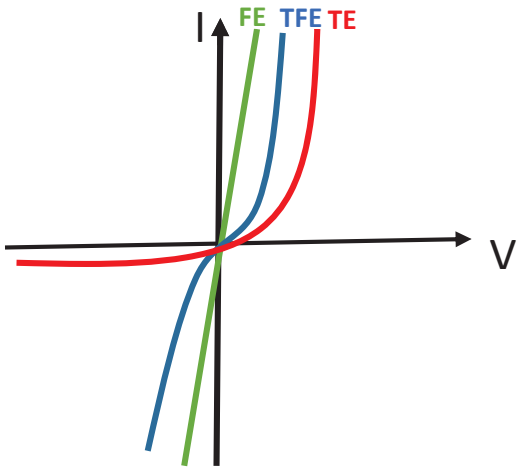

Figure 2.4-4: *Representative current versus voltage graph for TE, TFE, and, TE processes.*

We will focus on a traditional current density-voltage (J-V) expression given by thermionic emission theory:[9]

$$J_{TE} = J_S[\exp\left(\frac{qV}{nkT}\right) - 1] \qquad [\ 2.4\text{-}12\ ]$$

where T is the temperature, k is the Boltzmann constant, and n is the ideality factor and approximately equal to 1. J_S is the saturation value of the current density J_{TE} given by equation [2.4-13].

$$J_S = A^*T^2\exp[\frac{-q(\varphi_B - \Delta\varphi)}{kT}]* \qquad [\ 2.4\text{-}13\ ]$$

here A^* is the effective Richardson constant, and $\Delta\varphi$ is the image force barrier lowering and they are both voltage dependent. Hence, for applied voltages greater than $3kT/q$ the current density-voltage characteristics are simply written as follows;

$$J_{TE} = J_S\exp(\frac{qV}{nkT}) \qquad [\ 2.4\text{-}14\ ]$$

In the case of reverse direction, saturation current density J_S is generally used instead of current density J_{TE} because the barrier lowering becomes more important.[9] Schottky barrier requires detailed information on the distribution of interface states. Since it is hard to get all the information required, the barrier height of Schottky contact is usually determined from forward response reverse current-voltage (I-V) characteristics. The plot of J_S/T^2 versus $1/T$ is called a Richardson plot and by using this plot one can derive barrier height and the Richardson constant from a linear fit.[14]

$$\varphi_B = \frac{kT}{q}\ln\frac{A^*T^2}{J_S} \qquad [\ 2.4\text{-}15\ ]$$

where k is the Boltzmann constant, T is the absolute temperature of device, and A^* is the Richardson constant. It is important to note that the barrier height is derived at zero bias. The current will deviate from linear due to the series resistance at high biases.

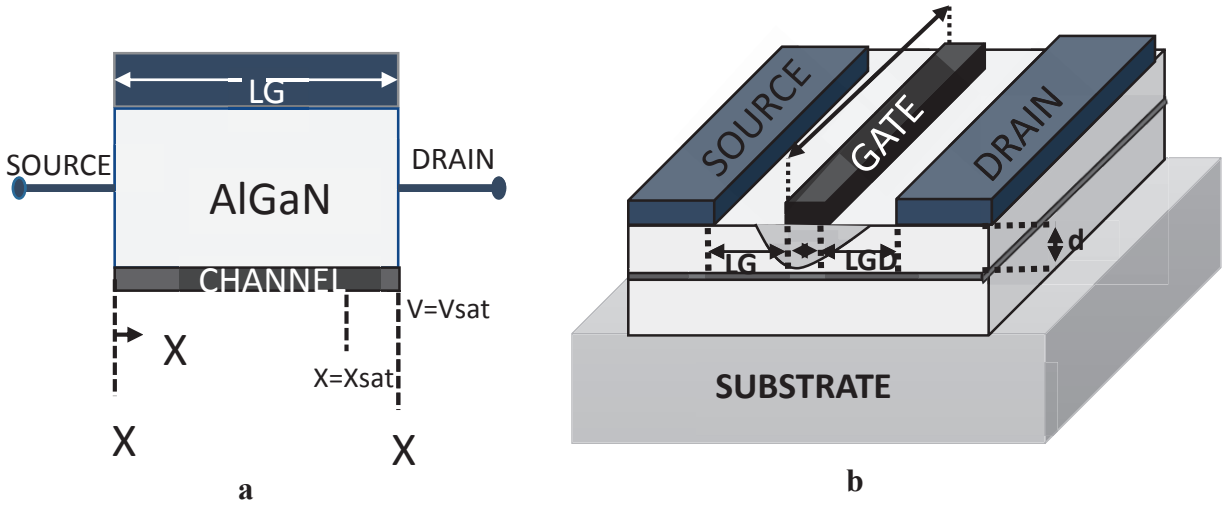

Figure 2.4-5: (*a) Intrinsic transistor with increasing potential V(x) from source (x = 0) to drain(x = L) when a current is flowing (b) Schematic draw of AlGaN/GaN HEMT.*

The basic geometrical parameters of the HEMTs are shown in the Figure 2.4-5. L_G is the gate length and W_G is the gate width. L_{GS} and L_{GD} are the gate to source and the gate to drain terminal spacing, respectively. The thickness of the active layer from the gate contact to the conductive channel is denoted by d. Dimension L_G is critical in determining the maximal frequency limits for the device. The gate width W_G is directly proportional to the drain current flowing through the device.[59] Consequently, while small-gate-width devices are used in low noise applications, for relatively low current applications larger-gate-width devices are utilized in power applications.

In a field effect transistor, a lateral field is produced *via* the drain bias. It is known that, the channel voltage varies along the channel between the source and drain, and reaches a value equal to the drain voltage. It is assumed that the channel voltage is added to the gate voltage for long channel devices with a very small drain bias. Assuming no extrinsic series source or drain resistance the channel 2DEG sheet carrier concentration n_S at any point x along the channel is given by equation [2.4-16].[12]

$$n_S = C_0\big(V_{GS} - V_{th} - V(x)\big) = \frac{\varepsilon_0 \varepsilon_r}{qd}(V_{GS} - V_{th} - V(x)) \qquad [\ 2.4\text{-}16\ ]$$

where, ε_0 is the dielectric constant of the vacuum, ε_r is the dielectric constant of the semiconductor, d is the distance of the gate to the 2DEG channel, V_{GS} is the intrinsic applied gate bias, and $V(x)$ is the voltage in the x direction between the source and drain contact. C_0 is the capacitance normalized to the gate and

assumed to be independent of n_S. In reality, with the increase of n_S the capacitance will slowly increase because of the decrease in d with the Fermi level variation. V_{th} is the threshold voltage where the sheet concentration in the channel is equal to zero and defined as follows;

$$V_{th} = \varphi_B - \Delta E_C - \frac{qN_D}{2\epsilon_0\epsilon_r} d^2 \qquad [\ 2.4\text{-}17\ ]$$

The DC behavior of HEMTs is characterized by the output characteristics of the channel current/drain current I_D. The I_D is typically depicted proportional to channel width W_G, so is given in [mA/mm]. Once the sheet carrier concentration n_S is calculated, I_D can be derived by multiplying n_S by its velocity ϑ and by the gate width W_G of the transistor.

$$I_D(x) = qW_G n_S(x)\vartheta(x) \qquad [\ 2.4\text{-}18\ ]$$

The carrier velocity under applied electric field can be calculated with the following formula which displays a transition from the constant-mobility regime to the constant saturation velocity ϑ_S regime as follows;

$$\vartheta(E_x) = \frac{\mu_0 E_x}{1 + (\mu_0 E_x/\vartheta_S)}) = \frac{\mu_0 E_x}{1 + (E_x/E_C)} \qquad [\ 2.4\text{-}19\ ]$$

here E_C is the critical electric field at the saturation point and equal to $E_C = \vartheta_S/\mu_0$, μ_0 is the low field mobility, and $E(x)$ represents the electric field in the channel and is equal to $E(x) = -dV(x)/dx$. The electronic transport in the HEMTs devices with short gate length works under high field.

By assuming the saturation velocity model drain current can be written as following by using equation [2.4-19].

$$I_D(x) = W_G \frac{\mu_0\epsilon_r\epsilon_0}{d}(V_{GS} - V_{th} - V(x))\frac{dV(x)/dx}{1 + \frac{\mu_0}{\vartheta_S}\frac{dV(x)}{dx}} \qquad [\ 2.4\text{-}20\ ]$$

After integrating equation [2.4-20] from the source end *(x=0)* of the channel with $V_{(x=0)} = 0$ to drain end of the channel $x=L_G$ with $V(x=L_G)=V_{DS}$ I-V characteristics for the linear region can be obtain as follows;

$$I_D(x) = W_G \frac{\mu_0 \epsilon_r \epsilon_0}{d} \frac{(V_{GS} - V_{th})V_{DS} - \frac{1}{2}V_{DS}^2}{L_G + \frac{\mu_0}{\vartheta_S}V_{DS}} \qquad [\ 2.4\text{-}21\ ]$$

L_G and V_{DS} are the gate length and the intrinsic applied source-drain bias, respectively. One should note that, this equation is valid until the drain current saturates and the saturation velocity ϑ_S approaches to infinity. Applied voltage at this point known as knee voltage. By assuming the velocity saturation by differentiating and setting the above equation to zero drain saturation current I_{Dsat} can be obtained as follows;

$$I_{D_{sat}} = W_G \frac{\epsilon_r \epsilon_0 L_G \vartheta_S^2}{2\mu_0 d} \left(\sqrt{1 + 2\frac{\mu_0}{L_G \vartheta_S}(V_{GS} - V_{th})} - 1 \right)^2 \qquad [\ 2.4\text{-}22\ ]$$

Considering constant mobility model and taking the conductivity σ equal to $qn_S\mu$ drain current can be expressed as follows;

$$I_D = \mu Q(x) \frac{dV(x)}{dx} \qquad [\ 2.4\text{-}23\ ]$$

When n_s is decreasing to zero at the end of the channel, where $x=L_G$ saturation drain current is given by equations [2.4-24].

$$I_{D_{sat}} = \frac{\mu \epsilon_0 \epsilon_r}{2L_G d}(V_G - V_{th})^2 \qquad [\ 2.4\text{-}24\ ]$$

This is true when the electric transport occurs at low electric field in the case of long gate devices ($L_G>10\mu m$). The intrinsic transconductance g_m^i which describes the modulation of the drain current by the gate-source voltage is an important parameter in HFETs and is defined by equation [2.4-25].

$$g_m^i = \left(\frac{\partial I_D}{\partial V_{GS}}\right)_{V_D = constant} \qquad [\ 2.4\text{-}25\ ]$$

Hence, intrinsic transconductance can be expressed as follows;

$$g_m^i = W_G \frac{\mu_0 \epsilon_r \epsilon_0}{d} \left(1 - \frac{1}{\sqrt{1 + 2\frac{q n_s d \mu_0}{\epsilon_0 \epsilon_r L_G \mu_0}}}\right) \qquad [\ 2.4\text{-}26\ ]$$

The current flow through the source/drain contacts and the ungated channel regions gives rise to voltage drops and during the device operation this should be taken into consideration. Both the intrinsic gate and the intrinsic drain biases are reduced because of these additional extrinsic voltage drops. As a result, one should consider the extrinsic transconductance g_m^e in device operation and it is defined as follows;

$$g_m^e = \frac{g_m^i}{1 + R_S g_m^i} \qquad [\ 2.4\text{-}27\ ]$$

where R_S is the source resistance and given by equation [2.4-28].

$$R_S = \frac{1}{W}(R_C + d_{GS} R_{SH}) \qquad [\ 2.4\text{-}28\ ]$$

where $R_{SH} = (q\mu_0 n_s)^{-1}$ is the 2DEG channel sheet resistance, and d_{GS} is gate –source distance. Another crucial parameter for device evaluation is the cutoff frequency f_T at which the current gain h_{12} becomes unity for short-circuits conditions. Current gain can be written as follows;

$$h_{12} = \frac{\partial I_D}{\partial I_G} = \frac{g_m \partial V_{GS}}{(j\omega C_G)} \qquad [\ 2.4\text{-}29\ ]$$

here C_G is the gate capacitance, and ω is the radial frequency, expressed as follows when the gain becomes unity.

$$\omega_T = \frac{g_m}{C_G} \qquad [\ 2.4\text{-}30\ ]$$

The cutoff frequency is expressed directly using the transconductance and the gate capacitance as follows;

$$f_T = \frac{g_m}{2\pi C_G} \qquad [\ 2.4\text{-}31\ ]$$

Typical I-V output curves of the HEMTs device on AlGaN/GaN are shown in the Figure 2.4-6.

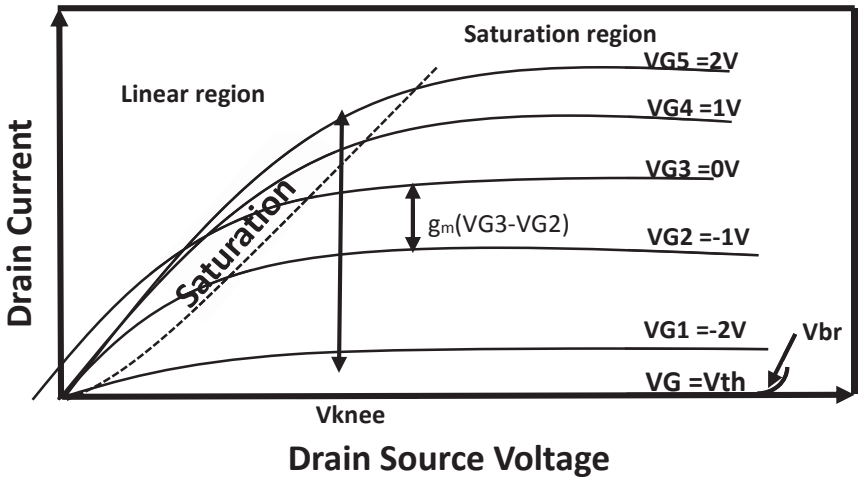

a

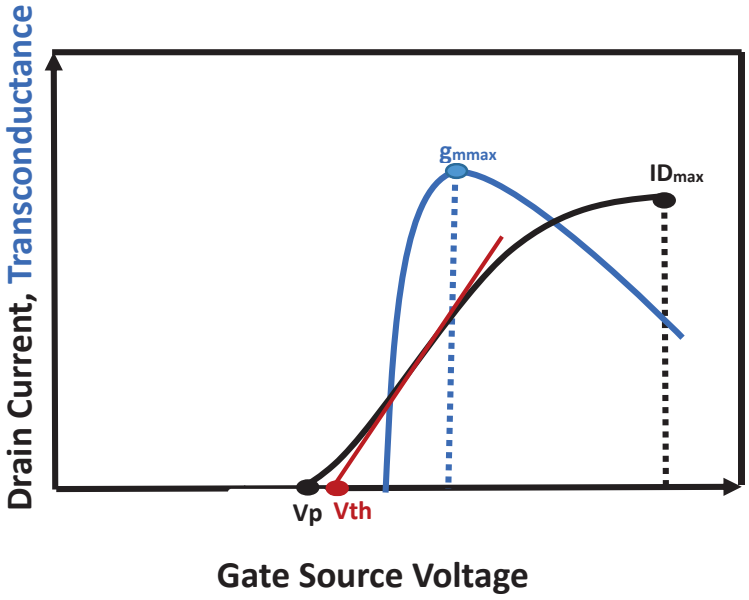

b

Figure 2.4-6: *(a) Transfer characteristics with transconductances, and (b) typical output characteristics for doped AlGaN/GaN HEMTs device.*

2.4.3.3 Capacitance – Voltage Characteristics

The total charge in the semiconductor is given by equation [2.4-32].[14]

$$Q = qN_D w = [2qN_D\varepsilon_S\left(V_{bi} - V_{ext} - \frac{kT}{q}\right)]^{1/2} \qquad [\ 2.4\text{-}32\ ]$$

here N_D is the donor concentration, ε_S is the dielectric constant of the semiconductor, V_{bi} is the built in potential given as the difference φ_m-φ_s, and V_{ext} is the external applied potential. w is the width of the depletion region and for a homogenously doped Schottky contact it is defined as follows;

$$w = \sqrt{\frac{2\epsilon_0\epsilon_r}{qN_d}(V_{bi} - V_{ext})} \qquad [\ 2.4\text{-}33\ ]$$

It is seen that the width of the depletion region can be modulated by applied voltage and depends on the metal contact. One can define the capacity $C = |dQ/dV|$ of the space charge region per unit area and can calculate it by using the following formula;

$$C = [\frac{qN_D\varepsilon_S}{2(V_{bi} - V_{ext} - \frac{kT}{q}}]^{1/2} = \frac{\varepsilon_S}{w} \qquad [\ 2.4\text{-}34\ ]$$

In addition, the capacitance across the depletion space charge with zero external bias for a heterostructure with 2DEG is given as follows; [60]

$$C = A.\frac{dQ}{dV}C = A\frac{\varepsilon_0\varepsilon_r}{d} \qquad [\ 2.4\text{-}35\ ]$$

where ε_r is relative permittivity, and d is the distance the Schottky contact from the 2DEG when the depletion region slightly touches 2DEG at zero applied voltage. Since doping concentration can be derived from measurement of $1/C^2$ as a function of the bias voltage, the above equation can also be written as follows;

$$\frac{1}{C^2} = \frac{2(V_{bi} - V_{ext} - \frac{kT}{q})}{eN_D\varepsilon_S} \qquad [\ 2.4\text{-}36\ ]$$

If the doping concentration is homogeneous, $1/C^2$ should be linearly dependent on the bias voltage. The doping concentration can be derived from the slope with the following equation [2.4-37].

$$N_D = -\frac{2}{e\varepsilon_S}\left[\frac{d}{dV_{ext}}\left(\frac{1}{C^2}\right)\right]^{-1} \qquad [\ 2.4\text{-}37\ ]$$

The built in potential V_{bi} can also be derived from extrapolation to $1/C^2 = 0$. Hence, the Schottky barrier height φ_B can also be determined from equation [2.4-38].[61]

$$\varphi_B = V_{bi} + V_n + \frac{kT}{q} - \Delta\varphi \qquad [\ 2.4\text{-}38\ ]$$

where $\Delta\varphi$ is the barrier lowering due to the image force effect between the flat-band and the zero bias cases. By using C-V spectroscopy inhomogeneous doping the depth profile of the doping can be determined.[14] Checking the quality and characterization of heterostructure layer with 2DEG C-V measurement is one of the most common techniques.[62,63] One can evaluate the concentration of 2DEG, distance of the 2DEG from the surface and mobility of charge carriers *via* C-V measurement.

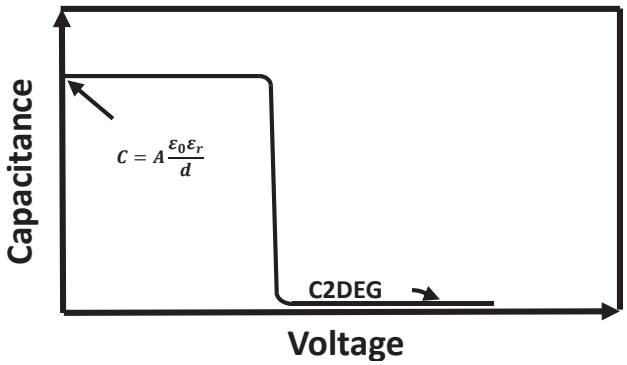

Figure 2.4-7: *Capacitance-voltage characteristics of Schottky diode with 2DEG*

Figure 2.4-7 displays ideal C-V characteristics of a Schottky diode with 2DEG and area A. The space charge under the contact starts to deplete with the application of negative bias and it will penetrate through 2DEG at higher bias. The capacitance will decrease rapidly when the depletion region completely penetrates through 2DEG because of very low capacitance of the depleted 2DEG channel C_{2DEG}. The total

sheet charge density of 2DEG can be derived by the integral of the charge under the C-V curve. The mobility can be calculated *via* equation [2.4-39].

$$R_{SH} = \frac{1}{qn_s\mu} \qquad [\ 2.4\text{-}39\ ]$$

where R_{SH} is the 2DEG channel sheet resistance of the semiconductor layer and can be obtained through TLM measurements. For a given gate bias and for low electric fields, the 2DEG sheet carrier density n_S can be approximated by equation [2.4-40].[64]

$$n_S = \frac{C_b}{q}[V_{GS} - V_{th}] \qquad [\ 2.4\text{-}40\ ]$$

here C_b is the gate capacitance. The gate capacitance is the sum of several capacitance contributions including the GaN cap, the AlGaN barrier, the AlN space layer and the contribution of the distance of the electron gas from the space layer $C_{\Delta d}$. Each of the contribution has the form of $C_i = \varepsilon_i / d_i$. The dielectric constant ε_i for GaN and $Al_xGa_{1-x}N$ can be obtained from the approximation $\varepsilon(x) = -0.5x + 9.5$.[16]

$$C_b^{-1} = C_{cap}^{-1} + C_{barrier}^{-1} + C_{spacing}^{-1} + C_{\Delta d}^{-1} \qquad [\ 2.4\text{-}41\ ]$$

The threshold voltage V_{th} with the total polarization induced charge P_T is expressed as follows;

$$V_{th} = \varphi_B - \Delta E_C - qC_b^{-1}P_T \qquad [\ 2.4\text{-}42\ ]$$

where ΔE_C is the conduction band offset at the AlGaN/GaN interface.

References

[1] T. Lei, M. Fanciulli, R. J. Molnar, T. D. Moustakas, R. J. Graham, and J. Scanlon, "Epitaxial growth of zinc blende and wurtzite gallium nitride thin films on (001) silicon", Appl. Phys. Lett. **59**, 944 (1991).

[2] R. C. Powell, N.-E. Lee, Y.-W. Kim, and J. E. Greene, "Heteroepitaxial wurtzite and zinc-blende structure GaN grown by reactive-ion molecular-beam epitaxy: Growth kinetics, microstructure, and properties", J. Appl. Phys. Lett. **73**, 189 (1993).

[3] J. N. Kuznia, J. W. Yang, Q. C. Chen, S. Krishnankutty, M. Asif Khan, T. George, and J. Frietas Jr., "Low pressure metalorganic chemical-vapor deposition of cubic GaN over (100) GaAs substrates", Appl. Phys. Lett. **65**, 2407 (1994).

[4] B. Daudin, G. Feuillet, J. Hübner, Y. Samson, F. Widmann, A. Philippe, C. Bru-Chevallier, G. Guillot, E. Bustarret, G. Bentoumi, and A. Deneuville, "How to grow cubic GaN with low hexagonal phase content on (001) SiC by molecular beam epitaxy", Appl. Phys. Lett. **84**, 2295 (1998).

[5] J. Wu, H. Yaguchi, H. Nagasawa, Y. Yamaguchi, K. Onabe, Y. Shirika, and R. Ito, "Crystal Structure of GaN grown on 3C-SiC substrates by metal organic vapor phase epitaxy", Jpn. J. Appl. Phys, **36**, 4241 (1997).

[6] H. Xia, Q. Xia, and A. L. Ruoff, "High pressure structure of gallium nitride: Wurtzite-to-rocksalt phase transition", Phys. Rev. B, **57**, 12925 (1993).

[7] R. Quay, "Gallium nitride electronics", Springer-Verlag, Berlin (2008).

[8] J. I. Pankove and T.D. Moustakas, "Gallium nitride (GaN)", Academic Press, San Diego (1998).

[9] H. Morkoç, "Nitride Semiconductors and Devices", Springer-Verlag, Berlin, (1999).

[10]M. E. Levinshtein, S. L. Rumyantsev, and M. S. Shur, "Properties of advanced semiconductor materials, GaN, AlN, InN, BN, SiC, SiGe", John Wiley & Sons, Canada (2001).

[11] F. Bernardini, V. Fiorentini, and D. Vanderbilt, "Spontaneous polarization and piezoelectric constants in III-V nitrides." Phys. Rev. B, **56**, R10024 (1997).

[12] H. Morkoç, "Handbook of nitride semiconductors and devices: GaN-based optical and electronic devices", Wiley-VCH Verlag, Weinheim (2009).

[13] A. Zoroddu, F. Bernardini, P. Ruggerone, and V. Fiorentini, "First-principles prediction of structure, energetics, formation enthalpy, elastic constants, polarization, and piezoelectric constants of AlN, GaN, and InN: Comparison of local and gradient-corrected density-functional theory", Phys. Rev. B **64**, 045208 (2001).

[14] M. Grundmann, "The Physics of Semiconductors: An introduction including devices and nanophysics", Springer-Verlag, Berlin (2006).

[15] G. O'Clock and M. Duffy, "Acoustic surface wave properties of epitaxially grown aluminum nitride and gallium nitride on sapphire", Appl. Phys. Lett. **23**, 55 (1973).

[16] O. Ambacher, J. Smart, J. R. Shealy, N. G. Weimann, K. Chu, M. Murphy, W. J. Schaff, L. F. Eastman, R. Dimitrov, L. Wittmer, M. Stutzmann, W. Rieger, and J. Hilsenbeck, "Two-dimensional electron gases induced by spontaneous and piezoelectric polarization charges in N- and Ga-face AlGaN/GaN heterostructures", J. Appl. Phys. **85**, 3222 (1999).

[17] A.S. Barker, Jr. and M. Ilegems, "Infrared Lattice Vibrations and Free-Electron Dispersion in GaN", Phys. Rev. B, **7**, 743 (1973).

[18] A. F. Wright, "Elastic properties of zinc-blende and wurtzite AlN, GaN, and InN", J. Appl. Phys. **82**, 2833 (1997).

[19] O. Ambacher, B. Foutz, J. Smart, J. R. Shealy, N. G. Weimann, K. Chu, M. Murphy, A. J. Sierakowski, W. J. Schaff, L. F. Eastman, R. Dimitrov, A. Mitchell and M. Stutzmann, "Two dimensional electron gases induced by spontaneous and piezoelectric polarization in undoped and doped AlGaN/GaN heterostructures", J. Appl. Phys. **87**, 334 (2000).

[20] I. Vurgaftman and J. R. Meyer, "Band parameters for nitrogen-containing semiconductors", J. Appl. Phys. **94**, 3675 (2003).

[21] A. Bykhovski, B. L. Gelmont, and M. S. Shur, "Elastic strain relaxation and piezoeffect in GaN-AlN, GaN-AlGaN and GaN-InGaN superlattices", J. Appl. Phys. **81**, 6332 (1997).

[22] A. Hangleiter, J. S. Im, H. Kollmer, S. Heppel, J. Off, and F. Scholz, "The role of piezoelectric fields in GaN-based quantum wells", MRS Internet J. Nitride Semicond. Res. **3**, 15 (1998).

[23] L. Hsu and W. Walukiewicz, "Effects of piezoelectric field on defect formation, charge transfer, and electron transport at $GaN/Al_xGa_{1-x}N$ interfaces", Appl. Phys. Lett. **73**, 339 (1998).

[24] I. P. Smorchkova, C. R. Elsass, J. P. Ibbetson, R. Vetury, B. Heying, P. Fini, E. Haus, S. P. DenBaars, J. S. Speck, and U. K. Mishra, "Polarization-induced charge and electron mobility in AlGaN/GaN heterostructures grown by plasma-assisted molecular-beam epitaxy", J. Appl. Phys. **86**, 4520 (1999).

[25] M. S. Shur, A. D. Bykhovski, and R. Gaska, "Two-dimensional hole gas induced by piezoelectric and pyroelectric charges", Solid-State Electron. **44**, 205 (2000).

[26] P. M. Asbeck, E. T. Yu, S. S. Lau, W. Sun, X. Dang, and C. Shi, "Enhancement of base conductivity via the piezoelectric effect in AlGaN/GaN HBTs", Solid-State Electron. **44**, 211 (2000).

[27] J .P. Ibbetson, P. T. Fini, K. D. Ness, S. P. DenBaars, J. S. Speck and U. K. Mishra, "Polarization effects, surface states, and the source of electrons in AlGaN/GaN heterostructure field effect transistors", Appl. Phys. Lett. **77**, 250 (2000).

[28] H. W. Jang, C. M. Jeon, K. H. Kim, J. K. Kim, S-B Bae, J-H Lee, J. W. Choi, and J-L Lee, "Mechanism of two-dimensional electron gas formation in $Al_xGa_{1-x}N$/GaN heterostructures", Appl. Phys. Lett. **81**, 1249 (2002).

[29] Y. Dong, R. M. Feenstra, and J. E. Northrup, "Electronic states of oxidized GaN (0001) surfaces", Appl. Phys. Lett. **89**, 171920 (2006).

[30] H. Kambayashi, Y. Satoh, S. Ootomo, T. Kokawa, T. Nomura, S. Kato, and T.S.P. Chow, "Over 100 A operation normally-off AlGaN/GaN hybrid MOS-HFET on Si substrate with high-breakdown voltage", Solid State Electron. **54**, 660 (2010).

[31] X. A. Cao, A. A. Syed, and H. Piao, "Investigation of the electronic properties of nitrogen vacancies in AlGaN", J. Appl. Phys, **105**, 063707 (2009).

[32] T. L. Tansley and R. J. Egan, "Point-defect energies in the nitrides of aluminum, gallium, and indium", Phys. Rev. B **45**, 10942 (1992).

[33] L. Bornstein, "New series, Group III" Springer-Verlag, Berlin, (1988).

[34] W. Shan, J. W. Ager III, K. M. Yu, W. Walukiewicz, E. E. Haller, M. C. Martin, W. R. McKinney, and W. Yang, "Dependence of the fundamental band gap of $Al_xGa_{1-x}N$ on alloy composition and pressure", J. Appl. Phys. **85**, 8505 (1999).

[35] H. Angerer, D. Brunner, F. Freudenberg, O. Ambacher, M. Stutzmann, R. Höpler, T. Metzger, E. Born, G. Dollinger, A. Bergmaier, S. Karsch, and H.-J. Körner, "Determination of the Al mole fraction and the band gap bowing of epitaxial $Al_xGa_{1-X}N$ films", Appl. Phys. Lett. **71,** 1504 (1997).

[36] Y. Koide, H. Itoh, M. R. H. Khan, K. Hiramatu, N. Sawaki, and I. Akasaki, "Energy band-gap bowing parameter in an $Al_xGa_{1-x}N$ alloy", J. Appl. Phys. **61**, 4540 (1987).

[37] F. Yun, M. A. Reshchikov, L. He, T. King, H. Morkoç, S. W. Novak, and L. Wei, "Energy band bowing parameter in $Al_xGa_{1-x}N$ alloys", J. Appl. Phys. **92**, 4837 (2002).

[38] M. S. Shur, "GaN and related materials for high power applications", Mater. Res. Soc. Symp. Proc. **483**, 15 (1998).

[39] S. M. Sze, "Physics of semiconductor devices", Wiley, New York (1981).

[40] B. J. Baliga, "Fundamentals of power semiconductor devices", Springer, New York (2008).

[41] T. Murata, M. Hikita, Y.Hirose, Y. Uemoto, K. Inoue, T. Tanaka, and D. Ueda, "Source resistance reduction of AlGaN–GaN HFETs with novel superlattice cap layer" IEEE Trans. Electron Devices, **52**, 1042 (2005).

[42] B. Van Daelea, G. Van Tendeloo, W. Ruythooren, J. Derluyn, M. R. Leys, and M. Germain, "The role of Al on ohmic contact formation on *n*-type GaN and AlGaN/GaN", Appl. Phys. Lett. **87**, 061905 (2005).

[43] D. F. Wang, F. Shiwei, C. Lu, A. Motayed, M. Jah, S. N. Mohammad, K. A. Jones, and L. Salamanca-Riba, "Low-resistance Ti/Al/Ti/Au multilayer ohmic contact to n-GaN", J. Appl. Phys. **89**, 6214 (2001).

[44] C. T. Lee and H. W. Kao, "Long-term thermal stability of Ti/Al/Pt/Au ohmic contacts to *n*-type GaN", Appl. Phys. Lett. **76**, 2364 (2000).

[45] S. Ruvimov, Z. Lilienthal-Weber, J. Washburn, K. J. Duxstad, E. E. Haller, Z. F. Fan, S. N. Mohammad, W. Kim, A. E. Botchkarev, and H. Morkoç, "Microstructure of Ti/Al and Ti/Al/Ni/Au ohmic contacts for n-GaN", Appl. Phys. Lett. **69**, 1556 (1996).

[46] V. Kumar, L. Zhou, D. Selvanathan, and I. Adesida, "Thermally-stable low-resistance Ti/Al/Mo/Au multilayer ohmic contacts on n–GaN", J. Appl. Phys. **92**, 1712 (2002).

[47] J. K. Kim, H. W. Jang, and J. L. Lee, "Mechanism for ohmic contact formation of Ti on *n*-type GaN investigated using synchrotron radiation photoemission spectroscopy", J. Appl. Phys. **91**, 9214 (2002).

[48] A. N. Bright, P. J. Thomas, M. Weyland, D. M. Tricker, C. J. Humphreys, and R. Davies, "Correlation of contact resistance with microstructure for Au/Ni/Al/Ti/AlGaN/GaN ohmic contacts using transmission electron microscopy", J.Appl. Phys. **89**, 3143 (2001).

[49] Q. Z. Liu, L. S. Yu, F. Deng, S. S. Lau, Q. Chen, J. W. Yang, and M. A. Khan, "Study of contact formation in AlGaN/GaN heterostructures", Appl. Phys. Lett. **71**, 1658 (1997).

[50] A. Motayed, R. Bathe, M. C. Wood, O. S. Diouf, R. D. Vispute, and S. Noor Mohammad", Electrical, thermal, and microstructural characteristics of Ti/Al/Ti/Au multilayer ohmic contacts to n -type GaN", J. Appl. Phys. **93**, 1087 (2003).

[51] S. Ruvimov, Z. Liliental-Weber, J. Washburn, D. Qiao, S. S. Lau, and P. K. Chu, "Microstructure of Ti/Al ohmic contacts for n-AlGaN", Appl. Phys. Lett. **73**, 2582 (1998).

[52] Q. Z. Liu and S. S. Lau, "A review of the metal-GaN contact technology", Solid State Electron. **42**, 677 (1998).

[53] A.C. Schmitz, A.T. Ping, M. A. Khan, Q. Chen, J.W. Yang, and I. Adesida, "Metal contacts to n-type GaN", J. Electron. Mater. **27**, 255 (1998).

[54] N. Miura, T. Nanjo, M. Suita, T. Oishi, Y. Abe, T. Ozeki, H. Ishikawa, T. Egawa, T. Jimbo, "Thermal annealing effects on Ni/Au based Schottky contacts on n-GaN and AlGaN/GaN with insertion of high work function metal", Solid-State Electron. **48**, 689 (2004).

[55] S.L. Rumyantsev, N. Pala, M.S Shur, R. Gaska, M.E Levinshtein, M.A Khan, G. Simin, X. Hu, and J. Yang "Effect of gate leakage current on noise properties of AlGaN/GaN field effect transistors", J Appl Phys. **88**, 6726 (2000).

[56] W. S. Tan, P. A. Houston, P. J. Parbrook, D. A. Wood, G. Hill, and C. R. Whitehouse, "Gate leakage effects and breakdown voltage in metalorganic vapor phase epitaxy AlGaN/GaN heterostructure field-effect transistors", Appl. Phys. Lett. **80**, 3207 (2002).

[57] S. Karmalkar, D. M. Sathaiya, and M. S. Shur, “Mechanism of the reverse gate leakage in AlGaN/GaN high electron mobility transistors”, Appl. Phys. Lett. **82**, 3976 (2003).

[58] M. Marso, “Grundlagen der elektrischen bauelement-charakterisierung, Internal report”, Institute of Thin Films and Interfaces, Research Centre Jülich, Germany, (1999.)

[59] J. M. Golio, E. N. Arnold, and W. B. Beckwith, “Microwave MESFETs and HEMTs”, Artech House London (1991).

[60] J. Bernát, “Fabrication and characterization of MSM diodes on AlGaN/GaN HEMT-structures for microelectronic and optoelectronic application”, Diploma thesis, ISI-FZ-Juelich (2002).

[61] A. M. Goodman, “Metal-semiconductor barrier height measurement by the differential capacitance method one carrier system”, J. Appl. Phys. **34**, 329 (1963).

[62] M. J. Uren, D. Lee, B. T. Hughes, P. J. M. Parmiter, J. C. Berbeck, T. Martin, R. H. Wallis, and S. K. Jones, “Electrical characterization of AlGaN/GaN heterostructure wafers for high-power HFETs”, J. Cryst. Growth, **230** 579 (2001).

[63] R. H. Wallis, R. A. Davies, S. K. Jones, R. Beanland, and W. A. Phillips, “A comparison of commercial sources of epitaxial material for GaN HFET fabrication”, J. Cryst. Growth, **230**, 569 (2001).

[64] J. Kuzmík, "Power Electronics on InAlN/(In)GaN: Prospect for a record performance", IEEE Electron Device Lett. **22**, 510 (2001).

Chapter 3

3 Surface, bulk, and interface defects

The deleterious effect of high concentration of defects on the performance of AlGaN/GaN HEMTs cannot be disregarded. Therefore, deep scientific investigation of both surface and interface defects is required for further improvements in device performance. Defect is defined as the deviation from the ideal structure in which each atom has its own designated positions.[1] Defects can be categorized as follows; *thermodynamic defects, dislocations, stacking faults, grain boundaries, antiphase, inversion domains*, *disorder, native defects, and point defects*.[1] *Thermodynamic defects* can be the enthalpy of vacancy, created by bringing an atom from the vacancy site to the surface or interstitial, created by bringing an atom from the surface to interstitial site.

Dislocations occur with a shift in the crystal lattice and are known as line defects. It is known that in GaN most dislocations are found at the low angle grain boundaries of columnar structure.[2] Some researchers have pointed out that different types of dislocations may introduce numerous energy levels in the band gap.[3,4] Wright *et al*.[3] showed that threading dislocations are expected to behave as deep donors in n-type material and deep acceptors in p type. Missing planes or additional planes in the ideal staking of planes are known as *staking faults* and they are a common form of strain relief in lattice mismatched hetero-epitaxy of group III nitrites.[2] It is commonly assumed that stacking faults cause a local variation of the energy bandgap.[2]

Grain boundaries are the boundaries of crystal grains (small crystals formed during the cooling of any material), which can behave like barriers for transport or like carrier sinks. In the case of a crystal shift with respect to one another by an antiphase vector p, *antiphase domains* take place. If there happens to be a change in the direction of two domains, then *inversion domains* take place. Deviations from the ideal structure on a microscopic scale are identified as *disorder*. The broken or distorted bonds in the semiconductors result in deep levels within the forbidden gap, and this situation causes defects known as

native defects. The charge state of a defect can be determined through the Fermi level, and defects can be either donor-type, acceptor-type or amphoteric.[2] It is known that a donor-type defect is positively charged if it is empty and neutral when it is full, whereas an acceptor-type defect is neutral when it is empty and negatively charged upon being fully occupied.[1] The presence of both donors and acceptors in semiconductors occurs quite often. Such semiconductors are known as *compensated* since under the equilibrium conditions some of the electrons from the donors will be captured by the acceptors.

Finally, *point defects* are described as the deviations from the ideal structure involving essentially only one lattice point.[1] Figure 3 displays a schematic diagrams of different types of point defects. All of these defects crucially affect the optical and electronic properties of the material by trapping charges. However, other than point defects, other defects do not contribute to luminescence so, in this dissertation, we will mainly focus on point defects. Point defects present to compensate the introduced dopants or as a consequence of nonstoichiometric growth or annealing.[5] Typically this is followed by a relaxation of the surrounding host atom.[1] The type and density of point defects are generally related to the carrier life time.[2]

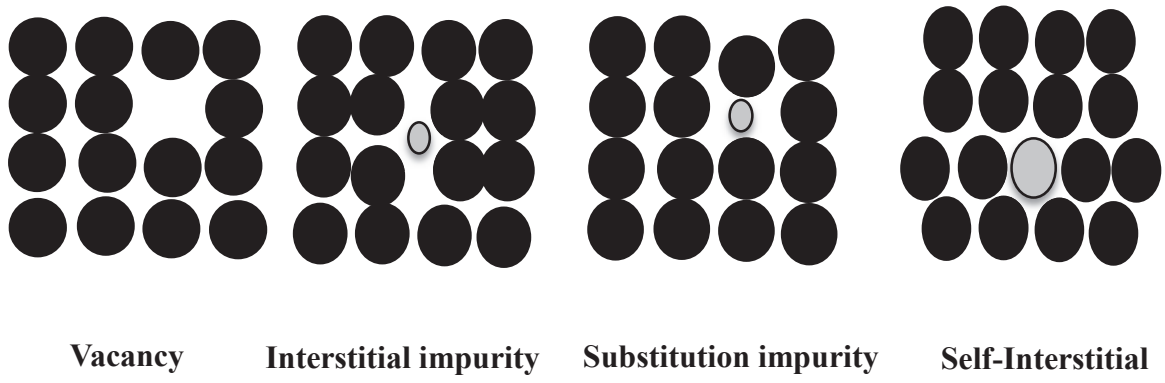

Figure 3: *Schematic diagram of different types of point defects.*

Point defects can be categorized as vacancy, impurity, antisite, and self-interstitials. Reschikov and Morkoc[5] observed high formation energies for interstitial and antisite defects and found that their existence in n-type GaN during growth is not likely. The presence of gallium (Ga) vacancies (V_{Ga}) in n-type and nitrogen (N) vacancies (V_N) in p-type GaN is more expected. *Vacancies* are simplest point defects which take place when an atom is missing from an atomic position.[1] Ga vacancies act as an acceptor like defect and are completely filled with electrons in n-type of GaN. With the light illumination, a radiative transition of an electron from the conduction band or from a shallow donor to the energy level of Ga vacancies occurs. On the other hand, N vacancies act as a donor. Since both Ga and N vacancies are mobile for different temperatures, they can form complexes with more stable defects by migrating. Maruska and Tietjen[6] are the first researchers who suggested the idea of the presence of V_N being responsible for the large electron concentrations. Although Perlin *et al*.[7] supported this idea, some other researchers pointed out those contaminants, such as Si or O_2 are responsible for the large electron concentrations.[8] It has been shown that V_N forms a shallow donor level in GaN, and this level gets deeper as the pressure on GaN increases or the Al mole fraction increases in AlGaN.[2] There is also divacancy which produces at least two deep levels in GaN bandgap and behaves as a double acceptor or donor in n-type and p-type GaN respectively.[9]

An impurity exists when an atom is populated with an atom of different order numbers. If the same number of valance electrons are observed in the atom as are present in the original one, this impurity is called as *isovalent*. When there are different numbers of valance electrons, the impurity adds extra charge to the crystals and it compensates with locally fixed charge in the nucleus. The most common shallow donors in GaN are known as C, Si, and Ge on Ga site; and C, Si, and Ge on the N sites are known as relatively shallow acceptors in this semiconductor.[5]

In the case of an AB compound, if an A atom sits on the B site, then an *antisite defect* occurs. An example would be the cations sitting on anion sites and vice versa. Both Ga on an N site (Ga_N) and N on Ga site (N_{Ga}) are antisite defects, and they lie deep within the energy bandgap.[2] *Self-interstitials* are the cases where additional atoms arise in between the lattice sites. Ga interstitials (Ga_I) results from the presence of the large size Ga atoms associated with a large lattice relaxation. Neugebauer and Van de

Walle[10] consider formation of antisites and interstitials in GaN as low probability, due to a small lattice constant of GaN and the large lattice mismatch between Ga and N atoms. In thermodynamic equilibrium, formation of Ga_I is not likely to happen in n-type or under N-rich conditions. It may happen under electron radiation in GaN or in p-type growth conditions. It is found that Ga_I is trapped by some other defect(s) and does not exist in GaN as an isolated defect in equilibrium.[5] High formation of energy in Ga rich conditions *via* N-N bond occurs because of nitrogen interstitials (N_I).[11,12,13] Finally, N_I is considered as a simple acceptor in n-type GaN.[5]

3.1 Physical Trapping Mechanism

In a typical AlGaN/GaN HFET, there are a variety of trapping effects. Those can be categorized as device and electron-hole effects. Device effects can be summarized as follows;

a. Semiconductor/dielectric surface traps,[14,15,16]
b. Barrier bulk traps,[17]
c. Interface trap at channel/barrier interface,[18]
d. Bulk traps in the buffer,[19]
e. Interface traps at the substrate/semiconductor interface and in the nucleation layer,[19]
f. Recombination/generation in depletion zones of the series resistance.[20]

A schematic diagram of the location of the traps in a typical AlGaN/GaN HFET can be seen in the Figure 3.1-1.

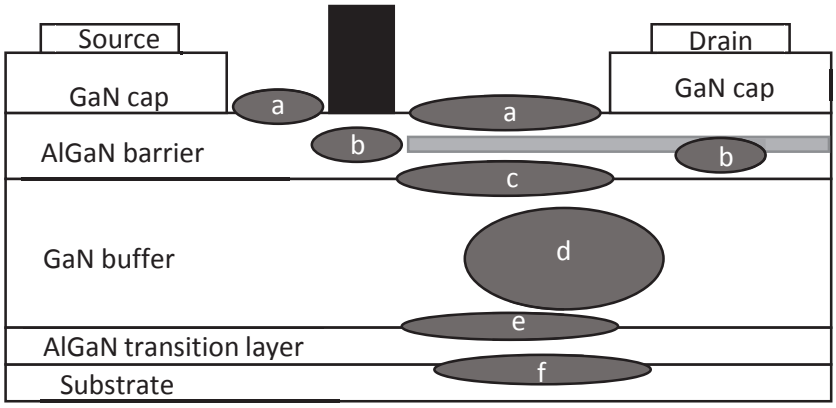

Figure 3.1-1: *Schematic diagram of the location of the traps in a typical AlGaN/GaN.* [18]

Physical effects of electrons and holes include the following;[21]

- Generation/recombination with surface traps at the passivation/barrier interface,
- Generation/recombination with AlGaN barrier traps,
- Generation/ recombination with GaN channel traps,
- Generation/ recombination with interface traps at the channel/barrier interface,
- Generation/ recombination with bulk traps in the buffer,[22]
- Dynamic generation/ recombination at the nucleation layer.

3.2 Generation and Recombination Mechanism

To understand the physics behind the transient spectroscopy measurement one should know the generation and recombination mechanisms in semiconductors. There are four possible processes as illustrated in the Figure 3.2-1;

i. The capture of an electron from the conduction band to the defect level,

ii. The emission of an electron from the defect level to the conduction band,

iii. The capture of a hole from the valence band to the defect or the emission of an electron from the defect to the valence band,

iv. The emission of a hole from the defect to the valence band or the capture of an electron from the valence band to the defect.

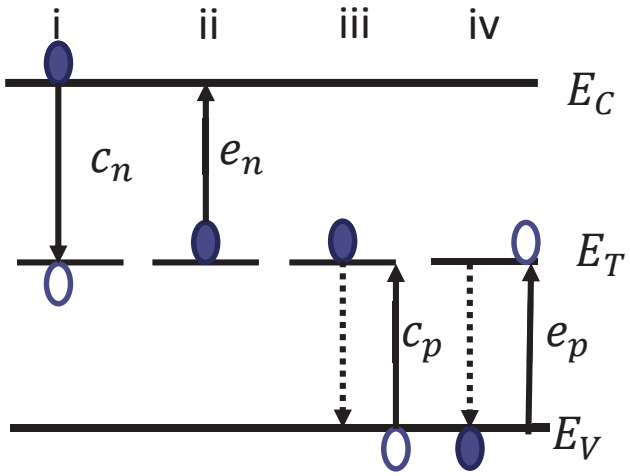

Figure 3.2-1: *Generation and recombination process involving a trap level.*

In the recombination process, a conduction band electron is captured by the defect (i), and emitted to the valance band (iii). Defects which mediate the recombination of minority and majority carriers are called recombination centers.[23] However, an electron captured by a defect (iv), and emitted into a conduction band (ii) is known as generation. In this case, defects involved in this process are known as generation centers. Defects are also known as traps when an electron is trapped for a period of time (i), and released into the band from which it originated (ii) or a trapped hole is emitted to the valance bands.[23] Table 3.2-1 compares the properties of traps and recombination centers[23]

Table 3.2-1: *Ideal properties for traps and recombination centers.*

Defect Property	Traps	Recombination Center
Charge state before capture of a minority carrier	Doubly charged opposite to minority carriers	Single charged opposite to minority carriers
Cross section for minority carriers	10^{-9} to 10^{-12} cm^2 (strongly attractive)	10^{-12} to 10^{-15} cm^2 (moderately attractive)
Cross section for minority carriers after capture	10^{-18} to 10^{-20} cm^2 (moderately repulsive)	10^{-15} to 10^{-17} cm^2 (neutral)
Depth(energy from minority carrier band edge)	Relatively small	Relatively large

Since majority carriers and double charged point defects have the same charge, the defect will be strongly repulsive to the majority carriers. The trap will release the minority carrier before capturing a majority carrier when the trap is close enough to the minority carrier band edge. This is due to the fact that even when the trap captures the minority carriers, it will still have the same charge and therefore, will repel the majority carrier. Conversely, a recombination center captures majority carriers before releasing the minority carriers when it is close enough to band edge of the majority carrier where high energy exists. [23] Traps are categorized as shallow levels and deep levels based on the energy difference associated with the trapped carrier between that state and the appropriate band edge.[24] While the energy difference for a donor is measured from the conduction band, it is measured from the valance band for an acceptor. Shallow levels tend to have an energy difference, which is on the order of a few thermal energy units (meV). When the energy difference is in the range of eV, the trap is called deep level. [23]

Compensated semiconductors contain both ionized acceptors and donors. Under equilibrium conditions some of the electrons from the donors will be captured by acceptors resulting in ionized donors (D^+) and acceptors (A^-). Upon illumination of the light electrons and holes created in the conduction and valance band, respectively. These carriers can be captured by D^+ and A^- sites, and yield neutral D^0 and A^0 centers. When the equilibrium conditions are met, some of the electrons on the neutral donors will radiatively recombine with some of the holes in the acceptor site. This process is known as *donor-acceptor pair* (DAP) transition.[25]

3.3 Point Defects in AlGaN Alloys: Electrical Properties

Si, O, and V_{III} are the three types of defects that have been identified as determining the conductivity properties of n-type AlGaN. Si is the commonly used impurity choice, acting as a donor covering the whole alloy range from GaN to AlN for n-type AlGaN. Its formation energy is estimated as -0.8eV and less than -1.5eV for GaN and AlN, respectively. Activation energies of 17meV, 75meV, and 55meV were found for GaN, AlN, and $Al_{0.7}Ga_{0.3}N$, respectively. For industrial applications activation ratios correspond to activation energies of alloy composites that are expected to be around 0.1. It is known that higher Si incorporation may result in occupation of an N site with Si. Highly conductive n-type AlGaN can be achieved by heavy doping with Si.

Oxygen (O) is another common impurity, which acts as an unintentionally incorporated donor during growth in III- nitrides. The energy of formation of this impurity has been estimated as 0.3eV and -0.1eV for GaN and AlN, respectively[26]. It has been noted that O incorporation can be related to the n-type background carrier concentration of GaN. On the other hand, O is expected to go under a DX, deep levels associated with donors in III-V semiconductors, transition at $x>0.3$ in AlGaN so that it can act as a deep acceptor. Since the intrinsic energy formation of this defect is slightly higher than expected, compensation from O in the alloy range is less likely.

Another important point defects is the III-vacancy in which three charged states (-1,-2,-3) and one neutral state can be stable in the system, along with their corresponding complexes with oxygen. Those three charged states act as ionized acceptors and compensate intentional donors in n-type wide bandgap semiconductors. In higher bandgap materials, formation energies of these defects become lower. In addition, formation energies of vacancies become lower near a dislocation. As a result, it is important to reduce dislocations to further enhance the electrical conductivity in n-type of material.[27]

3.4 Trapping effects in AlGaN/GaN HEMTs

As was clearly pointed out in the previous sections, the HEMTs based on AlGaN/GaN heterostructures are promising candidates for high-power, high-frequency, high-voltage and high-temperature electronic applications due to their unique material and electrical properties.[28] Despite the remarkable advances in optoelectronic and electronic device performances and growth methods for AlGaN/GaN HEMTs epi-structures, there still remain technical issues that have yet to be understood and resolved.[29] With regards to reliability and stability of AlGaN/GaN HEMTs, one of the major issues that remain unresolved is the deleterious effect of deep level defects present in the heterostructures on the device performance.[30] Usually, the effects of traps in device performances are observed as noises even at relatively low frequencies.[2]

Due to a lack of inexpensive, large area GaN substrates, AlGaN/GaN HEMTs epi-layers are usually grown heteroepitaxially on foreign substrates, such as Si, SiC, and sapphire.[31,32,33] Consequently, lattice/thermal expansion mismatches between the epi-layers and the foreign substrates result in high concentration of material defects in AlGaN/GaN HEMTs epi-structures. Figure 3.4-1 presents representative schematics of lattice/thermal expansion mismatches between the epi-layers and the foreign substrates. For instance, it is a widely held view that the use of sapphire substrates results in dislocations in the range of 10^{9}-10^{10}cm^{-2}.[5] These deep level defects can be point defects, such as Ga[5,34] or N vacancies.[5] They create localized levels inside the bandgap and can potentially act as charge carrier traps, causing anomalies that lead to a substantial reduction in device performance. Generally, they are observed in detectors as excess dark current, noise and reduced responsivity.

Defects cause reduction in the gain and increase in the noise, threshold current, slope efficiency, and operation lifetime.[5] The impact of deep level defects is significant in all device applications since defects degrade the device performance. Therefore, it is very important to elucidate the nature of the defects and their distribution across the wafer. Although the influence of the deep level defects gives rise to a similar degradation of AlGaN/GaN HEMTs current-voltage characteristics, the non-uniform distribution of deep

level defects across an AlGaN/GaN HEMTs wafer can result in dissimilar electrical characteristics for the devices fabricated at different locations. In order to improve the reproducibility of the device characteristics of AlGaN/GaN HEMTs, it is also of great importance to characterize how these defects are distributed across the wafer.

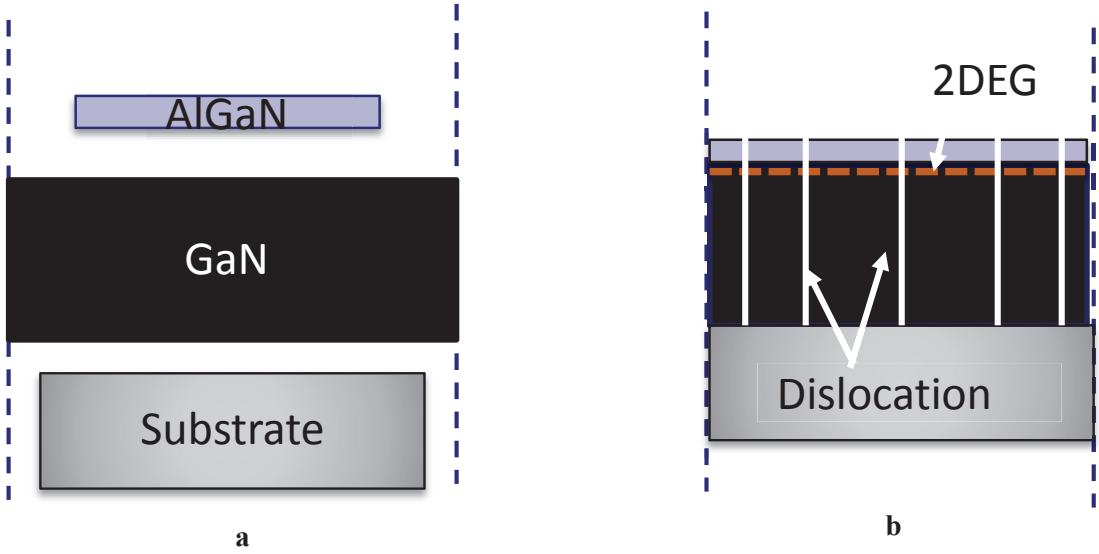

Figure 3.4-1: *Band diagram (a) before and (b) after GaN and AlGaN are brought together.*

3.4.1 Current Collapses

Current collapse phenomena were first observed at high applied drain voltages for Si metal oxide semiconductor FETs (MOSFETs)[35] and CdSe thin film transistors.[36] Fisher *et al*.[37] used the term "current collapse" for the first time in a study of collapse in AlGaAs/GaAs modulation-doped FETs (MODFETs) at cryogenic temperature. Anomalies due to the defects are detected through the output I-V characteristics of the field effect transistors. It should be noted that observed anomalies in the I-V characteristics are denoted by different terms, such as current collapse, kink, dispersion, drain lag, and current slump interchangeably[2].

First of all, in AlGaN/GaN HEMTs, the so-called "current collapse" occurs as a result of entrapment of charge carriers at the surface/interface and bulk trap sites and is known to reduce the drain current.[38] Current collapse is a hot carrier effect that is commonly observed in small device structures with

high applied electric field.[39] In this phenomena, high applied drain-source voltage causes hot carriers to transfer from the conducting channel to an adjacent region with higher concentrations of deep traps in the device structure.[38,40,41] Under these circumstances the injected carriers can become trapped and remain trapped in deep trapping centers even after removal of the high voltage. In equilibrium, the trapping carriers during the collapse must be empty since trapped carriers represent non equilibrium charge distribution.[39] Due to the reduction in the channel carriers through deep level defects, a large transverse electric field is produced resulting in collapse of the current. When current collapse occurs, the drain current goes down to actually zero and stays there for a while.[2] Current collapse is measured as the discrepancy between the DC and pulse measurements.[42]

For instance, drain current can be reduced due to the trapped charges in the surface states between the gate and drain, when the device is turned off. Trapped electrons can be emitted from the traps and contribute to current flow by turning the device on. However, although the gate voltage changes, drain current cannot follow it at high speeds of modulation. Hence, it takes a very long time for traps to be released. Consequently, higher on-resistance and low saturated-drain source current occur. A schematic demonstration of this phenomenon was provided in the Figure 3.4-2. Current collapse increases the knee voltage and decreases the maximum current. As a result, decreases in the achievable output power which is the product of maximum current (ΔI) and voltage swing (ΔV) is observed.

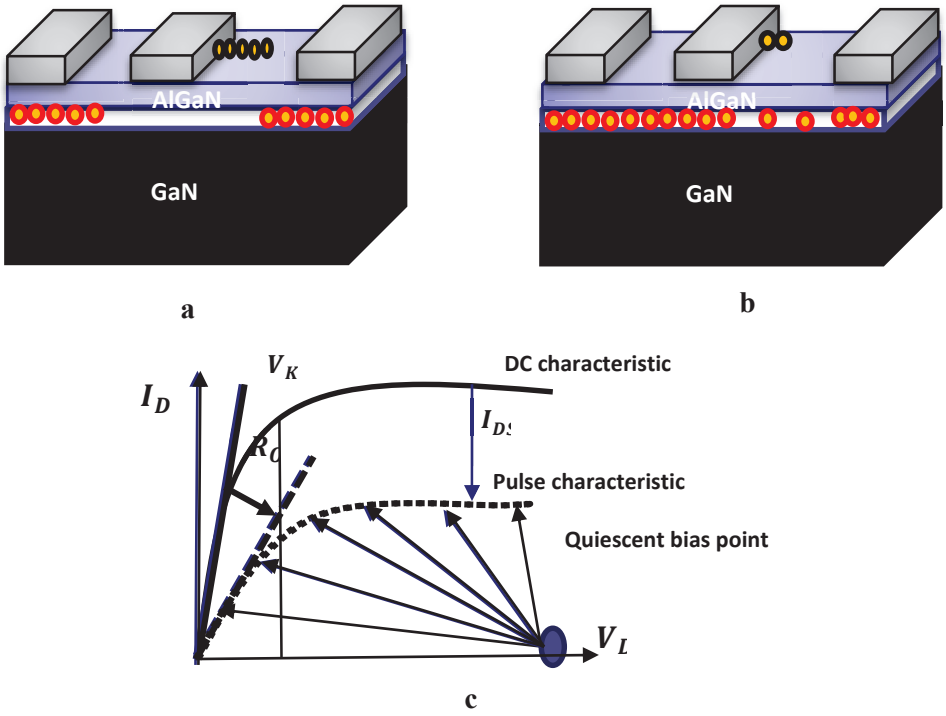

Figure 3.4-2: *(a) Schematic comparison of DC I-V characteristic and a dynamic I-V characteristic when the device shows dispersion phenomena. Traps behavior in a device when it is (b) turned –off and (c) turned on.* [2,18,42,43]

The effects of trapped charges within III-V nitrides have been extensively studied.[38,44,45] In AlGaN/GaN structures, where the AlGaN layer is undoped, the mechanism of hot carriers accelerated in the region between the gate and drain is not possible because of the lack of carriers in the AlGaN.[39] Modulation doped AlGaN/GaN structures would be susceptible to this type of collapse since they show the presence of a DX-type trapping center. It is believed that instabilities in positive compensation charge densities at AlGaN surface (σ_{comp}) which is caused by oxidation of AlGaN barrier, might be reason behind the current collapse phenomena in GaN based HFETs. To form 2DEG in the potential well at AlGaN/GaN interface, a positive sheet charge (σ_{comp}) must exist at the AlGaN/GaN surface to compensate negative surface charges (σ_{2DEG}) as well as the dipole polarization. Capture of electron traps in the trap states causes neutralization of the σ_{comp}. Due to the decrease in the σ_{comp}, reduction of 2DEG charges (σ_{2DEG}) occurs resulting in a decreased drain current, and therefore, lower output voltage.

It has been shown that passivation of the free AlGaN surfaces can effectively eliminate the reduction in drain current.[22,46,47,48] The most common surface passivation layer used is silicon nitride films (a-SiN_x:H or SiN) deposited by the plasma enhanced chemical vapor deposition (PECVD). Some researchers[49,51] reported the use of silicon dioxide (SiO2), scandium oxide (Sc2O3), and magnesium oxide (MgO) as passivation layer. There are several mechanism related to effect of passivation surface on preventing drain current. Mechanism behind the prevention of reduction in the drain current by silicon nitride (SiN) passivation layer relies on the fact that the total amount of positive charges are kept unchanged *via* passivation.[41, 46,48]

3.4.2 Breakdown Voltage

In addition, if these defects are electrical active, they can create parasitic conducting paths and cause the reduction of breakdown voltage.[43] The ability to support high voltages is one of the most distinctive properties of power semiconductor devices. When the calculated drain current difference with and without impact ionization is 3%, the drain –source voltage in this case is defined as the breakdown voltage.[2] Impact ionization is defined as the generation of electron hole pairs due to the energy obtained from the electric field inside the semiconductor.[50] Breakdown occurs in power devices when the large voltage is applied in the reverse direction resulting in a rapid current increase with small applied voltage.[1] Hence, breakdown limits the maximum operation voltage for power devices.

The inter/intra band impact ionization in the high field region of GaN channel is known as the main reason behind the off state breakdown voltage.[51] Recent findings show that premature off state breakdown may occur due to the electrons injected from the source to the high field region of the GaN channel.[52] It has been reported that drain induced barrier lowering (DIBL) due to the unintentional doping *via* residual donors or intrinsic point defects are the main reasons for source infection.[53] To compensate the source injection effect some researchers created a low leakage path by carbon (C) or iron (Fe) doping.[54,55]

Nevertheless, deep level acceptors are created because of doping and cause the device instability at high voltages.

3.4.3 Leakage Current

Finally, surface traps are believed to be the main reasons of the gate leakage current. In this phenomena, electrons tunnel from the drain edge of the gate into surface traps with the increase of drain bias resulting in a rise of the gate leakage current.[2] Some experimentalists[2] relate breakdown voltage with gate leakage current by defining it as the voltage when the gate leakage current reaches 1mA/mm. It has been shown that using high quality buffer layers suppresses the leakage current in GaN based HFET devices and enhance the off state breakdown voltage of the devices.[56] Hence, as stated above, to obtain semi-insulating or insulating GaN as a device buffer on different substrates, C doping has been widely used by many researchers to enhance the breakdown voltage.[57,58] Nonetheless, increase in dispersion phenomena (current collapse and knee walkout), leading to a reduction in the power switching efficiency, the maximum output power, and the power-added efficiency are observed with C doped GaN buffer of HFETs and other field-effect devices.[59,60,61]

3.5 Substrates

The availability of affordable, a large diameter, and high quality substrates in WBG semiconductors is important in the system electronics industry. Typically, commercially available GaN based devices are constructed on either silicon carbide or sapphire substrates which are relatively costly, hard to cleave and nonconducting (for sapphire).[62] Choosing the right substrate is important since substrates are responsible for conducting and dissipating the heat generation during device operation.

Heat flow equation with c being the heat capacity, κ being thermal conductivity, and H being heat generation rate ($H = \vec{j}.\vec{E}$) governs this process[63]

$$c\frac{\partial T}{\partial t} = \vec{\nabla}.\left(\kappa\vec{\nabla}T\right) + H \qquad [3.5\text{-}1]$$

Material parameters determining thermal behavior of substrates are summarized in the Table 3.5-1Table 3.5-1.

Table 3.5-1: *Material parameters that determine heat dissipation by the substrate. a) Reference [64], b) Reference. [65]*

Substrate	Thermal Conductivity(W.cm^{-1}K^{-1}	Heat Capacity(Jg^{-1}K^{-1})	Density (gcm^3)
Al_2O_3	0.35[a] 0.42[b]	0.77[a]	3.98[a]
Si(111)	1.5[b]		
4H-SiC	3.6[a] 3.3[b]	0.66[a]	3.21[a]
GaN	1.6[a] 1.7[b]	0.49[a]	6.1[a]

The most important physical properties, such as lattice-mismatch, thermal conductivity, coefficient of thermal expansion (CTE), and isolation of the substrate are given in the Table 3.5-2. According to this table, GaN is the most suitable substrate, but it is not available in sufficient diameter and quality.[66]

Table 3.5-2:*Basic properties of substrates.* [67,68,69]

Material	Lattice Constant a($\dot{A}$)	Mismatch to GaN (%)	κ_L (Wm^{-1}K^{-1})	CTE (10^{-6}K^{-1})	Isolation (Ωcm)
GaN	3.189	0	130	5.59	$\geq 10^9$
6H SiC	3.08	3.4	490	4.2	$\geq 10^{11}$
6H s.i. SiC	3.08	3.4	370	4.2	$\geq 10^{11}$
Sapphire	$4.758/\sqrt{3}$	13	50	7.5	----
Silicon	5.4301	17	150	3.59	1-3 10^4

SiC is known as the most attractive substrate for GaN high frequency applications because of its good thermal conductivity. Moreover, it has low lattice mismatch rate around 4% with GaN and density of location around $3x10^8 cm^{-2}$.[70] Traditionally sapphire (Al_2O_3) is the most commonly used substrate for GaN epitaxy. On the other hand, sapphire has the largest mismatch with GaN changing between 14% and 23% depending on their relative orientation. Although it is a relatively cheap material ($ 100 for a 2 inch wafer), it has the disadvantage of poor thermal conductivity, which results in overheating of the device.[71] Nonetheless, power results for GaN HFETs on sapphire substrates are 10 times higher than the one that can be achieved with GaAs HFETs.

Recently, Si has been regarded as one of the most promising substrates for the GaN based HEMTs devices because of its abundance, well-established processing technique and the availability of a large wafer size (up to 12 in. in diameter).[72,73] In addition, the conductivity of Si can be easily modulated within a significantly large range (0.01 Ωcm–106 Ωcm), and the GaN epitaxy on Si will facilitate the integration of microelectronics and optoelectronics.[74] Although Si possess 17% lattice mismatch with GaN, in terms of defects the quality of Si is outstanding compared to SiC and Al_2O_3. Despite the low cost of the Si substrate, the breakdown voltage (V_{BV}) of AlGaN/GaN HEMTs grown on Si (less than 600 V for 2 μm total nitride epilayer) is much lower than that grown on SiC (1.9 kV for 2 μm total epi-layer).[75] Recently, high power densities at 10GHz and minimum noise figure of 1.1dB were reported on Si substrates.[76,77]

References

[1] M. Grundmann, "The physics of semiconductors: An introduction including devices and nanophysics", Springer-Verlag Berlin Heidelberg (2006).

[2] H. Morkoç, "Nitride semiconductors and devices", Springer-Verlag, Berlin, (1999).

[3] A. F. Wright and U. Grossner, "The effect of doping and growth stoichiometry on the core structure of a threading edge dislocation in GaN", Appl. Phys. Lett. **73**, 2751 (1998).

[4] J. E. Northrup, "Theory of intrinsic and H-passivated screw dislocations in GaN", Phys. Rev. B **66**, 045204 (2002).

[5] M. A. Reshchikov and H. Morkoc, "Luminescence properties of defects in GaN", J. App. Phys. **97**, 061301 (2005).

[6] H. P. Maruska, and J. J. Tietjen, "The preparation and properties of vapor-deposited single-crystal-line GaN", Appl. Phys. Lett. **15**, 327 (1969).

[7] P. Perlin, T. Suziki, H. Teisseyre, M. Leszcynski, I. Gregory, J. Jun, S. Porowski, P. Boguslawski, J. Bernholc, J. C. Chervin, A. Polian, T. D. Moustakas, "Towards the identification of the dominant donor in GaN", Phys. Rev. Lett. **75**, 296 (1995).

[8] J. Neugebauer and C. G. Van de Walle, "Gallium vacancies and the yellow luminescence in GaN", App. Phys. Lett. **69**, 503, (1996).

[9] T. Mattila and R. M. Nieminen, "Point-defect complexes and broadband luminescence in GaN and AlN", Phys. Rev. B **55**, 9571 (1997).

[10] J. Neugebauer and C. G. Van de Walle, "Chemical trends for acceptor impurities in GaN", J. Appl. Phys. **85**, 3003 (1999).

[11] J. Neugebauer and C. G. Van de Walle, "Atomic geometry and electronic structure of native defects in GaN", Phys. Rev. B **50**, 8067 (1994).

[12] P. Boguslawski, E. L. Briggs, and J. Bernholc, "Native defects in gallium nitride", Phys. Rev. B **51**, 17255 (1995).

[13] S. Limpijumnong and C. G. Van de Walle, "Diffusivity of native defects in GaN", Phys. Rev. B **69**, 035207 (2004).

[14] J. Bernat, P. Javorka, A. Fox, M. Marsso, H. Luth, and P. Kordos, "Effect of surface passivation on performance of AlGaN/GaN/Si HEMTs", Solid State Electron. **47**, 2097 (2003).

[15] G. Koley, V. Tilak, L. Eastman, and M. Spencer, "Slow transients observed in AlGaN/GaN HFETs: effects of SiN x passivation and UV illumination", IEEE Trans. Electron Devices, **50**, 886 (2003).

[16] D. K. Sahoo, R. K. Lal, H. Kim, V. Tilak, and L. Eastman, "High field effects in silicon nitride passivated GaN MODFETs", IEEE Trans. Electron Devices, **50**, 1163 (2003).

[17] H. Kim, R. Thompson, V. Tilak, T. Prunty, J. Shealy, and L. Eastman, "Effects of SiN passivation and high-electric field on AlGaN-GaN HFET degradation", IEEE Electron Device Lett. **24**, 421 (2003).

[18] R. Quay, "Gallium nitride electronics", Springer-Verlag, Berlin, (2008).

[19] G. Meneghesso, A. Chini, E. Zanoni, M. Manfredi, M. Pavesi, B. Boudart, and C. Gaquiere, "Diagnosis of trapping phenomena in GaN MESFETs", IEDM'00 Technical Degist International, Electron Devices Meeting San Fransisco, 389 (2000).

[20] A. Koudymov, G. Simin, M. Khan, A. Tarakji, R. Gaska, and M. Shur, "Dynamic current–voltage characteristics of III-N HFETs", IEEE Electron Device Lett. **24**, 680 (2003).

[21] G. Verzellesi, R. Pierobon, F. Rampazzo, G. Meneghesso, A. Chini, U. Mishra, C. Canali, and E. Zanoni, "Experimental / numerical investigation on current collapse in AlGaN/GaN HEMT's", IEDM Technical Digest, Electron Devices Meeting San Fransisco 689 (2002).

[22] S. C. Binari, K. Ikossi, J. Rousos, W. Kruppa, D. Park, H. Dietrich, D. Koleske, A. Wickenden, and R. L. Heny, "Trapping effects and microwave power performance in AlGaN/GaN HEMTs", IEEE Trans. Electro Devices, **48**, 465 (2001).

[23] A. Rockett, "The materials science of semiconductors", Springer, NewYork (2008).

[24] A. Patane and N. Balkan, "Semiconductor research", Springer-Verlag Berlin Heidelberg (2012).

[25] P. Y. Yu and M. Cardona, "Fundamentals of semiconductors: Physics and materials properties", Springer-Verlag Berlin Heidelberg (1999).

[26] H.-J. Lewerenz and L. Peter, "Photoelectrochemical water splitting: Materials, process, architecture", The Royal Society of Chemistry, Cambridge, UK (2013).

[27] R. Collazo and N. Dietz, " The group III-nitride material class: from preparation to perspective in photoelectrocatalysis", "Chapter 8 in Photoelectrochemical Water Splitting by H. J. Lawerenz, and L. Peter", The Royal Society of Chemistry (2013).

[28] B. K. Li, W. K. Ge, J. N. Wang, and K. J. Chen, "Persistent photoconductivity and carrier transport in AlGaN ⁄ GaN heterostructures treated by fluorine plasma", Appl. Phys. Lett. **92**, 082105-3 (2008).

[29] J. Z. Li, J. Y. Lin, H. X. Jiang, and M. A Khan, "Effects of persistent photoconductivity on the characteristic performance of an AlGaN/GaN heterostructure ultraviolet detector", Appl. Phys. Lett. **72**, 2868 (1998).

[30] O. Mitrofanov and M. Manfra, "Mechanisms of gate lag in GaN/AlGaN/GaN high electron mobility transistors", Superlattices and Microstruc. **34**, 33 (2003).

[31] E. A. Douglas, S. J. Pearton, B. Poling, G. D. Via, L. Liu, and F. Ren, "Effect of drain bias on degradation of AlGaN/GaN high electron mobility transistors under X-band operation", Electrochem. Solid-State Lett. **14**, H464 (2011).

[32] B. Ozden, C. Yang, F. Tong, M. P. Khanal, V. Mirkhani, M. H. Sk, A. C. Ahyi, and M. Park, "Depth-resolved ultra-violet spectroscopic photo current-voltage measurements for the analysis of AlGaN/GaN high electron mobility transistor epilayer deposited on Si", Appl. Phys. Lett. **105**, 172105 (2014).

[33] M. Wolters, P. Javorka, M. Marso, A. Fox, R. Carius, A. Alam, M. Heuken, P. Kordoš, and H. Lüth, "Photoionization spectroscopy of traps in doped and undoped AlGaN/GaN HEMTs", Phys. Stat. Sol. (c), **0**, 82 (2002).

[34] Z. Q. Fang, D. C. Look, D. H. Kim, and I. Adesida, "Traps in AlGaN ⁄ GaN ⁄ SiC heterostructures studied by deep level transient Spectroscopy", Appl. Phys. Lett. **87**, 182115 (2005).

[35] T. H. Ning, C. M. Osburn, and H. N. Yu," Effect of electron trapping on IGFET characteristics", J. Electron. Mater. **6,** 65 (1977).

[36] F. C. Luo, "High voltage CdSe thin film transistor", J. Vac. Sci. Technol. **16**, 1045 (1979).

[37] R. Fischer, W. T. Masselink, T. Henderson, J. Klem, D. Arnold, and H. Morkoc, "Improvements in MBE grown $Al_xGa_{1-x}As$/GaAs single quantum well structures resulting from dimeric arsenic", IEEE Trans. Electron Devices, **31**, 1963 (1984).

[38] S. C. Binari, W. Kruppa, H. B. Dietrich, G. Kelner, A. E. Wickenden, and J. A. Freitas Jr, "Fabrication and characterization of GaN FETs", Solid-State Electron. **41**, 1549 (1997).

[39] P. B. Klein and S. C. Binari, "Photoionization spectroscopy of deep defects responsible for current collapse in nitride-based field effect transistors", J. Phys.: Condens. Matter, **15**, R1641 (2003).

[40] R. Fisher, T. J. Drummond, W. Kopp, H. Morkoc, K. Lee, and M. Shur, "Instabilities in modulation doped field-effect transistors (MODFETs) at 77 K", Electron. Lett. **19**, 789 (1983).

[41] P. B. Klein, J. A. Freitas, Jr., S. C. Binari, and A. E. Wickenden, "Observation of deep traps responsible for current collapse in GaN metal–semiconductor field-effect transistors", Appl. Phys. Lett. **75**, 4016 (1999).

[42] D. Visalli, "Optimization of GaN-on-Si HEMTs for high voltage applications", PhD dissertation, Katholieke Universireit Leuven (2011).

[43] J. E. Northrup, "Screw dislocations in GaN: the Ga-filled core model", Appl. Phys. Lett. **78**, 2288 (2001).

[44] A. Kastalsky and R. A. Kiehl, "On the low-temperature degradation of (AlGa) As / GaAs modulation-doped field-effect transistors", IEEE Trans. Electron Devices **33** 414 (1986).

[45] M. D. McCluskey, N. M. Johnson, C. G. Van de Walle, D. P. Bour, M. Kneissl, and W. Walukiewicz, "Metastability of oxygen donors in AlGaN", Phys. Rev. Lett. **80**, 4008 (1998).

[46] B. M. Green, K. K. Chu, E. M. Chumbes, J. A. Smart, J. R. Shealy, and L. F. Eastman, "The effect of surface passivation on the microwave characteristics of undoped AlGaN/GaN HEMT's", IEEE Electron Device Lett. **21**, 268 (2000).

[47] J. Li, S. J. Cai, G. Z. Pan, Y. L. Chen, C. P. Wen, and K. L. Wang, "High breakdown voltage GaN HFET with field plate", Electron. Lett. **37**, 196 (2001).

[48] R. Vetury, N. Q. Zhang, S. Keller, and U. K. Mishra, "The impact of surface states on the DC and RF characteristics of AlGaN/GaN HFETs", IEEE Transactions on Electron Devices, **48**, 560 (2001).

[49] B. Luo, J. W. Johnson, B. P. Gila, A. H. Onstine, C. R. Abernathy, F. Ren, S. J. Pearton, A. G. Baca, A. M. Dabiran, A. M. Wowchack, and P. P. Chow, "Surface passivation of AlGaN/GaN HEMTs using MBE-grown MgO or Sc2O3," Solid State Electon. **46**, 467 (2002).

[50] B. J. Baliga, "Fundamentals of power semiconductors", Springer, NewYork (2008).

[51] T. Nakao, Y. Ohno, S. Kishimoto, K. Maezawa, and T. Mizutani, "Study on off-state breakdown in AlGaN/GaN HEMTs", Phys. Stat. Sol. (C), **0**, 2335 (2003).

[52] M. J. Wang and K. J. Chen, "Source injection induced off-state breakdown and its improvement by enhanced back barrier with fluorine ion implantation in AlGaN/GaN HEMTs", IEDM Tech. Dig. 149 (2008).

[53] M. Wang and K. J. Chen, "Improvement of the off-state breakdown voltage with fluorine ion implantation in AlGaN/GaN HEMTs", IEEE Transitions on Electron Devices, **58**, 460 (2011).

[54] J. W. Webb, H. Tang, S. Rolfe, and J. A. Bardwell, "Semi-insulating C-doped GaN and high-mobility AlGaN/GaN heterostructures grown by ammonia molecular beam epitaxy", Appl. Phys. Lett. **75**, 953 (1999).

[55] S. Heikman, S. Keller, S. P. DenBaars, and U. K. Mishra, "Growth of Fe doped semi-insulating GaN by metalorganic chemical vapor deposition", Appl. Phys. Lett. **81**, 439 (2002).

[56] E. Bahat-Treidel, F. Brunner, O. Hilt, E. Cho, J. Würfl, and G. Tränkle, "AlGaN/GaN/GaN:C back-barrier HFETs with breakdown voltage of over 1 kV and low $R_{ON} \times A$", IEEE Transations on Electron Devices, **57**, 3050 (2010).

[57] Y. C. Choi, M. Pophristic, B. Peres, M. G. Spencer, and L. F. Eastman, "Fabrication and characterization of high breakdown voltage AlGaN/GaN heterojunction field effect

transistors on sapphire substrates", J. Vac. Sci. Technol. B, Microelectron. Process. Phenom. **24**, 2601 (2006).

[58] Z. Chen, Y. Pei, S. Newman, R. Chu, D. Brown, R. Chung, S. Keller, S. P. DenBaars, S. Nakamura, and U. K. Mishra, "Growth of AlGaN/GaN heterojunction field effect transistors on semi-insulating GaN using an AlGaN interlayer", Appl. Phys. Lett. **94**, 112 (2009).

[59] P. B. Klein, S. C. Binari, K. Ikossi, A. E. Wickenden, D. D. Koleske, and R. L. Henry, "Current collapse and the role of carbon in AlGaN/ GaN high electron mobility transistors grown by metalorganic vapor phase epitaxy," Appl. Phys. Lett. **79**, 3527 (2001).

[60] S. Rajan, A. Chakraborty, U. K. Mishra, C. Poblenz, P. Waltereit, and J. S. Speck, "MBE-grown AlGaN/GaN HEMTs on SiC", Proc. IEEE Lester Eastman Conf. High Performance Devices, 108 (2004).

[61] N. Ikeda, J. Li, K. Kato, S. Kaya, T. Kazama, T. Kokawa, Y. Sato, M. Iwami, T. Nomura, M. Masuda, and S. Kato, "High-power GaN HFETs on Si substrate", Furukawa Rev. **34**, 17 (2008).

[62] A. Ohtani, K. S. Stevens, and R. Beresford, "Microstructure and photoluminescence of GaN grown on Si (111) by plasma-assisted molecular beam epitaxy", Appl. Phys. Lett. **65**, 61 (1994).

[63] G. K. Wachutka, "Rigorous thermodynamic treatment of heat generation and conduction in semiconductor device modeling", Computer-Aided Design of Integrated Circuits and Systems", IEEE Transactions **9**, 1141 (1990).

[64] M. Kuball, G. J. Riedel, J. W. Pomeroy, A. Sarua, M. J. Uren, T. Martin, K. P. Hilton, J. O. Maclean, and D. J. Wallis, "Time-Resolved Temperature Measurement of AlGaN/GaN Electronic Devices Using Micro-Raman Spectroscopy", IEEE Electron Device Lett. **28** 86 (2007).

[65] T. Sadi, R. W. Kelsall, and N. J. Pilgrim, "Investigation of Self-Heating Effects in Submicrometer GaN/AlGaN HEMTs Using an Electrothermal Monte Carlo Method", Electron Devices, IEEE Transactions. **53**, 2892 (2006).

[66] K. Evans, Compound Semicond. **10** (2004).

[67] Y. Ohno and M. Kuzuhara, "Application of GaN-based heterojunction FETs for advanced wireless communication IEEE Trans", Electron Devices, **48**, 517 (2001).

[68] M. Rosker, "The wide and the narrow: DARPA/MTO programs for RF applications in wide bandgap and antimonide-based semiconductors" Compound Semiconductor IC Symposium Technical Digest, Palm Springs 13 (2005).

[69] D. Gaskill, L. Rowland, and K. Doverspike, "Properties of group III nitrides : EMIS Data reviews Series by J. Edgar", IEEE INSPEC, London (1994).

[70] D. Balaz, "Current collapse and device degradation in AlGaN/GaN heterostructure field effect transistors", PhD dissertation, University of Glasgow (2011).

[71] M. C. J. C. M. Kramer, "Gallium nitride-based microwave high power heterostructure field effect transistors: design, technology and characterization", Dissertation, Techische Universiteit Eindhoven (2006).

[72] A. Dadgar, J. Blasing, A. Diez, A. Alam, M. Heuken, and A. Krost, "Metalorganic chemical vapor phase epitaxy of crack-free GaN on Si (111) exceeding 1 μm in thickness", Jpn. J. Appl. Phys. **39**, L1183 (2000).

[73] A. Krost and A. Dadgar, "GaN-Based Devices on Si", Phys. Stat. Sol. (a) **194**, 361 (2002).

[74] P. R. Hageman, S. Haffouz, V. Kirilyuk, A. Grzegorczyk, and P. K. Larsen, "High quality GaN layers on Si (111) substrates: AlN buffer layer optimization and insertion of a SiN intermediate layer", Phys. Stat. Sol. **188**, 523 (2001).

[75] Y. Dora, A. Chakraborty, L. McCarthy, S. Keller, S. P. Denbaars, and U. K. Mishra, "High breakdown voltage achieved on AlGaN/GaN HEMTs with integrated slant field plates", IEEE Electron Device Lett. **27**, 713 (2006).

[76] D. Dumka, C. Lee, H. Tserng, P. Saunier, and M. Kumar", AlGaN/GaN HEMTs on Si substrates with 7W/mm output power density at 10GHz", Electron. Lett. **40**, 1023 (2003).

[77] A. Minko, V. Hoel, S. Lepilliet, G. Dambrine, J. DeJaeger, Y. Corider, F. Semond, F. Natalie, and J. Massieses, "High microwave and noise performance of 0.17-μm AlGaN-GaN HEMTs on high-resistivity silicon substrates", IEEE Electron Device Lett. **25**, 167 (2004).

Chapter 4

4 Device Processing Techniques

4.1 Introduction

Semiconductor processing techniques and equipment used for fabrication of Schottky contacts on AlGaN/GaN HEMTs heterostructures are summarized in this chapter. Mainly, we focused on theoretical description along with detailed experimental procedures and recipes of the fabrication employed in our research. Below we presented processing techniques which include sample cleaning, lithography, metallization, and annealing.

4.2 Growth

Special growth methods have been developed to control the thickness of layers in the active part of heterostuctures. Among these molecular beam epitaxy (MBE), chemical vapor deposition (CVD), metal organic vapor phase epitaxy (MOVPE) are the most common growth methods for III-V semiconductors. The samples used in this dissertation were grown by a private company by using metal organic chemical vapor deposition (MOCVD). Hence, in this dissertation I will focus on MOCVD.

4.2.1 Metal Organic Chemical Vapor Deposition (MOCVD)

Metal organic chemical vapor deposition (MOCVD) has become attractive for commercial GaN device applications with the achievement of blue LEDs. MOCVD is a nonequilibrium growth technique in which the precursors are transported and react with group III alkyls and group V hydrides in a heated zone.[1] The approach of Mansevit and Tietjen[2] is considered the origin of this technology. In this system, controlling mass flow rate and dilution of various components of the gas stream were used to control composition and growth rate. Organometallic group III sources are either liquid or solid and stored in the

bubbler through which a carrier gas flows. This carrier gas will saturate with vapor from the source and transport vapor to the heated substrate. In general, group V sources are gaseous e.g., ammonia (NH_3) for nitride growth. The substrate usually is kept on a block of graphite called a susceptor and heated by radio frequency (RF) coil, a resistance or a strip heater. Having walls colder than the heated interior is the most important feature of MOCVD since it helps to reduce reactant depletion effect that hot walls causes. The use of MOCVD in III-V materials is very common because of fast, precise, and successful growth of optoelectronic devices.[3] Figure 4.2-1 presents a schematic view of MOCVD growth of III-V materials[4] Typically, MOCVD is used in the mass transport limited regime in which the growth rate solely depends on the amount of metal organic supplied.[5] Growth temperature is in the range from 1050ºC for GaN up to 1500ºC for AlN. Reactor pressure may range from 100Pa to close to 100KPa (ambient pressure). Growth rates can be as high as 5um/hr. Major impurities found are oxygen, hydrogen, carbon, and silicon. [6]

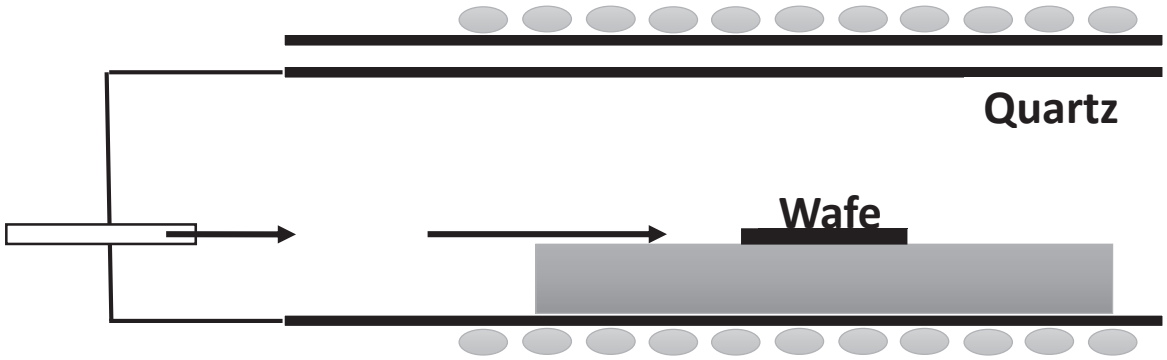

Figure 4.2-1: *Schematics of metal organic chemical vapor deposition (MOCVD) growth.*

4.3 AlGaN/GaN Wafers Used in This Work

For our experiments we used the AlGaN/GaN HEMT layers grown on the p-type 6 in. Si wafer *via* metal-organic chemical vapor deposition (MOCVD). The epilayer has the following structure: (1) 0.25 μm AlN nucleation layer, (2) multi-layer AlGaN buffer layer with varying aluminum (Al) concentrations between 20% and 75%, (3) 1 lm undoped GaN layer, (4) 20 nm AlGaN barrier layers, and (5) an ultra-thin (2 nm) GaN cap layer. A schematic diagram of the heterostucture is given in Figure 4.3-1.

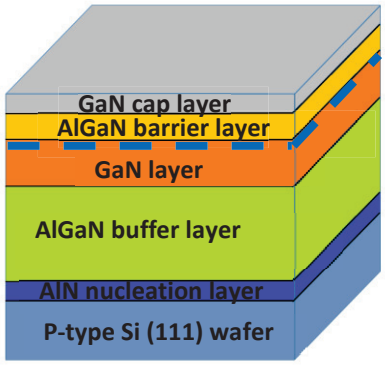

Figure 4.3-1: *Schematic diagram of the cross section of the heterostructure used in this dissertation.*

4.3.1 Cleaning

Surface cleaning processes are one of the most important parts of the semiconductor device fabrication step.[7] During the storage and device fabrication process, semiconductor wafer surface can easily be contaminated from the ambient air, processing materials (chemicals, gases, water, *etc*.), manufacturing tools and personal operation. As a result, contamination there could cause catastrophic failures in operation of the device. It is required to remove native oxides, organic contaminants, metallic impurities, particulate contaminants, adsorbed molecules, and residual species.[8,9,10] Native oxides can very easily grow on the exposed surfaces of most of the semiconductor wafers and can affect the metallic contacts and other optoelectronic properties.

Organic compounds present in the ambient air or inside the photoresist can be adsorbed into semiconductor surface. The most common metallic impurities are iron (Fe), copper (Cu), and aluminum (Al); along with ionic metals like sodium (Na) and calcium (Ca), which originate from the liquid chemicals,

water ,and handling and processing tools. Chemical contaminates, such as chorine (Cl), lead to unwanted etching from undesired areas, and create compounds that become hard to remove from the surface. There are two kinds of common methods wet and dry etching for removal of surface contaminants. Wet etching is more preferable compared to dry cleaning methods since they result in damaging the surface and making the material electrically unsuitable.[11]

For device fabrication, the 6″ HEMTs epitaxy wafer was diced into 1x1 cm individual pieces, the pieces from the center of the 6″ HEMTs epitaxy wafer were ultrasonically cleaned in the organic solvents in the following order: acetone, trichloroethylene (TCE), acetone, methanol, and methanol for 5 min. in each solvent. After removing organic residues, the samples were placed in a mixture of hydrochloric acid (HCl) and deionized (DI) water (1:1 by vol.) and subsequently heated at 110ºC for 10 min. Organic contaminates with particularly oily or greasy contaminants are removed by first using acetone and TCE. TCE is dissolved with the use of second acetone. Nevertheless, acetone will deposit the contaminants because it evaporates rapidly. Therefore, methanol is used to dissolve acetone without rapidly evaporating. The use of second methanol provides further cleaning for the samples. Moreover, the methanol was dissolved by rinsing the samples in DI water. Cleaning ionic contaminants is as important as removing organic contaminants, which is why an acid mix was used. Smith *et al*.[12] found that HCl:DI wet chemical processes produced the lowest coverages of oxygen and carbon contaminants.

Studies showed that acid cleaning increase chlorine (Cl) concentration and, it decreases the oxygen coverage on the surface.[13] Since adhesion of metals like Ni, Au, Pd, and Pt on GaN surface increases with the increase of Cl concentration, it is beneficial to use acid cleaning.[14] Furthermore, it is beneficial to prevent re-oxidation of the surface.[12] Finally rinsing and drying steps are performed to easily prevent sample recontamination with organics and particulates floating on the surface water. It is observed that residual oxide leads to reduce leakage but increased dispersion. Hence, with the partial oxide removal from under the gate, a trade-off between achieving either low-leakage and stronger current collapse or increase leakage and negligible current collapse is found.[4] Figure 4.3-2 displays a sample cleaning fume hood which is used during our experiments.

Figure 4.3-2: *Picture of one of cleaning fume hood in Physics' Departments clean room facilities.*

4.4 Device Fabrication

Affordable and wide ranges of electronic applications become available with the integration of massive transistors into complex circuits in the form of integrated circuits (ICs). Chemical and physical processes including lithopatterning, thin film deposition, etching, *etc*. are required to fabricate ICs. One of the most fundamental steps in any semiconductor device processing is lithography. In this section, we will discuss technologies involved in the fabrication processes.

4.4.1 Lithography

Lithography is the formation of three dimensional (3D) images on the substrate to transfer the pattern into the substrate.[15] There are two kinds of lithography as optical and electron beam. In this dissertation, we will focus on optical lithography or photolithograph which provides parallel illumination of wafer and so, provides a fast and cost efficient lithography.[16] Processing steps of a typical optical lithography can be summarized as substrate preparation, photoresist spin coat, post-applies bake, exposure,

post-exposure bake, and development. Example of typical sequence of lithography processing steps are given in the Figure 4.4-1.

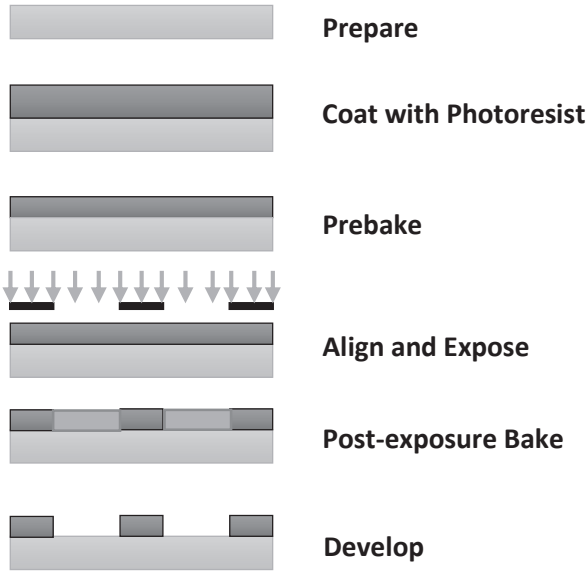

Figure 4.4-1: *Example of a typical sequence of lithographic processing steps illustrated for a positive resist.*

4.4.1.1 Photoresists Coating

The first step of lithography is the top surface coating with an ultraviolet (UV) light sensitive polymer called as photoresist. In this process, the liquid photoresists is poured onto the wafer, which is then spun on a turntable at a high speed. The liquid photoresist is pushed toward the edges by centrifugal forces because of spinning. The frictional force of viscosity opposes the centrifugal force, which decreases as the film thins. Moreover, evaporation of the resists increases the viscosity of the resists thus effects the thickness of the coating.

Thickness of the coating depends on the speed of spinner, viscosity of the resist, humidity, and substrate topography as given in the following formula;[17]

$$Thickness = k\frac{p^2}{\omega^{1/2}} \sim \frac{v^{0.4}}{\omega^{0.2}} \qquad [\ 4.4\text{-}1\ ]$$

with k being spinner constant, p being the resist solid content in the percentage, ω being the rotational speed of the spinner in revolution per minute *(RPM)/1000*, and *v* being liquid photoresist viscosity. If the spin speed is too high, it may result in nonuniform films. Our samples were spun coated at 4000 RPM for 30 seconds.

During the growth fabrication in our lab we used a positive photoresist, *AZ 5214-E*. Positive photo resists develop more rapidly in the exposed region with a rate *R* which is ten times greater than the unexposed rate R_0. In the positive resist exposure, UV light makes the resists more soluble in the developer. In the negative resist, the exposed region become harder to develop. While positive resist is removed from the underlying material, negative resists remain on the surface of the substrate where it is exposed. *AZ 5214-E* is capable of image reversal (IR), which results in a negative pattern on the mask. The image reversal capability becomes active in exposed areas at temperatures above 110ºC and is obtained by a special crosslinking agent in the resist formulation. When *AZ 5214-E* is baked, it turns to IR mode; in this mode longer exposed areas will be crosslinked (harden) to a higher degree than those with exposed lower dose based on their dissolution rates. After baking, when the samples are exposed a second time under the UV light the longer exposed areas become crosslinked. Since in our case, the area which we have the contact was exposed one time, photoresist in this area will be softer compared to everywhere else. Hence, when the samples are developed, photoresist on the contact will come out yet will stay elsewhere. The final result will be a negative wall profile ideally suited for lift-off. A schematic representation of use of positive and negative resists are presented in the Figure 4.4-2.

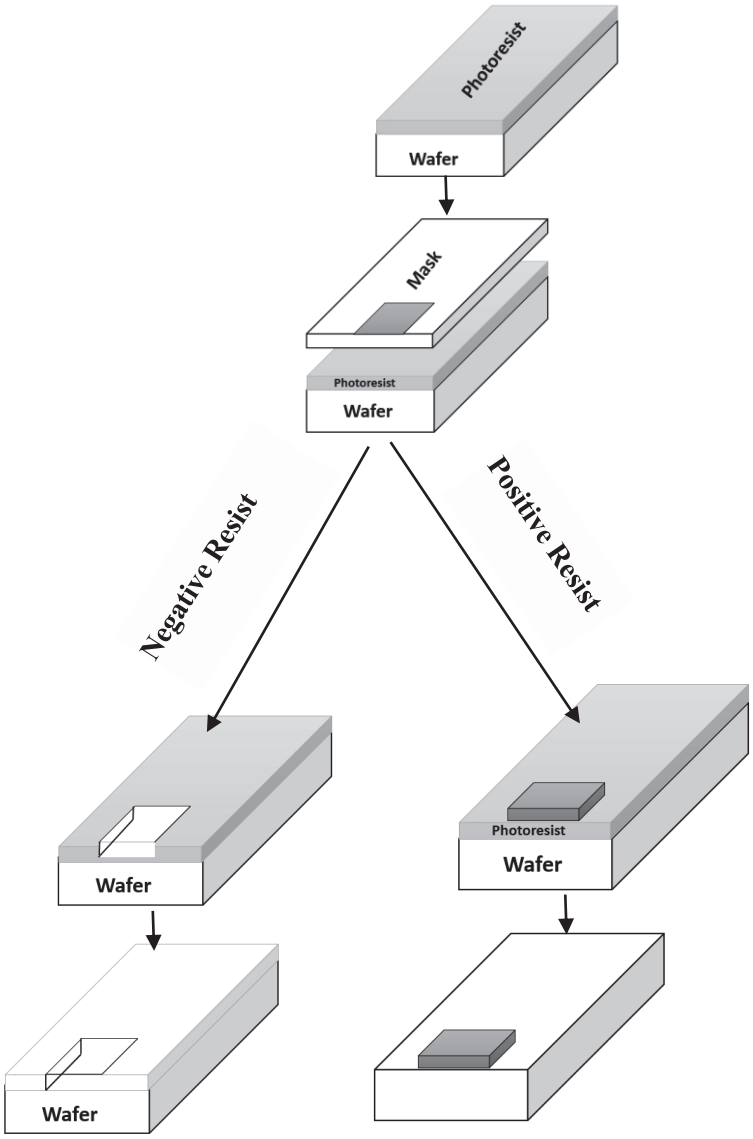

Figure 4.4-2: *Schematic representation of the use of negative and positive photoresists.*

4.4.1.2 Post-Apply Bake

20 to 40% of solvent by weight will remain on the resist film after coating.[15] To remove the excess solvent, the photoresist is dried after spin coating in a process known as post-apply baking, soft bake or prebake. An unbaked photoresist will lose solvent by evaporation at room temperature and as a result, the properties of the film will change. The main reason for soft baking the samples is to stabilize the resist film by reducing the solvent content. By removing the solvents, film thickness is reduced, post exposure bake and development properties are changed, adhesion is improved, and the film becomes less tacky and thus less susceptible to particle contamination. On the other hand, baking photoresist can results in some negative effects. In temperatures higher than 70ºC, photoactive compound (PAC) may decompose and crosslink the resist or it may oxidize. Consequently, it is important to optimize baking temperature. There are several methods to bake the samples. In our lab, we used the most common one, an oven bake. Our samples were soft baked at 110ºC for 60seconds. Since the baking is continuous as long as wafer is hot, it is also important to control the cooling of the wafer. The average thickness of the resist after this coating was approximately 1.4 μm.

4.4.1.3 Alignment and Exposure

After spin coating, the samples with resist on it was aligned and exposed to the radiation of a mercury (Hg) arc lamp at a power of ~ 160 watt (measured at 400 nm) for 30 seconds. The alignment and exposure tool in use is Karl Suss MJB3 photo-mask aligner as shown in the Figure 4.4-4. The photomask is a quartz photoplate containing the patterns to be produced as presented in the Figure 4.4-3. Clear field mask with the soft contact illumination mode is adopted in all of the fabrication processes (dark field mask = opaque background and clear images; clear field mask = clear background and opaque images). It is known that opaque regions on the mask block the UV light.

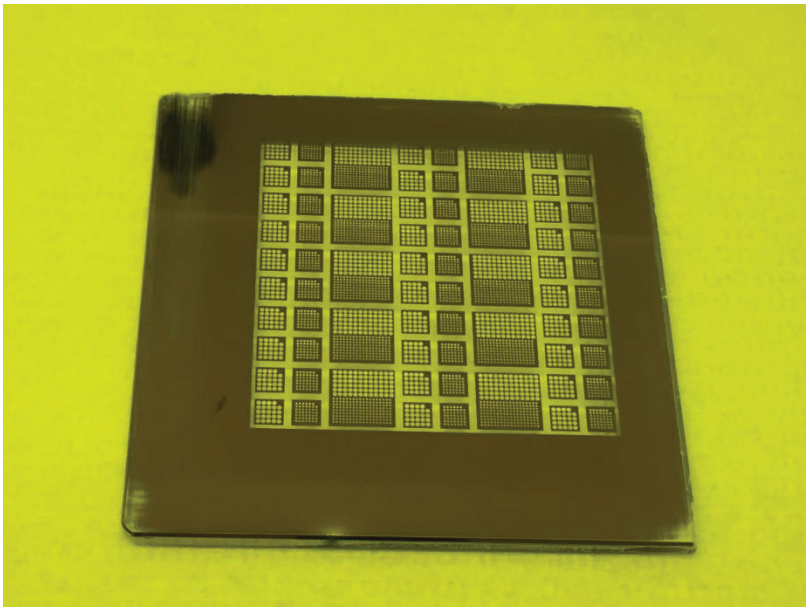

Figure 4.4-3: *Picture of the mask, which was used in our experiments.*

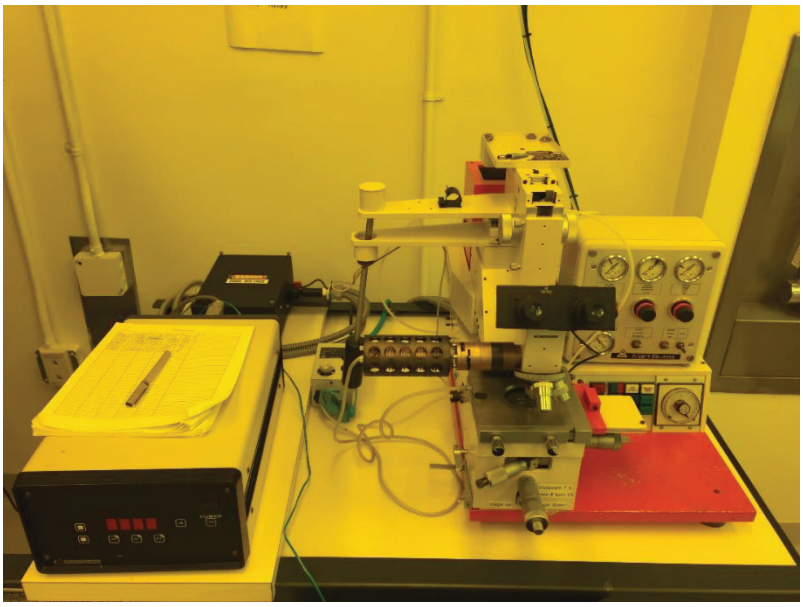

Figure 4.4-4: *Karl Suss MJB3 photomask aligner.*

As we explained above, photoresist operates based on the change in the solubility of the resist in a developer upon exposure to light. Normally, positive photoresist is not soluble in the developer unless it is exposed to UV light in the range of 350-440nm. With the exposure it is converted to very soluble product called carboxylic acid in the basic developer. Consequently, change in the energy of incident light will result in variation in the solubility of the resist.

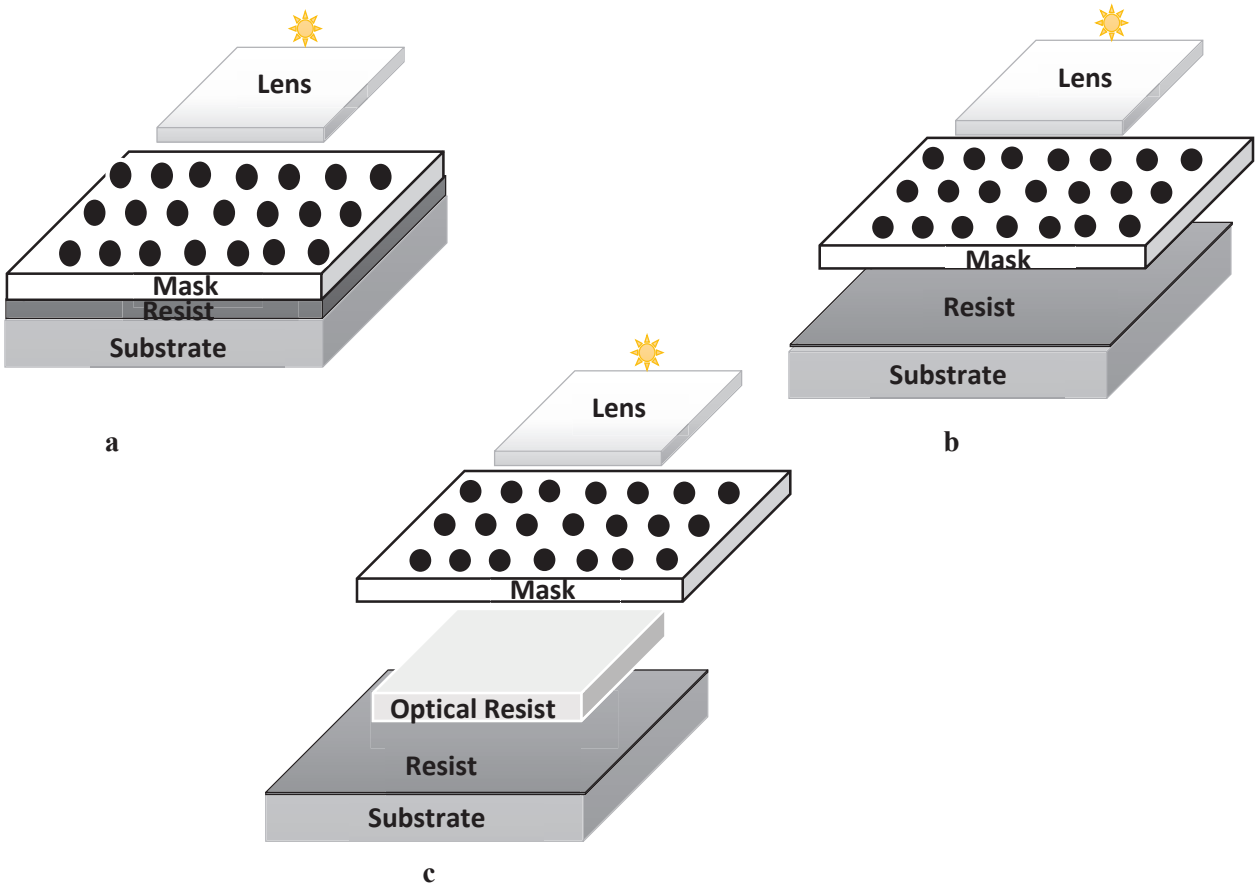

Figure 4.4-5: *Schematic diagram of three modes used in optical lithography namely; (a) contact (b) projection and (c) proximity mode.*

In general, there are three modes used in optical lithography: contact, projection, and proximity mode.[15] Each method has a different optical resolution based on the minimum feature size they can produce. Figure 4.4-5 (a) demonstrates the contact lithography in which the mask is in contact with the photoresist with an unchanged magnification. Although this mode yields a moderate resolution of about 1 μm or better it may damage the mask due to the residues of photoresists, scratching, imaging of the undesirable particles, *etc*. There are two approaches in the contact mode: soft contact with lesser pressure and hard contact with higher pressure to keep the mask and photoresist in contact. In proximity mode, photo mask and resist are separated by a gap as shown in the Figure 4.4-5 (b). Compared to contact mode this mode has a slightly smaller resolution due to the diffraction of the light yet similar magnification. The highest resolution is observed in the projection mode as shown in the Figure 4.4-5 (c) in which an optical system is used to

separate the mask and the resist. Nevertheless, this method requires expensive equipment and complicated set up.

The spatial resolution of the system is an important parameter in photolithography and defines the minimum feature size (MFS) which depends on the optical elements, and radiation wavelength. Higher resolution in optical lithography is achieved with a shorter wavelength exposure. According to the modified Rayleigh criterion the resolution of the optical lithography system is obtained by using following formulas;[18]

$$Resolution = k_1 = \frac{\lambda}{NA} \qquad [\ 4.4\text{-}2\ ]$$

$$Depth\ of\ focus = k_2 = \frac{\lambda}{NA^2} \qquad [\ 4.4\text{-}3\ ]$$

here λ is wavelength, NA is the numerical aperture, k_1 and k_2 are process constants. While better resolution can be obtained with the increase of wavelength and decrease of numerical aperture, depth of focus decreases. In today's lithography systems, wavelength of the radiation changes from blue wavelengths (436nm) up to UV wavelengths (10-14nm).

Before the exposure of the photoresist with an image of the mask, the image on the mask must be aligned with the previously defined patterns on the wafer. Since the tighter overlay controls the circuit features, the alignment process is very important. When the light is exposed, it travels down through the photoresists. In the case of reflective substrates, it is reflected back to photoresist and meets with incoming waves. As a result, a standing wave pattern with high and low intensity is formed at different depths in the photoresists. This pattern is replicated in the photoresist and causes ridges in the side walls of the resist. Figure 4.4-6 displays the relationship between the exposure energy and the percent of resist remaining after exposure and development.

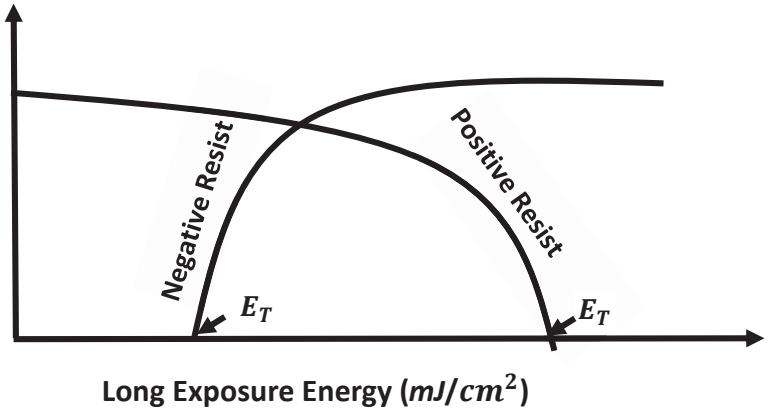

Figure 4.4-6: *A representative graph displaying the relationship between the exposure energy and percent resist remaining after exposure and development.*

4.4.1.4 Post-exposure bake

After the exposure, the samples were hard baked at 100°C for 60 seconds for the IR to take place. Later the samples were exposed without a mask for 60 seconds to make the previously unexposed area of the photoresist soluble in the developer solution. It is known that ridges can be prevented *via* post-exposure bake.[15] The use of high temperature enables diffusion of PAC, thus the standing wave ridges were smoothed out. Since high temperature baking has the same negative effects on post-exposure bake (PEB) as it has on post-apply bake (PAB), it is important to optimize the temperature. Since the presence of solvents increase diffusion, low temperature PAB results in greater diffusion for a given PEB temperature. The main importance of PEB is to remove the effect of standing wave in a conventional resist.

4.4.1.5 Development

The samples were next developed in an *AZ 726 MIF* developer. The final result will be a negative image of the mask pattern with the desired undercut as shown in the Figure 4.4-7 development is one of the most important steps of lithography. In general, aqueous bases, such as tetramethyl ammonium hydroxide (TMAH) are used as developers for common photoresists. The shape of the photoresist profile and the linewidth control are determined by the characteristics of the resist-developer interactions. In terms of

controlling uniformity of development and process latitude, the choice of the method of applying developer is important. Batch development in which 10-20 wafers are developed simultaneously in a large beaker was predominantly used in the past. Later, spin development in which developer is poured onto the rotating wafer become famous. Using of this technique reduces the developer usage and results in more uniform developer coverage. Puddle development is another method, which uses spinning of the wafer to spread the developer. A convex puddle is formed on the wafer due to the surface tension of the developing agent. Once developing time is completed, the wafer is rotated quickly to spin off the developer agent. Although this technique also reduces usage of developer, it may results in over developed areas.

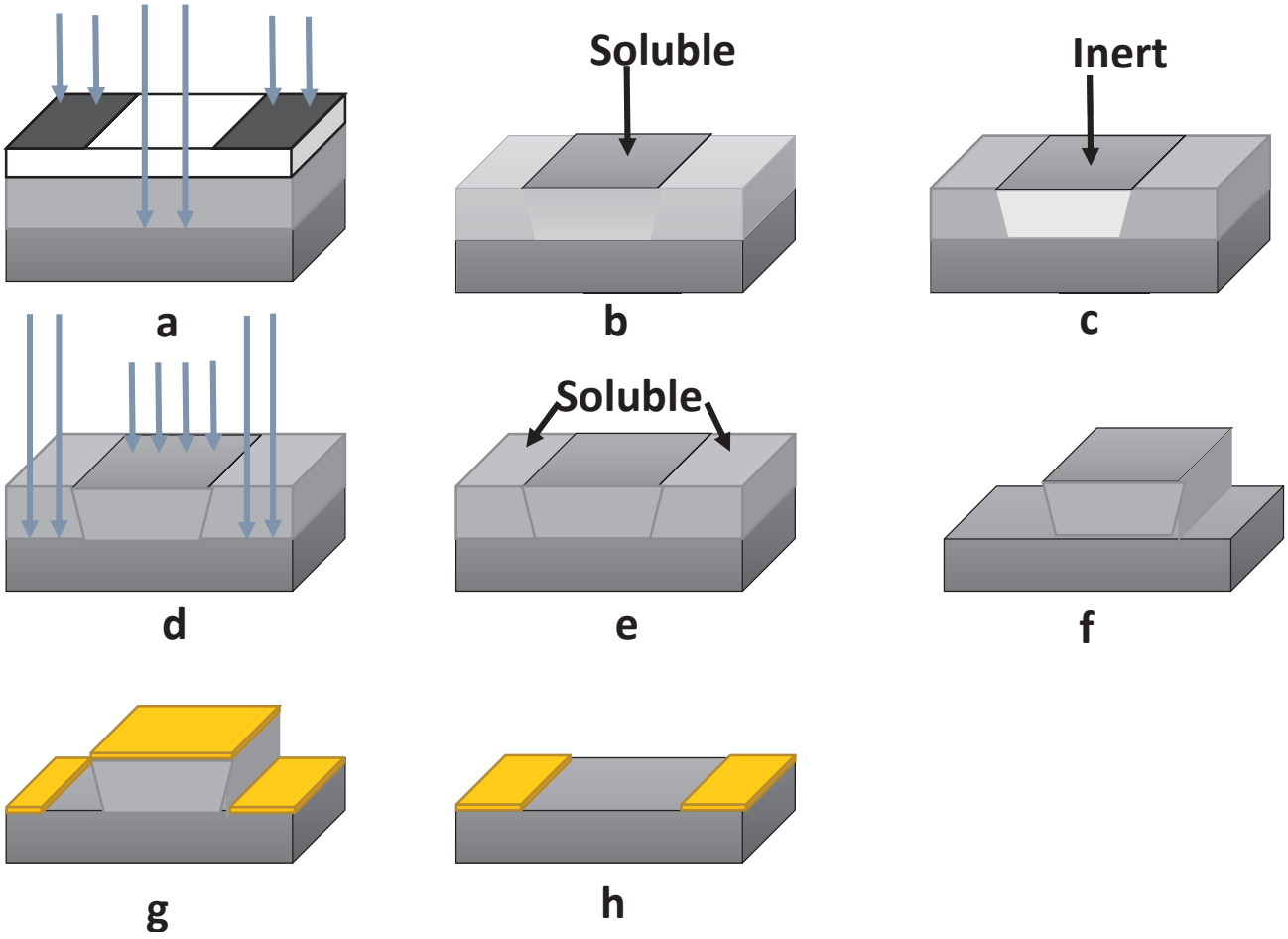

Figure 4.4-7: *Illustration of image reversal lithography process (a) aligned and exposed to the radiation (b) soluble portion after the exposure (c) inert exposed portion of the resist after hard backed (d) flood exposure without the mask (e) resist not exposed to radiation at first place gets soluble (f) after development the area exposed at first place remains g) sputtering deposition of the metals (h) lift-off.*

4.4.2 Plasma Processing

One of the most widely used chemical processes for thin film deposition and etching in microelectronic industry is the plasma processing.[19] Plasma processing relies on the creation and use of plasmas to activate a chemical reaction at a substrate surface. It is believed that plasma based surface processes are indispensable for manufacturing the large scale ICs.[20] In this dissertation, we will focus on deposition processes.

4.4.2.1 Metal Deposition: magnetron sputtering

Sputtering is the deposition process using the irradiation of energetic species to deposit the film of atoms from the surface material (target) onto the substrate. It was first observed by Bunsen and Grove in a gas discharge tube.[21] The basic principle relies on the irradiation of the cathode surface resulting in the disintegration of the cathode materials. In a common sputtering system, positive ions are accelerated from plasma to a target that has a negative potential with respect to plasma. A potential drop between the target and plasma makes ions to have an enough energy to reach the target surface. Target surface is the source of material from which films are grown. An energetic particle striking a solid can transfer its momentum to the target and causes atoms to eject from the surface of the target. A schematic diagram of the principle of sputtering is provided in the Figure 4.4-8.[22] Removed particles which are known as sputtered species are composed of highly energetic species. The energetic sputtered species lowers the temperature of the synthesis. Sputtering deposition can be conducted either in a vacuum or at low pressure, preventing gas phase collusion in the space between the target and the surface. Generally, argon is used as an inert gas plasma for non-reactive sputtering, whereas a variety of gases can be used for reactive sputtering. Plasmas of inherit gasses bombard the cathode which is designated as the target.

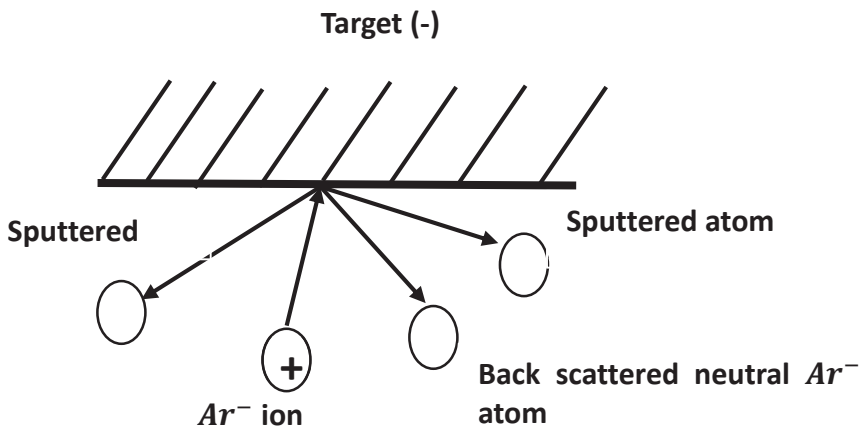

Figure 4.4-8: *Principle of sputtering.*

Nowadays, magnetron sputtering systems at pressure 0.1Pa and with power densities higher than 30W/cm^2 are used in industry. Magnetron sputtering is a high rate deposition method and can deposit films over the large areas. Magnetron sputter deposition is a line of sight collisionless process and produces films with compressive stress.[23] Two main magnetron sputtering types are direct current (DC) and radio frequency (RF) sputtering. While DC sputtering can be used to deposit metal thin films at high rates of oxide or nitrides with a reactive background gas, RF sputtering can be used to deposit metal and insulator thin films in inert or reactive atmospheres.[23] Moreover, as DC sources can be built to supply higher power, a higher deposition rate can be obtained through RF sources.

In DC magnetron sputtering, application of negative voltage on metal targets under a vacuum condition creates a glow discharge in low pressure inert gas.[24] A magnetic field parallel to the target is applied. Consequently, the secondary electrons circle around the magnetic field and stay nearby the surface resulting in an increase of the ionization efficiency. A magnetic field is generated by permanent magnets behind the target. The use of a magnetic field in the magnetrons behind the metal target enables sputtering to be conducted at low temperatures and voltages at a high deposition rate. The use of multiple magnetrons allows for the uniform deposition of the large and complex shaped components.

The energy of the ions bombarding the substrates can be increased by applying the negative voltage to the substrate. As a result of greater bombardment due to higher energetic ions, harder coatings with good wear-resistance and adhesion to substrate are produced. When an electric field E is applied perpendicular

to a magnetic field B, a drift develops in the direction perpendicular to both E and B. Consequently, electrons move on a close path parallel to the target surface. Finally, a ring shaped zone of high density plasma and a high sputtering rate is created *via* a high flux of electrons.[22]

Thin film deposition described in this work was done by the DC magnetron sputtering system as shown in the Figure 4.4-9. The vacuum chamber consists of four sputtering guns which were equipped with chimneys to facilitate the deposition and prevent cross-contamination. The samples were mounted on the top rotational plate, which is about 15 cm from the target. First, the chamber was pumped down to a sufficient base pressure of about 10^{-8} torr to remove the contaminants. Next, argon gas was introduced into it at the rate of 100 sccm for 5 minutes to fill the chamber and waited for the argon pressure inside the chamber to reach stability at 15 millitorr. After that DC voltage was applied between the target (cathode) and the substrate (anode) to start the plasma process and the deposition. Chilled water lines were maintained beneath the targets to cool them down during the sputtering process. Thin metal films deposited on the photo-patterned samples as shown in the Figure 4.4-10 were followed by a short pre-sputtering to remove the trapped impurities from the target surface.

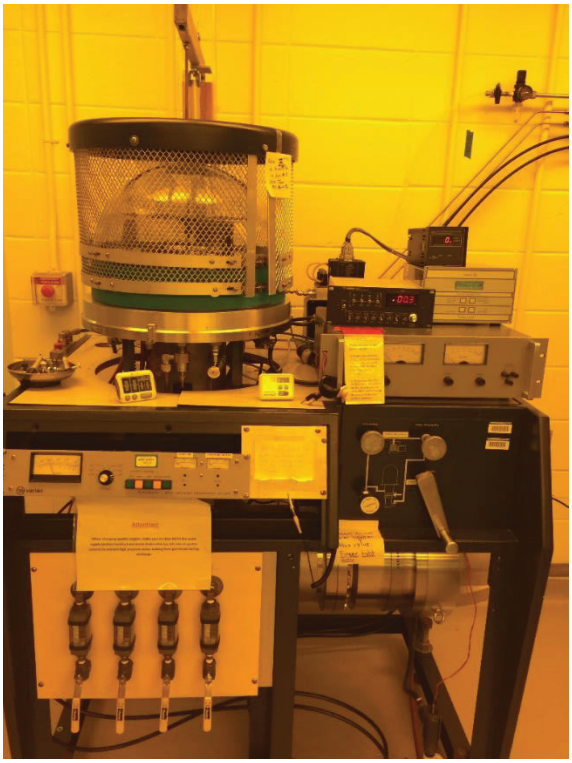

Figure 4.4-9: *DC Magnetron sputtering system for the metallic thin film*.

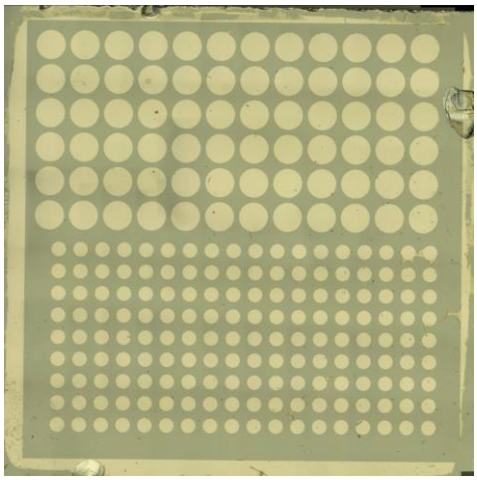

Figure 4.4-10: *Picture of the devices after fabrication.*

4.5 Rapid Thermal Annealing

Rapid thermal annealing (RTA) is a semiconductor fabrication process step, which serves to activate implanted dopants and interfacial diffusing of metal contacts in multilayers, change states of grown films, densify deposited film, and repair damage from ion implantation in order to change its electrical properties. RTA has the advantage of reduced thermal budget, and rapid heating and cooling rates in the range of 30 to 500^{o}/sec.[25] In the RTA, a single wafer is heated at a time using either lamp based heating, a hot chuck or a hot plate during a short duration of time. As soon as the wafer reaches the required temperature, it is held there for a few seconds finally, quenched slowly. In order to create low resistance metal semiconductor contacts, it is important to control some properties, such as temperature, ambient annealing gas, and time. The temperature of the wafer is determined with an indirect sensor, based on the radiation emitted by the wafer. The most common RTA ambient annealing gases are nitrogen (N_2) and argon (Ar). RTA is required to achieve ohmic behavior in the fabrication of AlGaN/GaN HEMTs.[26] Ohmic behavior requires narrow time-temperature process windows.

In our work, we used custom-made strip heater RTA system which consists of a vacuum chamber, a variable transformer, and an infrared optical pyrometer. First, the samples were loaded into the chamber

and the chamber and the chamber was pumped down a base pressure of 2×10^{-7} torr to remove the possible moisture and contaminant gases. Once the research-grade nitrogen gas was filled into the chamber, the current was ramped-up to anneal the samples at 750ºC temperature for 30 seconds with the samples in place on the strip and gas flow on. After the removal of the current the temperature was immediately brought down to room temperature. Figure 4.5-1 presents the picture of RTA system used in our experiments.

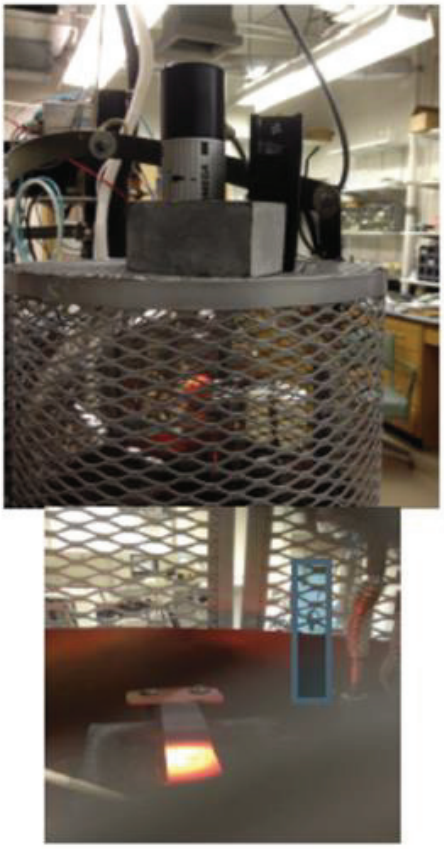

Figure 4.5-1: *Rapid thermal annealing chamber with infrared pyrometer and carbon strip heating system (top). Close up photograph of the carbon strip during annealing (bottom).*

4.6 Lift-off

Lift-off is a semiconductor processing step, which is used for patterning the metal deposited substrate. In lift-off, metal deposited substrate is dipped into the solvent resulting in dissolution of photoresist. As a result, the excess metal that is being deposited on top of the resist areas is lift-off. Duration of the lift-off depends on the quality of the film. For example, in the cases where thick film is deposited on the substrate, it takes longer to lift the metal off. In addition, properties, such as pre-bake and film deposition temperature, exposure dose, and type of resist developer have an effect on the duration of the lift-off. In this dissertation, acetone was used as a lift-off solvent. Furthermore, IR lithography process used in this dissertation, makes the lift-off process easy by creating an undercut profile with a negative slope.

References

[1] J. I. Pankove and T. D. Moustakas, "Gallium nitride (GaN) I semiconductors and semimetals", Academic Press, San Diego (1998).

[2] H. P. Maruska and J. J. Tietjen, "The preparation and properties of vapor deposited single crystal line GaN", Appl. Phys. Lett. **15**, 327 (1969).

[3] N. Nakamura, MRS Bulletin, Warrendale, 1145 (1998).

[4] R. Quay, "Springer series in material science: gallium nitride electronics", Springer-Verlag, Berlin, (2008).

[5] R. F. Davis, S. M. Bishop, S. Mita, R. Collazo, Z. J. Reitmeier, and Z. Sitar, "Epitaxial growth of gallium nitride", AIP Conf. Proc. **916**, 520 (2007).

[6] R. Collazo and N. Dietz, "The group III-Nitride material class: from preparation to perspective in photoelectrocatalysis chapter 8 in photoelectrochemical water splitting by H. J. Lawerenz, and L. Peter", The Royal Society of Chemistry (2013).

[7] W. Kern, "The evolution of silicon wafer cleaning technology", J. Electrochem. Soc. **137**, 1887 (1990).

[8] M. K. Sanganeria, M. C. Ozturk, G. Harris, K. E. Violette, I. Ban, C. A. Lee, and D. M. Maher, "Ultrahigh vacuum rapid thermal chemical vapor deposition of epitaxial silicon onto (100) silicon", J. Electrochem. Soc. **142**, 3961 (1995).

[9] G. R. Srinivasan, "Recent advances in silicon epitaxy and its application to high performance integrated circuits", J. Cryst. Growth **70**, 201 (1984).

[10] E. H. Rhoderick and R. H. Williams, "Metal-semiconductor contacts", Oxford University Press, New York (1988).

[11] R. J. Shul, G. A. Vawter, C. G. Willison, J. W. Lee, S. J. Pearton, and C. R. Abernathy, "Comparison of plasma etch techniques for III–V nitrides", Solid State Electron. **42**, 2259 (1998).

[12] L. L. Smith, S. W. King, R. J. Nemanich, and R. F. Davis, "Cleaning of GaN surfaces", J. Electron. Mater. **25**, 805 (1996).

[13] S. W. King, J. P. Barnak, M. D. Bremser, K. M. Tracy, C. Ronning, R. F. Davis and R. J. Nemanich, "Cleaning of AlN and GaN surfaces", J. Appl. Phys. **84**, 5248 (1998).

[14] M. Dialea, F. D. Aureta, N. G. Van der Berga, R. Q. Odendaala, and W. D. Roosb, "Analysis of GaN cleaning procedure", Appl. Surf. Sci. **246**, 279 (2005).

[15] C. Mack, "Fundamental principles of optical lithography", John Wiley & Sons Ltd. Chichester (2007).

[16] D. Fanning, L. Witkowski, J. Stidham, H. Tserng, M. Muir, and P. Saunier, "Proceedings of international conference on GaAs manufacturing technology", San Diego, (2002).

[17] S. A. Campbell, "The science and engineering of microelectronic fabrication", Oxford University Press, New York, (2001).

[18] M. Rothschild, T. M. Bloomstein, T. H. Fedynyshyn, R. R. Kunz, V. Liberman, M. Switkes, N. N. Efremow, Jr., S. T. Palmacci, Jan H.C. Sedlacek, D. E. Hardy, and A. Grenville, "Recent trends in optical lithography", Lincoln Laboratory Journal **14**, 2 (2003).

[19] F. F. Chen and J. P. Chang, "Lecture notes on principles of plasma processing", Springer Science Business Media, New York (2003).

[20] M. A. Lieberman and A. J. Lichtenbeg, "Principles of plasma discharges and materials processing", John Wiley & Sons, New Jersey (2005).

[21] K. Wasa, M. Kitabatake, and H. Adachi, "Thin film materials technology: sputtering of compound materials", William Andrew Publishing, Springer (2004).

[22] H. S. Nalwa, "Handbook of thin film materials: nanomaterials and magnetic thin films", Academic Press", San Diego (2002).

[23] P. I. John, "Plasma science and the creation of wealth", Tata McGraw-Hill Publishing Company Limited, New Delhi, (2005).

[24] S. Zhang and N. Ali, "Nanocomposite thin films and coatings: processing, properties and performance", Imperial College Press, London (2007).

[25] S. Fransilla, "Introduction to micro fabrication", John Wiley &Sons, Chichester (2004).

[26] M. O. Manasreh, E. T. Yu, "Optoelectronic properties of semiconductors and superlattices: III-V nitride semiconductors applications and devices", Taylor and Francis, NewYork (2003).

Chapter 5

5 Optical Measurements

5.1 Introduction to Raman Spectroscopy

Raman spectroscopy is based on the inelastic scattering of light by elementary excitations, such as phonons (quantized lattice vibrations) or plasmons (free carrier excitations) as a result of modulation of electronic polarizability.[1,2] In general, there are two types of scattering. If the scattered light has the same frequency as the incident photons, it is called as Rayleigh (elastic) scattering. Several sharp peaks next to Rayleigh lines are also observed due to the inelastic scattering of photons.[3] If the scattered light has the frequency $\omega_0 \pm \omega_m$, it is called as Raman scattering. The higher frequency $\omega_0 + \omega_m$ lines are called Stokes (first order) and lower frequency $\omega_0 - \omega_m$ lines are called anti-Stokes lines.[3] These distinctive peaks define a fingerprint-like identification to a molecule since they result from the change in vibrational, rotational or electronic energy of the excited molecule.[4] A schematic diagram of excitation state can be seen in the Figure 5.1-1.

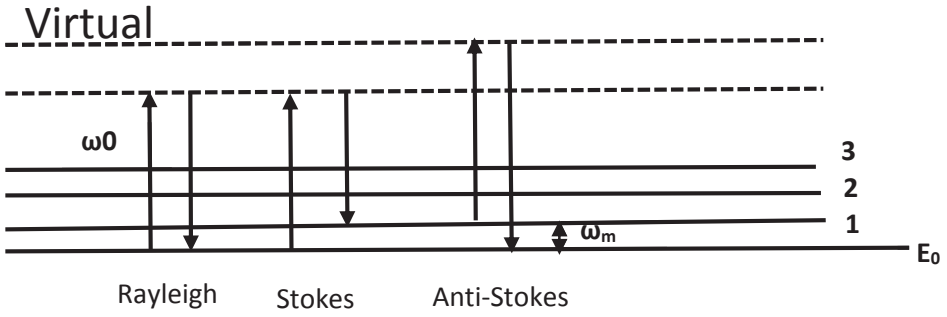

Figure 5.1-1: *Schematic diagram of excitation states. For the excitation energies smaller than the electronic bandgap energy in a semiconductor electron-hole pairs will be excited to a virtual state because of the lack of the real states for the excited electrons to occupy, excluding defect or impurity levels. Resonant Raman effects can be observed in GaN by the use of 325nm ultraviolet excitations since it is above bandgap energy.*

In the Raman spectroscopy, the vibrational frequency ω_m is measured as a shift from the incident beam frequency.[3] The Raman intensity I_{RS} can be approximated as follows for a simple oscillator-like molecule vibrating with angular frequency ω;

$$I_{RS}\sim(\frac{\partial\alpha}{\partial q}E_0[cos(\omega_0-\omega_m)\,t+cos(\omega_o+\omega_m)\,t])^2 \qquad [\ 5.1\text{-}1\ ]$$

here E_0 is the vibrational amplitude, α is the molecular polarizability given by $\alpha=\alpha_0+(\frac{\partial\alpha}{\partial q})_0 q_0+\cdots$, and q is the nuclear displacement given by $q=q_0 cos2\pi\omega_m t$. If $(\frac{\partial\alpha}{\partial q})_0$ equals to zero, the vibration is not Raman-active. This equation indicates that Stokes and anti-Stokes emissions can be amplified by increasing the field strength E_0. In Raman spectroscopy, the exciting line ω_0 is determined in a way that its energy is far below the first electronic excited states. The Stokes lines are stronger than the anti-Stokes lines since the population of the molecules at $\omega=0$ is much larger than that at $\omega=1$. As a result, in general, Stokes side of the spectrum is measured in Raman spectroscopy.[3]

Certain symmetry properties are possessed in a crystal structure and these properties are expressed by the mathematical theory of groups.[1] For the study of 3-dimensional space, square matrixes are used and these set of matrixes are called a representation of a group. Assigning the number "1" indicates a matrix with one column and one row, and satisfies all of the group conditions i.e., A_1. The wurtzite structures

belongs to the space group C_{6v}^4 containing the elements representing the translation reflection, and rotation operations. Since momentum is conserved in the light scattering process, the first order Raman scattering is produced by phonons with wavevector *k~0* (*Γ* point).[2] In hexagonal structures, eight normal phonon modes at $(2A_1 \oplus 2B_1 \oplus 2E_1 \oplus 2E_2)$ near *k=0* are predicted by using the results of the theory of groups.[5] The use of circular addition symbols is to emphasize that this is not a usual addition. As we stated above, among these modes, A and B are one dimensional irreducible representations, whereas E modes are two dimensional representations. A representation is a set of matrices with one set of matrices for each element of the group. For each letter representation, there are two phonon modes, which are transformed according to their letter representations. It is found that one of the A_1 and one of the E_1 phonon modes of wurtzite structure are acoustic modes of vibration, meaning that the atoms move in the same direction in the unit cell. Acoustic phonons have the zero frequency phonon curves at *Γ* point. The remaining six phonon modes $(A_1 \oplus 2B_1 \oplus E_1 \oplus 2E_2)$ are optical modes. Among these modes, while B_1 and E_2 are non-polar, A_1 and E_1 modes are polar and produce a net electric dipole in each unit cell.[1] A frequency splitting between the transverse (TO), and longitudinal (LO) optical vibrations is produced due to the presence of induced dipole by the polar modes. In the TO mode, dipoles do not add each other, rather they sum along the direction of propagation of LO mode. Non-polar modes do not show such a splitting. In GaN and AlN, the splitting of the LO and TO modes causes a continuous variation of LO and TO frequencies between that of the pure A_1 and E_1 modes, with respect to c-axis, and with an angle θ of propagation. This can be expressed as, phonon frequencies for GaN and AlN, at room temperature, as can be seen in the Table 5.1-2.

$$\omega_{QTO}^2(\theta) = [\omega_{E_1(TO)} cos\theta]^2 + [\omega_{A_1(TO)} sin\theta]^2 \qquad [\ 5.1\text{-}2\ ]$$

$$\omega_{QLO}^2(\theta) = [\omega_{A_1(TO)} cos\theta]^2 + [\omega_{E_1(TO)} sin\theta]^2 \qquad [\ 5.1\text{-}3\ ]$$

Table 5.1-1: *Phonon frequencies given in (cm^{-1}) for GaN and AlN at room temperature.*[6,7]

Zone Centers	E_2 (low)	A_1(TO)	E_1(TO)	E_2(high)	A_1(LO)	E_1(LO)
GaN	144	532	559	567	734	741
AlN	248	610	670	657	890	912

While the atomic displacements are along the c- axis for A_1 and B_1 modes, they are perpendicular to the c-axis for the E_1 and E_2 modes. The displacement for the E_2 and B_1 modes are a comparison of atoms, rather than a shear force which give rise to higher oscillation frequency. As a result, the two E_2 and B_1 modes are categorized as low and high. Moreover, although A_1 and E_1 modes are both Raman and infrared (IR) active, the two B_1 modes are neither Raman nor IR active and the two E_2 modes are only Raman active.[8] A_1 mode can be observed when the incident and scattered light have a parallel polarization, whereas E_1 mode is observed only in crossed polarization geometry. This means that in wurtzite structure, the Raman tensor has only diagonal components for A_1 mode, while in E_2 mode both diagonal and off diagonal components are observed in the Raman tensor.[9] The scattered geometric and their theoretically allowed modes in wurtzite structure are given in the Table 5.1-2.

Table 5.1-2: *Raman configuration of allowed modes in hexagonal nitrides. The scattering geometry described with conventional methods. The symbol on the left side of the parenthesis shows the direction of incident light, while the symbol on the right side shows the direction of scattered light. Inside the bracket from left to right the symbols show the polarization direction of the incident and scattered light, respectively, and the bar above the symbol indicates the negative direction. The x and y axes are any two perpendicular axes in the a- plane to the c-axis (z direction) of the wurtzite structure.*[1,2]

CONFIGURATION	MODE
$\boldsymbol{x(y,y)\bar{x}}$	A_1(TO),E_2
$\boldsymbol{x(z,z)\bar{x}}$	A_1(TO)
$\boldsymbol{x(z,y)\bar{x}}$	E_1(TO)
$\boldsymbol{x(y,z)y}$	E_1(TO), E_1(LO)
$\boldsymbol{x(y,y)z}$	E_2
$\boldsymbol{z(y,x)\bar{z}}$	E_2
$\boldsymbol{z(y,y)\bar{z}}$	A_1(LO), E_2
$\boldsymbol{z(x,x)\bar{z}}$	A_1(LO), E_2
$\boldsymbol{z(x,y)\bar{z}}$	E_2

Foreign signals induced by impurities can be also observed in Raman spectroscopy as well as phonon signals related to lattice. Atomic oscillation produced by the replacement of impurity atoms with heavier host lattice atoms is referred to as local vibrational mode (LVM). The LVM has a frequency above the optical branch, yet still between the acoustic and optical branch of phonons. Point defects can also cause a defect mode called the disorder-activated Raman scattering (DARS) mode. The peaks at 360 and 420cm^{-1} were assigned to LVMs due to Ga or N vacancies.[2] Some researchers believe that the peaks at 300 and 670 cm^{-1} near the E_2^H peak and signals at 560 and 730 cm^{-1} near the A_1(LO) peak should be assigned to DARS because of phonon density state like characteristics.[10]

5.1.1 The stress effect

Changes in stress or strain can be observed *via* shift of the phonon frequencies of the material, so the shift of the phonon frequencies depends on chemical bonding and atomic structure. Consequently, it is of great importance to use Raman measurements to determine the stress and strain in III-nitride materials. There are three typical stress situations for these types of materials: biaxial stress in the a-plane, uniaxial stress along the c-axis and hydrostatic stress. These biaxial and uniaxial stresses are generally caused by the lattice mismatch and difference in thermal coefficient between the hetero-epitaxial layers or between the deposited layers. Native defects or incorporated impurities can distort lattice structure around them and can result in hydrostatic stress.[2] Under these deformations the space group symmetry of the wurtzite structure is preserved, no phonon splitting occurs and only the frequency of the phonons shifts. Since the atomic position is characterized by the two hexagonal lattice constants a and c, the strain tensor can be obtained with following equations;[11]

$$\epsilon_{xx} = \epsilon_{yy} = (a - a_0)/a_0 \qquad [\ 5.1\text{-}4\ ]$$

$$\epsilon_{zz} = (c - c_0)/c_0 \qquad [\ 5.1\text{-}5\ ]$$

A force acting in a certain direction applied to a unit area of the plane of the solid is called as a stress component. All of the stress and strain components form a stress tensor, σ, and strain tensor, ϵ. The stress (e.g. $\sigma_{xy} = \sigma_{yx}$) and strain tensors follow the symmetry to eliminate effects of the rotational torque.[11,12] Hooke's law, *via* the stiffness tensor $C_{ijkl,}$ connects the stress and strain tensors with following equation;[13]

$$\sigma_{ij} = \sum_{k,l} C_{ijkl}\epsilon_{kl} \qquad [\ 5.1\text{-}6\ ]$$

Therefore, the in-plane strain ϵ_{xx} and ϵ_{zz} in GaN can be calculated from the stress σ_{xx} and σ_{zz} *via* equations [5.1-7] and [5.1-8].[14]

$$\sigma_{xx} = \sigma_{yy} = [(C_{11} + C_{12}) - \frac{2C_{13}^2}{C_{33}}]\epsilon_{xx} \qquad [\ 5.1\text{-}7\ ]$$

$$\sigma_{zz} = 2C_{13}\epsilon_{xx} + C_{33}\epsilon_{zz} \qquad [\ 5.1\text{-}8\ ]$$

where the elastic constants of GaN are C_{11}=390 GPa, C_{12}=145 GPa, C_{13}=106 GPa, and C_{33}=398 GPa.[15] For uniaxial stress along the c-axis $\sigma_{xx} = \sigma_{yy} = 0$, and for hydrostatic pressure $\sigma_{xx} = \sigma_{yy} = \sigma_{zz}$. The frequency shift $\Delta\omega_\lambda$ can be found by using Raman spectroscopy, and it can be given as follows;

$$\begin{aligned}\Delta\omega_\lambda &= 2a_\lambda\epsilon_{xx} + b_\lambda\epsilon_{zz} \\ &= 2\bar{a}_\lambda\sigma_{xx} + \bar{b}_\lambda\sigma_{zz}\end{aligned} \qquad [\ 5.1\text{-}9\ ]$$

where *a* & *b*, and $\bar{a}$ & $\bar{b}$ are deformation potentials in the case of given strain and stress, respectively. It is usually assumed that a particular stress is present in a material system before obtaining the stress and strain value by Raman spectroscopy.

Assuming this, the a-plane stress and strain *via* phonon frequency can be expressed as follows;[16]

$$\Delta\omega_\lambda = 2[a_\lambda - b_\lambda(C_{13}/C_{33})]\epsilon_{xx} = 2\bar{a}_\lambda\sigma_{xx} \quad [\ 5.1\text{-}10\ ]$$

Piezoelectric polarization in the Ga- and N-face domains can be calculated by using Raman spectroscopy and equation [5.1-11] as follows;

$$P_{PZ} = [e_{31} - (C_{13}/C_{33})e_{33}]2\epsilon_{xx} \quad [\ 5.1\text{-}11\ ]$$

where $e_{31} = -0.34\ C/m^2$ and $e_{33} = 0.67\ C/m^2$ are piezoelectric coefficients.[17]

Tensile or compressive stress of hexagonal GaN can be derived from the relative shift of the E_2^H and A_1(LO) peaks of GaN. Since the E_2^H mode generally gives the strongest signal and the frequency is sensitive to biaxial strain in the c-plane, while biaxial strain of the hexagonal GaN layer is generally obtained by observing E_2^H mode.[6,17,18] The relative shift of the peak is the difference between the reference point and the observed peak position. An increase in the phonon frequencies with respect to unstrained GaN indicates compressive stress, whereas a decrease points to tensile stress. The values of 567.2 and 734.0 cm^{-1} were used as the reference point which is the measure of unstrained GaN $E_2^{(2)}$ and A_1(LO) phonon frequencies, respectively.[6,17,19,20] The relationship between the frequency of the peak ω (cm^{-1}) and the Raman biaxial stress σ_b can be expressed as follows;

$$\omega_{E^2_{(2)}} = 567.2 - 4.2\sigma_b \quad [\ 5.1\text{-}12\ ]$$

$$c\omega_{A_{1(LO)}} = 734.0 - 2.76\sigma_b \quad [\ 5.1\text{-}13\ ]$$

here 4.2 and 2.76 cm^{-1} / GPa are the Raman biaxial pressure coefficients for the $E_2^{(3)}$ [17,21] and A_1(LO)[22] mode vibrations.

For GaN there is a well-known correlation between the free-carrier concentration, mobility, and the plasma frequency. The LO phonon-plasmon (LPP) the coupled modes, ω_+(LPP^+) and ω_-(LPP^-) allow for determining the free-carrier concentration of semiconductors using Raman spectroscopy.[23] The coupling is through the macroscopic electric fields of these excitations. There is a high dependency between the plasmon frequencies on character of coupled modes. When plasmon frequency is lower than the uncoupled

LO phonon frequency, the LPP^+ mode behaves like a plasmon, while the LPP^- mode is phonon-like.[24] It has been proposed that the frequency of the LPP^+ mode increases with the carrier concentration, and eventually at higher concentration, corresponds to that of the plasmon.[2,18,25,26] If damping is neglected, the frequencies of the LPP^+ and LPP^- modes can be calculated from equation [5.1-14].

$$\omega_{\pm}^2 = \frac{\omega_{LO}^2+\omega_P^2}{2} \pm [(\frac{\omega_{LO}^2+\omega_P^2}{2})^2 - \omega_P^2\omega_{TO}^2]^{1/2} \qquad [\ 5.1\text{-}14\ ]$$

where ω_p is the plasma frequency, ω_{TO} (533 cm^{-1})[21,27] and ω_{LO} (735 cm^{-1})[21,25] are the TO and LO phonon frequencies, respectively.

The free carrier concentration (n) can be calculated using equation [5.1-15].

$$\omega_p = (\frac{4\pi ne^2}{\varepsilon_\infty m^*})^{1/2} \qquad [\ 5.1\text{-}15\ ]$$

here ε_∞ (5.35)[20] is the high frequency dielectric constant and $m^*(0.2m_0)$ is the effective mass of the free carriers. A_1(LO) phonon mode propagates in the direction of the z axis and the on-axis (z) electron mobility (μ) can be obtained from equation [5.1-16] by using γ is the plasmon damping constant.

$$\gamma = \frac{e}{m^*\mu} \qquad [\ 5.1\text{-}16\ ]$$

Raman spectroscopy can be used to obtain information about the crystal quality, the stress, the free carrier charge concentration, the aluminum concentration, and the temperature related to vibrational states of GaN, AlGaN and AlN.[20] As a result, this information can be used for monitoring the growth process. In Raman spectroscopy, the scattering efficiency in covalent crystals is higher than that of ionic crystals. Since nitride semiconductors consist of ionic and covalent bonds, they are suitable for Raman spectroscopy.[2] In terms of Raman spectroscopy's non-destructive, contactless, and superior resolution properties, it has an advantage over the other methods. In addition, the presence of organic contaminants as small as 1μm, or films as thin as 1μm on Si wafers can be identified *via* Raman spectroscopy.[28] Moreover, this technique does not require any special sample preparation, such as thinning or polishing.[2]

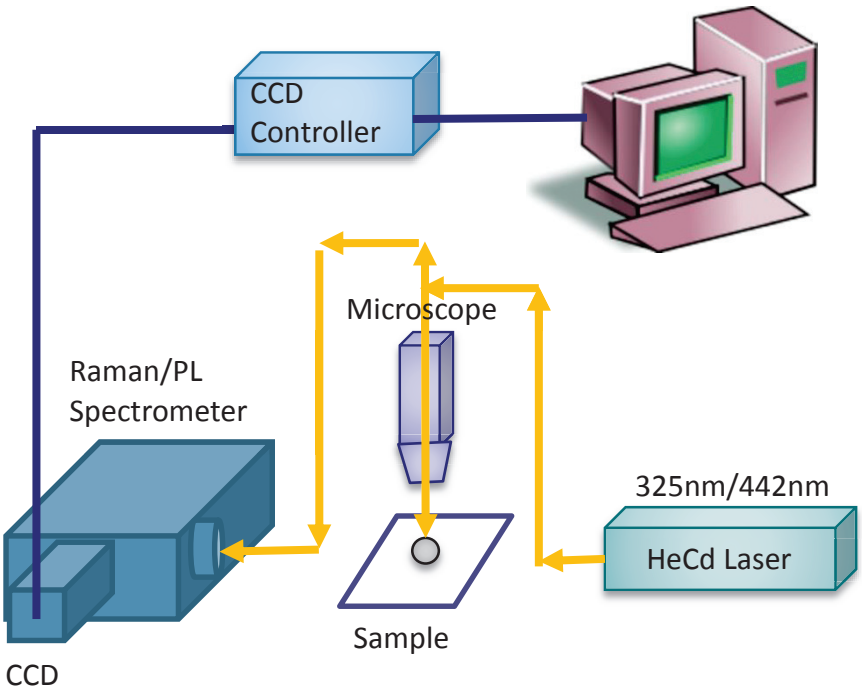

Figure 5.1-2: *Schematic diagram of Raman spectroscopy system.*

For selective probing of phonon and material properties averaged over sample layer thickness or in a surface layer, varying excitation wavelengths are used in Raman experiments.[20] The material properties of GaN, averaged over the sample layer thickness, can be probed by using visible illumination. UV excitation wavelengths are used to probe surface properties since UV laser light is absorbed in the sample.[29] Surface layer thickness examined by a laser can be calculated by using the absorption coefficient α at a given wavelength with the equation of $1/2\alpha$. (i.e., at 325nm $1/2\alpha = 40nm$).[30] To probe the surface layer of $Al_xGa_{1-x}N$ films of higher aluminum concentration, deep-UV micro Raman spectroscopy should be used. In this experiment, Raman spectroscopy was performed at room temperature using the 441.563nm He-Cd laser line (80mW).

The Raman system is home- made, and equipped with a Jobin Yvon spectrometer, as well as a thermally-cooled charge coupled device (CCD) detector (2048 by 512 pixels). The excitation laser beam was focused onto a small spot with a diameter of 5~10 μm. The laser enters the microscope through several reflective mirrors and illuminates the samples. A laser filter was applied to the entrance of the spectrometer to ensure that only the Raman signal is detected by CCD. High resolution scans were acquired from gratings

of 3600 lines/mm with 0.2 cm^{-1} resolution. A schematic diagram of the experimental setup was provided in the Figure 5.1-2.

5.1.2 Results and Discussion

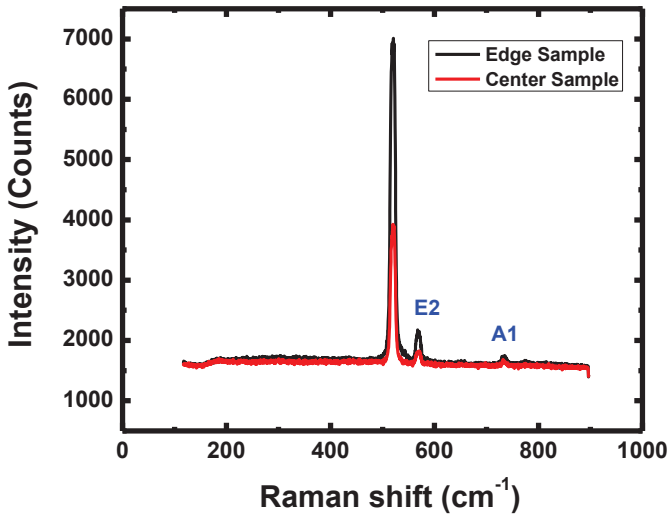

Figure 5.1-3: *Raman spectra from two different samples collected at room temperature in a backscattering configuration from the AlGaN/GaN HEMTs heterostructure on Si substrate.*

Figure 5.1-3 shows the room temperature Raman spectra (after baseline subtraction) that were collected from edge and center samples. These Raman spectra were collected in order to investigate the crystalline quality, the residual stress, and the possible origin of the defects. Lorentzian functions were employed to determine the peak positions and full-width-at-half-maximum (FWHM) of the Raman peaks. Wurtzite type GaN belongs to the space group C_{6v}^4 and has four atoms per unit cell. According to group theory, nine optical modes reduce to the following optical modes at the Γ point of the Brillouin zone[31]: $A_1(z)+2B_1+E_1(x,y)+2E_2$. Among these modes, the A_1 and E_1 modes are both Raman and infrared active, the two B_1 modes are silent, and the two E_2 modes are Raman active.[32] The A_1 and E_1 modes split into longitudinal (LO) and transverse optical (TO) components due to their polarity. In this experiment, we observed 2 peaks with the *z (-,-) z* backscattering geometry for each sample; $E_2^{(H)}$ mode of GaN at around 569 cm^{-1} and $A_1(LO)$ mode of GaN at around 734 cm^{-1} for both of the samples. The Raman peak positions

observed were in an agreement with the results of others.[7,33,34] The $A_1(TO)$ was not observed, which may indicate that c-axis of the layer is parallel to the growth direction.

Although the information on the crystalline quality can be obtained from the width of the $E_2^{(H)}$ peak, the type and level of stress can be derived from the $E_2^{(H)}$ frequency.[20] The FWHM values of the $E_2^{(H)}$ peak for the two samples were 13 cm^{-1}, indicating that the two devices have a same crystalline quality. The relative shift of the peak is the difference between the reference point and the observed peak position. The value of 567.2 cm^{-1} has been used as the reference point[6,19] which is the measure of unstrained GaN $E_2^{(H)}$. The relationship between the frequency of the peak ω (cm^{-1}) and the Raman biaxial stress σ_b can be expressed as follows;

$$\omega_{E_{(2)}^H} = 567.2 - 4.2\sigma_b \qquad [\ 5.1\text{-}17\ ]$$

where 4.2 cm^{-1}/GPa is the Raman biaxial pressure coefficients for the $E_2^{(H)}$.[17,21] From the Raman measurement, it was determined that the GaN layer is under compressive stress of 0.43 GPa. In conclusion, it was found that both of the devices displayed similar crystalline quality and stress.

5.2 Introduction to Photoluminescence Spectroscopy

Luminescence is defined as the transition from a real excited electronic state to a lower energy state by illuminating the light to the material. In the case of photoluminescence (PL), the excited electronic state is created by the absorption of photon(s) from incident radiation.[35] The conventional PL spectroscopy is based on the measurement of secondary-emission spectrum at fixed parameters of the primary radiation.[36] In the luminescence process, electron-hole pairs are generated with the incident light, which then return to a lower energy state by the emission of the light by losing some of their energy (relaxation) and recombine. In principle, PL signals can be observed for an incident light excitation with a photon energy greater than the electronic bandgap of the material. In semiconductors, luminescence can be distinguished as intrinsic, extrinsic and exciton.[36] A radiative recombination is observed in the direct bandgap materials i.e., materials in which the conduction and valance band extrema exist at the same momentum k position. This process is

known as intrinsic. Radiative recombination is a process, which results in photon emission. Electron hole pairs (EHPs) are produce at the same rate as the generation (i.e., one photon is emitted for each photon is absorbed) during steady state excitation.

In indirect semiconductors, phonons are generated predominantly so, there is less likely to be radiation recombination unless a highly localized center assists the phonons. This type of luminescence is known as extrinsic. In reality, growth of a semiconductor without impurities (e.g. dopants) and defects is almost impossible. Therefore, most of the semiconductors have shallow donor or acceptor energy levels in the bandgap, and these are dominated by band to band transition at high temperatures. Nevertheless, free-to-bound transition can be observed through the radiative recombination of free electrons (free holes) with holes (electrons) are trapped at the acceptor (donor) levels at adequately low temperatures.[13] Materials containing defects have a strong tendency to be trapped at the ionized donor and acceptor sites, then return to equilibrium.[35] Finally, an exciton luminescence occurs due to the recombination of free, impurity-bond or localized excitons.[36] The simplest example of an excitation and recombination mechanism in photoluminescence for a semiconductor with trap levels is given in the Figure 5.2-1.

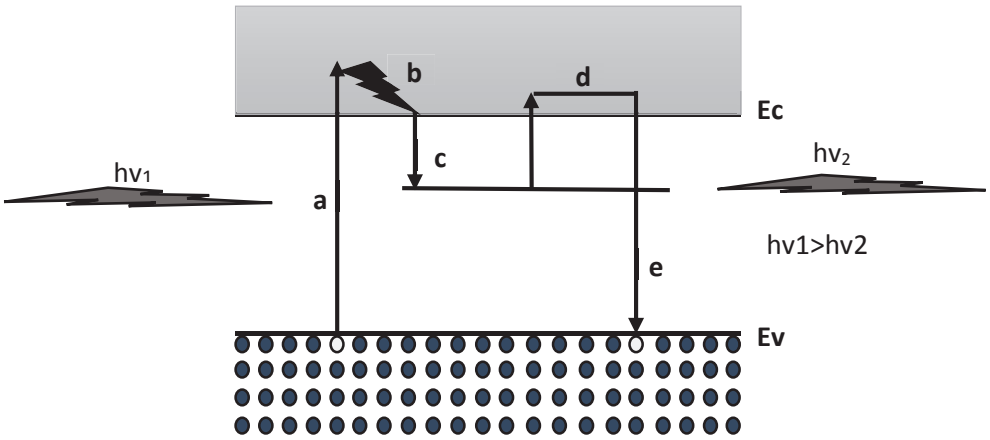

Figure 5.2-1: *Schematic diagram of the light excitation from a semiconductor. (a) absorption of an incoming photon with an energy $hv_1 > E_g$ creating EHPs (b) the excited electron gives up energy to the lattice by scattering until it nears the bottom of the conduction band (c) electrons are trapped until thermally reexcitation (d) and (e) direct recombination of the electron with a hole in the valance band and release of a photon with an energy hv_2.*

Photoluminescence spectroscopy is a nondestructive and highly sensitive method to determine the bandgap and impurity levels of semiconducting materials as well as their defect sites. In a typical PL experiment, an excitation source of a specific energy transition is achieved *via* use of single unique wavelength laser. The emitted spectrum of the light is observed as a plot of light intensity versus wavelength by a photodetector. In wurtzite GaN, there are three type of excitation referred to as A (3.485eV), B (3.491eV) and C (3.530eV) due to the split of the band into three states.[37] Nonetheless, the presence of donor levels make it difficult to observe these signals since donor bond excitation at 3.47eV typically dominate in GaN.[17] The values of band peaks might change based on the growth techniques, which are used, and some of the values obtained by other researchers with different growth techniques were summarized in the Table 5.2-1.

Electronic energy states near the middle of the band gap are referred to as deep level states and they also cause radiative recombination. It is possible to observe PL signals from deep level radiative recombination centers, even for the excitation energies below bandgap energy. Hence, PL spectroscopy is an important technique to detect deep centers.

Table 5.2-1: *Parameters of the PL bands in undoped GaN analyzed in Reshchikov and Morkoc laboratory.*[38]

PL Band	Growth Method	Peak Position(eV)	FWHM(eV)
BL[a]	MOCVD	2.86	0.34
YL[a]	MBE	2.20-2.30	04-0.5
GL[a]	HVPE	2,48	0.53

5.2.1 Experiment

Photoluminescence (PL) is an efficient tool to study the excited electronic states in solids. In many cases, it has advantages in analyzing the fine structure of excited states over absorption or reflection spectra because the luminescence intensity is determined both by the population of excited states and the optical transition properties.[36] In contrast to Raman measurements, which can use an excitation laser energy below the band gap of GaN, preventing interference of the measurement technique with device operation, PL

measurements must be taken using an excitation source with photon energy above the band gap of GaN. The resulting light absorption may provide benefits by determining the properties of the device very near to the AlGaN/GaN device channel.[39] The PL measurement were carried out at room temperature using a continuous wave He-Cd laser with 325nm line as an excitation source, and PL spectra was dispersed by a 2400 lines/mm diffraction grating. The PL signal was collected by an objective lens, directed to a spectrometer, and detected by a CCD detector.

5.2.2 Results and Discussion

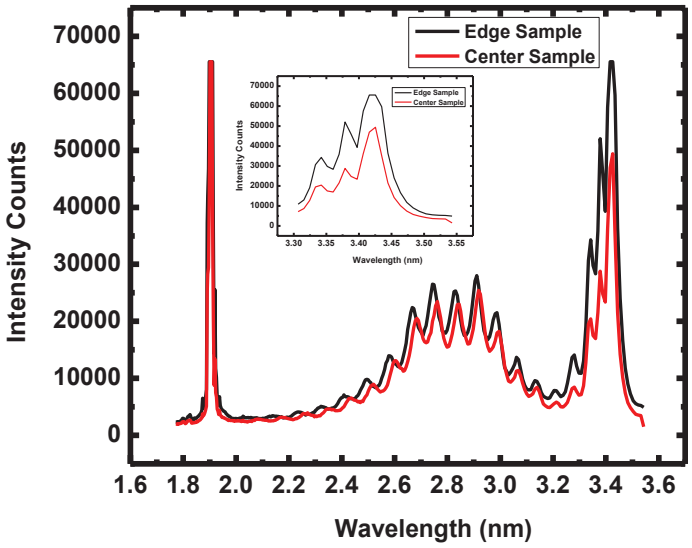

Figure 5.2-2: *Typical room temperature PL spectra from AlGaN/GaN HEMTs heterostructure on Si recorded under 325 nm laser line excitation. The inset shows the high resolution PL spectra of near-band-edge emission (NBE) with a maximum at 3.42 eV for Edge sample and Center sample.*

Typical room temperature PL spectra for the piece of the HEMTs wafer investigated are shown in the Figure 5.2-2. The PL spectra exhibit two main bands: a near-band-edge emission (NBE) with a maximum at 3.42eV as well as a broad and strong blue luminescence (BL) band peaking at 2.79eV. The near-band-edge emission peaks in high resolution PL spectra for edge sample and center sample are shown in the Figure 5.2-2 is attributed to annihilation of free excitons.[38,40] The spectrum is dominated by exciton emission which is believed to be originated from the flat-band region of the GaN epitaxial layer. The

presence of these unresolved excitonic transitions in edge and center samples reflects the high quality of the hetero interfaces rather than the quality of the GaN layers alone.[41] All of the PL spectra showed an interference fringe pattern, which is attributed to the superposition of the light emitted from the contacts and reflected by different heterostructure interfaces.[42,43]

The BL band peak position reported in this paper is similar to values obtained by other researchers, which varies between 2.7 and 3.0 eV.[38,44,45] Seager *et al*. attributed the BL band transition from C_{Ga} donor to C_N acceptor (DAP transition) [46] It is known that the spectral peak position of the BL shifts when the intensity of the excitation laser is changed. However, in some circumstances, such as when the impurity concentration is low, DAP transitions can still exist.[45] In GaN PL spectra, the yellow luminescence (YL) band[38] is typically observed at around 2.2 eV. The YL peak can be attributed to carbon impurity,[45] Ga vacancy,[47] Ga interstitial,[48] N antisite,[49] and substitution oxygen.[50] Recently, some researchers showed that yellow YL at ~2.2 eV and BL at ~2.8 eV is related to the hot-electron-induced kink[51,52] and degradation[53,54] effects in AlGaN/GaN HFETs. Nonetheless, no YL band was observed from our spectra, which can be an indication of reasonably good equalities of HEMTs structure with the buffer layers used in this growth.[55]

References

[1] J. M. Hayes, "Raman Scattering in GaN, AlN, AlGaN: Basic material properties, processing and devices", PhD dissertation, University of Bristol (2002).

[2] H. Harima, "Properties of GaN and related compounds studied by means of Raman scattering", J. Phys.: Condens. Matter, **14**, R967 (2002).

[3] J. R. Ferraro, K. Nakamoto, C. W. Brown, "Introduction to Raman spectroscopy", Academic Press, California (2003).

[4] E. Smith and G. Dent, "Modern Raman spectroscopy, a practical approach", Wiley, NewYork, (2005).

[5] D. L. Rousseau, R. P. Bauman, and S. P. S. Porto, "Normal mode determination in crystals", J. Raman Spectrosc. **10**, 253 (1981).

[6] V. Y. Davydov, Y. E. Kitaev, I. N. Goncharuk, A. N. Smirnov, J. Graul, O. Semchinova, A. P. Mirgorodsky, and R. A. Evaretov "Phonoon dispersion and Raman scattering in hexagonal GaN and AlN", Phys. Rev. B, **58**, 12899 (1998).

[7] P. Perlin , C. J. Carillon, J. P. Itie, A. S. Miguel, I. Grzegory, and A. Polian. "Raman scattering and x-ray absorption spectroscopy in gallium nitride under high pressure", Phys. Rev. B, **45** 83 (1992).

[8] M. Cardona, "Light scattering in solids II (Springer Topics in Applied Physics)", Springer, Berlin, (1982).

[9] R. Loudon, "The Raman effect in crystals", Adv. Phys. **13,** 423 (1964).

[10] J. C Nipko, C.-K. Loong, C. M. Balkas, and R .F. Davis, "Phonon density of states of bulk gallium nitride", Appl. Phys. Lett. **73** 34 (1998).

[11] J. M. Wagner and F. Bechstedt, "Phonon deformation potentials of α-GaN and AlN: An ab initio calculation", Appl. Phys. Lett, **77**, 346 (2000).

[12] C. Kittel, "Introduction to solid state physics" John Wiley & Sons, Inc, (1996).

[13] P. Y. Yu and M. Cardona, "Fundamentals of semiconductor", Springer-Verlag, Berlin (1996).

[14] J. Gleize, F. Demangeot, J. Frandon, M.A. Renucci, F. Widmann, and B. Daudin, "Phonons in a strained hexagonal GaN–AlN superlattice", Appl. Phys. Lett. **74**, 703 (1999).

[15] A. Polian, M. Grimsditch, and I. Grzegory, "Elastic constants of gallium nitride", J. Appl. Phys. **79**, 3343 (1996).

[16] F. Tong, "Fabrication and characterization of ZnO and GaN devices for electronic and photonic applications", PhD dissertation, Auburn University, (2013)

[17] C. Kisielowski, J. Krüger, S. Ruvimov, T. Suski, J. W. III Ager, E. Jones, Z. L. Weber, M. Rubin, E. R. Weber, M. D. Bremser, and R. F. Davis, "Strain-related phenomena in GaN thin films", Phys. Rev. B, **54** 17745 (1996).

[18] T. Kozawa, T. Kachi, H. Kano, H. Nagase, N. Koide, and K. Manabe, "Thermal stress in GaN epitaxial layers grown on sapphire substrates", J. Appl. Phys. **77** 4389 (1995).

[19] M. Park, J. J. Cuomo, B. J. Rodriguez, W.-C. Yang, and R. J. Nemanich, "Micro-Raman study of electronic properties of inversion domains in GaN based lateral polarity heterostructures", J. Appl. Phys. **93**, 9542 (2003).

[20] M. Kuball, "Raman spectroscopy of GaN, AlGaN and AlN for process and growth monitoring/control", Surf. Interface Anal. **31**, 987 (2001).

[21] F. Demangeot, J. Frandon, M. A. Renucci, O. Briot, B. Gil, and R. L. Aulombard, "Raman determination of phonon deformation potentials in α-GaN", Solid State Commun. **100**, 207 (1996).

[22] J. Y. Lu, Z. J. Wang, D. M. Deng, Y. Wang, K. J. Chen, K. M. Lau, and T. Y. Zhang, "Determining phonon deformation potentials of hexagonal GaN with stress modulation", J. Appl. Phys. **108**, 123520 (2010).

[23] A. Mooradian and G. B. Wright, "Observation of the Interaction of Plasmons with Longitudinal Optical Phonons in GaAs", Phys. Rev. Lett. **16**, 999 (1966).

[24] K. Jeganathan, R. K. Debnath, R. Meijes, T. Stoica, and R. Calarco, "Raman scattering of phonon-plasmon coupled modes in self-assembled GaN nanowires", J. Appl. Phys. **105**, 123707 (2009).

[25] B. B. Varga, "Coupling of plasmons to polar phonons in degenerate semiconductors", Phys. Rev. **137**, A1896 (1965).

[26] M. V. Klein, B. N. Ganguly, and P. J. Colwell, "Theoretical and experimental study of Raman scattering from coupled LO-phonon-plasmon modes in silicon carbide", Phys. Rev. B, **6**, 2380 (1972).

[27] H. Harima, H. Sakashita, S. Nakashima, "Raman microprobe measurement of under-damped LO-phonon-plasmon coupled mode in n-type GaN", Mater. Sci. Forum, **1363**, 264 (1998).

[28] J. M. Lerner and F. Adar, "Laser Focus World", Pennwell Publishing Co. (1989).

[29] M. Kuball, J. M. Hayes, J. Jun, T. Suski, M. Leszczynski, J. Domagala, H. H. Tan, J. S. Williams, C. Jagadish, "High-pressure high-temperature annealing of ion-implanted GaN films monitored by visible and ultraviolet micro-Raman scattering", J. Appl. Phys. **87**, 2736 (2000).

[30] J. F. Muth, J. H. Lee, I. K. Shmagin, R. M. Kolbas, H. C. Casey, Jr. B. P. Keller, U. K. Mishra, and S. P. DenBaars, "Absorption coefficient, energy gap, exciton binding energy, and recombination lifetime of GaN obtained from transmission measurements", Appl. Phys. Lett. **71**, 2572 (1997).

[31] W. Hayes and R. Laudon, "Scattering of light by crystals*",* Wiley, New York (1978).

[32] P. Perlin, J. Camassel, W. Knap, T. Taliercio, J. C. Chervin, T. Suski, I. Grzegory, and S. Porowski, "Investigation of longitudinal-optical phonon-plasmon coupled modes in highly conducting bulk GaN", Appl. Phys. Lett. **67**, 2524 (1995).

[33] T. Azuhata, T. Sota, K. Suzuki, and S. Nakamura, "Polarized Raman spectra in GaN", J. Phys.: Condens. Matter. **7**, L129 (1995).

[34] H. Siegle, G. Kaczmarczyk, L. Filippidis, A. P. Litvinchuk, A. Hoffmann, and C. Thomsen, "Zone-boundary phonons in hexagonal and cubic GaN", Phys. Rev. B, **55**, 7000 (1997).

[35] B. G. Streetman and S. K. Banerjee, "Solid state electronic devices", Pearson Education Inc. New Jersey (2005).

[36] E. L. Ivchenko, "Optical spectroscopy of semiconductor nanostructures", Alpha Science International Ltd. UK, Harrow (2005).

[37] G. D. Chen, M. Smith, J. H. Lin, H. X. Jiang, S. -H. Wei, M. A. Khan, and C. J. Sun, "Fundamental optical transition in GaN", Appl. Phys. Lett. **68**, 2784 (1996).

[38] M. A. Reshchikov and H. Morkoç, "Luminescence properties of defects in GaN", J. Appl. Phys. **97**, 061301 (2005).

[39] T. Batteb, A. Manoi, M. J. Uren, T. Martin, and M. Kuball, "Temperature analysis of AlGaN/GaN based devices using photoluminescence spectroscopy: Challenges and comparison to Raman thermography", J. Appl. Phys. **107**, 074502 (2010).

[40] M. A. Reshchikov, "Evaluation of GaN by photoluminescence measurement", Phys. Status Solidi C **8**, 2136 (2011).

[41] G. Martinez-Criado, A. Cros, A. Cantarero, C. R. Miskys, O. Ambacher, R. Dimitrov, and M. Stutzmann, "Photoluminescence of Ga-face AlGaN/GaN single heterostructures", Materials Science and Engineering, **B82**, 200 (2001).

[42] J. K. Larsen, S.-Y. Li, J. J. S. Scragg, Y. Ren, C. Hägglund, M. D. Heinemann, S. Kretzschmar, T. Unold, and C. Platzer-Björkman, "Interference effects in photoluminescence spectra of Cu_2ZnSnS_4 and $Cu(In,Ga)Se_2$ thin films", J. Appl. Phys, **118**, 035307 (2015).

[43] M. Ramírez-López, Y. L. Casallas-Moreno, M. Pérez-Caro, A. Escobosa-Echevarria, S. Gallardo-Hernández, J. Huerta-Ruelas, and M. Lopez-Lopez, "Study of interference effects on the photoluminescence of AlGaN/GaN quantum wells", Phys. Status Solidi C, **12**, 365 (2015).

[44] L. Lv, X. Ma, J. Zhang, Z. Bi, L. Liu, H. Shan, and Y. Hao, "Proton irradiation effects on AlGaN/AlN/GaN heterojunctions", IEEE Transaction on Nuclear Science, **62**, 300 (2015).

[45] R. Armitagea, Q. Yang, and E. R. Weberb, "Analysis of the carbon-related "blue" luminescence in GaN", J. Appl. Phys, **97**, 073524 (2005).

[46] C. H. Seager, A. F. Wright, J. Yu, and W. Götz, "Role of carbon in GaN", J. Appl. Phys. **92**, 6553 (2002).

[47] J. Neugebauer and C. G. Van de Walle, "Gallium vacancies and the yellow luminescence in GaN", Appl. Phys. Lett. **69**, 503 (1996).

[48] D. M. Hofmann, D. Kovalev, G. Steude, B. K. Meyer, A. Hoffmann, L. Eckey, R. Heitz, T. Detchprom, H. Amano, and I. Akasaki, "Properties of the yellow luminescence in undoped GaN epitaxial layers", Phys. Rev. B **52**, 16702 (1995).

[49] H. M. Chen, Y. F. Chen, M. C. Lee, and M. S. Feng, "Yellow luminescence in n-type GaN epitaxial films", Phys. Rev. B **56**, 6942 (1997).

[50] X. Li, P. W. Bohn, and J. J. Coleman, "Impurity states are the origin of yellow-band emission in GaN structures produced by epitaxial lateral overgrowth", Appl. Phys. Lett. **75**, 4049 (1999).

[51] G. Meneghesso, F. Rossi, G. Salviati, M. J. Uren, E. Munoz, and E. Zanoni, "Correlation between kink and cathodoluminescence spectra in AlGaN/GaN high electron mobility transistors", Appl. Phys. Lett. **96**, 263512 (2010).

[52] M. Meneghini, A. Stocco, N. Ronchi, R. Rossi, G. Salviati, G. Meneghesso, and E. Zanoni, "Extensive analysis of the luminescence properties of AlGaN/GaN high electron mobility transistors", Appl. Phys. Lett. **97**, 063508 (2010).

[53] C. H. Lin, D. R. Doutt, U. K. Mishra, T. A. Merz, and L. J. Brillson, "Field-induced strain degradation of AlGaN/GaN high electron mobility transistors on a nanometer scale", Appl. Phys. Lett. **97**, 223502 (2010).

[54] C. Hodges, N. Killat, and M. Kuball, paper presented at the 9th International Conference on Nitride Semiconductors, Glasgow, J1.5. (2011) in C.Y.Hu, T. Hashizume, "Non-localized trapping effects in AlGaN/GaN heterojunction field-effect transistors subjected to on-state bias stress" J. Appl. Phys. **111**, 084504 (2012).

[55] L. Liu, C.-F. Lo, Y. Xi, F. Ren, S. J. Pearton, O. Laboutin, Y. Cao, J. W. Johnson, and I. I. Kravchenko, "Effect of buffer structures on AlGaN/GaN high electron mobility transistor reliability", J. Vac. Sci. and Tech. B, **31**, 011805 (2013).

Chapter 6

6 Trap Characterization

Dynamic transient analysis is used to characterize the nature of the traps. There are many studies on characterization of traps and defects in III-V devices on the semiconductor level. Some of the methods are luminescence investigations,[1] photoionization spectroscopy,[2] surface potential analysis,[3] deep level transient spectroscopy (DLTS)[4]. Typically information, such as the changes of the device terminal characteristics under the pulse condition[5], the energy characteristics, the cross section of the traps [6], and their decaying time constant[2] can be obtained with the investigation of the traps. Moreover, surface potential at the interface[2] and thermal relaxation time of terminal currents of HFETs[7] can be extracted.

6.1 Photoconductivity

Photoconductivity is of great importance for investigation of solids, and improving of device performance. Photoconductivity emerged first in 1873 with the observation of the conductivity in Selenium by W. Smith[8] Later on, R.W. Pohl[9] showed the similarity between the absorption of light, luminescence and photoconductivity in terms of their dependence on photon wavelength. As we mentioned before, electronic and optical properties of semiconductors are effected by imperfections, such as point defects, dislocations, and interfaces. Although there are many ways to determine defect parameters, most of the characterization techniques suffer from the limitations imposed by the normally small thickness of the epitaxial layer. Consequently, on many cases optical characterization techniques, such as photoconductivity, luminescence, and transient spectroscopy are more preferable compared to chemical identification methods of defects.[10] Information, such as the band-gap energy of bulk semiconductors, excitonic transitions in low dimensional semiconductors, and the presence of crystal imperfections can be

obtained *via* photoconductivity measurement. Change in the conductivity of a material system caused by an excess of carriers generated by optical excitation can be defined as the basic process of photoconductivity.[11] Frequently photoconductive effect is confused with photovoltaic effect since both processes have photogenerated excess EHPs. While in photoconductivity e-h pairs contribute to the change of channel conductivity, in the photovoltaic effect, they contribute to the change of effective built in junction voltage and junction capacitance.[12] Photoconductivity converts the electromagnetic radiation into an electrical current. In the simplest case of an intrinsic semiconductor, excited electrons at the conduction band or holes at the valance band *via* optical excitation move freely in the semiconductor and contribute to the conductivity. This kind of photoconductivity is known as the intrinsic photoconductivity.

For extrinsic photoconductivity, electrons can be excited from a bound state at donor levels into the conduction band or from the valance band to acceptor centers in an n-type and p-type semiconductor, respectively. Hence, it can be deduced that photoconductivity can occur only when wavelength of the excitation radiation is large enough to exceed, the energy gaps involved.[8] When light is only introduced to source and drain, the photoconductivity effect is negligible compared to the photovoltaic effect because the electric field in this area is small. If light is illuminated on the gate, a large electric field exists, and there will be an increase in photoconductivity.[13]

Absorption processes for intrinsic photoconductivity and processes for extrinsic photoconductivity where trap levels involved are demonstrated in the Figure 6.1-1. In this figure, I indicates band to band transition, II represents a transition from the valance band to a trap level, and final III shows a transition from a trap level to the conduction band.

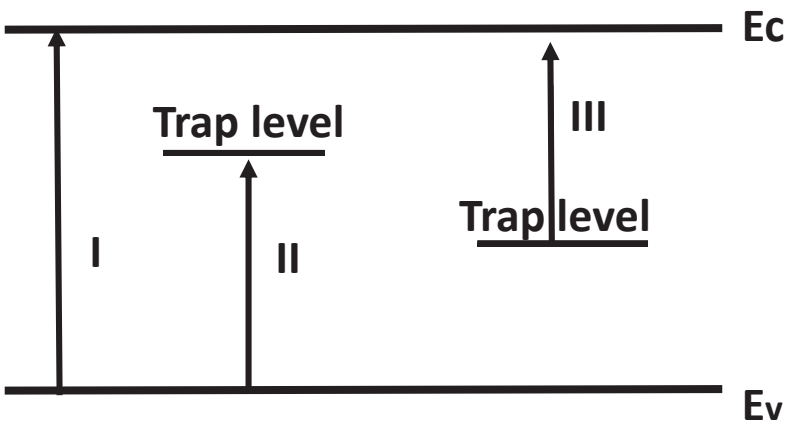

Figure 6.1-1: *Schematic diagram of absorption processes for intrinsic and extrinsic photoconductivity.*

Chang *et al*.[14] summarized the possible mechanism with illumination in AlGaAs as follows;

i. the photogenerated carriers due to the DX centers,
ii. band-to-band electron-hole generation in the AIGaAs layer,
iii. band-to-band electron hole generation in the bulk GaAs,
iv. pumping of electrons from gate metal into the AIGaAs layer,
v. pumping of electrons from 2DEG channel into the AIGaAs layer or bulk GaAs.

Some researchers claim that AlGaN/GaN materials have a similar illumination mechanism as AlGaAs.[2]

The dark electrical conductivity is given by the equation [6.1-1] in which *e* is the electron charge, *n* and *p* are the free electron or hole concentration, which depends on material being doped or undoped, μ_n and μ_p are the electron and hole mobility, respectively.[10]

$$\sigma = e(n\mu_n + p\mu_p) \qquad [\ 6.1\text{-}1\ ]$$

Similarly, the excess carriers generated by the absorption of photons result in a change in the conductivity of a homogenous material which is known as the photoconductivity, and expressed with following equation;[10]

$$\Delta\sigma = e(\Delta n\mu_n + \Delta p\mu_p) \qquad [\ 6.1\text{-}2\ ]$$

where Δn and Δp is the excess electron and hole concentrations, respectively. To calculate photoconductivity by using above equation one should assume that excess carriers in semiconductors are only a small perturbation to the values of n and p, and mobility does not change with the photoexcitation. Photocurrent can be calculated by using photoconductivity as follows;

$$\Delta I = JA = \Delta\sigma \frac{A}{l} V \qquad [\ 6.1\text{-}3\ ]$$

where, J is the photocurrent density, A is the cross-section of the semiconductor, $\Delta\sigma$ is the photoconductivity, l is the length of the semiconductor and V is the applied voltage. Photocurrent can be measured, by applying end electrodes and a small field in the illuminated environment.

6.2 Persistent Photoconductivity

In a photoconductivity experiment, an increase in the photoexcited carriers is observed through a rise in the photocurrent when the light is turned on. In the cases, where recombination of the electrons and ionized donors can be prevented by the local potential barrier around the deep level traps, continues of carrier concentration and so non- zero photoconductivity is observed when the light is turned off.[15] This phenomenon is known as persistent photoconductivity in which photoinduced conductivity remains after the termination of illumination. The persistent photoconductivity (PPC) includes multiple processes, such as photon absorption, carrier recombination, and transport.[16] Figure 6.2-1 displays an example decay characteristic of the current with applied bias

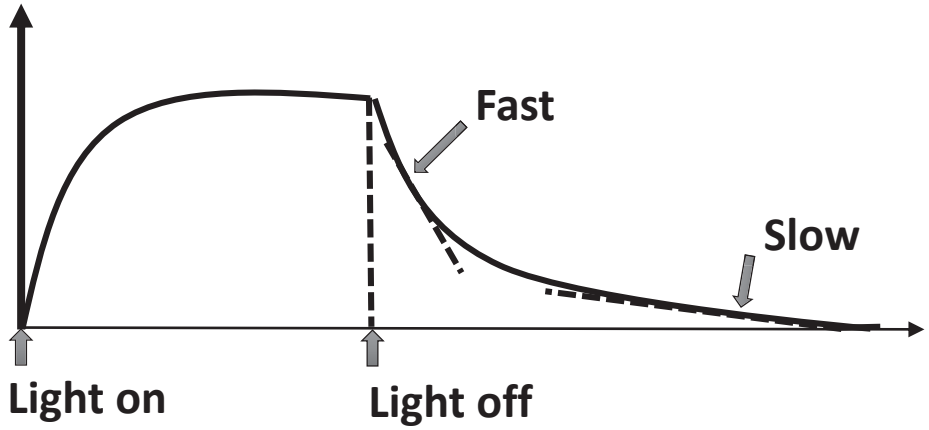

Figure 6.2-1: *Transient photoconductivity and exponential decay characteristics of current voltage graph.*

Previously, the PPC studies have been performed on bulk GaN[17] and AlGaN/GaN heterostructures,[18] and most of these studies were conducted under the above-bandgap UV illumination with a fixed wavelength and energy greater than the bandgap.[19] Chang *et al*.[14] found that the decay of photoconductivity in AlGaN is extremely slow and it takes from tens of minutes to several hours for the conductivity return to its dark state after exposed to light. It has been claimed by many researchers that the PPC effects in bulk GaN are caused by the deep level defects, such as DX-like and AX-like centers (where D and A stands for donor and acceptor, and X stands for an unknown intrinsic defect at the time of discovery) in n-type[20] and p-type[21] GaN, respectively. Li *et al.*[21] attributed the increase of the PPC to the photoionization of the deep level impurities, such as DX-like centers in the AlGaN barrier material. Reddy *et al.*[22] stated that if PPC arises from a DX-like defects, a steep rise in photocurrent is expected when the photon energy equals the ionization energy of the deep level defects, followed by a saturation even with a small increase in the photon energy. It was also suggested that the PPC effect can be attributed to unintentionally incorporated cubic-phase crystallites in a hexagonal matrix[23] or random potential fluctuations due to the heterointerfaces.[20]

Lin *et al*.[24] proposed that PPC effect in an AlGaN/GaN heterostructure can be understood as follows. When electron-hole pairs are created in the AlGaN layer due to the photoexcitation, electrons travel across the AlGaN/GaN interface and fall into triangular well in the GaN side, and they contribute to the PC response. Similar explanation was proposed for Flourine (F) treated AlGaN/GaN HEMTs as follows.[18] With the illumination of the excitation source, the electrons trapped by deep level are excited (step 1 in the

Figure 6.2-2); then photo excited electrons drift to the channel region (step 2 in the Figure 6.2-2) and increasing the observed photocurrent by contributing to the 2DEG density. When the light illumination turns off, photoexcited electrons will be recaptured slowly by these deep centers (step 3 in the Figure 6.2-2).

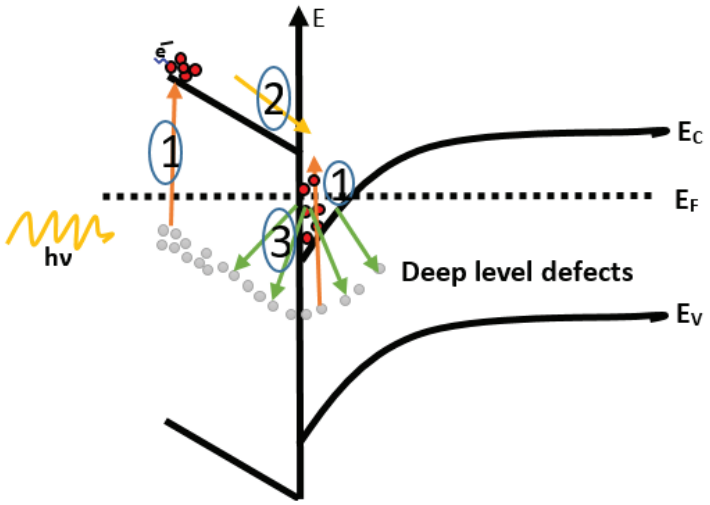

Figure 6.2-2: *Schematic diagram of the motion of the careers in the presence of deep level defects.*

In addition, some researchers[25] claimed that both long and short decay time constants contribute to the PPC of n-type GaN, which implies the presence of more than one types of PPC process. Although hole trap contribution to the PPC is generally ignored, their presence was observed in n-type GaN.[26]

6.2.1 Experimental

The AlGaN/GaN epi-structure used in this work was an AlGaN/GaN HEMTs structure grown on the p-type 6″ Si wafer *via* MOCVD. The structure consists of 0.25 µm AlN nucleation layer, multi-layered AlGaN buffer with Al concentrations ranging from 20% to 75%, 1µm thick undoped GaN layer, 20nm thick AlGaN barrier layers, and an ultra-thin (2nm) GaN cap layer. The details of the fabrication steps were explained in chapter 4. An array of Schottky contacts composed of the DC magnetron sputtered Ni layers with the diameter of 600µm were used. In this experiment, samples were chosen from the center and edge

named as sample A and B, respectively. Samples A and B which were used in the time resolved photocurrent experiment were utilized for the PPC experiment. -12 V was supplied to the Schottky contact by a Keithley 6487 pico-ammeter/voltage. The excitation source was a Xenon lamp with wavelength of 700 nm.

6.2.2 Results and Discussion

Figure 6.2-3 (a) and (b) display the transient photo current of samples A and B, respectively measured near the initial dark current equilibrium state and the final dark current state for the 7th consecutive times at -12V with the exposure of the light at 700nm. For each measurement, the delay time (600s) before starting the excitation, the excitation time (60s), and after exposure, the recovery time (600s) were kept constant. As we can see from Figure 6.2-3 the PC transient characteristics are different for the initial and the subsequent measurements. For sample A, initial current decreases down to 3rd measurement, it increases, and decreases again. In contrast, final dark current is increasing up to 4th measurement and starts to decrease again. Similar effects have been observed by other scientists as well.[27] As suggested by Han *et al*.[27] this may indicate involvement of two mechanisms working together on the present photoconductivity. It should be noted that, the changes mentioned here are small changes on the same order of magnitude. For sample B, both initial dark current and final dark current increase with the growth of the number of measurements. Moreover, at 700nm energy level of excitation is lower than the energy gap of GaN, yet we still observed the increase in the conductivity indicating the persistent of current for a long period of time after the removal of illumination. Similar effects have been shown before by other researchers as well.[28] For both of the samples the initial dark current level of the transient is always lower than that of the final dark current of the same transient.

Because of the multiple exposure times and assuming the traps are not emptied, it is expected that after each repetitive exposure there will be an increase in the final saturation current, which corresponds to initial dark current of the consecutive measurement. The reason why this is not observed in the case of sample A might be that most of the traps with activation energy higher than 1.77 eV(700nm) might be emptied after

the couple of first exposure at 700nm. For sample B, it takes more time for carriers to return to its original dark current level. Therefore, it is expected to have a higher initial dark and final dark current with each repetitive measurement. Furthermore while sample A reaches the highest current with the exposure of the light after the 3rd measurements sample B reaches the same highest current after the 5th measurements. It can be said that for both samples after several measurements all the traps are emptied. In general, as also stated by Li *et al*.[28] the conclusion can be drawn from Figure 6.2-3 might be the fact that the selectivity (or sensitivity) of the dark current level of Schottky contacts fabricated from AlGaN/ GaN HEMTs heterostructures will depend on the device history.

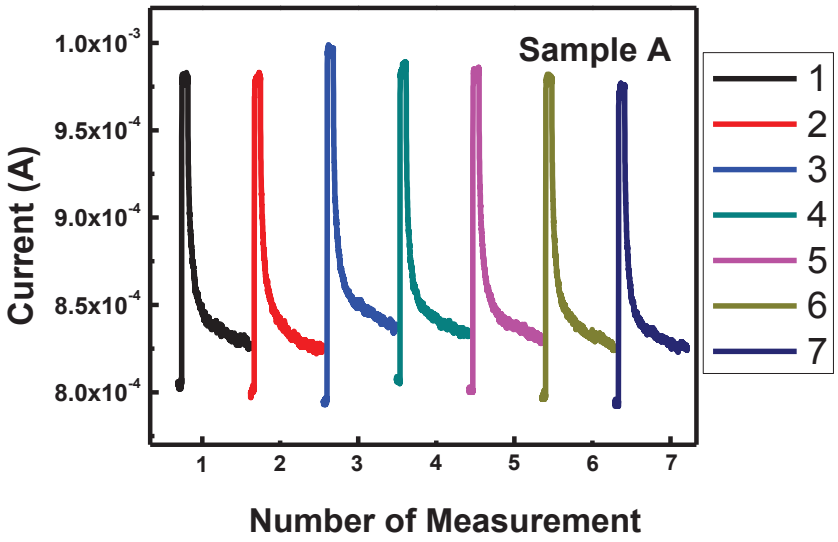

a

Figure 6.2-3: *Typical photoresponses of an AlGaN/GaN heterostructure measured under a successive light excitation (λ_{exc}=700nm) with applied bias of -12V for (a) sample A*

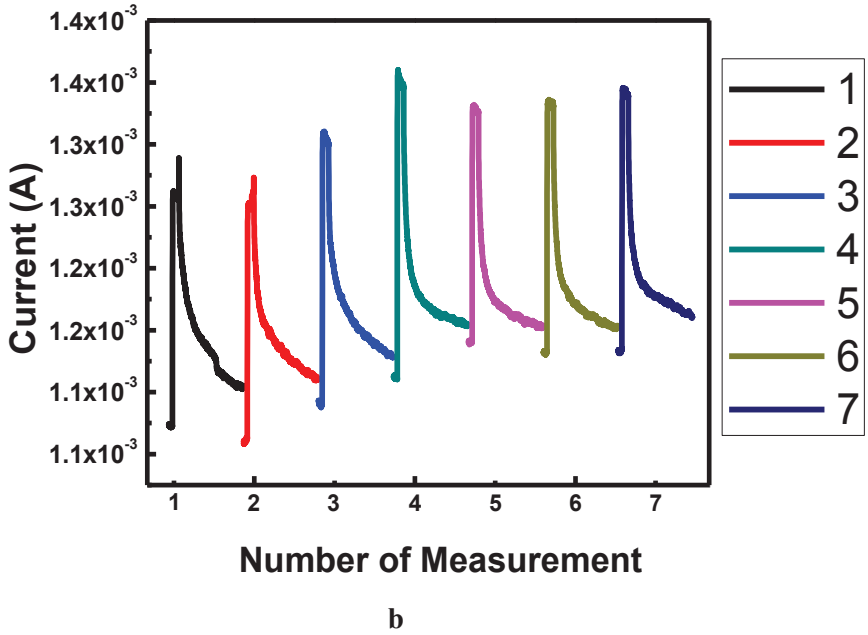

Figure 6.2-3: *Typical photoresponses of an AlGaN/GaN heterostructure measured under a successive light excitation (λ_{exc}=700nm) with applied bias of -12V for (b) sample B.*

Difference between initial dark current and final dark current in terms of number of measurements was summarized in the Figure 6.2-4 (a) and (b) for samples A and B, respectively. The highest differences observed at 4th and 5th measurements for samples A and B as expected from the above graphs. In both of the graphs, there was an increase followed by a decrease and another increase. This might indicate that traps are filled gradually and emptied at certain point, and retrapped again.

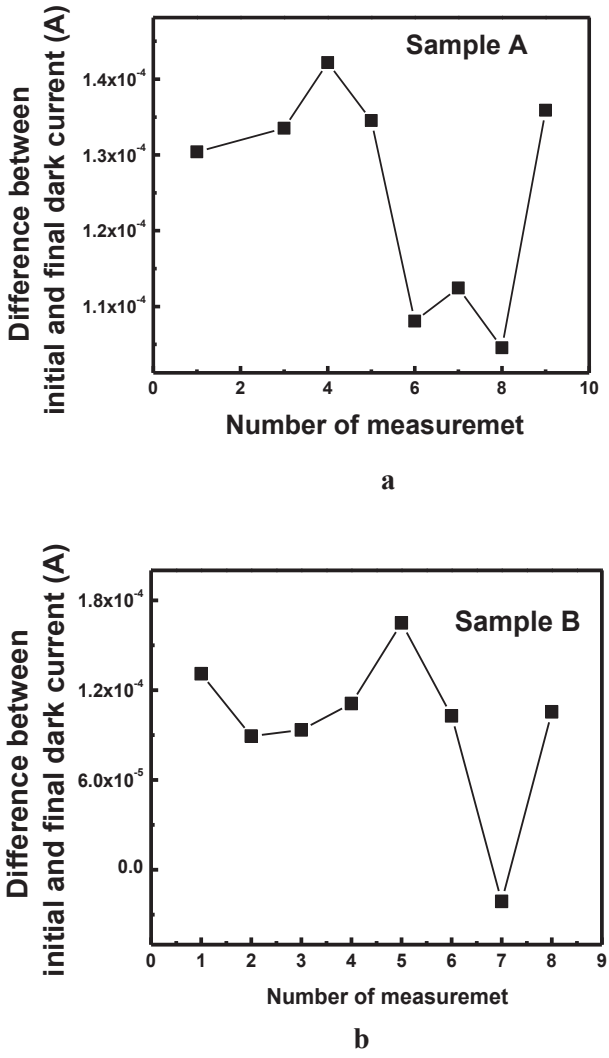

Figure 6.2-4: *Difference between initial dark current and final dark current in terms of number of measurements for (a) sample A and (b) sample B.*

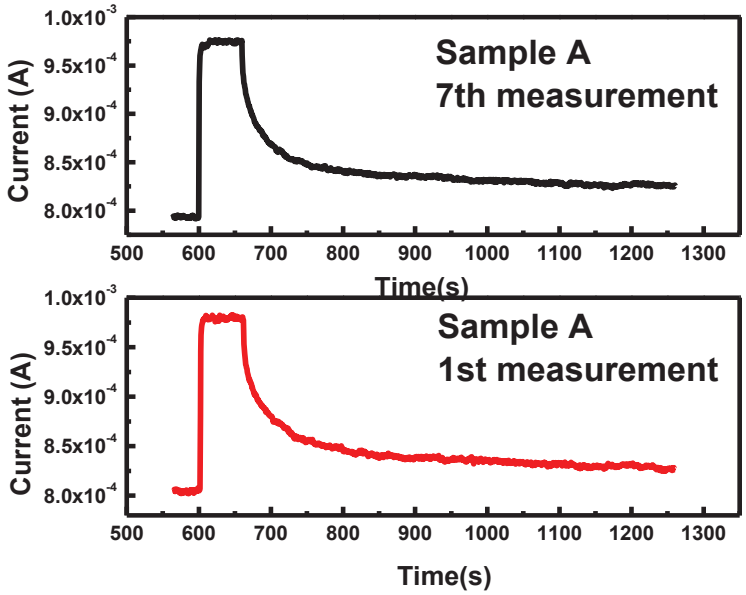

a

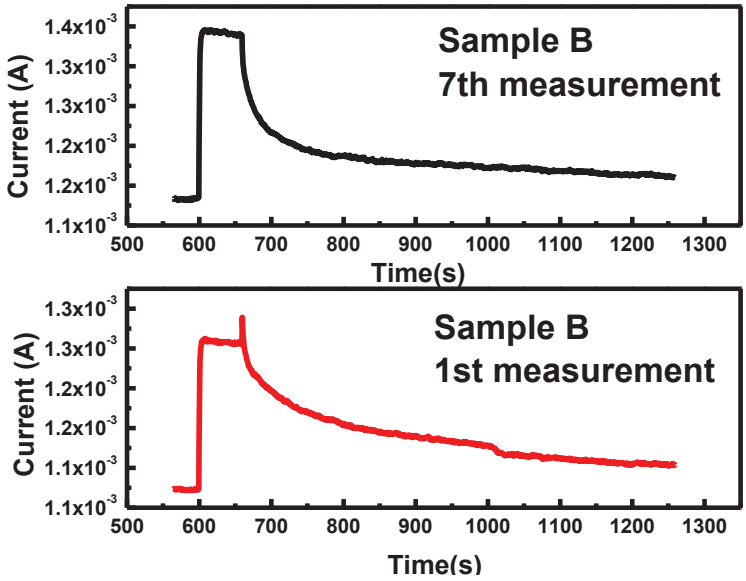

b

Figure 6.2-5: P*hotocurrent transient measured r the initial dark equilibrium state and after 7th measurement for (a) sample A and (b) sample B, respectively at 300K. The solid decays are the least squares fit of the photocurrent decay transients to an exponential function* $I_{PPC}(t) = I_d + (I_1 - I_d)e^{(-\frac{t}{\tau})}$.

To identify PPC mechanism we formulated its decay and buildup kinetics. Figure 6.2-5 shows a more detailed view of PPC behavior near the initial dark equilibrium state and after 7th measurement for sample A (a) and sample B (b), respectively. In general, a stretched exponential function is used to define PPC decay $I_{PPC}(t)$ for III-V and II-VI semiconductors.[17,29,30]

$$I_{PPC}(t) = I_d + (I_1 - I_d)e^{(-t/\tau)^{\beta}} \qquad [\ 6.2\text{-}1\ ]$$

However, as illustrated in the Figure 6.2-5, the PPC decay kinetics in this experiment studied here can no longer be described by equation [6.2-1]. Instead, the observed PPC decay behavior follows;

$$I_{PPC}(t) = I_d + (I_1 - I_d)e^{(-\frac{t}{\tau})} \qquad [\ 6.2\text{-}2\ ]$$

where I_d is the initial dark current, I_1 is the current level immediately after termination of excitation source, τ is the decay time constant, and β is the decay exponent.

Decay times were derived as 53s and 224s for the first excitation of sample A and B, respectively. For the last excitation of sample A and B, 604s and 352s were recorded as decay time constants, respectively. Arslan *et al*.[31] suggested that trapped photoexcited carriers are the origin of PPC and they spatially separated by local potential fluctuations, resulting in suppression of the recombination. Polyakov *et al*.[32] indicated that PPC effect related to deep level defect centers and fluctuation effects can be distinguished by observing quenching effect. In the case of observed quenching effects it is more likely to observe for persistent photoconductivity related to potential fluctuations. Whereas there should not be optical quenching by sub-bandgap light for persistent photoconductivity which is caused by DX centers. Therefore, PPC effect observed here is more likely caused by DX centers. We suggest that differences in the decay times might indicate the involvement of different traps. In summary, we observed that when we increase the number of excitation decay time gets longer and longer. Similar trend has been observed by other researchers as well.[28] We believe that when the samples were exposed multiple times to the light, previously excited carriers are excited again before they return to their original states.

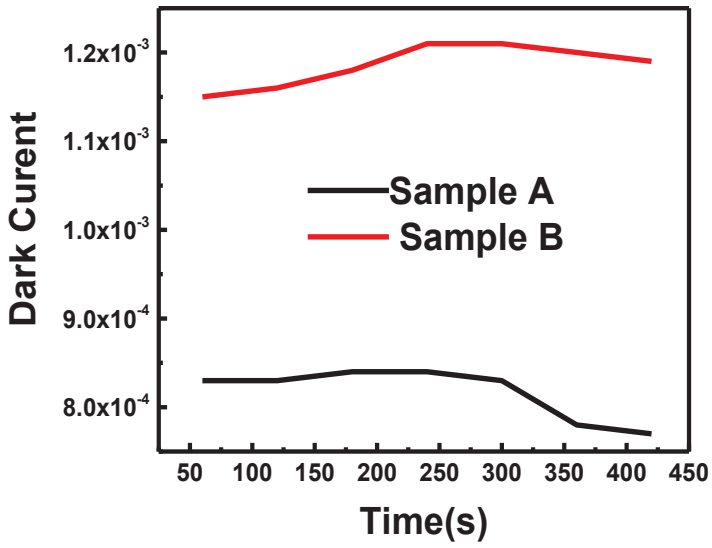

a

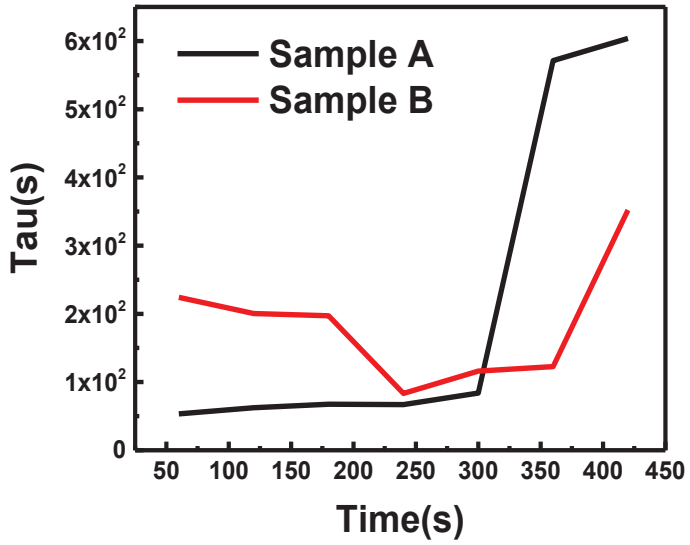

b

Figure 6.2-6: *Characteristic parameters of PC transients vs pulsed illumination time. (a) The dark conductivity level, and (b) the PC decay time constant,* τ.

In the Figure 6.2-6, we replot characteristic parameters of PC transients for dark current level (a), and the PC decay time constant (b), τ with respect to pulsed illumination time based on the fitted values of decay characteristics. We were expecting they would follow similar characteristics as shown by other researchers.[28] Instead, our results demonstrated different behavior. Fitted dark current values for both

samples A and B are almost constant by ignoring small fluctuations. Those small changes in the dark current values follows with the fluctuations in the experiment. As we stated before, we observed an increase in the values of τ with the increase of exposure time.

Furthermore, we used following I_{PPC}^{b} to fit Figure 6.2-5, which is used to derive the PPC build up I_{PPC}^{b}kinetics in AlGaAs by other researchers[33,34]

$$I_{PPC}^{b}(t) = I_d + (I_{max} - I_d)(1 - e^{-\alpha t}) \qquad [\ 6.2\text{-}3\ ]$$

where α is a constant, I_d is the initial dark conductivity, and I_{max} is the PPC saturation level.

Both samples exhibit an initial fast increase followed by a steady enhancement. It has been claimed that deep level impurities are the reason behind such a buildup behavior since electrons are slowly captured by these centers.[21,34] The widely used exponential fit showed good agreement for each transient on a linear time scale. Furthermore, since the decay time constant of 600s is much higher than 60s of illumination time one can conclude that PPC build up process is the main reason behind the dark pulsed illumination time dependence of the dark level.[28] Since excitation energy level is less than the energy gap of GaN, the energy of the excitation photons is not large enough to generate electron hole pairs in the GaN layer. To investigate the possible source of PPC effect further experiments under higher energy light illumination than the energy bandgap of GaN were conducted.[35] It was demonstrated that PPC buildup effect is contributed by the transfer of photoexcited electrons from the deep level impurities in either GaN or AlGaN layers close to the surface.

Another experiment was done to observe the effect of PPC. In this experiment, after initial current was measured in reverse bias, the same experiment was repeated under dark condition for an hour by repeating the measurement every 4 minutes. Figure 6.2-7 (a) shows the initial light photo current measurements followed by 14 consecutive dark current measurements. By looking at the decrease in the dark current with time we can say the effect of photo current persist. In the Figure 6.2-7 (b), nice exponential decay of dark current is observed after the termination of the light. This also indicates the persistence of photoconductivity.

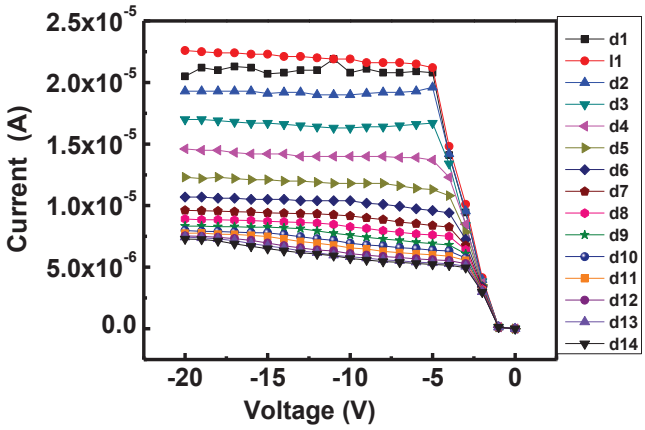

a

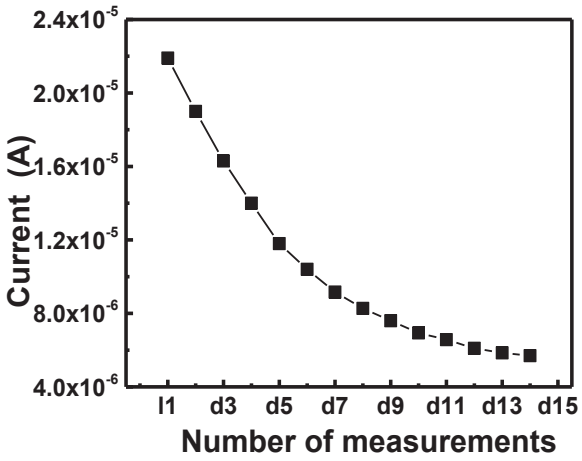

b

Figure 6.2-7: (*a) Initial dark current followed by photocurrent measurement and 14 final dark current measurements (b) Exponential decay of the dark current with time.*

In summary, we investigated PPC effect on AlGaN/GaN HEMTs heterostructures. The PPC effect is analyzed in the context of exponential decay and buildup then comparisons are made between the two different samples. We observed that two samples showed different PPC characteristics after multiple illuminations. This can be concluded as the selectivity (or sensitivity) of the dark current level of Schottky contacts fabricated from AlGaN/ GaN HEMTs heterostructures will depend on the device history. It was found that the decay of photoconductivity after exposure to light is extremely slow and it takes from tens of minutes to several hours for the conductivity to return to its dark state for our samples. While the exponential decay analysis is insufficient to provide direct information on the nature of the PPC by

formulating the PPC buildup and decay kinetics, we attributed PPC to the photoionization of deep level impurities.

6.3 Photoionization Spectroscopy/ Spectroscopic Photocurrent Measurements

Ejection of an electron through absorption of a photon of electromagnetic radiation by quantum system is defined as *photoionization*.[36] In this case, energy of absorbed atom should be greater than the lowest energy of the target atom or ion "*S*". The absorption results in a higher state ionization S^+ and electron with a kinetic energy equal to the excess photon energy.[37]

$$hv + S = S^+ + e \qquad [\ 6.3\text{-}1\ ]$$

Photoionization spectroscopy gained attention as a simple method for detecting excited atoms against the background of unexcited ones in early 1970s by Letokhov.[38] By studying the wavelength dependence of the drain current recovery in more detail, Klein *et al*.[39] successfully identified the signatures of specific trap levels that are responsible for current collapse. The technique depends on the release of trap carriers responsible for current collapse during illumination with light that reflects the photoionization spectrum of the traps. It is believed that this spectrum can be used to identify the defects by relating increase in the number of carriers ejected from the traps upon illumination to the increase in the current.

In this experiment, the device first is initialized by proximity illumination for reproducible measurements of current collapse. A drain- source voltage is applied to fill the traps and the fully collapsed drain current is measured both under dark and various wavelength λ illumination for duration t repetitively. The difference between the dark and light-on drain current at a fixed drain voltage V_0 is calculated for each wavelength. The increase in the light on drain current compared to dark current represents the number of ejected carriers from the traps upon illumination. In summary, this spectroscopy measures the increase of the drain current in a fully collapsed device upon illumination with monochromatic light.

This study provides information on experimentally measured response function *S(λ)* which is measured by normalizing the fractional increase $\frac{[I(\lambda)-I_{Dark}]}{I_{Dark}} = \frac{\Delta I(\lambda)}{I_{Dark}}$ in the drain current, which reflects the fraction of the traps emptied upon illumination by the total number of incident photon at each wavelength $\phi(\lambda)t$ (photon/cm^2) as follows;[39,40]

$$S(\lambda) = (\frac{\Delta I(\lambda)}{I_{Dark}})(\frac{1}{\phi(\lambda)t}) \qquad [\ 6.3\text{-}2\ ]$$

where $\phi(\lambda)$ is the incident photon flux, t is illumination duration, $\Delta I(\lambda)$ is increase in the drain current upon illumination and I_{Dark} is the drain current measured under dark conditions. If *S(λ)* is measured under the following conditions; (1) the light illumination is weak ($\sigma\phi(\lambda)t \ll 1$), where σ is the photoionization cross-section) and (2) the measurement of drain current increase is made at a drain voltage within the linear regime of the I–V characteristic, and *S(λ)* is proportional to photoionization spectrum of the deep trap. By using this information which is obtained from photoionization spectroscopy one obtains information about absorption threshold energy, linewidth, absorption cross section and lattice coupling.[41]

One should note that obtaining photoionization spectrum from a trap in a FET structure through direct optical measurement might be difficult. To produce a change in transmission of only 0.1% requires a trap with a reasonably large cross-section ($\approx 10^{-15}$ cm^2) and at a substantial concentration (10^{17} cm^{-3}), a 100 nm layer (i.e.,$\sim 10^{12}$ cm^{-2}) neglecting background absorption from the thick sapphire or SiC substrate.[41] Klein *et al*.[39] found two broad absorptions below the GaN bandgap corresponding to the photoionization of carriers from two distinct traps that are located approximately 1.8 eV and 2.85 eV below the conduction band, respectively are observed. While the trap at 1.8 eV is suggested to be related to dislocations and grain boundaries[39] and the trap at 2.85 eV is related to carbon (C) incorporation, which increases as growth pressure decreases.[42] Same broad trap-related absorptions and a rapid increase at the GaN bandgap were shown in the photoionization studies on AlGaN/GaN HFETs.[43] Reddy *et al*.[22] observed a spectral threshold at -1.6±0.2eV for the photoionization of a deep level defect, which is attributed to YL

band in silicon doped GaN. Wolter *et al*. observed photoionization spectra thresholds in the region hv > 2.5eV on MOCVD grown AlGaN/GaN HEMTs devices.[44,45]

6.3.1 Experimental

The layers of AlGaN/GaN HEMTs layers were grown on the p-type 6″ Si wafer *via* MOCVD. The epilayer has the following structure as shown in the Figure 6.3-1.(a); (1) 0.25µm AlN nucleation layer, (2) multi-layer AlGaN buffer layer with varying Al concentrations between 20% and 75%, (3) 1µm undoped GaN layer, (4) 20nm AlGaN barrier layers, and (5) an ultra-thin (2nm) GaN cap layer.

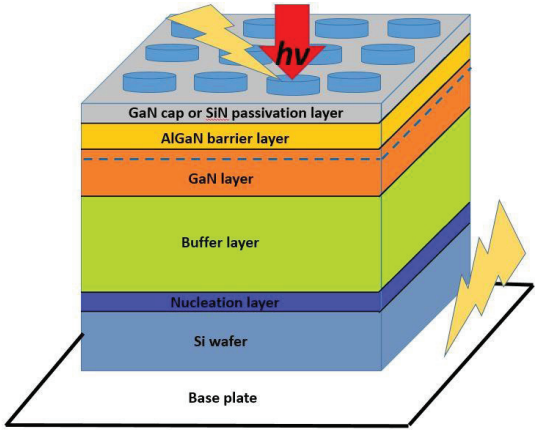

Figure 6.3-1*:(a) Schematics of sample and measurement configuration*

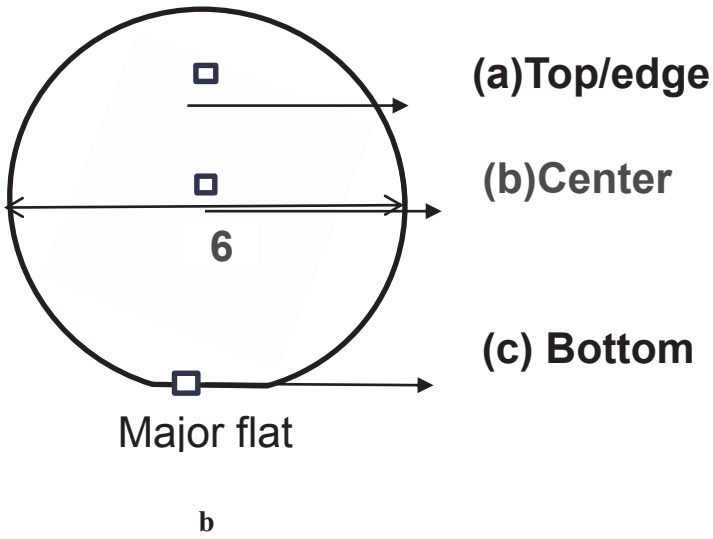

Figure 6.3-1*: (b) Configuration and naming direction of the wafer from top to bottom.*

For device fabrication, the 6″ AlGaN/GaN HEMTs epitaxy wafer was diced into 1 x 1 cm individual pieces, and three pieces from the top (sample A), center (sample B), and bottom (sample C) of the 6″ AlGaN/GaN HEMTs epitaxy wafer were chosen as shown in the Figure 6.3-1 (b). They were ultrasonically cleaned in the organic solvents with the following order; acetone, TCE, acetone, methanol, and methanol for 5 minutes in each solvent. After removing organic residues, the samples were placed in a mixture of HCl and DI water (1:1 by vol.) and subsequently heated at 110℃ for 10 minutes.

An array of the Schottky contacts were photolithographically constructed using DC magnetron sputtering, followed by lift-off. The circular Ni layers with the diameter of 600μm and thickness of 20nm were used as Schottky contacts. The spectroscopic photo I-V measurements were carried out at room temperature. An Apex 150W Xenon lamp was used for optical illumination. Wavelength of the light was changed from 800nm to 400nm by using a stepping motor controlled monochromator. The direction of the varying wavelength was chosen in a way such that the higher energy levels excited with decreasing wavelength. A Keithley 6487 pico-ammeter/voltage source was used to sweep the applied voltage from – 20 to + 5V. The system was controlled by the LabVIEW program. A schematic diagram of the spectroscopic photocurrent system is shown in the Figure 6.3-2.

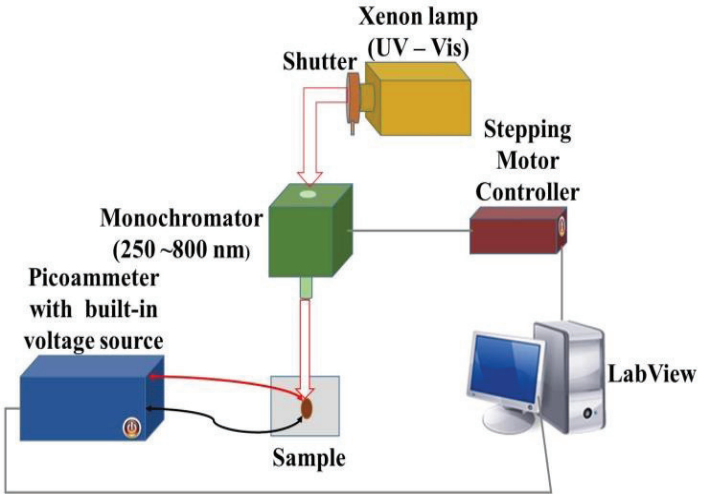

Figure 6.3-2: *Schematics of spectroscopic photo I-V measurement system.*

Reproducibility of the measurement was insured by bringing the device in the same state for each measurement. This was accomplished by irradiating the device with a red light before applying the bias. It is believed that this procedure led to reproducible results and presumably emptied all of the traps, thus eliminating the depletion and returning the device back to the equilibrium condition.[2]

6.3.2 Results and Discussions

Figure 6.3-4 (a), (b), and (c) show the spectroscopic photo I-V data collected from samples A,B, and C were taken from top, center, and bottom parts of the 6″ AlGaN/GaN HEMTs heterostructure. In these graphs, we focused on the change of the photocurrent in reverse bias region since the dark current level is lower in the reverse bias than that in the forward bias regime. All three samples displayed different spectroscopic photo I-V characteristics. For all the samples lowest photocurrent was higher than the observed dark current values. Tong *et al*.[46] previously observed lower photocurrent values than the dark current and they related this effect to the decaying PPC produced when sample was exposed to ambient light. Sample A reached its highest photocurrent at 650nm (1.91eV) with the light illumination and photocurrent reduced without following any pattern when the wavelength was changed. For sample B photocurrent has jumped up to its highest photocurrent value at 700nm (1.77eV) and this time the

photocurrent gradually decreased as the illumination wavelength decreases. Finally, in sample C the highest photocurrent was achieved at 550nm (2.25eV) followed by at 500 and 700nm, and gradually decreased with time.

The top sample showed the maximum current at 1.91eV, center sample reached the maximum current at 1.77eV and bottom sample exhibited the maximum current at 2.25eV. With the application of the bias hot carriers are trapped at the deep centers. Upon the illumination of the trapped carriers can be photoionized and the spectral dependence of this effect might reflect the photoionization spectrum of the trap.[2] Photoexcitations belong to the electric active type of light absorption since they generate free charge carriers, unlike the electric inactive type, e.g., excitonic absorption and internal defect absorption. Electric active and inactive excitations can be distinguished by the demonstration of photocurrents with externally applied electric fields.

Khan *et al*.[47] observed the removal of the trapped electrons with the 1.91 eV (650 nm) radiation for the AlGaN/GaN heterostructure insulated gate field effect transistors. Bouya *et al*.[48] reported recovery of the current collapse under monochromatic light near 1.75 eV (710 nm). Nakano *et al*.[49,50] observed defects at 2.2eV as well as the ones at 1.7eV and they were associated with threading dislocations and Ga vacancies (V_{Ga}) for the AlGaN/GaN heterostructures.

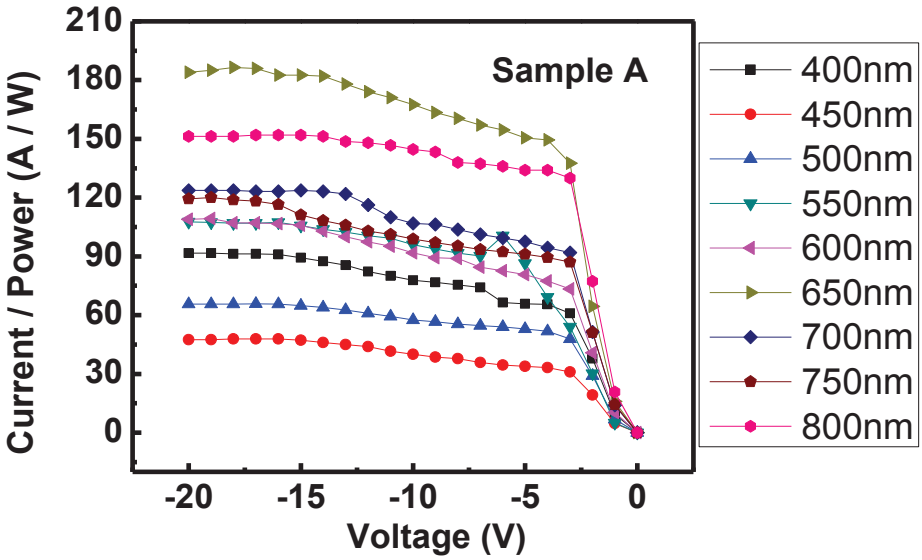

a

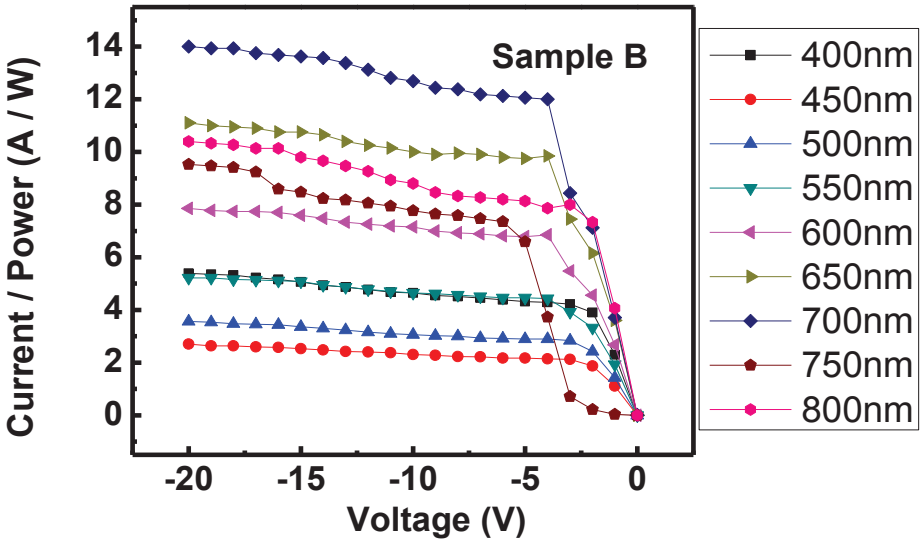

b

Figure 6.3-3: *Spectroscopic photo I–V collected from device fabricated on (a) Sample A (top/edge) (b) Sample B (center) of 6-inch AlGaN/GaN HEMTs wafer.*

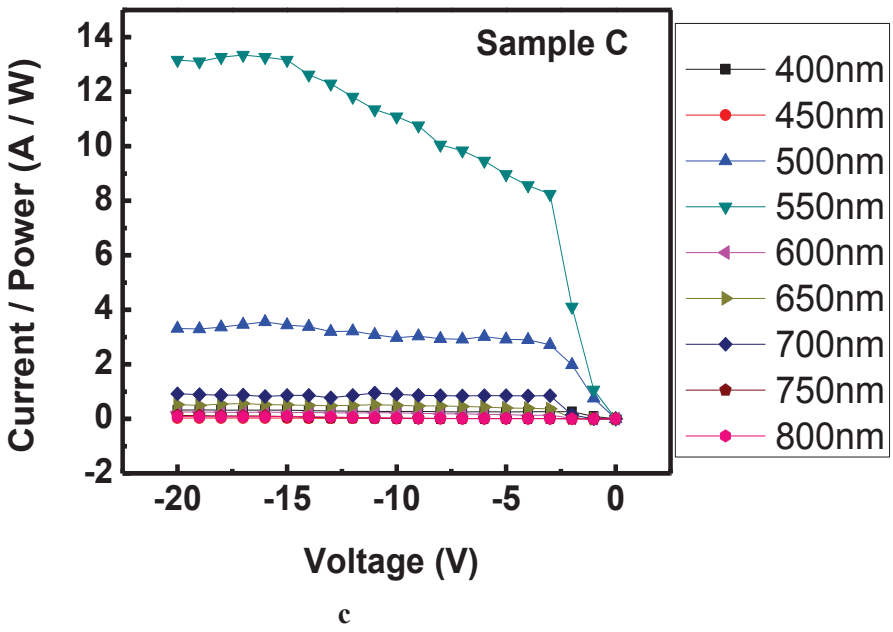

c

Figure 6.3-3: *(c) Spectroscopic photo I–V collected from device fabricated on Sample C (bottom) of 6-inch AlGaN/GaN HEMTs wafer.*

Before the measurement carried out with illumination by light of different wavelengths (λ) for duration (t) of 15s, we applied voltage up to -20V and measured under dark conditions. The current (I) for each measurement, in the case of light off and on is then extracted from the data at a chosen, fixed voltage (V_0) at -10V for both measurements. This difference was normalized relative to dark current by the total number of incident photons at each wavelength, response function is obtained by using the equation [6.3-2] mentioned above. Figure 6.3-4 displays the result of the response function $S(\lambda)$ as a function of incident photon energy ($h\upsilon$). Samples A, and B had two peaks point followed by one another and sample C showed one peak point at 2.3 eV. The peaks for sample A were at 1.7 and 2.1 eV, and sample B has peaks at 1.9 and 2.3eV. These results showed similarities with our previous results as expected. Plotting the data in terms of response function allows us to observe additional traps levels which are overshadowed by the highest photocurrent values in our previous representation.

For samples A and B at wavelengths 650 and 700nm, the spectrum from the traps at 2.1 and 2.3eV might overlap with the traps at 1.7 and 1.91eV. The contribution from the traps at 2.1 and 2.3eV might be dominant at 590 and 540nm. One should note that response function is not sufficient to determine whether

one of the traps in the Figure 6.3-4 is dominant in causing the current collapse phenomena generally observed in these samples. Building on the conclusions derived by Klein *et al.*[39], we can say that while wavelengths higher than 650nm and 700nm the contribution from traps at 1.7 and 1.91eV is independent from of that at 2.1 and 2.3 eV, for shorter wavelengths both traps contribute. Based on these results we might say each sample has one common defect and based on the location of the defects in the sample they may have additional defect levels.

Klein *et al.*[39] obtained similar results and they referred to the trap level at 1.8eV as deep level trap. Furthermore Reddy et al.[22] and Hirsch *et al.*[51] observed similar spectral dependences to that trap at 1.8eV in their PPC studies on GaN. Biyikli *et al.*[52] observed small amount of PPC at 2.3eV on their PPC studies on AlGaN/AlN/GaN heterostructures. Meneghesso et al.[7] came to the conclusion that traps found at 1.75, and 2.32 eV were responsible for hot electron induced current collapse. This may indicate the traps we observed at 1.7 and 1.9 might be responsible for PPC reported in these studies. Wolter *et al.*[44] showed the presence of hole traps in the GaN buffer at 2.1eV. Same trap energy (2.1eV) was related to the carbon (C) impurities by Nakano *et al.*[53] In addition, some researchers suggested that similar shapes in the spectral response behavior might indicate the presence of same type of traps.[44] Based on this information, one might say all 3 samples have same traps, in addition, samples A and B has additional trap different from what it is already exists in sample C.

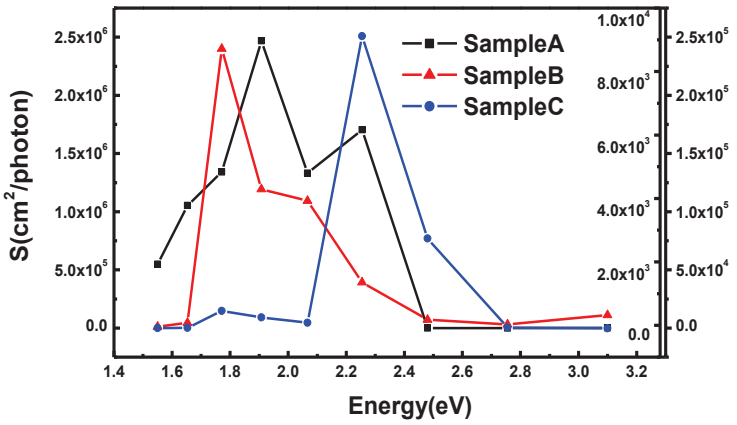

Figure 6.3-4: *Spectral dependence of the current collapse response function S(hυ).*

Finally, we compared our experimental results with theoretical calculations of the defect formation energies in GaN and AlGaN materials. Neugebauer and Van de Walle studied the defects with formation energies below 3 eV (i.e., for the vacancies) for wurtzite bulk GaN.[54] Figure 6.3-5 (a) summarizes all the defect formation energies as a function of the Fermi energy for the nitrogen-rich case ($\mu_N=\mu_{N_2}$). Low formation energies for vacancies was observed in which V_{Ga} has the lowest value. Energetically less favorable behavior of antisites and interstitials was observed. Further investigations were conducted by Neugebauer and Van de Walle indicated that silicon and oxygen donors also have a lower formation energy.[55] Figure 6.3-5 (b) summarizes all the defect formation energies as a function of the Fermi energy for native defects (nitrogen and gallium vacancies) and donors (oxygen and silicon) in GaN. These results suggest that the defects we observed based on their energy levels are most probably V_{Ga} because of their lower formation energies at around 2eV.

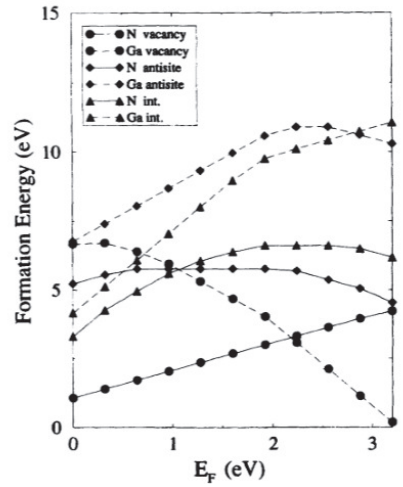

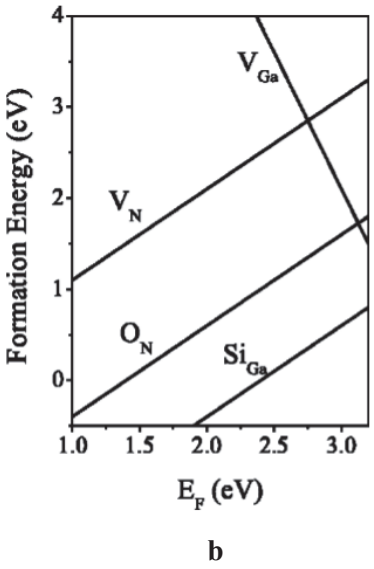

Figure 6.3-5: (a) *Defect formation energies as a function of the Fermi level for all native defects in GaN under nitrogen-rich conditions. The slopes of the defect formation energies characterize the charge state; a change in the slope indicates a transition from one charge state to another.* E_F*=0 corresponds to the top of the valence band*[54] *(b) Formation energy vs Fermi energy for native defects (nitrogen and gallium vacancies) and donors (oxygen and silicon) in GaN.*[55]

In addition, the formation energies of defects in AlGaN were investigated even though studies that explicitly address point defects in alloys are rare to date. Bogusławski and Bernhol[56] focused on identifying trends in the formation energy of nitrogen vacancies in AlGaN alloys. They found that formation energy differences between Ga- terminated vacancies and Al-terminated vacancies is 2.8eV in AlGaN. From this

information, we might conclude that either Ga or Al- terminated vacancies exist in our system because the energy difference between the observed peaks is less than 2.8eV. Since there is no detailed information about alloys, the properties of native defects in AlGaN as a first approximation were derived by interpolating between AlN and GaN. First-principles calculations of formation energies of native defects in AlN were performed by Mattila and Nieminen,[57] Gorczyca *et al*.,[58] Fara *et al.*,[59] and Stampfl and Van de Walle.[60] Figure 6.3-6 displays the defect formation energies as a function of fermi level for defects and impurities in AlN under Al-rich conditions. Conclusions derived from these figures by these researchers are that only vacancies have a low enough formation energy to occur in high enough concentrations to affect the electronic properties self-interstitials and antisites in wurtzite AlN.

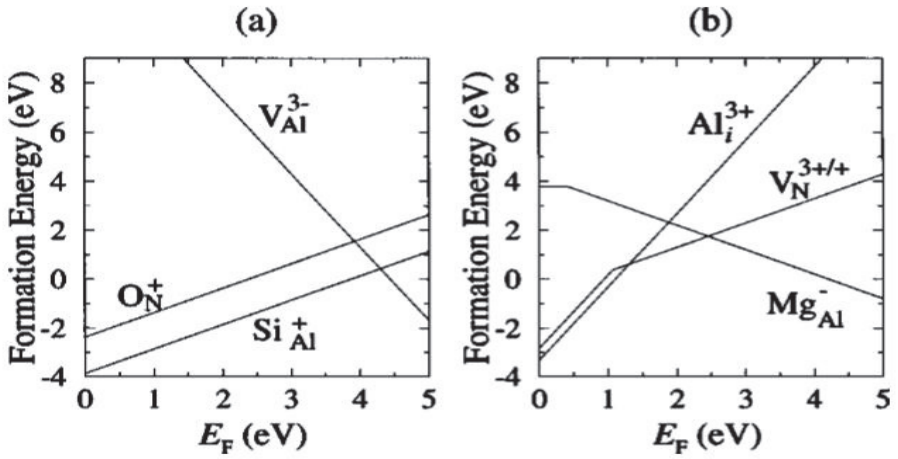

Figure 6.3-6: *Defect formation energies as a function of the Fermi level for defects and impurities in AlN under Al-rich conditions. (a) Donor impurities (O and Si) and the al vacancy, relevant for n-type doping. (b) Mg acceptor, N vacancy, and Al interstitial, relevant for p-type doping. EF50 corresponds to the valence-band maximum. Note the formation energy of Ali is significantly higher in wurtzite AlN.*[60]

In summary, 6″ AlGaN/GaN HEMTs heterostructures were investigated in terms of their defect distribution within the wafer. Spectroscopic photo IV measurements revealed the presence of sub-bandgap defects as well as their nonhomogeneous distribution across the wafer. The trap levels observed in our devices were also reported elsewhere for AlGaN/GaN heterostructures. Among these reports, the traps at 1.7eV and 2.2eV are observed in the GaN buffer layer. Consequently, it is more likely that the traps observed in our devices are also mainly located in the GaN buffer layer. Plotting the results in terms of response function revealed the presence of similar trap energy levels in all three samples, as well as

additional trap energies. In addition, we compared our results with the theoretical values of defect formation energies. We concluded that observed defects based on their activation energy levels are more likely due to the vacancies in GaN or in AlGaN. To investigate the location of these traps, further studies were conducted below. In conclusion, it was demonstrated that spectroscopic measurements can be a very useful diagnostic tool for the quick evaluation of the nature and distributions of surface defects in the AlGaN/GaN HEMTs wafer industry.

6.4 Depth-resolved ultra-violet spectroscopic photo current-voltage measurements

Many studies have been done to determine the location of traps in GaN based transistors. Khan *et al*.[47] were first to correlate current collapse phenomena with electron trapping in the gate insulator near the drain edge of the gate. Binari *et al*.[61] state the idea of hot electrons trapped in GaN buffer layers of GaN based MESFETs causing the current collapse is for the first time in 1997. Li *et al.*[28] attributed trap locations inside AlGaN/GaN HFETs with in the AlGaN barrier layer. Some researcher related the current collapses in GaN MESFET to the presence of the traps within the semi-insulating GaN layer.[61] Smith *et al*.[62] showed that while negative charges are trapped at or near the AlGaN/GaN heterojunction interface, positive charges are trapped at the AlGaN surface and within the GaN buffer layer in their study on AlGaN/GaN FET. Their observations are confirmed by other scientist.[63] Nguyen *et al.*[64] determine the presence of the traps in the AlGaN barrier layer or at the AlGaN surface.

6.4.1 Experiment

This experiment demonstrates the application of the depth-resolved UV spectroscopic photo I-V (DR-UV-SPIV) with ultra-violet (UV) light illumination for analyzing the depth-dependent electrically-active defect distributions along the epi-layer growth direction. This method is based on the fact that the penetration depth of light varies as a function of the wavelength for a semiconductor with above-bandgap illumination. Thus, by changing the wavelength of the light, the thickness of the region which is probed

will vary. In general, as the wavelength of the photon increases (as the photon energy decreases), the penetration depth of the photon increases (absorption coefficient decreases), probing more deeply into the bulk. Since the energy of the photon illuminated is higher than that of the bandgap, it is expected that all of the defect states in the bandgap are photoionized. It is expected that the use of this technique will shed light on the depth-dependent information in the electrically active defect distribution. The information will be useful for the AlGaN/GaN HEMTs wafer vendors for rapid diagnostics of the wafer.

We used the AlGaN/GaN HEMTs layers grown on the p-type 6″ Si wafer *via* MOCVD. The epilayer has the following structure; (1) 0.25μm AlN nucleation layer, (2) multi-layer AlGaN buffer layer with varying Al concentrations between 20% and 75%, (3) 1μm undoped GaN layer, (4) 20nm AlGaN barrier layers, and (5) an ultra-thin (2nm) GaN cap layer.

For device fabrication, the 6″ HEMTs epitaxy wafer was diced into 1 x 1 cm individual pieces, the piece from the center of the 6″ HEMTs epitaxy wafer were ultrasonically cleaned in the organic solvents with the following order; acetone, TCE, acetone, methanol, and methanol for 5 minutes in each solvent. After removing organic residues, the samples were placed in a mixture of HCl and DI water (1:1 by vol.) and subsequently heated at 110℃ for 10 minutes.

An array of the Schottky contacts were photolithographically constructed using DC magnetron sputtering, followed by lift-off. The circular Ni layers with the diameter of 600μm were used for Schottky contact. DR-UV-SPIV measurements were carried out at RT. An Apex 150W Xenon lamp was used for optical illumination. Wavelength of the light was changed from 280nm to 400nm by using a stepping motor controlled monochromator. The direction of the varying wavelength was chosen in a way such that the light would penetrate deeper into the samples bulk with increasing wavelength. A Keithley 6487 pico-ammeter/voltage source was used to sweep the applied voltage from - 20 to + 5V. The system was controlled by the LabVIEW program.

6.4.2 Results and Discussion

The variation of the band-gap energy of $Al_xGa_{1-x}N$ at T=300 K as a function of the Al concentration "x" in the solid solution can be approximated by the following formula;[65,66]

$$Eg(x) = x \cdot Eg^{AlN} + (1-x) \cdot Eg^{GaN} - bx(1-x) \qquad [\ 6.4\text{-}1\ ]$$

where "*x*" is the Al mole fraction (0.25), *Eg (x)* is the band-gap of the $Al_xGa_{1-x}N$, Eg^{AlN} is the band-gap energy of the AlN (6.2 eV)[46,67,68], Eg^{GaN} is the band-gap energy of the GaN (3.43eV)[10,13 ,69], b is the band-gap bowing parameter where 1 was used.[70,71,72,73] The band-gap of $Al_{0.25}Ga_{0.75}N$ was calculated to be 3.89 eV which is in good agreement with the experimental value reported by Shan *et al*. (3.88eV for $Al_{0.20}Ga_{0.80}N$).[69]

According to the Beer-Lambert rule;

$$\frac{I}{I_0} = Exp[-\alpha \cdot d] \qquad [\ 6.4\text{-}2\ ]$$

here α is the absorption coefficient, d is the distance from the surface of the material, and I and I_0 are the intensity of light measured at the depth and at surface *d*, respectively. Penetration depth (PD) is defined as a distance from the surface when the intensity of light has decayed to 1/e (~37%) of the original. Thus, penetration depth can be calculated from the absorption coefficient as follows;

$$PD = \frac{1}{\alpha} \qquad [\ 6.4\text{-}3\ ]$$

Since the absorption coefficient is a function of wavelength of the light, the PD is as well. The absorption coefficient can be calculated from the extinction coefficient *K;*

$$\alpha = \frac{4\pi K}{\lambda} \qquad [\ 6.4\text{-}4\ ]$$

Figure 6.4-1 shows the calculated PD as a function of the wavelength and energy for GaN and $Al_{0.25}Ga_{0.75}N$. In this evaluation, the absorption coefficient determined from the transmission measurement by Muth *et al*.[74] was used to calculate the PD as described above. The non-zero absorption coefficient for below band-gap excitation is possibly produced due to the absorption of light by in-gap states. As can be seen from the Figure 6.4-1, PD in AlGaN and GaN increases with the increasing wavelength of light, and exhibit an abrupt increase starting from around 320 nm and 360 nm for AlGaN and GaN,

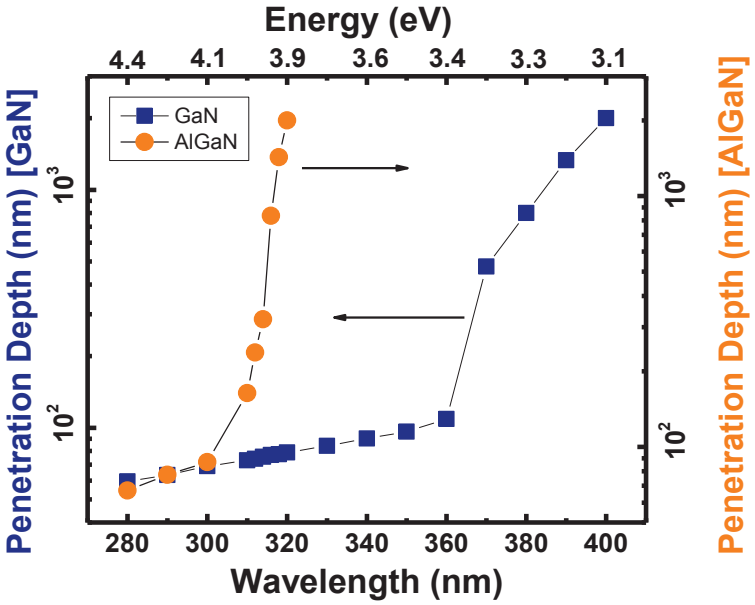

Figure 6.4-1: *Penetration depth as a function of wavelength and energy for GaN (blue/square) and $Al_{0.25}Ga_{0.75}N$ (orange/circle).*

Figure 6.4-2 (a) and (b) show the spectroscopic UV photo I-V data collected from the devices located on 2 different regions (hereafter to be referred to as device A and device B) on the piece chosen from the center of the 6″ AlGaN/GaN MOCVD-grown HEMTs on a Si wafer, respectively**.** For the spectroscopic UV photo I-V characterization, we preferred monitoring the change in the reverse bias photocurrent rather than the forward bias photocurrent due to a lower level of dark current at the reverse bias. Although these two devices displayed similar dark current characteristics (not shown here), they showed strikingly different photo I-V characteristics in terms of their spectral responses. For device A (Figure 6.4-2 a), the photocurrent at 290 nm was slightly higher than the dark current. The photocurrent

showed a jump at 300 nm with the UV illumination and reached the maximum with 370 nm (3.35 eV). For device B (Figure 6.4-2 b), the photocurrent at 280 nm was much higher than the dark current and the maximum photocurrent was observed at 310 nm (4 eV) UV illumination. The spectral response of the photocurrent is related to the in-gap states or traps located at different depths in the epi-layer structure.

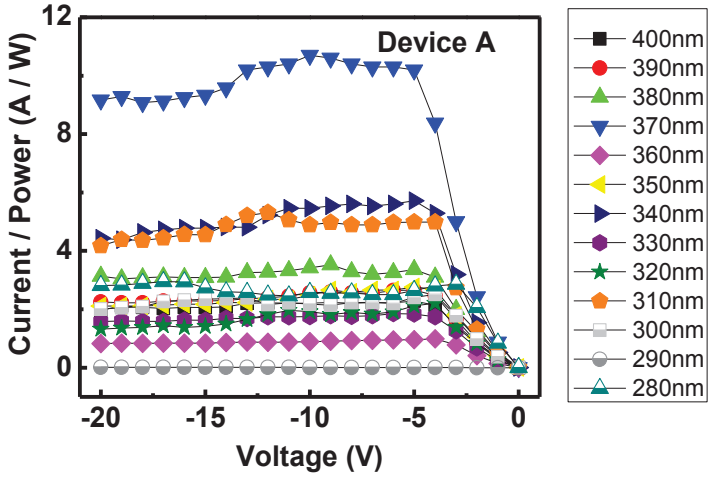

a

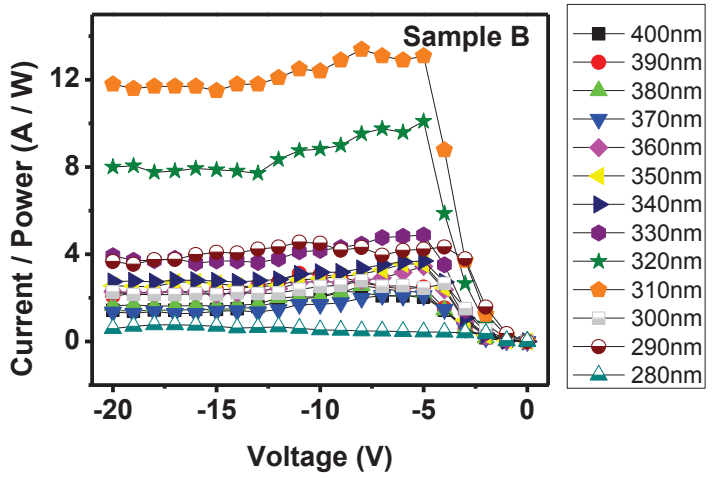

b

Figure 6.4-2: *Spectroscopic UV photo I-V collected from (a) sample A and (b) sample B on the piece chosen from the center of the 6 in. AlGaN/GaN MOCVD-grown HEMTs on a Si wafer, respectively.*

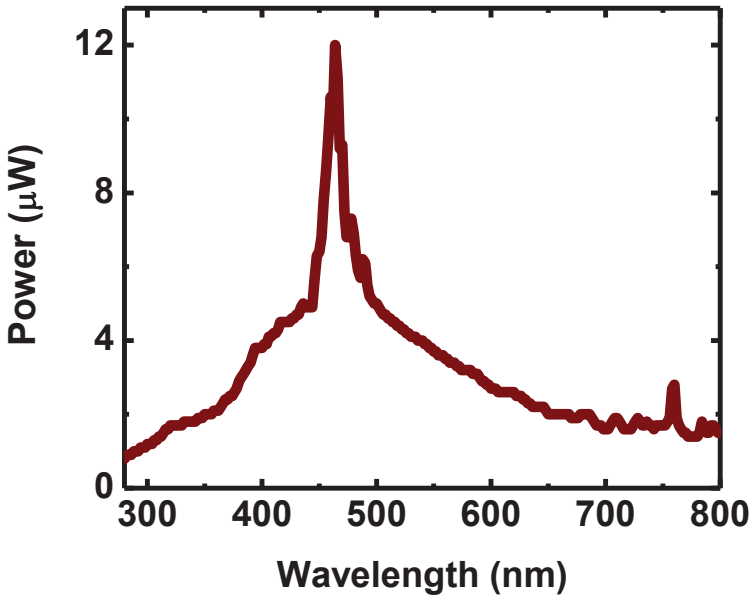

Figure 6.4-3: *Power of the Xenon lamp used in this experiment as a function of wavelength.*

In order to make sure that sub-gap traps exist, visible photo I-V measurement was performed with the sub-bandgap light illumination. We observed the spectral response of the photo current from these samples, which can provide the evidence for the presence of the traps. In the sub bandgap spectroscopic photo current measurement section, visible photo I-V measurement was reported on two different samples. One of the samples showed the maximum photocurrent at 750 nm**,** and the other one exhibited the maximum photocurrent at 650 nm, the peak of the energy level of trap locations showed a reasonable agreement with those measured by other workers[47,75] Variations of spectral responses from different areas in the wafer are presumably related to the local traps across the wafer.

Figure 6.4-4 shows the normalized current as a function of wavelength for sample A (square) and B (circle). To normalize the figures we measured the power of the Xenon lamb and it was plotted in the Figure 6.4-3 as a function of wavelength. As can be seen from Figure 6.4-2 and Figure 6.4-4, the device B has more defects close to the interface of the 6″ AlGaN/GaN MOCVD-grown HEMTs on a Si wafer while device A has predominant defects deeper into the bulk.

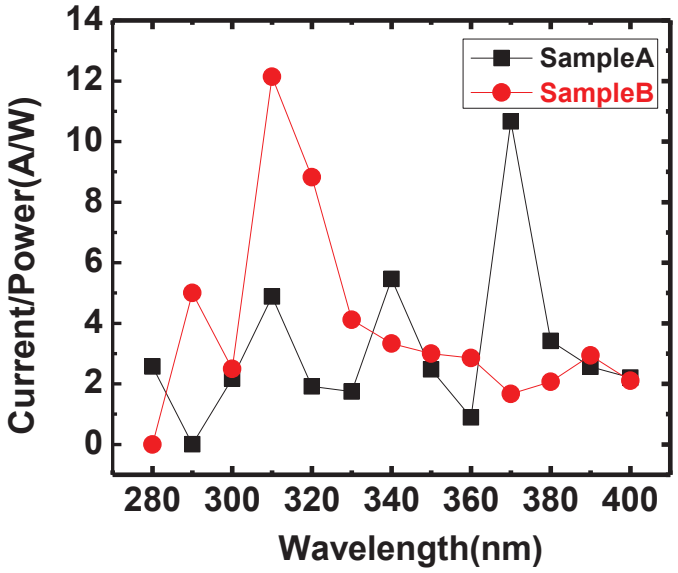

Figure 6.4-4: *Normalized current as a function wavelength for samples fabricated on device A (square) and device B (circle) of the piece chosen from the center of 6 in. HEMT wafer.*

In summary, we demonstrated the applicability of DR-UV-SPIV technique for analyzing the depth-dependent distribution of the deep level traps in AlGaN/GaN HEMTs epi-structures. Deep-level defects in the AlGaN/GaN HEMTs devices result in undesirable current collapse issues which limit actual device performances at high frequencies. Therefore, it is necessary to investigate deep level defects in the AlGaN/GaN HEMTs structures. The AlGaN/GaN HEMTs structures used in this study were grown on a 6″ Si wafer by MOCVD. A monochromatized UV light illumination from a Xe lamp was used to perform the DR-UV-SPIV measurements. We observed variations in the depth-dependent defect distribution across the wafer detected by the DR-UV-SPIV measurement. In addition to previously demonstrated spectroscopic photo-IV measurement with the sub-bandgap excitation, the DR-UV-SPIV measurement can be performed to make a quick analysis of the depth-dependent electrical homogeneity of the electrically-active defect distribution in the AlGaN/GaN HEMTs epi-structure grown on a Si wafer with least sample preparation.

6.5 Voltage dependent spectroscopic photo current-voltage measurement

6.5.1 Experiment

The same experimental setup and devices as in our previous experiments were used to investigate voltage dependence of spectroscopic photocurrent measurements.

6.5.2 Results and Discussion

Figure 6.5-1 illustrates the bias-dependent spectral responsivity of the Ni Schottky contact on AlGaN/GaN HEMTs structure under the illumination. 280nm to 400nm wavelengths for above bandgap measurements were used to perform photo response measurement. While there are four peaks at 280, 310, 340 and 370nm appearing in the spectra for sample A, two sharp peaks at 290 and 310nm were observed for sample B. Kumar *et al*.[76] associated the peaks at 280nm and 290nm with the intrinsic transitions above the band edge of AlGaN and the peak at 340nm with intrinsic transitions above the band edge of GaN. Since current/power values for the zero bias are much smaller compared to the same values at higher voltages, the relationship shown in the Figure 6.5-1 appears linear. When it is plotted itself, it follows a similar pattern as other voltages. As a result, one can say that responsivity spectra do not depend on the device bias.

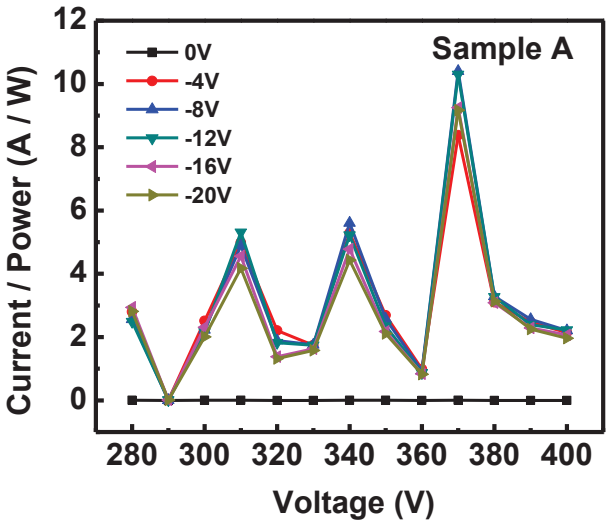

a

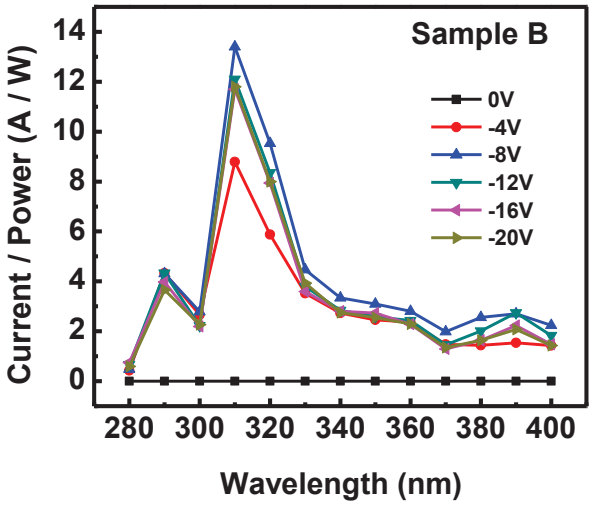

b

Figure 6.5-1: *Voltage dependent spectroscopic UV photo I-V collected from (a) sample A and (b) sample B on the piece chosen from the center of the 6 in. AlGaN/GaN MOCVD-grown HEMTs on a Si wafer, respectively.*

For both samples, we did not observe a relationship between the applied bias and current/power values. The voltage-insensitive photocurrent characteristic of the AlGaN/GaN heterostructure can be interpreted as arising from a significant density of trap states with fast trapping of the charges such that the mean-free path of the charge carriers (the distance traveled before being trapped) is less than the thickness of the active layer, as suggested by Li *et al*.[77] It is suggested that the recombination of trapped charge transport would be limited by the time spent traveling between the traps that should show a voltage dependence in the case of rapid detrapping and in the absence of efficient recombination of trapped charge transport. For further investigation, time dependent photocurrent experiments were conducted to observe the decay dynamics.

Kumar *et al*.[76] observed an increase in their responsivity measurements with the increase of reverse bias voltage. The values of the responsivity were estimated to be higher than the theoretical value (i.e., ~0.22 A/W at an incident wavelength of 280 nm); when reverse bias was applied at 1 V and at an incident wavelength of 340 nm, it was higher than the theoretical value[78] (i.e., ~0.27 A/W) at –2 V bias. The AlGaN/GaN Schottky contacts showed a considerable internal gain. Such a gain has been widely observed in various photodetectors, and considered to be advantageous for required high responsivity application.[79] Several theories have been suggested to explain the gain mechanism, such as photoconductive gain[80], avalanche carrier multiplication,[81] and trapping of photocarriers at the semiconductor/metal interface.[82] Since we already observed the presence of the traps, we propose that the trapping of photo-carriers at the semiconductor/metal interface could be a possible mechanism for the observed gain.

The possible energy band diagram of the AlGaN/GaN HEMTs heterostructure for Schottky contact is displayed in the Figure 6.5-2. According to Kumar *et al*.'s[76] theory, the photo-excited electrons from the absorption region of AlGaN will be moved to the conduction band and driven to the quantum well at the interface. The photo-excited electrons in the GaN layer absorption region near the interface are forced to move into the quantum well by the built-in electric field at the interface. Since photons can travel deeply into the GaN layer, the photo-excited electrons may generate in the deeper side of the GaN layer and they may also partly reach into the quantum well due to the built-in electric field influence by diffusion.

Consequently, there will be fewer excitation energies than those in the band gap of bulk GaN and the photo-excited electrons in the non-depleted region will recombine after some time. Based on this theory it is more likely that contributions to photocurrent in these structures are mainly due to the carriers generated in the AlGaN and GaN layers mainly.

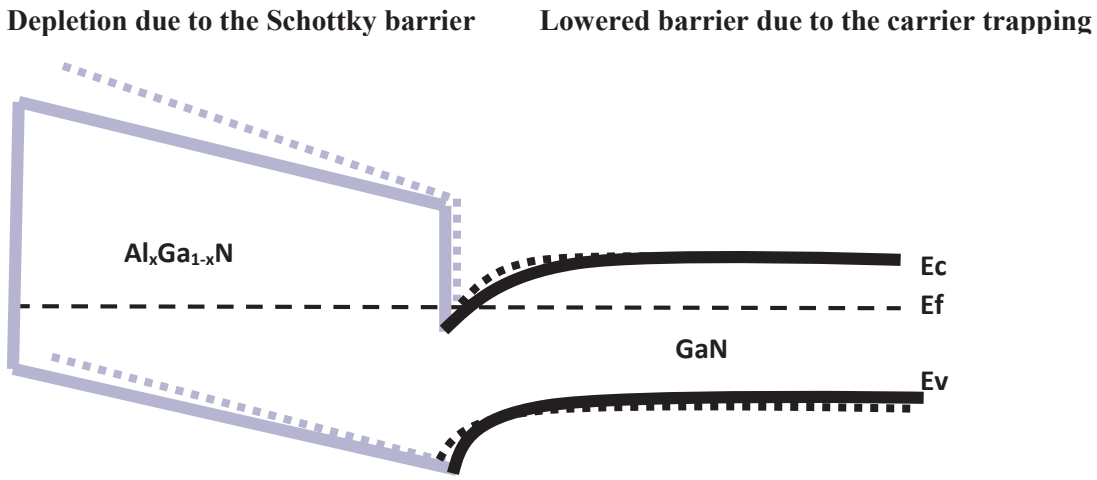

Figure 6.5-2: *Schematic energy band diagram of an AlGaN/GaN HEMTs heterostructure for a Schottky contact inspired from Kumar et al.*[76]

We also calculated depletion width under applied voltage changing between -5V and -20V for different doping concentration by using equation [6.5-1].[83]

$$W_D = \sqrt{\frac{2\varepsilon_s(\varphi_i - V_{ext})}{qN_d}} \qquad [\ 6.5\text{-}1]$$

where ε_S is the permittivity of GaN ($7.88\text{x}10^{-13}$F/cm)[84], φ_i is the built in potential, V_{ext} is the applied external bias, q is the electron charge and N_d is the doping concentration. We used five different doping concentration as $1\text{x}10^{15}$, $5\text{x}10^{15}$, $1\text{x}10^{16}$, $1\text{x}10^{18}$, and $1\text{x}10^{20}$ cm^{-3}. φ_i is calculated as follows;

$$\varphi_i = \varphi_n - (\phi_m - \varkappa_s) \qquad [\ 6.5\text{-}2]$$

where $q\varphi_n = \left(E_g/2 \right) - \varphi_B$, $\varkappa_S$ (4.1eV)[85] is the electron affinity of the semiconductor, ϕ_m (5.24eV)[86] is the work function of the metal. φ_B is calculated for different doping concentrations as follows;

$$q\varphi_B = kTln(N_D/n_i) \qquad [6.5\text{-}3]$$

where k is the Boltzmann constant, T is the temperature, N_D is the doping concentration, n_i ($1.9\text{x}10^{-10}$)[87] is the intrinsic carrier concentration of the semiconductor. The calculated depletion widths for voltages between -5V and -20V, and for doping concentrations between 10^{15} and 10^{20} cm^{-3} were summarized in Table 6.5-1. According to results in this table, depletion with decreases from $4\text{x}10^3$ nm to 60nm with the increase of the doping. We also observed that depletion width of different doping concentrations increases with the increase of the applied voltages. We compared our depletion width results to the penetration depth values of GaN and AlGaN given in Figure 6.4-1. We concluded that for doping concentration higher than $1\text{x}10^{15}$ cm^{-3} (i.e. $5\text{x}10^{15}$) penetration depth is higher than the calculated values of depletion width. Further research is required to understand the exact correlation of relative difference between penetration depth and depletion width and photocurrent increase.

In conclusion, bias dependence of AlGaN/GaN heterostructures under light illumination were investigated. Observed voltage independent photocurrent increases were related to density of trap states with fast trapping of the charges such that the mean-free path of charge carriers is less than the thickness of the active layer. Higher responsivity values than usual were observed, suggesting that a small internal gain exists within the structure. The internal gain phenomenon is described by Schottky barrier lowering due to photo-generated carriers that are trapped at the semiconductor/metal interface.

Table 6.5-1: *Summary of the calculated depletion width in nm for different doping concentration and applied biases*.

Applied Voltage	**N_D=1x10^{15} cm^{-3}**	**N_D=5x10^{15} cm^{-3}**	**N_D=1x10^{16} cm^{-3}**	**N_D=1x10^{18} cm^{-3}**	**N_D=1x10^{20} cm^{-3}**
-5V	2012.114	895.3078	631.6915	622.3998	61.29674
-6V	2243.472	999.244	705.33	697.0207	68.86111
-7V	2453.106	1093.344	771.9758	764.3913	75.67308
-8V	2646.184	1179.963	833.3084	826.2871	81.92056
-9V	2826.102	1260.645	890.4264	883.8589	87.72423
-10V	2995.232	1336.465	944.095	937.9034	93.16707
-11V	3155.31	1408.208	994.8727	988.999	98.30903
-12V	3307.649	1476.47	1043.182	1037.581	103.1951
-13V	3453.274	1541.712	1089.35	1083.989	107.86
-14V	3593.002	1604.303	1133.64	1128.489	112.3314
-15V	3727.496	1664.542	1176.264	1171.3	116.6315
-16V	3857.304	1722.676	1217.396	1212.601	120.7786
-17V	3982.883	1778.911	1257.183	1252.54	124.788
-18V	4104.621	1833.423	1295.749	1291.245	128.6725
-19V	4222.852	1886.359	1333.2	1328.822	132.4431
-20V	4337.861	1937.85	1369.627	1365.366	136.1092

6.6 The time-dependent evolution of the photoconductivity/ Transient Photoconductivity

There are many techniques to measure the photoconductivity. In this work, we will focus on transient photoconductivity measurement. Transient spectroscopy relies on the trapping and de-trapping of charge carriers.[10] In this measurement, excess charge carriers are produced with the illumination of the light and when the light is switch off the photoconductivity decays exponentially. To observe the transient photoconductivity one can either record the voltage drop across the load resistor by a bandwidth oscilloscope or can record the current drop by time *via* a computer program.[10] Transient spectroscopy is more suitable for studying defects in epitaxial layers and give more information activation energies, cross sections, and density of individual defects.[10]

For an n type semiconductor with a steady state photocurrent ΔI_0, photoconductivity is expected to decay exponentially to zero when the illumination is suddenly removed at $t = t_0$. The time dependency of the photocurrent can be described as follows;[10]

$$\Delta I = \Delta I_0[1 - \exp(t/\tau_p)] \qquad (0 \le t \le t_0) \qquad [\ 6.6\text{-}1\ ]$$

$$\Delta I = \Delta I_0\big[1 - \exp\big(t/\tau_p\big)\big]\exp[-(t - t_0)/\tau_p]\ (t \ge t_0) \qquad [\ 6.6\text{-}2\ ]$$

where τ_p is a time constant and it can be determined *via* transient behavior of the photoconductivity in the absence of the traps.[88] In this case, the photoconductivity decay contains only a fast component which corresponds to radiative recombination from conduction band to valance band.[10] Since there is slower release rate of the traps in the case of the presence of the traps, a single exponential decay is not enough to describe the transient photoconductivity.[10] Consequently, in the presence of traps photoconductivity decay can consists of several decay mechanisms with different time constants. In these cases, photoconductivity decay curve fitting can be expressed as the sum over exponential functions each characterized by a different time constant. Erol and Çetin stated that in the photoconductive decay curves which can be expressed by two exponential function while initial fast decay corresponds to recombination of photoexcited carriers, slower decay exponential is due to the thermal release of electrons from traps.[10]

The time-dependent evolution of the photocurrent decay upon the termination of the excitation has been also analyzed with a stretched-exponential function.[18,18] Lin *et al*.[29] stated that the long-term relaxation does not follow an exponential function. Instead, it can be described by the stretched exponential relation as follows;[24]

$$I(t) = I_0\ exp[-(t/\tau)^{\alpha}] \qquad [\ 6.6\text{-}3\ ]$$

where t is the time, τ is the characteristics time constant for decay of photocurrent, α is the stretching exponent ($0 < \alpha < 1$), and I_0 is PPC level at the moment light excitation is turned off (current immediately after the termination of excitation). The stretching exponent α can take a value between 0 and 1, and will be unity when simple exponential decay is expected.[89] Since the physical significance of α is not clear, caution needs to be exercised in its interpretation. However, it may be suggested that the origin of the decay processes are different for various α values.[90]

There are several reasons that can explain non-exponential photocurrent transient; Mitrofanov *et al*.[91] suggested that electrons are trapped on various separate trap levels where the transient is a sum over exponential decays with different rates and amplitudes. Another possibility might be that the trapping centers form a continuously distributed energy levels and electrons are captured into all the levels of the trap distribution. In this case, one generally observes a stretched exponential response for the transient characteristics. Finally, if the decay process is assisted by an electrical field, the non-uniform field distribution in the structure results in variation of the charge-carrier release rate from the traps.

6.6.1 Sub bandgap time resolved photocurrent measurements

6.6.1.1 Experiment and Results

In this experiment, the time-resolved photocurrent (TRPC) spectroscopy which exploits the PPC to elucidate the nature and distributions of electrically-active deep level traps. A wavelength of the sub-bandgap light was varied to selectively de-trap the charge carriers trapped in deep level traps with different activation energies. After the analysis of the decaying spectra, a correlation between the wavelength of the illuminated light and parameters of decay characteristics were made. We showed that the traps whose de-trapping energies are the same can exhibit different PC decay dynamics. Therefore, the analysis of time transient behavior of PC decay can shed light on origin/nature of the deep level defects.

The AlGaN/GaN epi-structure used in this work was an AlGaN/GaN HEMTs structure grown on the p-type 6″ Si wafer *via* MOCVD. The structure consists 0.25 μm AlN nucleation layer, multi-layered AlGaN buffer with Al concentrations ranging from 20% to 75%, 1μm thick undoped GaN layer, 20nm thick AlGaN barrier layers, and an ultra-thin (2nm) GaN cap layer. The details of the fabrication steps were reported previously.[35] An array of Schottky contacts composed of the DC magnetron sputtered Ni layers with the diameter of 1mm were used. The two devices (hereafter to be referred to as samples A and B with the same dark current characteristics were chosen for the analysis.

The spectroscopic photo I-V measurement and the time-resolved photocurrent (TRPC) spectroscopy were performed at the room temperature with a varying wavelength. An illumination was provided by an Apex 150W Xenon lamp. Details of the spectroscopic photo I-V measurement process can be found above. For the TRPC experiment, an optical pulse was generated by a mechanical shutter. The light was dispersed by a monochromator, providing excitation wavelength in the range of 400-800 nm with 50nm wavelength step for each measurement. The monochromatized light was focused onto the Schottky contacts through optical lens. The photocurrent was measured using Keithley 6487 Pico-ammeter/voltage source with top Schottky contact reverse-biased with respect to the bottom ohmic contact. The entire measurement process was controlled *via* LabVIEW and the spectra was recorded by a computer. The sample was kept under the darkness at room temperature for 24 hours prior to the light illumination to ensure that the measurement is not affected by decaying photocurrent generated from previous or unwanted light exposure.

6.6.1.2 Results and Discussion

Figure 6.6 -1 (a) and (b) show the spectroscopic photo I-V data collected from samples A and B, respectively. Sub-bandgap light with varying wavelength was used to produce the photocurrent. As can be seen from the figure, those two devices respond to the different wavelengths in a similar fashion.

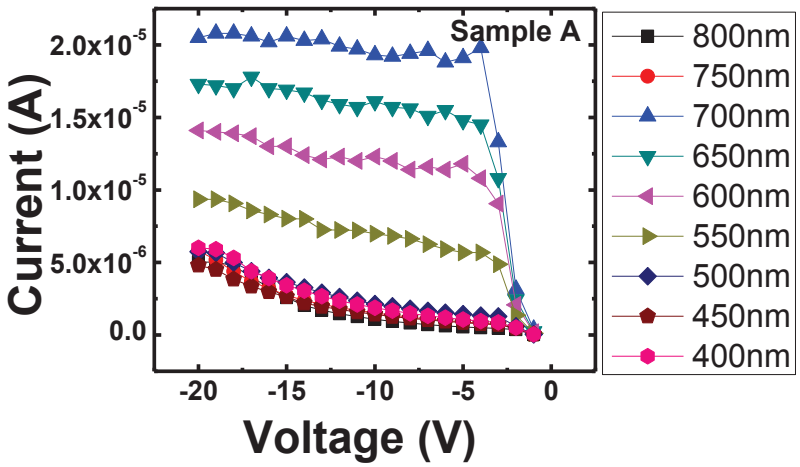

a

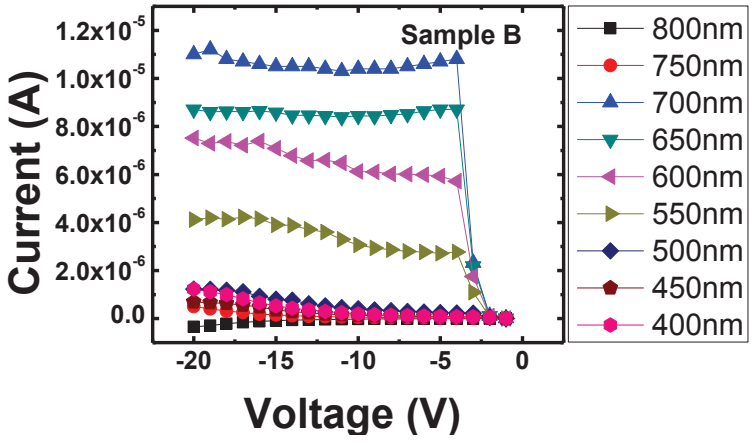

b

Figure 6.6-1: *Spectroscopic photo I-V data with sub-bandgap excitation for (a) sample A and (b) B.*

Figure 6.6-2 (a) and (b) show the normalized TRPC spectra of samples A and B, respectively. Overall, it was found that in all the studied AlGaN/GaN HEMTs epi-structures the photocurrent decay after light

exposure is extremely long, ranging from tens of minutes to several hours for the current to return to the level of dark current. A sub-bandgap PPC effect is obviously observed from all of the samples. PPC effect is a light induced enrichment in conductivity and the photoconductivity persists for a long time after the termination of illumination.[19] The PPC includes multiple processes, such as photon absorption, carrier recombination and transport.[16]

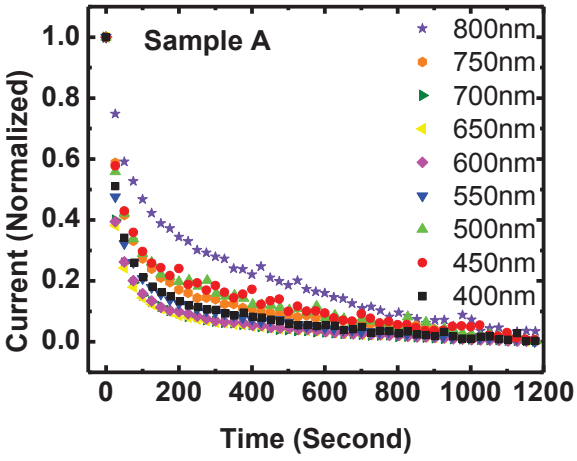

a

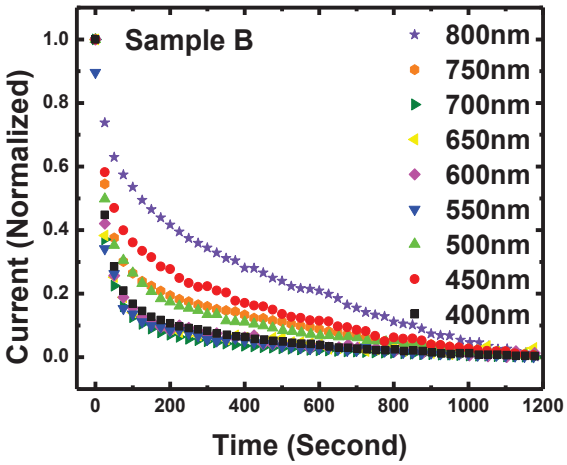

b

Figure 6.6-2: *Room temperature PPC decay kinetics of the Al0.25Ga0.75N/GaN/Si heterostructure as a function of excitation wavelength for (a) samples A and (b) sample B.*

Previously, PPC study have been performed on bulk GaN[17] and AlGaN/GaN heterostructures, and most of these studies were conducted under the above-bandgap ultra-violet (UV) illumination with a fixed wavelength. It has been claimed by many researches that PPC effects in bulk GaN is caused by the deep level defects, such as AX-like center in p-type GaN or DX-like and AX-like centers in n-type[20] and p-type[21] GaN, respectively. Li *et al.*[1818] attributed the increase of PPC to the photoionization of deep level impurities, such as DX-like centers in the AlGaN barrier material. Reddy *et al.*[22] stated that if PPC arises from a DX-center like defect, a steep rise in photocurrent is expected when the photon energy equals the ionization energy of the deep level defects, followed by a saturation even with a small increase in the photon energy. It was also suggested that the PPC effect can be attributed by the unintentionally incorporated cubic-phase crystallites in a hexagonal matrix[23] or random potential fluctuations due to heterointerfaces.[20] In addition, some researchers claimed that both long and short decay time constants contribute to the PPC of n-type GaN, which implies the presence of more than one type of PPC. [25] Although hole trap contribution to PPC is generally ignored, their presence has been observed in n-type GaN.[26] In this investigation, we used the wavelength-dependent persistent photocurrent decay to elucidate the nature of sub-bandgap defects in AlGaN/GaN heterostructures grown on 6 inch Si wafers.

The time-dependent evolution of the photocurrent decay upon the termination of the excitation has been analyzed with a stretched-exponential function. [18,18] Lin *et al*.[29] stated that the long-term relaxation does not follow an exponential function. Instead, it can be described by the stretched exponential relation,

$$I(t) = I_0\, exp[(-t/\tau)^{\alpha} \qquad [\ 6.6\text{-}4\ ]$$

where t is the time, τ is the characteristics time constant for decay of photocurrent, α is the stretching exponent ($0 < \alpha < 1$), and I_0 is PPC buildup level at the moment of light excitation is turned off (current immediately after the termination of excitation).

In this investigation, the following expression of combined exponential and stretched exponential functions were used to fit the experimental data of Figure 6.6-1 (a) and (b);

$$I(t) = A + B[exp(-(t/\tau_1)] + C[exp(-\left((t/\tau_2)^{\alpha}\right)] \qquad [\ 6.6\text{-}5\ ]$$

here τ_1 and τ_2 are decay time constants for exponential and stretched exponential functions, respectively, A is a constant for fitting adjustment, and the pre-exponential factors B and C are measure for relative contribution of exponential and stretched exponential functions to the fit. Each decay curve was normalized to unity at $t = 0$ which is the moment when the light excitation is terminated. In addition, the dark current was subtracted. All samples displayed diverse transient photocurrent dynamics when reaching their saturated dark current levels. A least square fit to the experimental data was performed to determine the decay exponent α, pre-exponential factors B and C, and decay time constants τ_1 and τ_2. Figure 6.6-2 shows the decay time constants τ_1 and τ_2 as a function of wavelength. Slow decay is followed by fast decay and such a behavior was observed by other researchers.[17] Both fast and slow decay time constants vary with wavelength, which implies that both the decay processes are governed by light activated process. It was observed that fast decay exhibited exponential behavior while the slow decay displayed non-exponential behavior.[92] We also observed that τ_2 values are generally higher than τ_1 values. Therefore, it can be conjectured that fast and slow decay can be associated with exponential and stretched exponential behaviors, respectively.

There are several reasons that can explain non-exponential photocurrent transient; Mitrofanov *et al*.[91] suggested that electrons may be trapped on various separate trap levels, where the transient is a sum over exponential decays with different rates and amplitudes. Another possibility might be that the trapping centers form a continuously distributed energy levels and electrons are captured from all the levels in the trap. In this case, one generally have a stretched exponent for the transient character. Finally, if the decay process is assisted by an electrical field, the non-uniform field distribution in the structure results in variation of the release rate.

Although the two samples show similar characteristics for wavelength-dependency on photocurrent generation (Figure 6.6-1), they exhibited a dissimilar time-dependent photocurrent decay dynamics. This implies that TRPC spectroscopy can be used to distinguish the traps which have different origins but have the same de-trapping energy. Since the PPC decay rates in device A and device B are different, it implies that the underlying trapping mechanism responsible for the PPC effects is also different.[91]

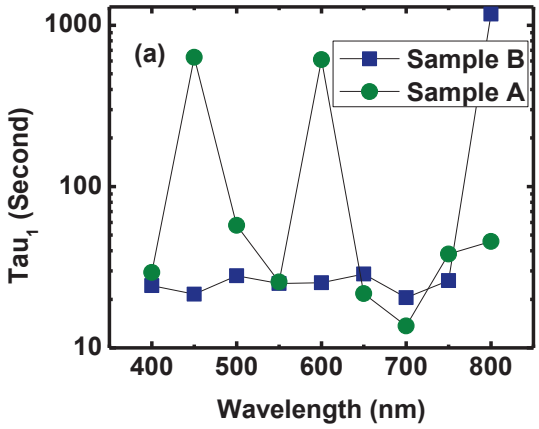

a

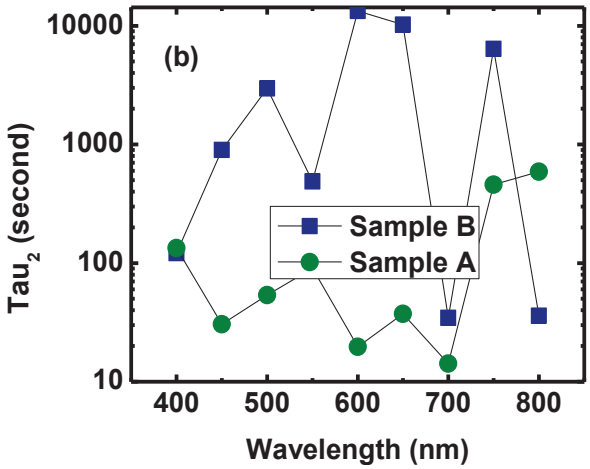

b

Figure 6.6-3: *Decay time constants for (a) exponential and (b) stretched exponential functions*.

Figure 6.6-4 (a) shows the fitted values of the stretching exponent α for samples A and B also the values plotted as a function of wavelength. The stretching exponent α can take a value between 0 and 1, and will be unity when simple exponential decay is expected.[89] Since the physical significance of α is not clear, caution needs to be exercised in its interpretation. Nonetheless, it may be suggested that the origin of the decay processes are different for various α values.[90] Moreover, equal values of α were observed for both samples at 700 and 750nm. This might be related to the fact that both samples have the highest photocurrent at 700nm.

Figure 6.6-4 (b) demonstrates the voltage dependence of α at 700nm. While smaller voltages α values showed similar trend for both samples A and B, for higher voltages different trends were observed for two samples. Furthermore same values of α was observed for both samples at -10V. Monroy *et al*.[93] did not observe any dependence of bias on photocurrent decay for their AlGaN photodetectors. In our experiment, different voltage values, except 10V, used than the one this is used in AlGaN photodetectors experiment. This may tell us that different biases might affect the photocurrent decay. The dependence of exposure time on α was analyzed to acquire the accurate exposure time, as shown in the Figure 6.6-4 (c). It was showed that both samples have similar characteristics of α values at for higher exposure time constants. Similar α values for both samples were observed for 60s exposure time, as a result 60s exposure length were used in our measurements.

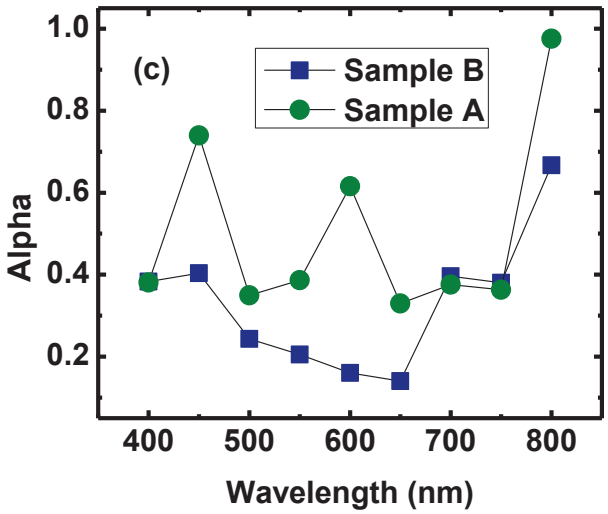

a

Figure 6.6-4: *Stretching exponent as a function of (a) wavelength*

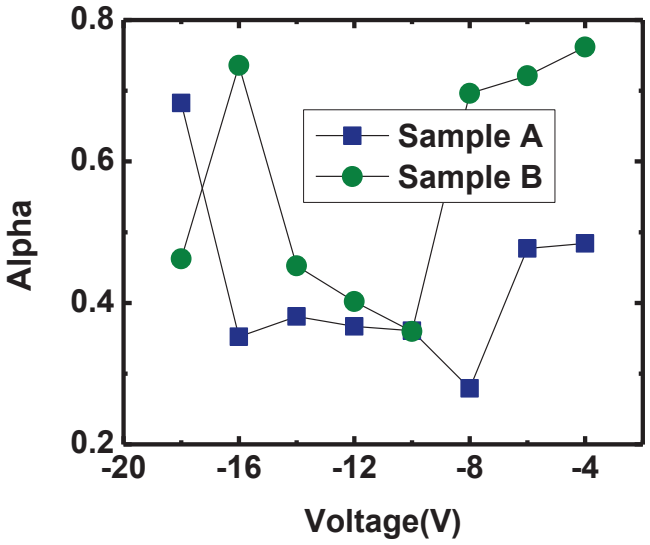

b

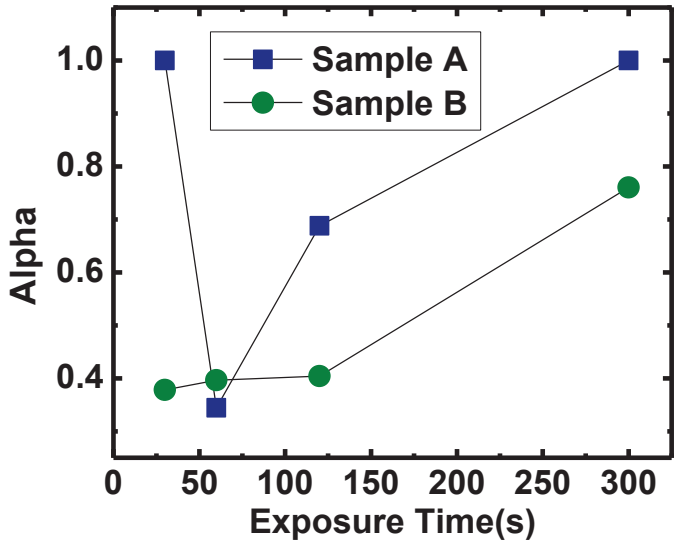

c

Figure 6.6-4: *Stretching exponent as a function of (b) voltage and (c) exposure time.*

The pre-exponential constants for the exponential and stretched exponential functions (B and C) indicate relative dominancy between the exponential and stretched exponential components. Wavelength-dependent variation of *B* and *C* for samples A and B are shown in the Figure 6.6-5 (a) and (b), respectively. Our results indicated that stretched exponential has shown the dominant characteristics for both of the samples. In the Figure 6.6-5 (c) and (d), the effect of each exponential according to change in wavelength

was plotted for each sample. While pre-exponential constants of stretched exponential function showed similar wavelength dependency for both samples, different wavelength dependence of pre-exponential constants of exponential function were observed for samples A and B.

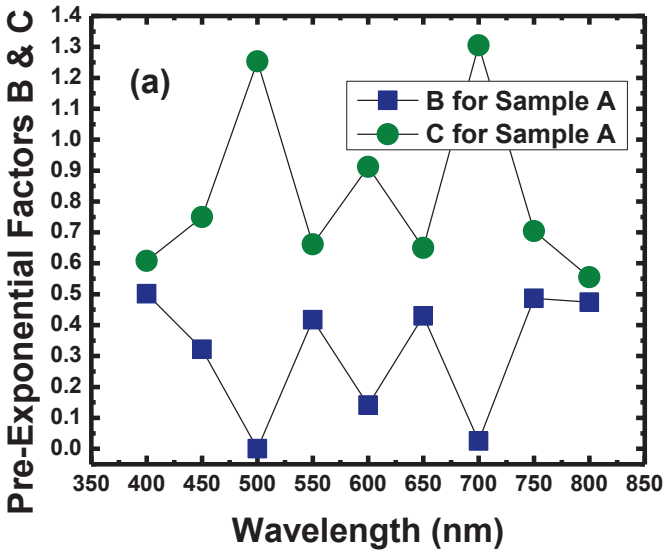

a

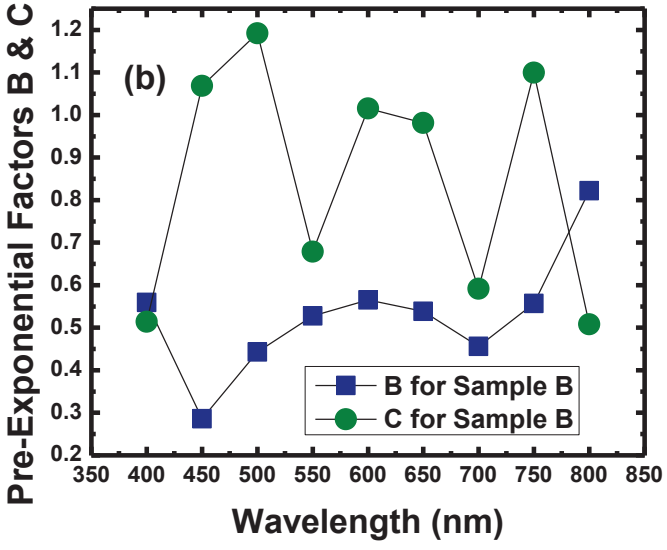

b

Figure 6.6-5: *Pre-exponential factors (a) B&C for sample A (b) B&C for sample B*

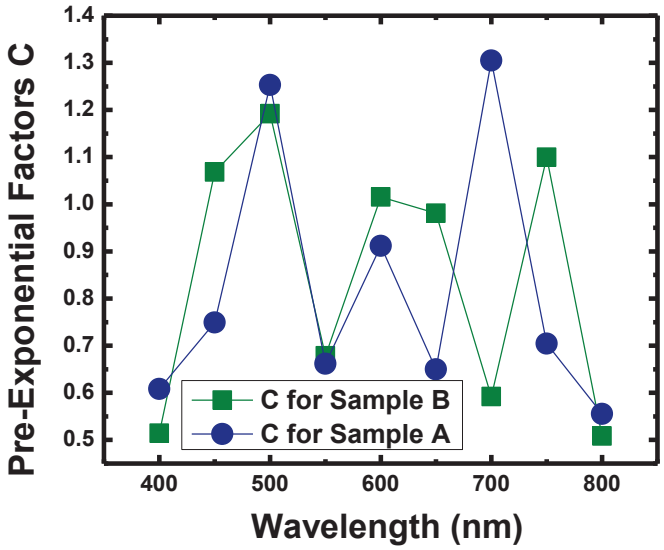

c

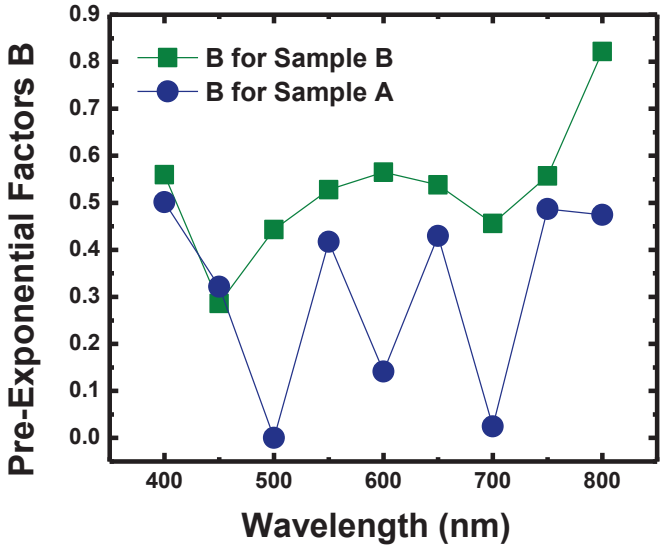

d

Figure 6.6-5: *Pre-exponential factors (c) B for sample A&B and (d) C for sample A&B.*

In conclusion, TRPC spectroscopy with a variable-wavelength sub-bandgap light excitation was used to study the dynamics of the decaying photocurrent generated in the heterostructures of the AlGaN/GaN HEM) layers. The two samples show similar characteristics for wavelength-dependency on photocurrent generation were shown different TRPC spectra, which means that TRPC spectroscopy can be used to shed light on elucidation of underlying mechanisms (different origins) responsible for PPC effect. We demonstrated that the TRPC spectroscopy is useful for AlGaN/GaN HEMTs wafer vendors as a diagnostic tool for assessment of wafer quality in terms of the distribution of electrically active defects.

6.6.2 Above bandgap time resolved measurements

6.6.2.1 Experiments

A similar experiment was conducted for two different sets of wavelengths one between 220 nm (5.63 eV) and 300 nm (4.13eV) which are above bandgap of both GaN (3.4 eV= 360nm) and $Al_{0.25}Ga_{0.75}N$ (3.89eV= 319nm), and the other between 320nm (3.87eV) and 360nm (3.44eV) which are above the only the bandgap of GaN.

6.6.2.2 Results and Discussion

Figure 6.6-6 (a) and (b) show the time resolved spectroscopic photo I-V data collected from samples A and B, respectively, under the illumination of the light between 220nm and 300nm. For the clarity of the graphs, we omitted every 50 points in the graphs. The equation [6.6-5], sum of exponentials with up to two components, was also used to fit the experimental data of Figure 6.6-6. After the dark current was subtracted, each decay curve was normalized to a unity at $t = 0$ which is the moment at which the light excitation is terminated. Two devices showed different decay characteristics to the light illumination with the wavelengths ranging between 220 and 300nm.

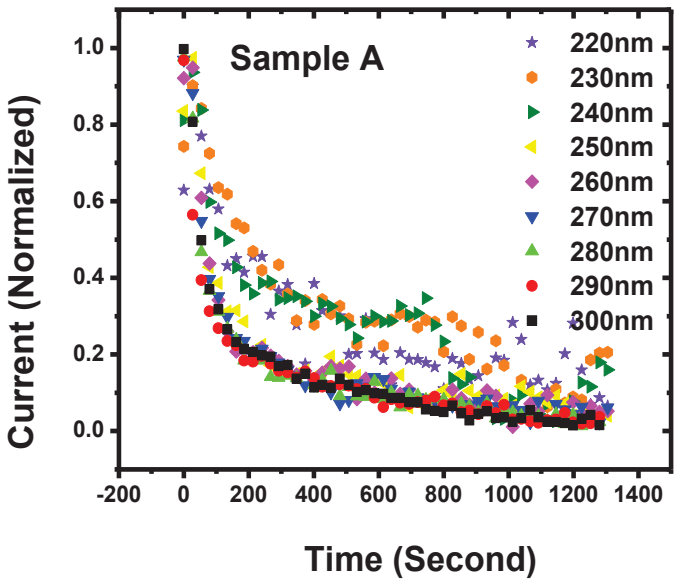

a

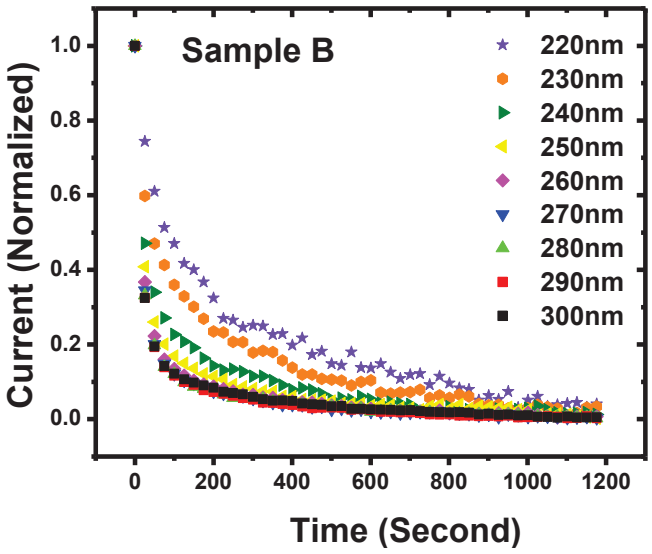

b

Figure 6.6-6: *Room temperature PPC decay kinetics of the $Al_{0.25}Ga_{0.75}N$/GaN/Si heterostructure as a function of excitation wavelength for (a) sample A and (b) sample B.*

Figure 6.6-7 (a) and (b) show the decay time constants τ_1 and τ_2 as a function of wavelength. As in our previous results slow decay is followed by fast decay and such a behavior has been observed by other researchers.[17] Both fast and slow decay time constants vary with wavelength, which implies that both the decay processes are governed by light activated process. It was observed that fast decay exhibited exponential behavior while the slow decay displayed non-exponential behavior.[92] We also noticed that τ_2 values were generally higher than τ_1 values. Therefore, fast and slow decay can be associated with exponential and stretched exponential behaviors, respectively. Furthermore, while two samples display similar fast decay characteristics, their slow decay characteristics differ a lot. This might indicate that while they have similar band to band transition characteristics, they have different slow decay characteristics due to the involvement of different trap levels.

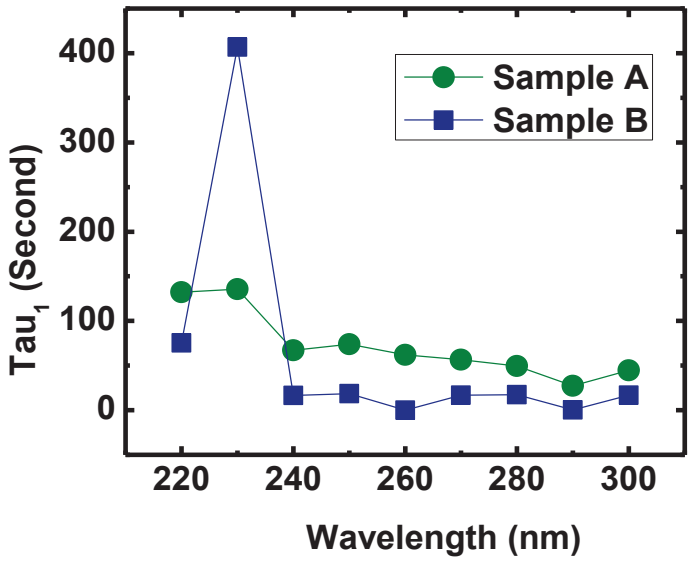

a

Figure 6.6-7: *Decay time constants for (a) exponential*

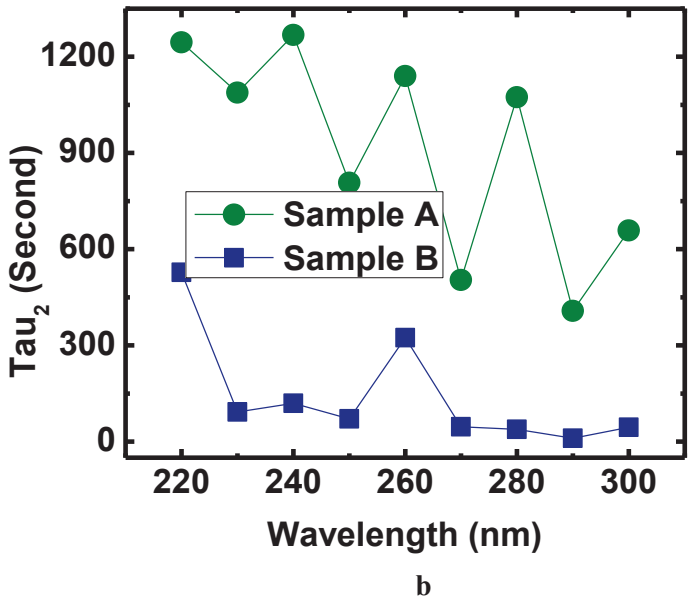

Figure 6.6-7: *Decay time constants for (b) stretched exponential functions.*

Figure 6.6-8 shows the fitted values of the stretching exponent α for samples A and B and the values plotted as a function of wavelength. As we stated before, the physical significance of α is not clear, and hence, caution needs to be exercised in its interpretation. However, it may be suggested that the origin of the decay processes are different for various α values.[90] In contrast to sub bandgap measurement we did not observed similar values of α for two samples. For sample A, most of the values of α are closer the unity, except two wavelengths at 270nm and 290nm. The values of α being equal to one indicates that sample A might be also represented by the sum of two exponential function instead of the sum of exponential and stretched exponential functions. Furthermore similar values of α for different wavelengths in sample A might indicate the involvement of the similar type of defects or only the band to band transitions. If the observed effects for sample A are dominated by band to band transitions, after comparing these results to sample B one can conclude that sample B might have contribution of additional factors, such as deep level impurities other than band to band transitions.

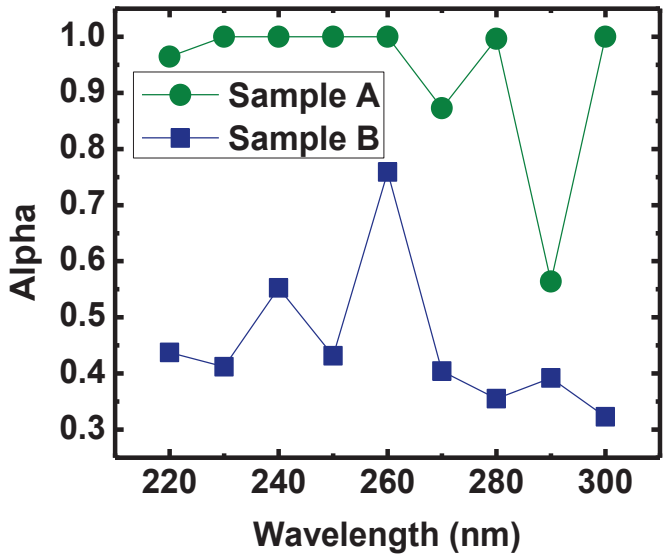

Figure 6.6-8: *Fitted values of the stretching exponent α for samples A and B and the values plotted as a function of wavelength.*

As we stated before, the pre-exponential constants for the exponential and stretched exponential functions (B and C) indicate relative dominancy between the exponential and stretched exponential components. Wavelength-dependent variation of *B* and *C* for samples A and B are shown in the Figure 6.6-9 (a), and (b), respectively. Our results indicate that while stretched exponential had shown the dominant characteristics for sample B, exponential decay was more prevalent for sample A. These results support the observation that the values of α being equal to unity actually means the involvement of exponential decays instead of stretched exponential. In the Figure 6.6-9 (c) and (d), the effect of each exponential according to change in wavelength was plotted for each sample. Both pre-exponential constants of stretched exponential function and exponential function showed different wavelength dependencies for both samples. Despite the fact pre-exponential constants of stretched exponential are bigger for sample B, in sample A pre-exponential constants of exponential function are higher compared to the values of sample B. In fact, these results prove that for sample A, exponent function is more dominant compared to stretched exponent function.

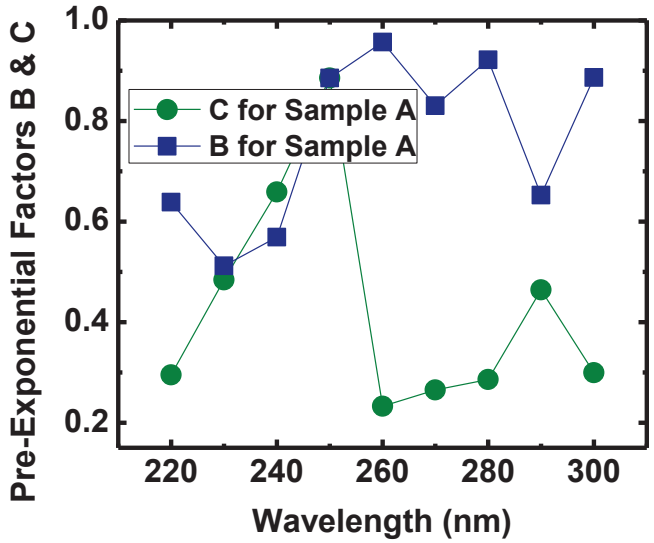

a

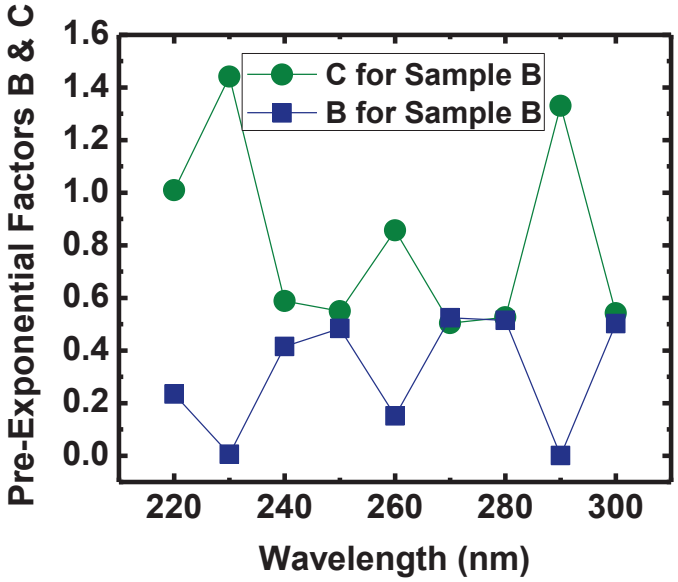

b

Figure 6.6-9: *Pre-exponential factors (a) B&C for sample A (b) B&C for sample*

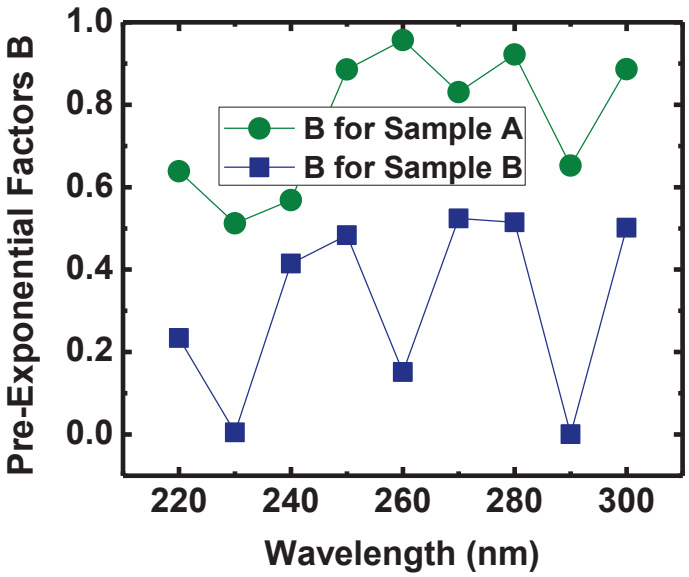

c

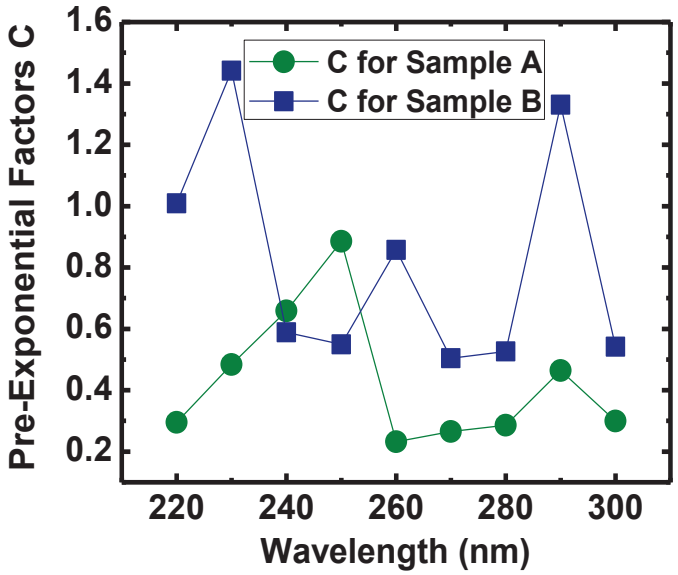

d

Figure 6.6-9: *Pre-exponential factors B (c) B for sample A&B and (d) C for sample A&B.*

Figure 6.6-10 (a) and (b) show the spectroscopic photo I-V data collected from samples A and B, respectively, under the illumination of the light between 320nm and 360nm which are below the bandgap of GaN but above the bandgap of AlGaN. Although for the clarity of the graphs we omitted every 50 points in the graphs as we did for the previous graph, the decay characteristics for different wavelengths were not as distinguishable as those in other graphs. Equation [6.6-4] , the sum of exponentials with up to two components, was also used to fit the experimental data of Figure 6.6-10 (a) and (b). After the dark current was subtracted, each decay curve was normalized to a unity at $t = 0$ which is the moment at which the light excitation is terminated. For the wavelength measurements of 320 and 360nm, two samples showed different decay characteristics. Li *et al*.[28] explains the mechanism of the above band excitation at 337 nm as follows;

i. PC increases in the GaN layer with the photoexcitation of the charge carriers (electrons and holes).

ii. Due to the electric field inside the interface depletion layer, photoexcited electrons and holes in the GaN layer are quickly separated and display a recombination of photoexcited charge carries, which causes the decay after illumination.

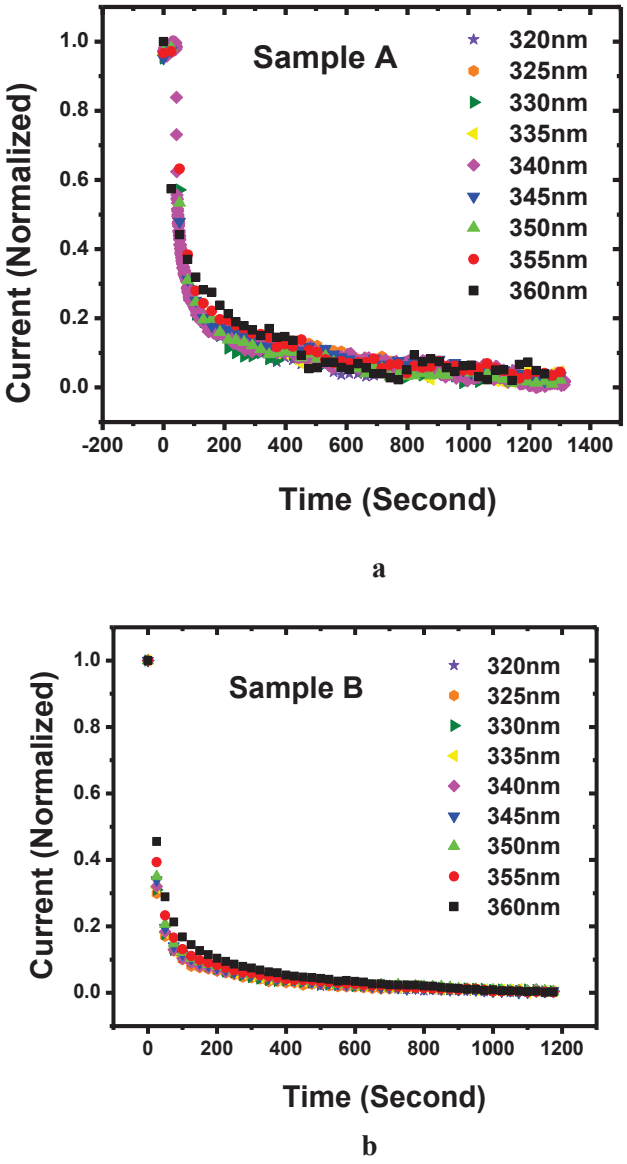

Figure 6.6-10: *Room temperature PPC decay kinetics of the $Al_{0.25}Ga_{0.75}N$/GaN/Si heterostructure as a function of excitation wavelength for samples A (a) and B (b).*

Figure 6.6-11 (a) and (b) show the decay time constants τ_1 and τ_2 as a function of wavelength. As in our previous results slow decay is followed by fast decay and such a behavior has been observed by other researchers.[17] τ_1 values for both of the samples are similar, except at 340 nm (3.64 eV) the values of τ_1 for sample B show a higher value. In contrast, τ_2 values of sample A show differences for each wavelength, as similar values of τ_2 for sample B were observed. This might indicate that slow decay of sample A and fast

decay of sample B are governed by light activated process. For sample B although the τ_1 and τ_2 values look almost equal there should be only one decay, yet our mathematical analysis showed that two decay components gave a better fit. Furthermore the actual values of τ_1 and τ_2 are quite different from each other. Therefore, we can conclude both samples A and B still have a fast decay followed by a slow decay.

In our measurements with illumination of light whose wavelength is changing between 220nm and 300nm, we had concluded that sample B has additional defects. The decay values of sample B are less wavelength dependent for the wavelengths of 320 and 360nm. This may imply that those additional defects referred to in the previous experiment might come from GaN layer since their effect was not observed for the wavelengths below the energy bandgap of GaN. To further investigate the source of the defects depth dependent photo current voltage experiments were conducted and explained below.

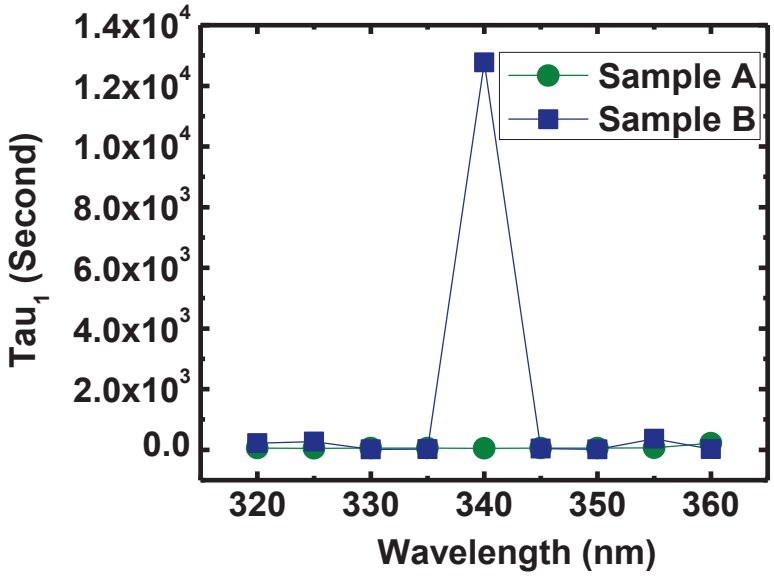

a

Figure 6.6-11: *Decay time constants for (a) exponential*

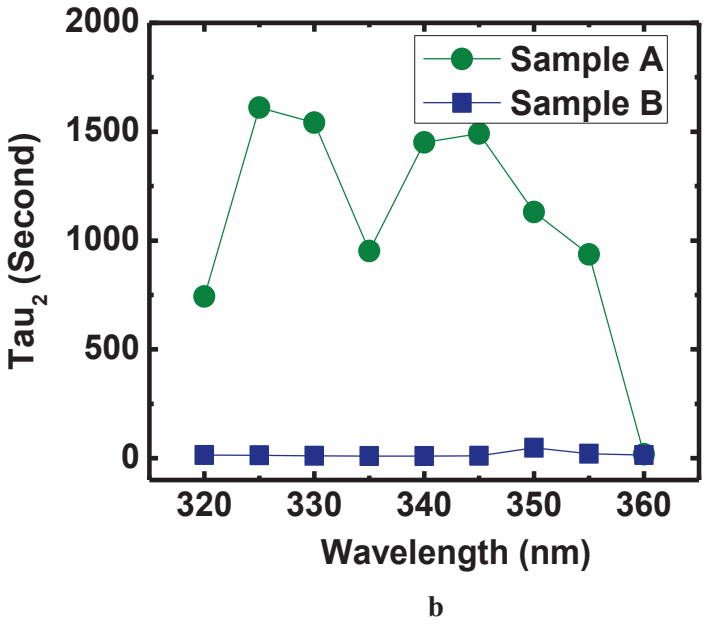

Figure 6.6-11: *Decay time constants for (b) stretched exponential functions.*

Figure 6.6-12 shows the fitted values of the stretching exponent α for samples A and B and the values plotted as a function of wavelength. It was stated before, that different α values might indicate that the origin of the decay processes are different. For sample A, most of the values of α are closer to the unity, except two wavelengths at 335nm and 360nm. The values of α being equal to one indicates that sample A might be also represented by the sum of two exponential functions instead of the sum of exponential and stretched exponential functions. These results are similar to the ones that we observed for wavelengths above the bandgap of AlGaN.

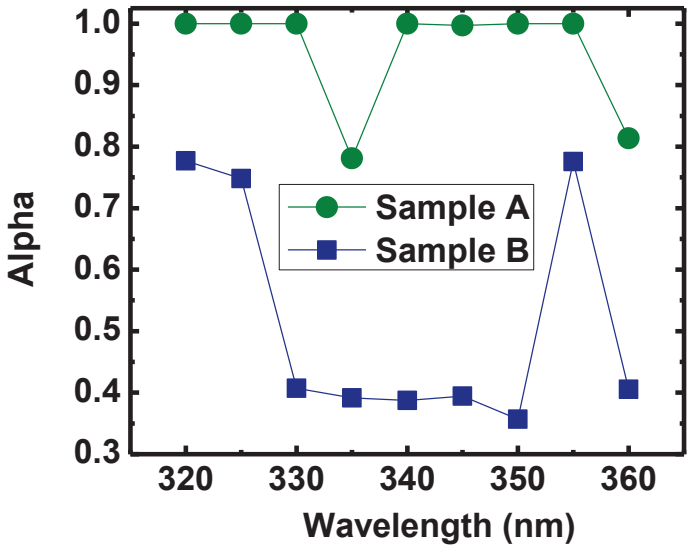

Figure 6.6-12: *Fitted values of the stretching exponent α for samples A and B and the values plotted as a function of wavelength.*

Figure 6.6-13 (a) and (b), respectively, displays the wavelength-dependent variation of *B* and *C* for samples A and B. While the stretch exponent is more dominant in sample B, the exponent function is more dominant is sample A. These results support the fact that α values are close to unity for sample A. In the Figure 6.6-13 (c) and (d), the effects of each exponential according to change in wavelength were plotted for each sample. While pre-exponential constants of stretched exponential function showed similar wavelength dependency for sample A, for sample B similar values were observed for the pre exponential function and the exponential function.

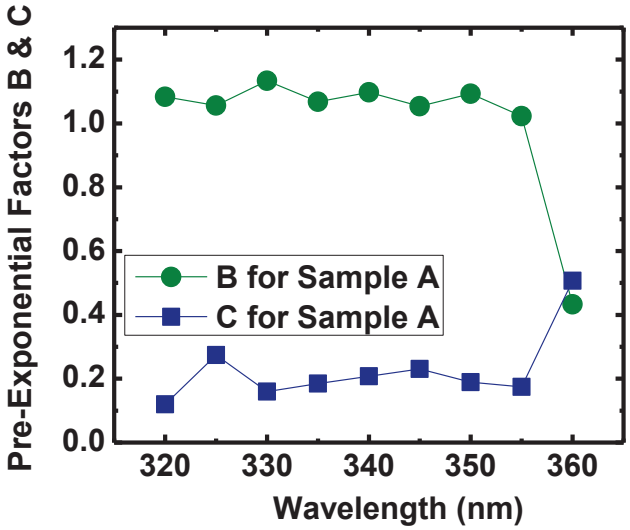

a

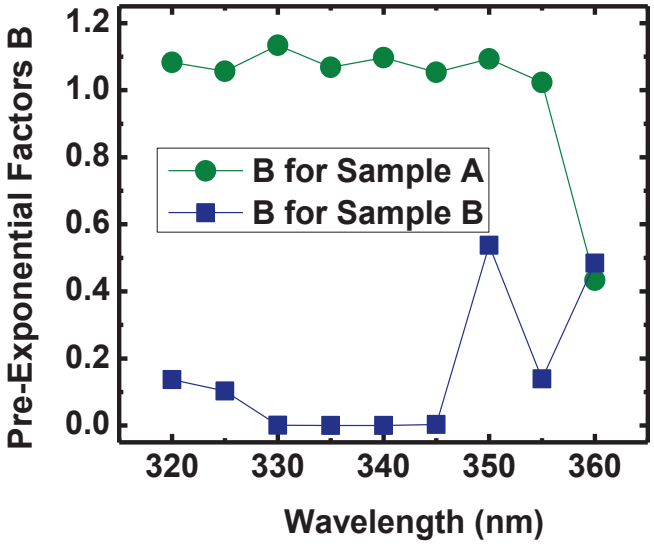

b

Figure 6.6-13: *Pre-exponential factors (a) B&C for sample A (b) B&C for sample B*

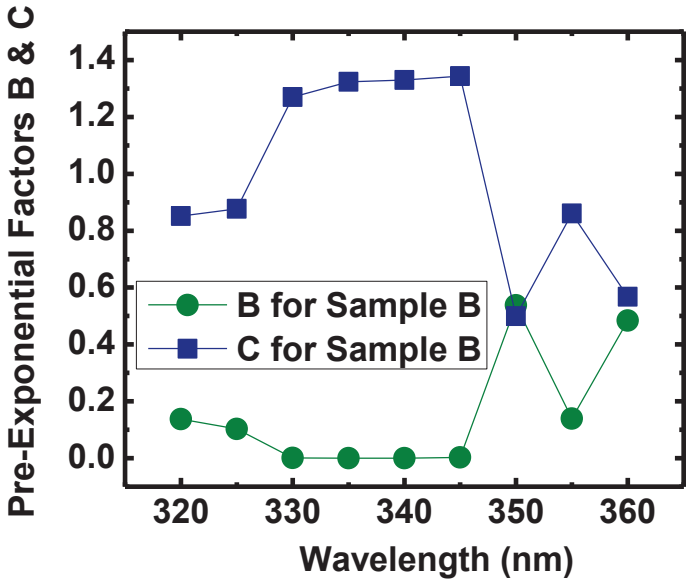

c

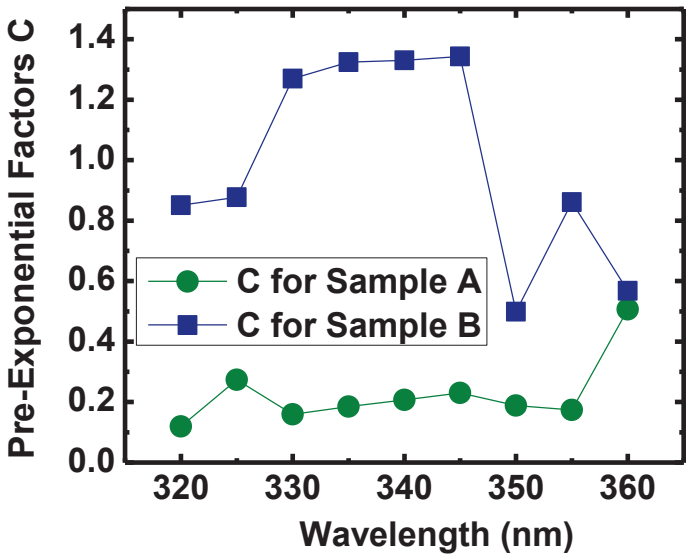

d

Figure 6.6-13: *Pre-exponential factors (c) B for samples A&B, and (d) C for samples A&B.*

In summary, time resolved spectroscopic photo current voltage measurements were conducted for both below and above bandgap wavelengths including the range from 220nm to 800nm. For each wavelength range, we observed differences between both samples and measurements. The results indicate that TRPC measurements are wavelength dependent. Based on the involvement of different trap centers decay characteristics can display differences from sample to sample. We conclude that the TRPC method can be used to distinguish two or more samples that have similar structures but different defect involvements with minimum sample preparation.

6.7 Effect of Solution on spectroscopic photo current-voltage measurements

AlGaN/GaN wide bandgap semiconductors are of interest due to their ability to ability for high temperature/frequency operation, high electron mobility as well as hardness and resistance to chemicals Moreover, AlGaN/GaN heterostructures even work in hostile and toxic environments since they have a high physical and chemical stability.[94] It is also known that because of the effect of the surface potential on its sheet carrier density AlGaN/GaN heterostructures are very promising candidates as sensors for ions, polar liquids and gases. Investigation of the surface and defects of the AlGaN/GaN heterostructures are important from the standpoint of semiconductor physics and design of semiconductor devices. Since both unsteady and uncontrollable surface/interface defects result in the unstable operation of semiconductor devices, it is important to investigate the properties of the surface and effect of the defects on device operation.

Many studies have been done to investigate the interaction of light with solid liquid systems.[95,96] The nature of the absorption mechanisms of photons by heterogeneous systems results in differences in such interactions. Photoexcitation of delocalized electronic states with the absorption of the light is associated with (i) luminescence and energy and/or electron transfer along the layer of adsorbed molecules, or to molecules in the liquid phase or to the bulk of the solid, (ii) photoconductivity, (iii) formation of defects by trapping of carriers, by intrinsic defects, and by impurities or by utilizing the type of electronic excitation

that displaces lattice ions to irregular positions, and (iv) by secondary chemical processes in which absorbed energy or charge transfer toward the surface.[97,98] Based on the initial and final electronic states involved in the light induced electronic transition, three cases can occur as (i) intradefect transition, in which both states are localized, (ii) band to band transition in which both states are delocalized, and (iii) defect level to band transition in which initial state is delocalized, but final state is localized.[97] Emeline *et al*. [97] give transfer of the electrons in the dopant transient metal ions in a sea of anionic ligand fields as an example of intradefect transitions. In our case, band to band transition is less likely to occur since excitation energy is less than the energy band of the top layer material. In the 3rd case, excitation of the electronic subsystem of the solids with the light which has energy in the range below the impact displacement energy threshold results in the generation of free electrons and free holes. Under steady-state conditions, a certain concentration gradient of carriers is generated in the semiconductor, and the concentration of the electron and hole at the surface of the crystal is altered.[99]

The effect of certain chemicals on photogeneration of defects for different semiconducting materials has been studied by many researchers. However, to the best of our knowledge, the effect of different chemicals on photogeneration in AlGaN/GaN HEMTs heterostructures has not been studied yet. Considering the increase in the areas and the applications that AlGaN/GaN HEMTs heterostructures were used, it is also important to investigate defects in these materials under different conditions. Therefore, in the present work we have studied the photogeneration of defects which occur under steady-state excitation of the AlGaN/GaN HEMTs heterostructures and their relationship with photochemical reactions that take place at solid/liquid interfaces in polar liquid. Studies on influence of polar liquids (acetone (CH_3COCH_3), methanol (CH_3OH), and deionized (DI) water) on the photo responsivity of solid/ liquid interfaces were undertaken to explore the correlation between the surface chemistry and the nature of preexisting or photogenerated defect centers. It is known that the chemical species were attracted by an electrostatic thin film on the surface of a semiconductor.[100] Also, attraction of these species results in the creation of surface defects that acquire the role of surface traps and are called chemisorbed particles.[99,101] In general, chemisorbed defects cannot be distinguished from the defects of historical origin other than being able to

escape from the surface to enter the has phase.[99] These surface charges either from adsorption or historical origins give rise to bending of the energy bands in the layer of the semiconductor near the surface and change the electrical conductivity of the surface.[99] In our experiment, we see that the manner in which chemisorption influences the conductivity depends on the nature of the absorbed particles (acceptor or donor particles).

Analyses were undertaken on the nature of the traps at the AlGaN/GaN HEMTs heterostructures both before and after the solution treatment. A comparison of the results reported in the literature was also presented. Our results show that different photocurrent spectra have resulted when different polar liquid were applied. However, it was shown that there is no correlation between the polarity and the concentration of polar liquid and the amplitude of the photocurrent output. It was concluded that the increase in the photocurrent imply that defect levels are also photocatalytically active.

6.7.1 Experiment

The AlGaN/GaN epi-structure used in this work was an AlGaN/GaN HEMTs structure grown on the p-type 6″ Si wafer *via* MOCVD. The structure consists of a 0.25 μm AlN nucleation layer, a multi-layered AlGaN buffer with Al concentrations ranging from 20% to 75%, a 1μm thick undoped GaN layer, 20nm thick AlGaN barrier layers, and an ultra-thin (2nm) GaN cap layer. The details of the fabrication steps were reported previously. An array of Schottky contacts composed of the DC magnetron sputtered Ni layers with the diameter of 600μm were used. A sample from the middle of 6″ Si wafer was chosen. The same experimental set up as in our previous experiments was used. The spectral response between 800 and 400nm wavelengths was provided along with the applied voltage between 0 and -20V. After the probes landed on the sample, the liquid was dropped on the device slowly. Figure 6.7-1 represents a schematic diagram of the heterostructure and liquids that were used in our experiments.

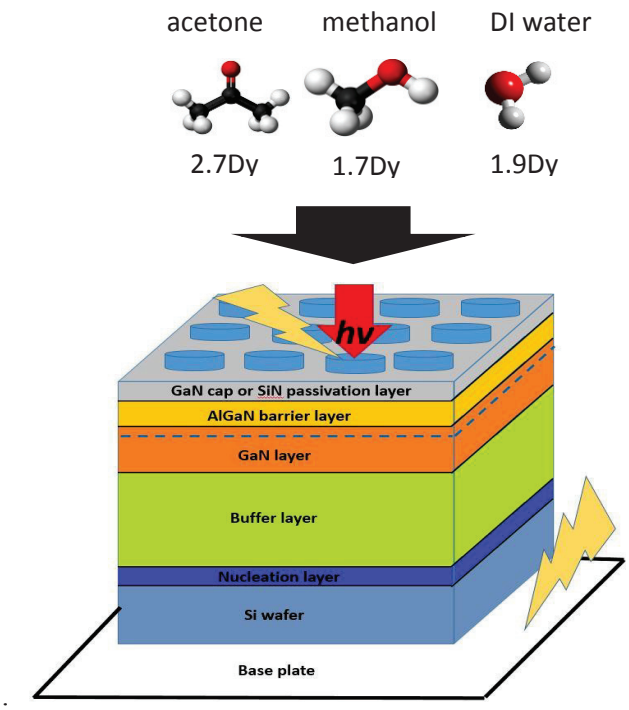

Figure 6.7-1: *AlGaN/GaN HEMT structure expose to different polar liquids under light illumination.*

6.7.2 Results and Discussion

Figure 6.7-2 illustrates the spectral responsivity of AlGaN/GaN HEMTs structure with Ni Schottky contacts under the illumination inside different chemical solutions, such as acetone (b), methanol (c), DI water (d), and in ambient air (a). Wavelength of the light was varied from 800nm to 400nm to perform the sub-bandgap photocurrent measurement. Initially, measurements were performed without using any chemicals at room temperature. Figure 6.7-2 shows changes in photo IV spectra from the HEMT structure as the different polar liquids are introduced to the surface. The spectroscopic photocurrent measurement was repeated with different chemical solutions by using the same experimental set up. We observed the highest current at 750nm, which is consistent with our previous measurements in an ambient air. After the sample was kept under dark conditions for 48 hours CH_3COCH_3 was poured and the second measurement was conducted. 700nm was recorded as the highest photocurrent measured inside the CH_3COCH_3. Observation of the highest photocurrent at a different energy level than its clean-air value, might be an

indication of the presence of new defect levels in the same quantity. One should take caution before deriving any conclusion since our previous measurements on the similar sample in similar air conditions showed the highest photocurrents at 750, 700, and 650 nm. Therefore, one might conclude that although they occupy different positions in the energy spectrum they may have the same nature as the original levels. Although the amplitude of photoresponse values in the CH_3COCH_3 and in the clean-air looks similar when we took a closer look at it, we observed slight increase in the values of responsivity in CH_3COCH_3. Other researchers observed a decrease in their dark current measured inside CH_3COCH_3 relative to the ones inside the clean air. [102,103] Therefore, this may indicate there might be an additional current increase due to a chemical reaction as a result of interaction of light with CH_3COCH_3.

Next, the sample was left to dry for 48 hours under dark condition and the third measurement inside the CH_3OH solution was taken. It was observed that the photo IV data collected with CH_3OH exhibits an entirely unique peak structure in comparison to the data collected from samples with other liquids. For this measurement, the highest photo current was observed at 400nm (3.4 eV), which was not observed in our previous spectroscopic photocurrent measurements. Similar results have been observed by other researchers. For instance, a Q-DLTS measurement was conducted on AlN Quantum Fingerprint sensors exposed to vapors from methanol and a trap was observed at approximately 3.2eV.[104] Finally, the sample was left to dry for 48 hours and the photo response of the samples with the DI water was collected. 700nm was also recorded as the highest photocurrent inside DI water as it was inside the acetone. As we mentioned above since it is an expectable wavelength for this sample there may not be additional contributions in terms of defects other than the increase in the photoresponsivity. The order of the solutions was chosen in the same order as we used in the cleaning procedure.

While in air and acetone, photo responsivity of the sample are similar in terms of their photocurrent intensities. The intensity of the photocurrent was 10 times higher in methanol and 20 times higher in DI water than the intensity values obtained in the ambient air and the acetone. Rothenberger *et al*.[104] related the amplitude of responses to the amount of alcohol vapor in the chamber. This may not be the case in our experiment since the same amount of liquid were used in each time. Furthermore, Hong *et al.*[105] suggested

that decrease in the emission intensities with higher oxygen pressure might result from the decrease of the oxygen vacancies. By using similar logic, one can conclude that the decrease in the intensity of the photo current might result from the increase in the defect concentrations. Among these polar liquids, acetone exhibits the highest dipole moment (2.7 Dy), followed by DI water (1.9 Dy) and finally methanol (1.7 Dy). We have not observed any correlation between the magnitude of the changes in photocurrent and the dipole moment of the liquids. Similar results have been observed by Pearton *et al.*[106] and they indicated that this may suggest steric hindrance effects or the exact orientation of the molecule when it adsorbs on the surface must play a role. There is still much to understand about the mechanism of the current changes in relation to the adsorption of the polar liquid molecules on the AlGaN/GaN surface. Unfortunately, at this point, we are not yet able to explain the change in the amplitude of the photocurrent signal quantitatively. Neuberger *et al.*[102] related the individual current levels to the differences in dipole moment and molecular structure. Mehandura *et al.*[103] stated van der Waals type interactions between the molecules result in surface changes which are induced by polarization in AlGaN/GaN heterostructures and result with changes in the induced electron density in the two dimensional electron gas that resides just below the AlGaN/GaN interface.

Furthermore, we realized that after vaporization of each individual liquid the dark current returns slowly to its initial clean-air value. Hence, we believe that this process might be reversible and the effects observed are due to the liquids. Volkenshtein[99] stated if there is an involvement of photoadsorption, the process is irreversible based on the data collected by other investigators. This may indicate that even if there is an additional amount adsorbed that appears on the surface with the nation of the light, it will leave the surface after removal of the light.

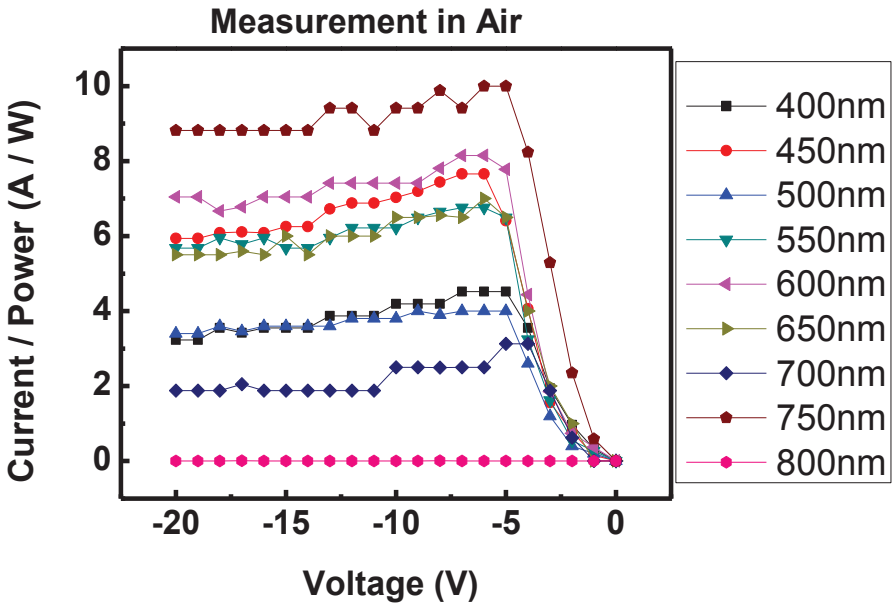

a

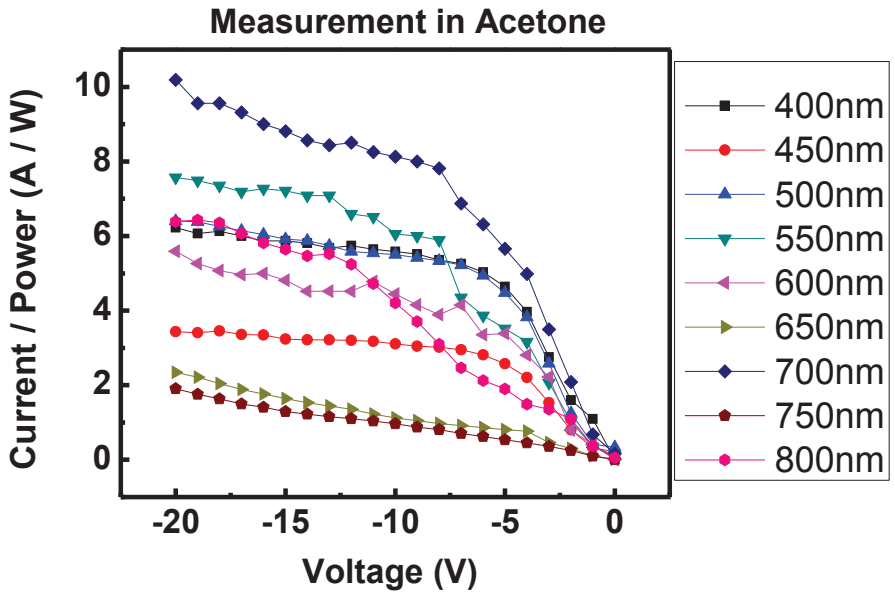

b

Figure 6.7-2: *Spectroscopic photocurrent measurements (a) in ambient air (b) in acetone*

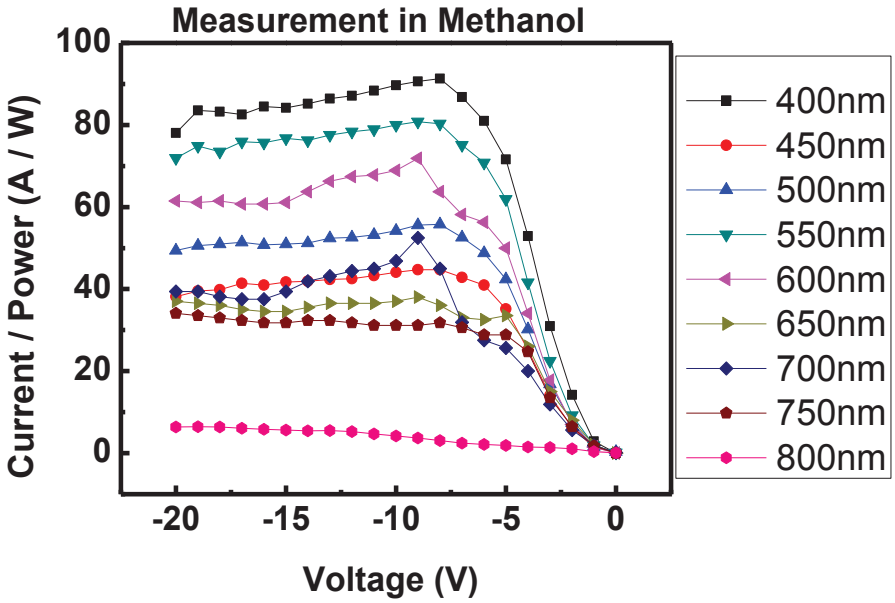

c

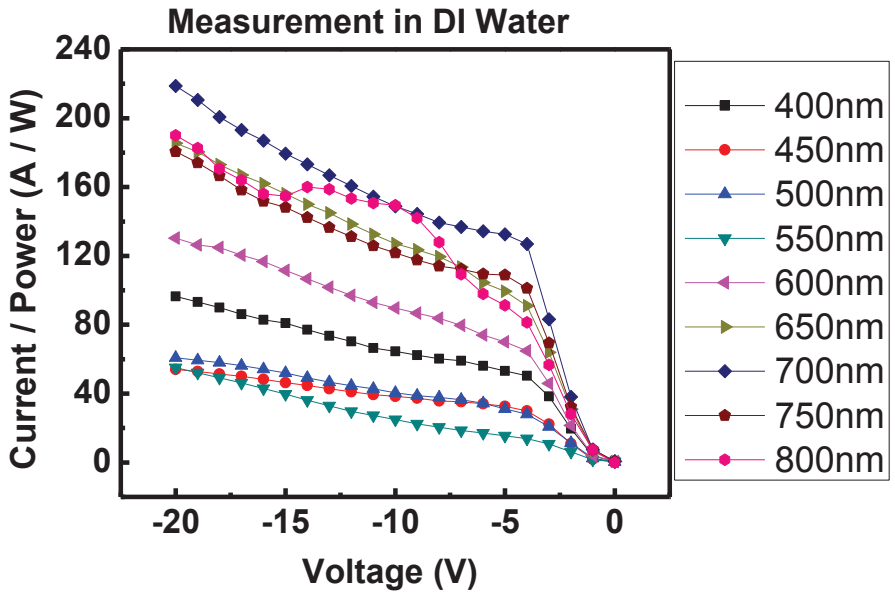

d

Figure 6.7-2: *Spectroscopic photocurrent measurements (c) methanol (d)DI water.*

In conclusion, photocurrent intensity was affected by the type of the solution in which the measurement taken. The samples which were exposed in DI water and acetone, had a similar peak structure that differs significantly from the one which was exposed in methanol. This effect may be the result of the different trap origins which were identified from the photocurrent characteristics of AlGaN/GaN heterostructures. It has been shown that there is no correlation between the polarity and the concentration of polar liquid and the amplitude of the photoresponse output. It was concluded that the increase in the photocurrent imply that defect levels are also photocatalytically active. The results might suggest the possibility of functionalizing the surface for application as biosensors regarding similar photoresponses of AlGaN/GaN HEMTs structure inside different polar liquids (i.e., acetone and DI water).

6.8 Temperature dependence spectroscopic photo current-voltage measurements

As stated before, studying wide bandgap materials for high power and high temperature applications is of great interest.[107] It is important to study the Schottky barrier height of the metal on the AlGaN/GaN structure for device designs since it controls the two-dimensional electron gas density at the AlGaN/GaN interface. Therefore, in this section, we have studied Schottky barrier height of Ni contact on AlGaN/GaN heterostucture.

The electrical characteristics of metal contacts to AlGaN/GaN have been examined by numerous research groups. The mechanism of leakage current through AlGaN/GaN Schottky interfaces is discussed using temperature dependent current voltage (I–V–T) measurements.[108] It was found that the barrier thinning caused by unintentional surface-defect donors enhances the tunneling transport processes, leading to the large leakage currents through GaN and AlGaN Schottky interfaces.[109] In the present study, Schottky contacts on AlGaN/GaN HEMTs heterostructures were formed, and the temperature dependent photo IV characteristics of the obtained Ni Schottky contacts were measured over the temperature range 25–125ºC with a temperature step of 25ºC.

6.8.1 Experiment

The AlGaN/GaN epi-structure used in this work was an AlGaN/GaN HEMTs structure grown on the p-type 6″ Si wafer *via* MOCVD. The structure consists of a 0.25 μm AlN nucleation layer, a multi-layered AlGaN buffer with Al concentrations ranging from 20% to 75%, a 1μm thick undoped GaN layer, 20nm thick AlGaN barrier layers, and an ultra-thin (2nm) GaN cap layer. The details of the fabrication steps were reported previously. An array of Schottky contacts composed of the DC magnetron sputtered Ni layers with the diameter of 600μm were used. A sample from the middle of the HEMT on 6″ Si wafer was chosen for this investigation. The same experimental set up as in our previous experiments was used. The spectral response between 800 and 400nm wavelengths was provided along with the applied voltage between 0 and -20V. A homemade heater plate was used to heat the samples. The temperature of the heater plate was changed from 25ºC to 125ºC by using a Powerstat type 116 variable autotransformer variac. In this section, dark current photoresponse properties are discussed with regard to the carriers transport mechanisms across the AlGaN/GaN HEMTs heterostuctures at various temperatures. The sub bandgap photo IV was measured under light illumination in which $hv<Eg$ of GaN at different temperatures between 25ºC and 125ºC.

6.8.2 Results and Discussion

The temperature dependent dark I-V characteristics were obtained to elucidate the current transport mechanism and are displayed in the Figure 6.8-1. The dark current in reverse bias regime relatively independent of bias voltage change for the samples measured below 100ºC. On the other hand, there was a sharp increase in the reverse current with increasing negative bias for the sample measured at 100ºC and 125ºC. Overall, dark current in the reverse bias regime increases with increasing temperature from RT to 125ºC. Since the diameter of the Schottky contacts are large enough, it is appropriate to use one-dimensional current transport theory.[110] Furthermore, Wang *et al*.[110] previously determined that the characteristic energy

level, E_{00} is smaller than kT (~25meV at RT) for similarly structured circular Shottky diodes. Hence, the forward I-V of the vertical Schottky contacts in the dark at different temperatures was analyzed by the thermionic emission (TE) theory which is given by;[111]

$$I_{TE} = I_S\{\exp\left(\left[\frac{q(V - IR_S)}{nkT}\right] - 1\right)\} \qquad [\ 6.8\text{-}1\ ]$$

where n is ideality factor, and I_s is the saturation current with the following expression;[111]

$$I_S = AA^*T^2\exp(-\frac{q\emptyset_{Bn}}{kT}) \qquad [\ 6.8\text{-}2\ ]$$

where A is the contact area, A^* is the effective Richardson's constant, and ϕ_{Bn} is the Schottky barrier height (SBH).

The experimental values of barrier height and ideality factor were obtained from the intercepts and slopes of the *ln(I)* vs. *V* plot obtained in forward bias regime at each temperature. The barrier heights were determined using the theoretical value of the Richardson constant which is 26.4 $Acm^{-2}K^{-2}$ for GaN.[112] The observed temperature dependence of SBH between 0.45eV and 0.48eV is shown in the inset of Figure 6.8-1. Dogan *et al*.[108] explained the decrease in the SBH with the decrease in the temperature by the discrepancies of lateral distribution of barrier height. This observed phenomenon in real Schottky diodes generally is attributed to the Schottky barrier height inhomogeneity.[113] The ideality factor of the Schottky contact was unreasonably high for both reverse and positive voltages and the Schottky barrier height was around 0.475 eV at RT. Theoretically, a linear temperature dependence of SBH was expected, and yet we did not observe that. Therefore, it is hard at this time to make quantitative comparisons between the results presented here and values reported in the literature. In general, SBH values obtained in this experiment were smaller than the values obtained by other researches.[114,115]

In addition, the Arrhenius plot was used to further study the current transport characteristics. Barrier height can also be obtained by rearranging the equation [6.8-2], as follows;[111]

$$\ln\left(\frac{I_0}{T^2}\right) = \ln(A^*) - \frac{q\phi_{Bn}}{kT} \qquad [\ 6.8\text{-}3\ ]$$

Figure 6.8-1 (b) shows the plot of $ln(I_0/T_2)$ versus $1000/T$ from which activation energy can be deduced. In theory, $ln(I_0/T_2)$ is expected to be inversely proportional to $1000/T$. However, experimental results showed linear proportionality. SBH and A^* can be determined from the slope and intercept of the $ln(I_0/T_2)$ versus $1000/T$ plot, respectively. The value of A^* at RT was 14.23 $Acm^{-2}K^{-2}$ and was in good agreement with the value of 11.2 $Acm^{-2}K^{-2}$ which were obtained by Schmitz *et al*.[116] On the other hand, we should note that the measured value was lower than the theoretically calculated value of 26.4 $Acm^{-2}K^{-2}$. Some researchers explained the variations between the obtained and the theoretical value of the Richardson constant *via* the temperature dependence of the barrier height due to the presence of surface inhomogeneities in the GaN semiconductor layer.[117] Others related the low values of A^* to either electron tunneling through the interfacial barrier or a decrease of effective contact area.[112] SHB was calculated to be 0.99eV at RT, which is in good agreement with the values obtained by other researchers.[116] The inset of the Figure 6.8-1 (b) shows the temperature dependence of the ideality factor for both forward and reverse bias characteristics calculated using the following expression;

$$\gamma n = \frac{q}{kT(\frac{dV}{dlnI})} \qquad [\ 6.8\text{-}4\ ]$$

For the reverse bias, the ideality factor decreased with increasing temperature. On the other hand, in the case of forward bias it increased with increasing temperature. Such temperature dependency has been observed by other researchers and it is believed that it may be resulted from the presence of surface inhomogeneities in the GaN semiconductor layer.[118] The abnormal values of the ideality factor were obtained. This result could be a consequence of the collection of insufficient data with higher voltage steps.

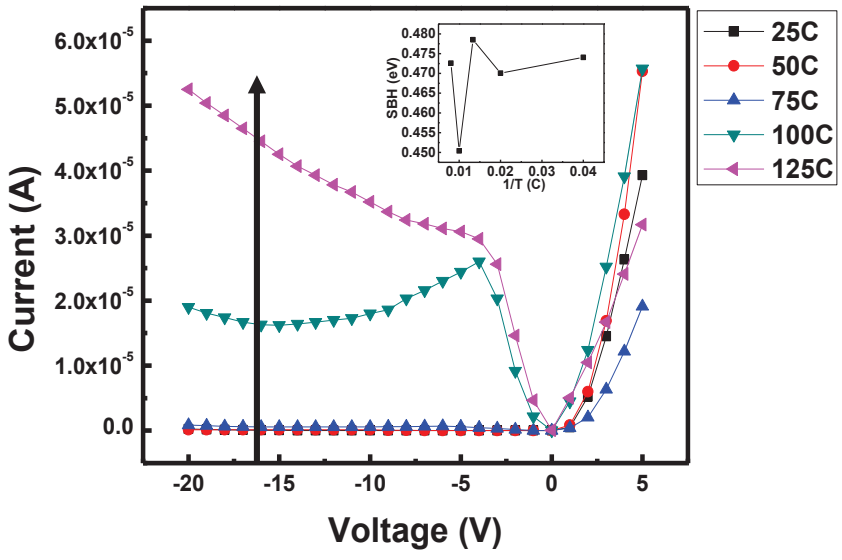

a

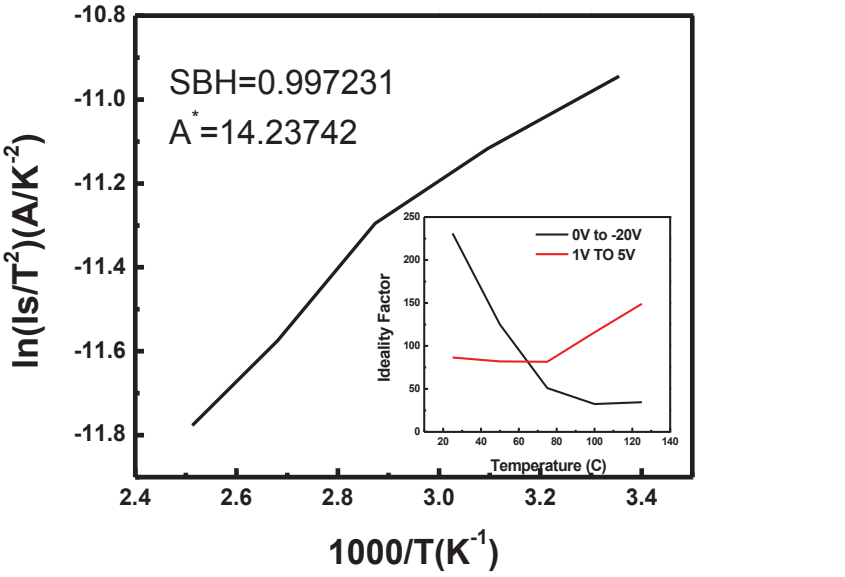

b

Figure 6.8-1: (a) *Dark I-V characteristic of device B as the temperature was elevated from RT to 125°C The inset shows the temperature dependence of the apparent barrier height for the Schottky contact. (b) The conventional activation energy ln(I_S/T^2) versus 1000/T plot with inset of ideality factor for negative (black) and positive (red)biases.*

Temperature dependent photo current (PC) spectra that were measured at various voltages are shown in the Figure 6.8-2. Initially, we measured the sub-bandgap photo IV of the sample at room temperature without turning the heat on. We observed the highest photo current at 700nm. After that, the sample was heated up to RT (RT=25ºC). We still observed the highest photo current at 700nm, and responsivity of the sample was lowered to one third of the initial measurement. A relatively linear behavior with increasing temperature was observed at various voltages. This linear dependence on the voltage is attributed to the competition between the drift and diffusion of photogenerated free charges to the electrode.[119] Temperature was further increased to 50ºC and the highest current was observed at 800nm. For the next two measurements up to 125ºC, the corresponding wavelength for the highest observed photo current remained at 800nm, even though the responsivity of the sample increased significantly. At 125ºC, 650nm was recorded as the wavelength where the highest current was detected. In our previous sub bandgap measurements, the wavelength of the highest photocurrent were related to the energy level of the defects. Consequently, additional defects were observed in the phototocurrent measurements due to the temperature increase which thermally activates the localized carriers to overcome the potential barrier increases.[120]

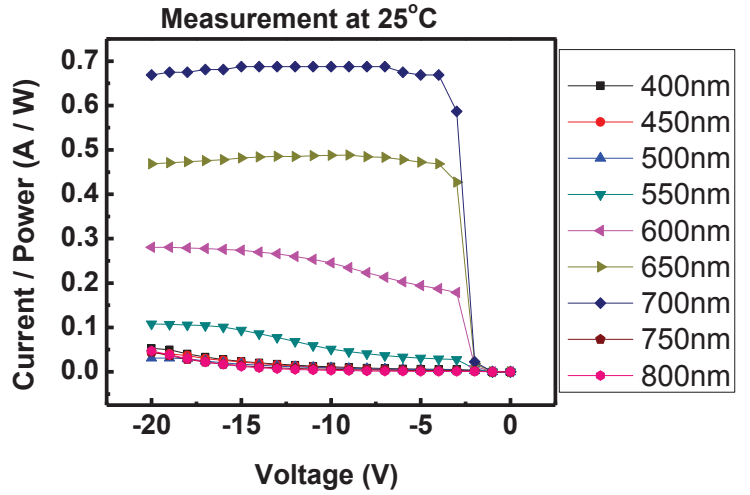

a

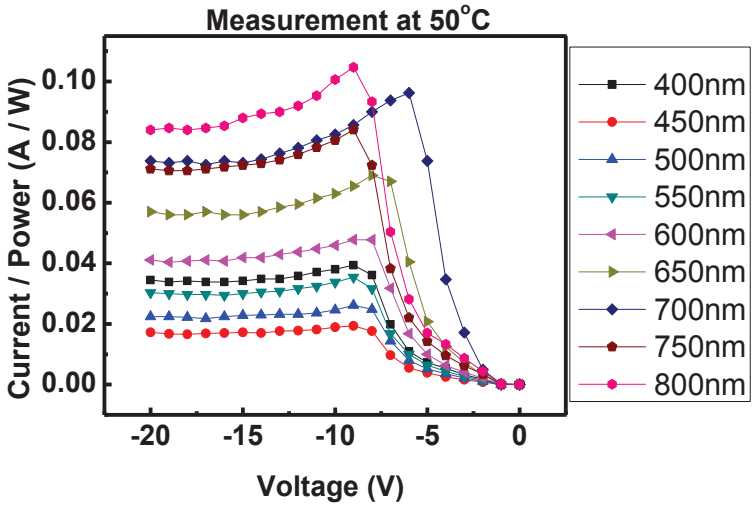

b

Figure 6.8-2: *Spectroscopic photocurrent measurements a) at room temperature (RT) 25ºC (b)50ºC*

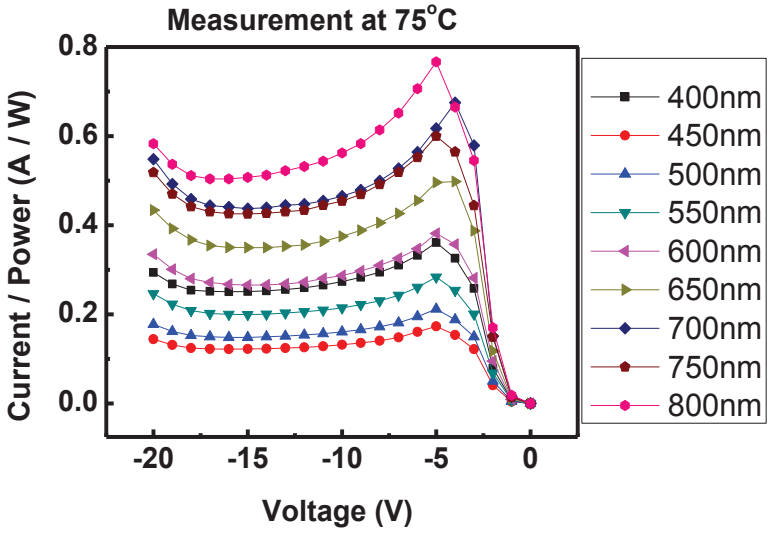

c

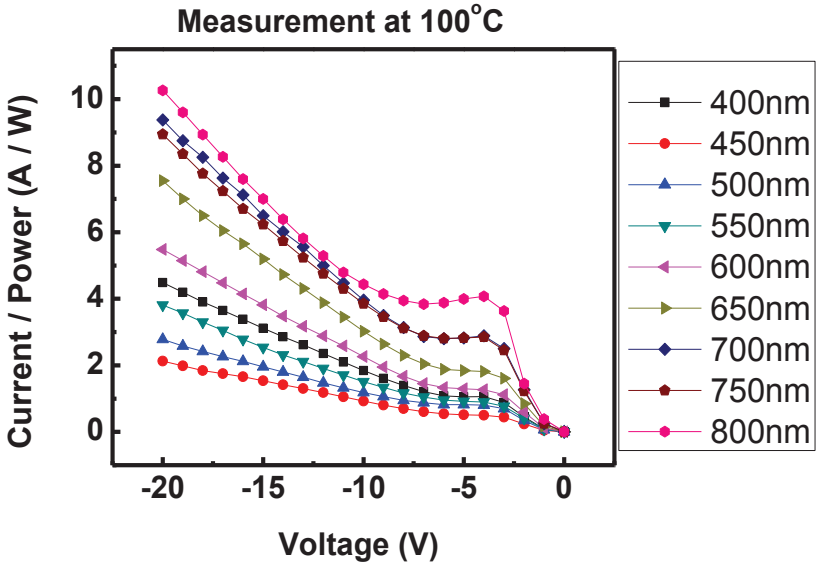

d

Figure 6.8-2: *Spectroscopic photocurrent measurements (c) 75°C (d) 100°C*

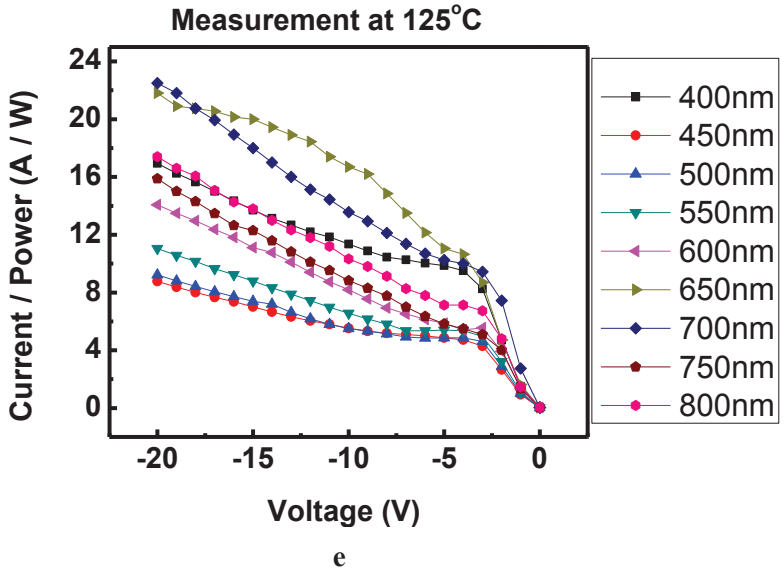

Figure 6.8-2: *Spectroscopic photocurrent measurements (e)125ºC.*

Moreover, at this temperature (125ºC), responsivity of the sample increased almost 25%. Since more carriers start to occupy the extended states of the upper part of the bandgap with the increasing temperature, an increase in carrier density with temperature is expected. Therefore, an increase in responsivity with temperature is also anticipated. To explain this behavior, we used a model developed by Miczek *et al*.[121] In this approach, they suggest that at the zero bias E_F at the AlGaN/GaN interface (E_{F0}) is below the step in the $\eta_e(E)$ curve and the interface charge might be frozen. This state is known as occupied state in which both acceptors and donors cannot emit electrons since they are below E_{F0}, even in the cases where E_F is lowered *via* the application of negative bias. At higher temperatures, applying the negative bias causes the emission of electrons from the deeper acceptor states. The effect is demonstrated schematically in the Figure 6.8-3.

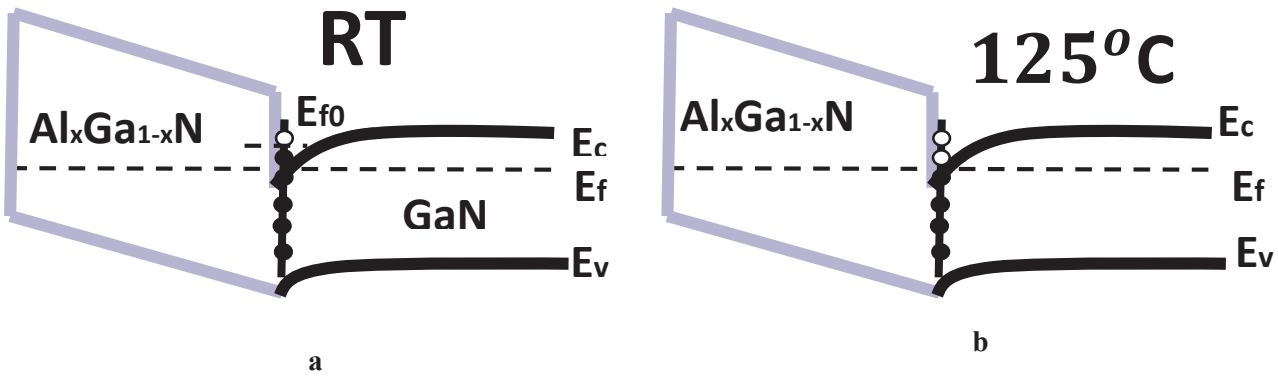

Figure 6.8-3: *(a)Schematıc vıew of the AlGaN/GaN interface at RT for a gate bias slightly below zero and without electron emission from the interface states beneath the zero gate bias Fermi level (E_{F0}). The filled circles represent occupied states, and the empty circle the unoccupied state (b) A similar view at 125 °C. The arrows indicate the electron emission from the interface states to the GaN conduction band.*

The temperature dependent PC spectra measured at zero bias and -20V bias are shown in the Figure 6.8-4 (a) and (b), respectively. According to these figures temperature dependence below 100ºC is relatively compared to temperatures higher and equal to 100ºC. Figure 6.8-4 also confirms that, the PC signals increase abruptly with the increase of temperature. As defined previously, the strength of the PC is determined by the charge carriers which have escaped from the traps inside the material at a certain sub bandgap energy level. In the case of the escape of the carriers, acceleration of the carriers occurs by the built-in electric field and it results in collection of the carriers by the top and bottom electrodes, which manifest in increase in PC signals. As a result, competition between the recombination rate and escape rate from certain energy levels determines the collected PC strength.[122]

The escape of carriers from the traps can consist of two processes: (i) light absorption provides enough energy to carriers to escape from traps (field emission FE) (ii) thermionic emission helps carriers to escape from the trap level to the conduction band. Consequently, the total escape rate may be given by $1/\tau_{esc} = 1/\tau_{il} + 1/\tau_{th}$, where τ_{il} and τ_{th} are illumination stimulated and thermionic emission lifetimes. At high temperatures competition between the escape and recombination rates increases when the carriers start to be activated. Accordingly, the collected PC signals become more intense. Similar effects have been observed by other researchers.[122]

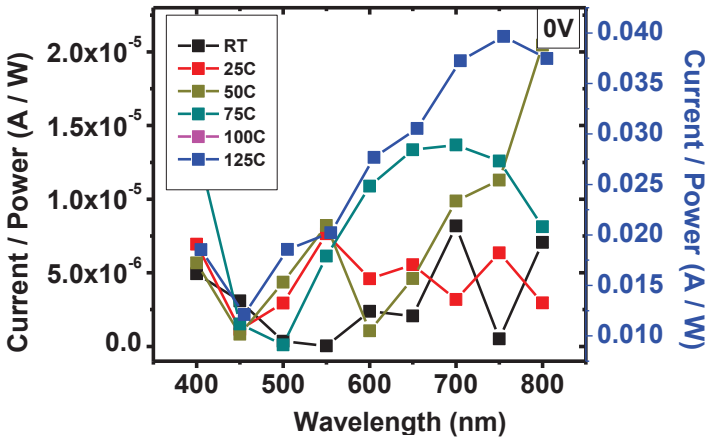

a

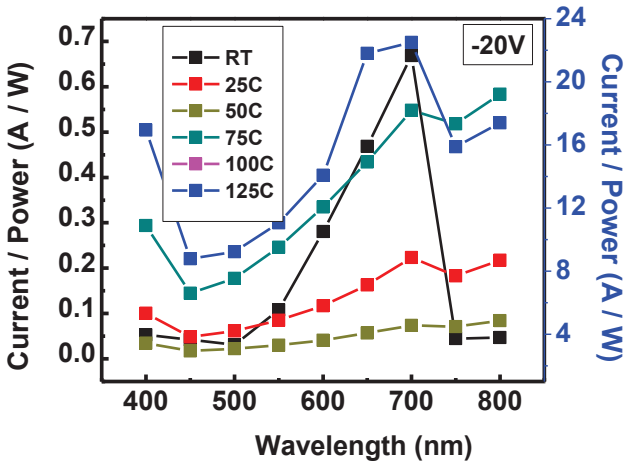

Figure 6.8-4: *Photocurrent spectra at 0V (a) and -20 V (b) as the temperature increasing from RT to 125ºC.*

In the Figure 6.8-5 (a), PC collected as a function of voltage at various temperatures with 700 nm light illumination is reported. The responsivity increases from 0.2 to 0.5 A/W as the temperature increases from RT to 75ºC and reaches 23A/W at 125ºC. For different temperatures, some common characteristics can be noted. At smaller voltages, a sharp increase in PC was observed whereas PC increases more slowly at higher voltages. Again, this graph confirms the increase of PC with the increase of temperature. For voltages up to -3V, it was fitted with TE. For voltages higher than -3V, thermionic field emission (TFE) was used to fit the graphs.[123]

The TFE current density is given by[124]

$$J_{TFE} = J_S \exp\left(\frac{V}{E_0}\right)[1 - \exp\left(-\frac{qV}{kT}\right)] \qquad [\ 6.8\text{-}5\ ]$$

$$E_0 = E_{00}\coth(\frac{E_{00}}{kT}) \qquad [\ 6.8\text{-}6\ ]$$

$$E_{00} = \frac{qh}{4\pi}\sqrt{\frac{N_t}{m^*\varepsilon_s}} \qquad [\ 6.8\text{-}7\ ]$$

where ε_s is the dielectric constant, m^* is the electron effective mass, and h is the Plank constant. E_{00} reflects the tunneling probability. Unfortunately our attempts to fit this data with TFE model were not successful. We also plotted responsivity versus voltage for various temperatures under constant light illumination at 700nm in the Figure 6.8-5 (b). It should be noted that the photoresponsivity still shows a thermal stability as the temperature increases from RT to 75ºC. An increase in the responsivity was observed as the temperature further increases to 125ºC (25 A/W at −20 V). Similar effects have been observed by other researchers.[122]

\

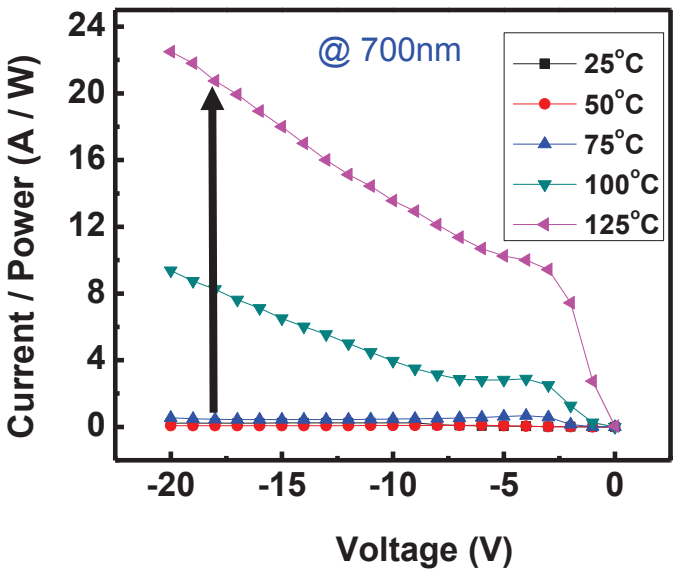

a

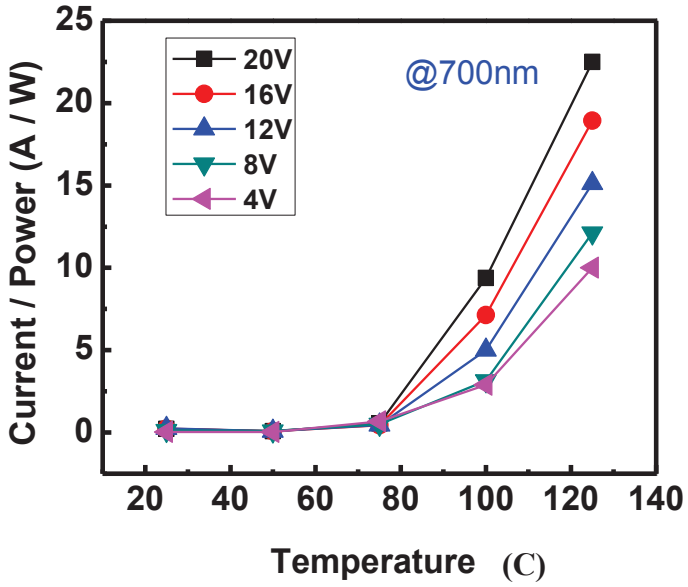

b

Figure 6.8-5: *(a) Photocurrent as a function of voltage at 700nm with variable temperatures (b) Photocurrent as a function of temperature at 700nm with variable biases.*

Sang *et al.*[123] defined the ratio of the net photocurrent to dark current as the photo to dark current ratio (PDCR). PDCR variation as the measurement temperature at 0V and -20 V was displayed in the Figure 6.8-6. The obtained PDCR values were as high as 5.5 for -20V and 4.5 for 0V when the sample was illuminated at 700nm. We observed that PDCR values decrease from 2.2 at RT to 0.4 at 125ºC under -20V. Although the values of PDCR changes between RT and 125ºC, they stayed almost similar at these specific temperatures. The variations of the PDCR value with temperature for different devices were also observed by other researchers.[125]

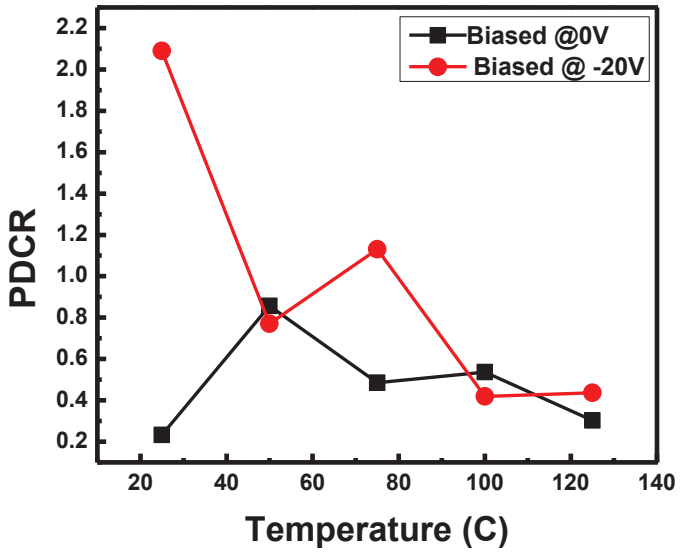

Figure 6.8-6: *The PDCR variation as the measurement temperature at 0V and -20 V.*

In summary, the temperature dependent photo current voltage characteristics of AlGaN/GaN HEMTs heterostuctures with Schottky contact were analyzed. The anomalous temperature dependence of SBH, ideality factor and Richardson constant calculated from the I-V-T characteristics based on TE. The barrier height increased and the ideality factor decreased with increasing temperature. Such a temperature dependence of the barrier height was attributed to the presence of barrier-height inhomogeneities at the Ni/GaN interface. TFE and TE tunneling mechanisms were used to interpret the photocurrent gain at reverse bias from RT to 125ºC. For voltages lower than -10V, we observed a better fit with TE. Nonetheless, our

fits for higher voltage values for TFE were unsuccessful. Increase in the photocurrent is related to the presence of the traps.

References

[1] S. Bradley, A. Young, L. Brillson, M. Murphy, W. Schaff, and L. Eastman, "Influence of AlGaN deep level defects on AlGaN/GaN 2DEG carrier confinement", IEEE Trans. Electron Devices. **48**, 412, (2001).

[2] P. Klein, S. Binari, J. Freitas, and A. Wickenden, "Photoionization spectroscopy of traps in GaN metal-semiconductor field-effect transistors", J. Appl. Phys. **88**, 2843 (2000).

[3] G. Koley, V. Tilak, L. Eastman, and M. Spencer, "Slow transients observed in AlGaN/GaN HFETs: effects of SiNx passivation and UV illumination", IEEE Trans. Electron Devices, **50**, 886 (2003).

[4] B. H. Leung, N. H. Chan, W. K. Fong, C. F. Zhu, S. Ng, H. F. Lui, K. Tong, C. Surya, L. Lu, and W. Ge, IEEE Trans. Electron Devices, **64**, 887 (1994).

[5] S. D. Meyer, C. Charbonniaud, R. Quere, M. Campovecchio, R. Lossy, and J. Wurfl, "Mechanism of power density degradation due to trapping effects in AlGaN/GaN HEMTs", IEEE International Microwave Symposium Digest, (2003).

[6] P. Klein, S. Binari, K. Ikosso-Anastasiou, A. Wickenden, D. Koleske, R. Henry, and D. Katzer, "Effect of deep traps on sheet charge in AlGaN/GaN high electron mobility transistors", Electron. Lett. **37**, 661(2001).

[7] G. Meneghesso, A. Chini, E. Zanoni, M. Manfredi, M. Pavesi, B. Boudart, and C. Gaquiere, "Diagnosis of trapping phenomena in GaN MESFETs", IEDM Technical Degist, San Fransisco, (2000).

[8] W. Smith, "Effect of light on selenium during the passage of an electric current", Nature **7**, 303 (1873).

[9] R. W. Pohl, "Electron conductivity and photochemical processes in alkali-halide crystals", Proc. Phys. Soc. **49**, 3 (1937).

[10] A. Patane and N. Balkan, "Semiconductor research", Springer-Verlag Berlin Heidelberg (2012).

[11] T. S. Moss, "Photoconductivity, Reports on Progress in Physics" (1965).

[12] D. M. Kim, S. H. Song, H. J. Kim, and K. N. Kang, "Electrical characteristics of an optically controlled n-channel AlGaAs/GaAs/InGaAs Pseudomorphic HEMT", IEEE Electron Device Lett. **20**, (1999).

[13] Y. Takanashi, K. Takahata, and Y. Muramoto, "Characteristics of InAlAs/InGaAs high-electron-mobility transistors under illumination with modulated light", IEEE Transaction on Electron Devices, **46**, (1999).

[14] C. S. Chang, H. R. Fetterman, D. Ni, E. Sovero, B. Mathur, and W. J. Ho, "Negative photoconductivity in high electron mobility transistors", Appl. Phys. Lett. **51**, 2233 (1987).

[15] A. Polyakov, "Properties of Si and persistent photoconductivity in AlGaN", Solid States Electronics, **42**, (1998).

[16] A.V. Buyanov, J. P. Bergman, J. A. Sandberg, B. E. Sernelius, P. O. Holtz, J. Dalfors, B. Monemar, H. Amano, and I. Akasaki, "Photoconductivity in n-type modulation-doped GaN/AlGaN heterostructures", J. Cryst. Growth, **189/190**, 753 (1998).

[17] C. Johnson, J. Y. Lin, H. X. Jiang, M. Asif Khan, and C. J. Sun, "Metastability and persistent photoconductivity in Mg-doped p-type GaN", Appl. Phys. Lett. **68**, 1808 (1996).

[18] B. K. Li, W. K. Ge, J. N. Wang, and K. J. Chen, "Persistent photoconductivity and carrier transport in AlGaN/GaN heterostructures treated by fluorine plasma", Appl. Phys. Lett. **92**, 082105 (2008).

[19] D. V. Lang and R. A. Logan, "Large-lattice-relaxation model for persistent photoconductivity in compound semiconductors", Phys. Rev. Lett. **39**, 635 (1977).

[20] G. Beadie, W. S. Rabinovich, A. E. Wickenden, D. D. Koleske, S. C. Binari, and J. A. Feritas Jr., "Persistent photoconductivity in n-type GaN", Appl. Phys. Lett. **71**, 1092 (1997).

[21] J. Z. Li, J. Y. Lin, H. X. Jiang, A. Salvador, and A. Botchkarev, and H. Morkoç, "Nature of Mg impurities in GaN", Appl. Phys. **69**, 1474 (1996).

[22] C. V. Reddy, K. Balakrishnan, H. Okumura, and S. Yoshida, "The origin of persistent photoconductivity and its relationship with yellow luminescence in molecular beam epitaxy grown undoped GaN", Appl. Phys. Lett. **73**, 244 (1998).

[23] W. Rieger, R. Dimitrov, D. Brunner, E. Rohrer, O. Ambacher, and M. Stuzmann, "Defect-related optical transitions in GaN", Phys. Rev. B **54**, 17596 (1996).

[24] T. Y. Lin, H. M. Chen, M. S. Tsai, Y. F. Chen, F. F. Fang, C. F. Lin, and G. C. Chi, "Two-dimensional electron gas and persistent photoconductivity in $Al_xGa_{1-x}N$/GaN heterostructures", Phys. Rev. B **58**, 13793 (1998).

[25] A. J. Ptak, V. A. Stoica, L. J. Holbert, M. Moldovan, and T. H. Myers, "An investigation of long and short time-constant persistent photoconductivity in undoped GaN grown by RF-plasma assisted molecular beam epitaxy", MRS Internet J. Nitride Semicond. Res. **5S1**, W11.445, 629 (2000).

[26] S. Cai, G. Parish, J. M. Dell, and B. D. Nener, "Contribution of hole trap to persistent photoconductivity in n-type GaN", J. Appl. Phys. **96**, 1019 (2004).

[27] Y. Han, X. Zheng, M. Fu, D. Pan, X. Li, Y. Guo, J. Zhao, and Q. Chen, "Negative photoconductivity of InAs nanowires", Phys. Chem. Chem. Phys. **18**, 818 (2016).

[28] J. Z. Li, J. Y. Lin, and H. X. Jian, and M. A. Khan, "Effects of persistent photoconductivity on the characteristic performance of an AlGaN/GaN heterostructure ultraviolet detector", Appl. Phys. Lett. **72**, 2868 (1998).

[29] J. Y. Lin, A. Dissanayake, G. Brown, and H. X. Jiang, "Relaxation of persistent photoconductivity in $Al_{0.3}Ga_{0.7}As$", Phys. Rev. B **42**, 5855 (1990).

[30] H. X. Jiang and J. Y. Lin, "Percolation transition of persistent photoconductivity in II-VI mixed crystals" Phys. Rev. Lett. **64**, 2547 (1990)

[31] E. Arslan, S. Bütün, S. B. Lisesivdin, M. Kasap, S. Ozcelik, and E. Ozbay, "The persistent photoconductivity effect in AlGaN/GaN heterostructures grown on sapphire and SiC substrates", J.Appl. Phys. **103**, 103701 (2008).

[32] A. Y. Polyakov, N. B. Smirnov, A. V. Govorkov, M. G. Mil'vidskii, J. M. Redwing, M. Shin, M. Skowronski, D. W. Greve, and R. G. Wilson, "Properties of Si donors and persistent photoconductivity in AlGaN", Solid-State Electron. **42**, 627 (1998).

[33] C. G. Van de Walle, "DX-center formation in wurtzite and zinc-blende $Al_xGa_{1-x}N$", Phys. Rev. B **57**, R2033 (1998)

[34] A. Dissanayake, M. Elahi, H. X. Jiang, and J. Y. Lin, "Kinetics of persistent photoconductivity in $Al_{0.3}Ga_{0.7}As$ and $Zn_{0.3}Cd_{0.7}Se$ semiconductor alloys", Phys. Rev. B, **45**, 13996 (1992).

[35] B. Ozden C. Yang, F. Tong, M. P. Khanal, V. Mirkhani, M. Hassan Sk, A. Claude Ahyi, and M. Park "Depth-resolved ultra-violet spectroscopic photo current-voltage measurements for the analysis of AlGaN/GaN high electron mobility transistor epilayer deposited on Si", Appl. Phys. Lett. **105**, 172105 (2014).

[36] U. Becker, D. A. Shirley, "Physics of Atoms and Molecules: VUV and Soft X-ray Photoionization", Plenum Press, New York and London (1996).

[37] L. Marton, "Method of Experimental Physics Volume 9-Part A Plasma Physics", Academic Press Inc., New York (1970).

[38] V. S. Letokhov, "Laser photoionization spectroscopy", Academic Press Inc. (1987).

[39] P. B. Klein, J. A. Freitas Jr., S. C. Binari, and A. E. Wickenden, "Observation of deep traps responsible for current collapse in GaN metal–semiconductor field-effect transistors", Appl. Phys. Lett. **75**, 4016 (1999).

[40] P. B. Klein "Photoionization spectroscopy in AlGaN/GaN high electron mobility transistors", J. Appl. Phys. **92**, 5498 (2002).

[41] P. B. Klein and S. C. Binari, "Photoionization spectroscopy of deep defects responsible for current collapse in nitride-based field effect transistors", J. Phys.: Condens. Matter **15** R1641 (2003).

[42] P. B. Klein, S. C. Binari, K. Ikossi, A. E. Wickenden, D. D. Koleske, and R. L. Henry, "Current collapse and the role of carbon in AlGaN/GaN high electron mobility transistors grown by metalorganic vapor-phase epitaxy", Appl. Phys. Lett. **79**, 3527 (2001).

[43] P. B. Klein, S. C. Binari, K. Ikossi-Anastasiou, A. E. Wickenden, D. D. Koleske, R. L. Henry, and D. S. Katzer, "Investigation of traps producing current collapse in AlGaN/GaN high electron mobility transistors", Electron. Lett. **37**, 661 (2001).

[44] M. Wolter, P. Javorka, M. Marso, A. Alam, R. Carius, A. Fox, M. Heuken, H. Luth, and P. Kordos, "Investigations on the influence of traps in AlGaN/GaN HEMTs", Proc. Int. Symp. Electron Devices for Microwave and Optoelectronic Applications Piscataway, NJ: IEEE, 149 (2001).

[45] M. Wolter, P. Javorka, A. Fox, M. Marso, H. Luth, P. Kordos, R. Carius, A. Alam, and M. Heuken, "Photoionization spectroscopy of traps in AlGaN/GaN high-electron mobility transistors", J. Electron. Mater. **31** 1321 (2002).

[46] F. Tong, K. Yapabandara, C.-W. Yang, M. Khanal, C. Jiao, M. Goforth, B. Ozden, A. Ahyi, M. Hamilton, G.Niu, D.A. Ewoldt, G. Chung, and M. Park, "Spectroscopic photo I–V diagnostics of nitride-based high electron mobility transistor structures on Si wafers", Electron. Lett. **49,** 1547, (2013).

[47] M. A. Khan, M. S. Shur, Q. C. Chen, and J. N. Kuznia, "Current/voltage characteristic collapse in AIGaN/GaN heterostructure insulated gate field effect transistors at high drain bias", Electron. Lett. **30**, 2175 (1994).

[48] M. Bouya, N. Malbert, N. Labat, D. Carisetti, P. Perdu, J. C. Clément, B. Lambert, and M. Bonnet, "Analysis of traps effect on AlGaN/GaN HEMT by luminescence techniques", Microelectronics Reliability, **48** 1366 (2008).

[49] Y. Nakano, Y. Irokawa, and M. Takeguchi, "Deep-level optical spectroscopy investigation of band gap states in AlGaN/GaN hetero-interfaces", Appl. Phys. Express **1**, 091101 (2008).

[50] Y. Nakano, Y. Irokawa, Y. Sumida, S. Yagi, and H. Kawai, "Photo-capacitance spectroscopy investigation of deep-level defects in AlGaN/GaN hetero-structures with different current collapses", Phys. Status Solidi. (RRL), **4**, 374 (2010).

[51] M. T. Hirsch, J. A. Wolk, W. Walukiewicz, and E. E. Haller, "Persistent photoconductivity in n-type GaN" Appl. Phys. Lett. **71**, 1098 (1997).

[52] N. Biyikli, Ü. Özgür, X. F. Ni, Y. Fu, H. Morkoç, and Ç. Kurdak, "Illumination and annealing characteristics of two-dimensional electron gas systems in metal-organic vapor-phase epitaxy grown $Al_xGa_{1-x}N$/AlN/GaN heterostructures", Proceedings EDMO, Vienna (2001).

[53] Y. Nakano, Y. Irokawa, Y. Sumida, S. Yagi, and H. Kawai, "Effect of carbon impurity incorporation on band-gap states in AlGaN/GaN hetero-structures", Electrochem. Solid-State Lett. **15** (2) H44 (2012).

[54] J. Neugebauer and C. G. Van de Walle, "Atomic geometry and electronic structure of native defects in GaN", Physical Rev. B, **50**, 8067 (1994).

[55] C. G. Van de Walle and J. Neugebauer, "First-principles calculations for defects and impurities: Applications to III-nitrides", J.Appl. Phys. **95**, 3851 (2004).

[56] P. Bogusławski and J. Bernholc, "Segregation effects at vacancies in $Al_xGa_{1-x}N$ and Si_xGe_{1-x} alloys", Phys. Rev. B, **59**, 1567 (1999).

[57] T. Mattila and R. M. Nieminen, "Point-defect complexes and broadband luminescence in GaN and AlN", Phys. Rev. B **55**, 9571 (1997).

[58] I. Gorczyca, A. Svane, and N. E. Christensen, "Theory of point defects in GaN, AlN, and BN: Relaxation and pressure effects", Phys. Rev. B **60**, 8147 (1999).

[59] A. Fara, F. Bernardini, and V. Fiorentini, "Theoretical evidence for the semi-insulating character of AlN", J. Appl. Phys. **85**, 2001 (1999).

[60] C. Stampfl and C. G. Van de Walle, "Doping of $Al_xGa_{1-X}N$", Appl. Phys. Lett. **72**, 459 (1998).

[61] S. C. Binari, W. Kruppa, H. B. Dietrich, G. Kelner, A. E. Wickenden, and J. A. F. Jr, "Fabrication and characterization of GaN FETs", Solid State Electron. **41**, 1549 (1997).

[62] K. V. Smith, X. Z. Dang, E. T. Yua, and J. M. Redwing, "Charging effects in AlGaN/GaN heterostructures probed using scanning capacitance microscopy", J. Vac. Sci. Tech. B, **18**, 2304 (2000).

[63] X. Dang, P. M. Asbeck, E. T. Yu, K. S. Boutros, and J. M. Redwing, "Long time-constant trap effects in nitride heterostructure field-effect transistors", in Proc. Mater. Res. Soc. Symp. **622**, T6.28.1 (2000).

[64] C. Nguyen, N. X. Nguyen, and D. E. Grider, "Drain current compression in GaN MODFETs under large-signal modulation at microwave frequencies", Electron. Lett. **35**, 1380 (1999).

[65] H. Morkoç, "Nitride Semiconductors and Devices", Springer-Verlag, Berlin, (1999).

[66] S. R. Lee, A. F. Wright, M. H. Crawford, G. A. Petersen, J. Han, and R. M. Biefeld, "The band-gap bowing of $Al_xGa_{1-x}N$ alloys", Appl. Phys. Lett. **74**, 3344 (1999).

[67] L. Bornstein, "New series, group III", Springer-Verlag, Berlin, (1988).

[68] R. Quay, "Gallium nitride electronics", Springer-Verlag, Berlin, (2008).

[69] W. Shan, J. W. Ager III, K. M. Yu, W. Walukiewicz, E. E. Haller, M. C. Martin, W. R. McKinney, and W. Yang, "Dependence of the fundamental band gap of $Al_xGa_{1-x}N$ on alloy composition and pressure", J. Appl. Phys. **85**, 8505 (1999).

[70] X. L. Sun, S. H. Goss, L. J. Brillson, D. C. Look, R. J. Molnar, "Depth-dependent investigation of defects and impurity doping in GaN/sapphire using scanning electron microscopy and cathodoluminescence spectroscopy" J. Appl. Phys**. 91**, 6729 (2002).

[71] H. Angerer, D. Brunner, F. Freudenberg, O. Ambacher, M. Stutzmann, R. Höpler, T. Metzger, E. Born, G. Dollinger, A. Bergmaier, S. Karsch, and H.-J. Körner, "Determination of the Al mole fraction and the band gap bowing of epitaxial $Al_xGa_{1-x}N$ films", Appl. Phys. Lett. **71,** 1504 (1997).

[72] Y. Koide, H. Itoh, M. R. H. Khan, K. Hiramatu, N. Sawaki, and I. Akasaki, "Energy band-gap bowing parameter in an $Al_xGa_{1-x}N$ alloy", J. Appl. Phys. **61**, 4540 (1987).

[73] F. Yun, M. A. Reshchikov, L. He, T. King, H. Morkoç, S. W. Novak, and L. Wei, "Energy band bowing parameter in $Al_xGa_{1-x}N$ alloys", J. Appl. Phys. **92**, 4837 (2002).

[74] J. F. Muth, J. D. Brown, M. A. L. Johnson, Z. Yu, R. M. Kolbas, J. W. Cook, JR. and J. F. Schetzina, "Absorption coefficient and refractive index of GaN, AlN and AlGaN alloys", MRS Internet J. Nitride Semicond. **537**, 6 (1999).

[75] S. DasGupta, M. Sun, A. Armstrong, R. J. Kaplar, M. J. Marinella, J. B. Stanley, S. Atcitty, and T. Palacios, "Slow detrapping transients due to gate and drain bias stress in high breakdown voltage AlGaN/GaN HEMTs", IEEE Trans. Electron Devices, **59**, 2115 (2012).

[76] M. Kumar, C. Y. Lee, H. Sekiguchi, H. Okada, and A.Wakahara, "Demonstration of a large-area AlGaN/GaN Schottky barrier photodetector on Si with high detection limit", Semicond. Sci. Technol. 28 (2013).

[77] Z. Li and C. R. McNeill, "Transient photocurrent measurements of PCDTBT: PC70BM and PCPDTBT: PC70BM solar cells: Evidence for charge trapping in efficient polymer/fullerene blends", J. Appl. Phys. **109**, 074513 (2011).

[78] B. Chitara, L. S. Panchakarla, S. B. Krupanidhi, and C. N. R. Rao, "Infrared photodetectors based on reduced graphene oxide and graphene nanoribbons", Japan. J. Appl. Phys. **50** 100206 (2011).

[79] B. Poti, A. Passaseo, M. Lomascolo, R. Cingolani, and M. De Vittorio "Persistent photocurrent spectroscopy of GaN metal–semiconductor–metal photodetectors on long time scale", Appl. Phys. Lett. **85** 6083 (2004).

[80] E. Munoz, E. Monroy, J. A. Garrido, I. Izpura, F. J. S´anchez, M. A. S´anchez, E. Calleja, B. Beaumont, and P. Gibart, "Photoconductor gain mechanisms in GaN ultraviolet detectors", Appl. Phys. Lett. **71** 870 (1997).

[81] W. Gao, A. S. Khan, P. R. Berger, and R. G. Hunsperger "$In_{0.53}Ga_{0.47}As$ metal-fefsemiconductor-metal photodiodes with transparent cadmium thin oxide Schottky contacts", Appl. Phys. Lett. **65** 1930 (1994).

[82] O. Katz, G. Bahir, and J. Salzman "Persistent photocurrent and surface trapping in GaN Schottky ultraviolet detectors", Appl. Phys. Lett. **84** 4092 (2004).

[83] R. S. Muller, T. I. Kamins, "Device electronics for integrated circuits", John Willey &Sons, New York (1977).

[84] Available online: at http://www.iue.tuwien.ac.at/phd/vitanov/node53.html, May (2016)

[85] Available online: http://www.ee.sc.edu/ personal /faculty/simin /ELCT871 /11% 20Ohmic%20contacts. pdf, May (2016).

[86] Available online: http://www.kayelaby.npl.co.uk/atomic_and_nuclear_physics /4_3/4_3.htm, May (2016).

[87] Available online: https://www.ecse.rpi.edu/~schubert/Course-reference-materials/Materials-Semiconductors-Si-Ge-GaAs-&-GaN.pdf, May (2016).

[88] R. A. Smith, "Semiconductors", Cambridge University Press, Cambridge, UK (1978).

[89] Y. H. Lee, J. H. Kang, and S. W. Ryu, "Enhanced photocurrent and persistent photoconductivity in nanoporous GaN formed by electrochemical etching", Thin Solid Films, **540**, 150 (2013).

[90] S. Yasuno, T. Kita, S Morita, T Kugimiya, K. Hayashi, and S. Sumie, "Transient photoconductivity responses in amorphous In-Ga-Zn-O films", J. Appl. Phys. **112**, 053715 (2012).

[91] O. Mitrofanov, and M. Manfra, "Mechanisms of gate lag in GaN/AlGaN/GaN high electron mobility transistors", Superlattices Microstruct. **34**, 33 (2003).

[92] Y. Kanemitsu, "Photoluminscence spectrum and dynamics in oxidized silicon nanocrystals: A nanoscopic disorder system", Phys. Rev. B. **53,** 13515 (1996).

[93] E. Monroy, F. Calle, E. Muñoz, and F. Omnès, "AlGaN metal–semiconductor–metal photodiodes", Appl. Phys. Lett. **74**, 3401 (1999).

[94] C. Buchheim, G. Kittler, V. Cimalla ,V. Lebedev, M. Fischer, S. Krischok ,V. Yanev, G. Ecke, J. A. Schaefer, and O. Ambacher, "Surface modifications of AlGaN/GaN sensors for water based nano- and picodroplets" Sensors, Proceedings of IEEE, **2**, 1007 (2004).

[95] P. V. Kamat and D. Meisel, "Semiconductor nanoclusters - physical, chemical, and catalytic aspects, (Studies in surface science and catalysis); Eds.; Elsevier: Amsterdam (1997).

[96] K. I. Zamaraev and V. N. Parmon, "Photocatalytic transformation of solar energy heterogeneous, homogeneous and organized molecular structures", Eds. Nauka: Novosibirsk, Russia (1991).

[97] A. V. Emeline, G. V. Kataeva, V. K. Ryabchuk, and N. Serpone, "Photostimulated generation of defects and surface reactions on a series of wide band gap metal-oxide solids", J. Phys. Chem. B, **103**, 9190 (1999).

[98] A. V. Emeline, G. V. Kataeva, A. S. Litke, A. V. Rudakova, V. K. Ryabchuk, and N. Serpone, "Spectroscopic and Photoluminescence studies of a wide band gap insulating material: powdered and colloidal ZrO_2 Sols", Langmuir, **14**, 5011 (1998).

[99] F. F. Volkenstein, "Electronic processes at the surface of a semiconductor during chemisorption", Sov. Phys. Usp. **9** 275 (1967).

[100] M. A. Prelas, T. Ghosh, R.V. Tompson, D. Viswanath, and S. K. Loyalka, in: W.I.P. Organization (Ed.), The Curators of the University of Missouri, United States (2007).

[101] T. Wolkenstein, "Electronic processes on semiconductor surfaces during chemisorption", Plenum Publishing, New York (1991).

[102] R. Neuberger, G. Müller, O. Ambacher, and M. Stutzmann, "High-electron-mobility AlGaN/GaN transistors (HEMTs) for fluid monitoring applications", Phys. Stat. Sol. A **185**, 85 (2001).

[103] R. Mehandru, B. Luo, B. S. Kang, J. Kim, F. Ren, S. J. Pearton, C.-C. Panc G.-T. Chen, and J.-I. Chyi, "AlGaN/GaN HEMT based liquid sensors", Solid State Electronics, **48**, 351 (2004).

[104] J. B. Rothenberger , D. E. Montenegro, M. A. Prelas, T. K. Ghosh, R. V. Tompson, and S .K. Loyalka, "An Aluminum Nitride-based chemical sensor using Q-DLTS", Diamond & Related Materials, **23** 72 (2012).

[105] R. Hong, H. Qi, J. Huang, H. He, Z. Fan, and J. Shao, "Influence of oxygen partial pressure on the structure and photoluminescence of direct current reactive magnetron sputtering ZnO thin films", Thin Solid Films, **473,** 58, (2005).

[106] S. J. Pearton, B. S. Kang, S. Kim, F. Ren, B. P. Gila, C. R. Abernathy, J. Lin, and S. N. G. Chu, "GaN-based diodes and transistors for chemical, gas, biological and pressure sensing", J. Phys.: Conden. Matt. **16**, (2004).

[107] H. Morkoc, Hand book of nitride semiconductors and devices, Materials properties, physics and growth", Springer, Berlin (2007).

[108] S. Doğan, S. Dumana, B. Gürbulak, S. Tüzemen, H. Morkoc, "Temperature variation of current–voltage characteristics of Au/Ni/n-GaN Schottky diodes", Physica E **41**, 646 (2009).

[109] T. Hashizume, J. Kotani, H. Hasegawa, "Leakage mechanism in GaN and AlGaN Schottky interfaces", Appl. Phys. Lett.84, 4884 (2004).

[110] Y. Wang, S. Alur, Y. Sharma, F. Tong, R. Thapa, P. Gartland, T. Issacs-Smith, C. Ahyi, J. Williams, M. Park, M. Johnson, T. Paskova, E. A Preble, and K. R Evans, "Ultra-low leakage and high breakdown Schottky diodes fabricated on free-standing GaN substrate", Semicond. Sci. Technol. **26** 022002 (2011).

[111] M. Grundmann "The Physics of Semiconductors: An introduction including device and nanophysics", Springer- Verlag, Berlin (2006).

[112] P. Hacke, T. Detchprohm, K. Hiramatsu, and N. Sawaki "Schottky barrier on n-type GaN grown by hydride vapor phase epitaxy", Appl. Phys. Lett. **63** 2676 (1993).

[113] Y. Zhou, D. Wang, C. Ahyi, C. C. Tin, J. Williams, M. Park, N. M. Williams, A. Hanser, and E. A. Preble, "Temperature-dependent electrical characteristics of bulk GaN Schottky rectifier", J.Appl. Phys. **101**, 024506 (2007).

[114] M. L. Lee, J. K. Sheu, and S.W. Lin, "Schottky barrier heights of metal contacts to n-type gallium nitride with low temperature grown cap layer", Appl. Phys. Lett, **88**, 032103 (2006).

[115] L. S. Yu, Q. J. Xing, D. Qiao, S. S. Lau, K. S. Boutros, and J. M. Redwing , "Internal photoemission measurement of Schottky barrier height for Ni on AlGaN/GaN heterostructure", Appl. Phys. Lett. **73**, 3917 (1998).

[116] A. C. Schmitz, A. T. Ping, M. A. Khan, Q. Chen, J. W. Yang, and I. Adesida, "Schottky barrier properties of various metals on n-type GaN", Semicond. Sci. Technol. **11** 1464 (1996).

[117] Y. P. Song, R. L. Van Meirhaeghe, W. H. Laflere, and F. Cardon, "On the difference in apparent barrier height as obtained from capacitance-voltage and current-voltage-temperature measurements on Al/p-InP Schottky barriers", Solid State Electron**. 29**, 633 (1986).

[118] S. Karadeniz, M. Sahin, N. Tugluoglu, and H. Safak, "Temperature-dependent barrier characteristics of Ag/p-SnS Schottky barrier diodes", Semicond. Sci. Technol. **19**, 1098 (2004).

[119] V. D. Mihailetchi, J. Wildeman, and P. W. M. Blom, "Space-charge limited photocurent", Phys. Rev. Lett. **94**, 126602 (2005).

[120] Z. Minglan, Y. Ruixia, L. Naixin, and W. Xiaoliang, "Persistent photoconductivity in neutron irradiated GaN", J. Semicond. **34**, 093005-1 (2013).

[121] M. Miczek, C. Mizue, T. Hashizume, and B. Adamowicz, "Effects of interface states and temperature on the C - V behavior of metal/insulator/AlGaN/GaN heterostructure capacitors", J. Appl. Phys. **103**, 104510 (2008)

[122] W.-H.Chang, T. M. Hsu, C. C. Huang, S. L. Hsu, C. Y, Lai, N. T. Yeh, T. E. Nee, and J.-I. Chyi, "Photocurrent studies of carrier escape process from InAs self-assembled quantum dots", Phys. Rev. B, **62**, 6959 (2000).

[123] L. Sang, M. Liao, Y. Koide, and M. Sumiya, "High-temperature ultraviolet detection based on InGaN Schottky photodiodes", Appl. Phys. Lett. **99**, 031115 (2011).

[124] Z. Q. Shi and W. A. Anderson, "MIS diodes on n-InP having an improved interface", Solid-State Electron. **34**, 285 (1991).

[125] F. R. Juang, Y. K. Fang, Y. T. Chiang, T. H. Chou, and C. I. Lin, "Comparative study of carbon monoxide gas sensing mechanism for the LTPS MOS Schottky diodes with various metal oxides", IEEE Sens. J. **11**, 150 (2011).

Chapter 7

7 Conclusions

As a conclusion, surface/ interface defects and their distributions in AlGaN/GaN high electron mobility transistors HEMTs heterostrucures grown on 6″ Si wafers have been investigated by using optoelectronic spectroscopic techniques. For the measurement two samples from the edge and center of the 6″ wafer was chosen and the results of the experiments for these samples were compared to make a qualitative analysis of surface/interface defects in these wafers.

Raman spectroscopy displayed that two samples have a similar crystalline quality and stress. Photoluminescence measurements revealed that samples possessed strong near band edge peak at around 3.42 eV and broad blue luminescence. No yellow luminescence band was observed. The spectroscopic photo current-voltage measurements with sub-bandgap illumination exhibited the presence of sub-bandgap defects with different activation energies for each sample. In addition, observed persistence photoconductivity effects showed that the sensitivity of the dark level of Schottky contacts fabricated from AlGaN/ GaN HEMTs heterostructures will depend on the device history.

The depth-resolved ultra-violet spectroscopic photo current-voltage (DR-UV-SPIV) measurements revealed that the depth dependent distribution of the defects for these samples are different. Time-resolved photocurrent (TRPC) spectroscopy exhibited dissimilar time-dependent photocurrent decay dynamics implying that TRPC spectroscopy can be used to distinguish between the traps that have the same de-trapping energy but have the different physical origins. The variation of the photocurrent in different solutions was observed and was attributed to the differences in dipole moment and molecular structure of the solution used. The temperature dependent photo current voltage characteristics of AlGaN/GaN HEMTs heterostuctures revealed the presence of the additional traps which are activated by temperature.

In summary, it was demonstrated that even though electrically active defects for two devices on the same pieces of AlGaN/GaN HEMTs heterostructures cannot be distinguished in Raman spectroscopy and

PL measurements, they can be differentiated by using the spectroscopic photo I-V with sub-bandgap illumination, DR-UV-SPIV, and TRPC spectroscopy measurements. As a result of the experiments which was completed during this dissertation, it was revealed that spectroscopic photo I-V measurements can be used to assess the uniformity of in-depth and spectral distribution of sub-band gap point defects across the AlGaN/GaN wafers, respectively.

7.1 Future work

The research work illustrated in this dissertation focused primarily on the investigation of the uniformity of large diameter AlGaN/GaN HEMTs heterostructures in terms of their defect distributions. As we stated before, this information will be useful for wafer vendors. However, it would be more useful, if we could give more information about the nature of the defects. For this purpose, several methods can be applied to determine the nature of the defects.

First, AlGaN/GaN HEMTs heterostructures will be grown layer by layer, and spectroscopic photocurrent experiments will be repeated for each layer. Based on the information obtained from this experiment, we will be able to tell where the defects are produced inside the structure. In the literature, there are many theoretical works that give the energy level of the defects for specific materials that exist in our heterostructure. Therefore, we will derive the information on the nature of defects by comparing the experimental results with the theoretical work.

Next, we will implement specific types of ions which are believed to be responsible in the observed current increase in our experiment, to the structure and we will repeat the experiment. We believe with this experiment, we will be able to determine the nature of defects that are possibly involved in the increase of the photocurrent. In addition, we will conduct mobility experiments to determine whether these defects are electron or hole types by looking at the increase or decrease in the mobility.

Finally, we had radiated our samples with a Co^{60} gamma ray source. We will repeat similar experiments on the same samples and we will observe the effect of radiation on the defects. We believe that this experiment will be very useful to investigating the device performance for space applications.

Appendices

Appendix A

Consistency and repeatability of the time dependent decay experiment

To observe the consistency and repeatability of the time dependent decay experiment two additional experiment were conducted. Both experiments were conducted at 700nm exposure wavelength and -12V applied bias. For the first experiment we consecutively repeated the time resolved photocurrent experiment for 8th times for both of the samples and we observed the difference between the two samples .In the second experiment we repeated the same experiment 3 times with 10 days waiting time between each experiment.

Li *et al*.[1] stated that the sensitivity, dark level, and decay time constant of Schottky contacts fabricated on AlGaN/GaN HEMTs epi- layers will depend on the device history. Hence, the time resolved decay transient experiment was repeated for 3 times with 10 days intervals and decay characteristics for each day were plotted as a function of time in the figures below for samples A and B, respectively. As seen in these figures, time decay constants of the samples are very close to each other. As a results, if someone waits long enough between the measurements, the data can be reproducible. Furthermore, fabricated Schottky contacts showed a very low dark current sometimes even smaller than 0.1μA at -12V. According to Monroy *et al*.[2] it is an indication of high quality Schottky barriers.

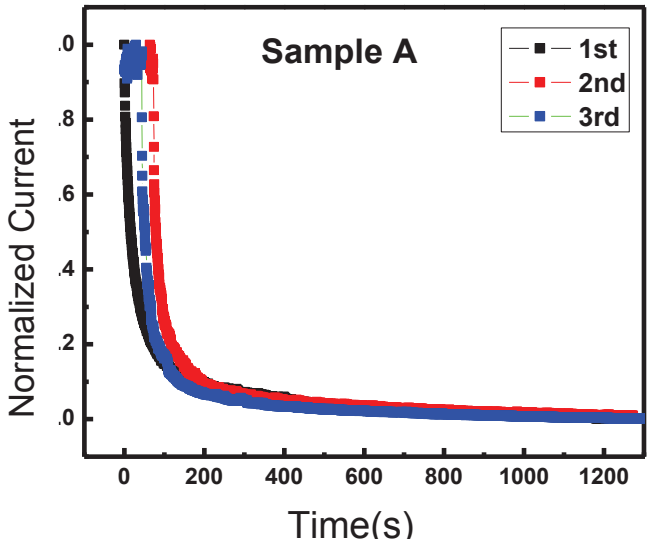

a

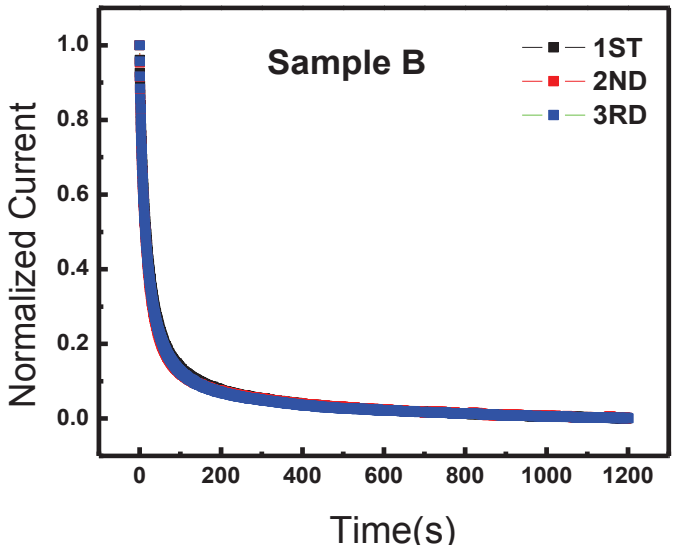

b

Figure: *Decay characteristics of sample A (a), and B (b) measured 3 times with 10 days intervals.*

Appendix B

Responsivity and quantum efficiency

In our graphs, for current divided by power we prefer not to use responsivity for the clarification. However, we are aware that current divided by incident power can be used as responsivity. In this section, responsivity is explained. In semiconductor photodetectors, the creation of electron hole pairs occurs with the absorption of the photons in the semiconductor. By the use of electric field, due to either the built in voltage or the applied voltage, these photogenerated carriers are separating, which results in a current increase that is proportional to the photon flux. In semiconductor physics, different parameters are used to define the properties of these detectors, and responsivity is one of them. The ratio between the photocurrent and the incident optical power is defined as responsivity R_i. It is determined by the quantum efficiency, η, (number of electron–hole pairs generated per incident photon) using the following expression;

$$R_\lambda = \frac{I_{ph}}{P_{opt}} = \frac{\lambda\eta}{hc}e$$

$$\eta \approx \frac{R_\lambda}{\lambda}x(1240W.\frac{nm}{A})$$

here, λ is the radiation wavelength, h is Planck constant, c is the speed of light, and e is the electron charge. In our experiments, a relatively high spectral responsivity (A/W) was observed. It is not uncommon to observe high responsivity in GaN and related materials. High responsivity values are observed by other scientists.[3,4,5] In addition, Wu *et al*. ascribed the high responsivity to the trapping effects.[6]

Appendix C

X-ray Photoelectron Spectroscopy (XPS)

X-ray photoelectron spectroscopy (XPS) studies the energy of atomic core levels *via* the Einstein photoelectric equation $\tau_e = h\upsilon - E_b$, here τ_e is the kinetic energy of the photoemitted electron and E_b is the binding energy of the core level.[7] Atoms are measured at slightly different binding energies since atoms in different chemical environments experience different chemical shits. As a result, XPS can characterize the different types of biding sites for similar atoms, and measure their abundance by measuring relative intensities of XPS emission from different species.

In this experiment, we compared two AlGaN/GaN HEMTs heterostructures, one with a GaN top layer and with a AlGaN top layer to observe differences in terms of involvement of chemicals on them. Elemental compositions were analyzed using XPS. During our research, we tried to investigate the energy levels, physical locations, and physics origins of surface/interface defects in AlGaN/GaN heterostructures. We thought that if we observed a difference in terms of the involvement of chemicals in AlGaN/GaN, we might come with conclusion on the physical origins of these defects in AlGaN and GaN layers.

The figures below display the XPS results obtained from samples with a GaN (a) top layer and a AlGaN top layer (b). The tables below the figures show the percentage of elemental composition on these samples. Both of the samples had the same type of elements, such as Ga, Al, C, O, Co, and Zn on their surfaces. The percentages of the elements in of each the sample were very similar. Hong *et al*.[8] showed the adsorption of the oxygen on the AlGaN surface by comparing the ratios of the *O1s* and *Ga2p* peaks in two different samples. They concluded that oxygen binding on AlGaN released the donor-like traps due to the loss of nitrogen during the fabrication process. In our case, both of the samples exhibited similar *O1s* and *Ga2p* ratios. Researchers attributed the shift of the Fermi level toward the conduction-band edge which results in a reduction of the surface barrier height in the AlGaN/GaN heterostructure, to the shift of *Ga3p* peak.[9,10] It was observed that Ga3p peak has the same binding energy.

In conclusion, XPS measurements were performed to investigate the differences between AlGaN and GaN layers in terms of their elemental compositions. It was determined that both samples exhibit similar elemental compositions. Consequently, we could not obtain any useful information to determine the origin of the defects in these samples because there was no difference in the results.

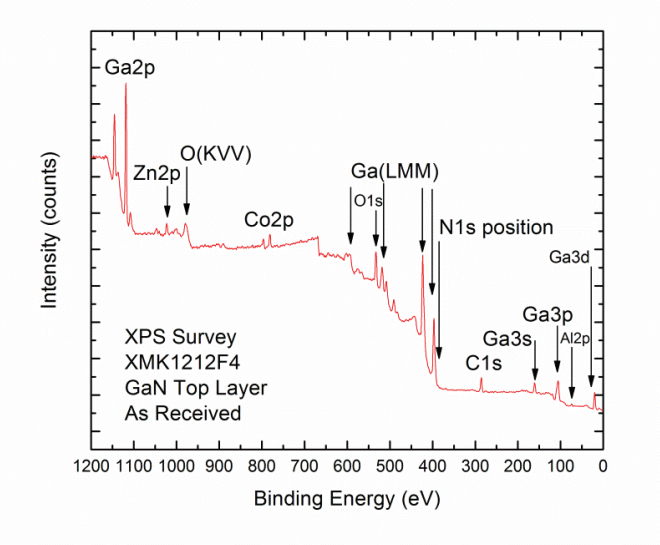

XPS Surface Elemental Composition (at %)						
Element	**Ga**	**Al**	**C**	**O**	**Co**	**Zn**
	4.7	9.9	51.8	30.7	2.0	0.9

a

Figure: *XPS spectra of (a) GaN top layer. The table below the graphs show the percentage of elemental composition on this sample..*

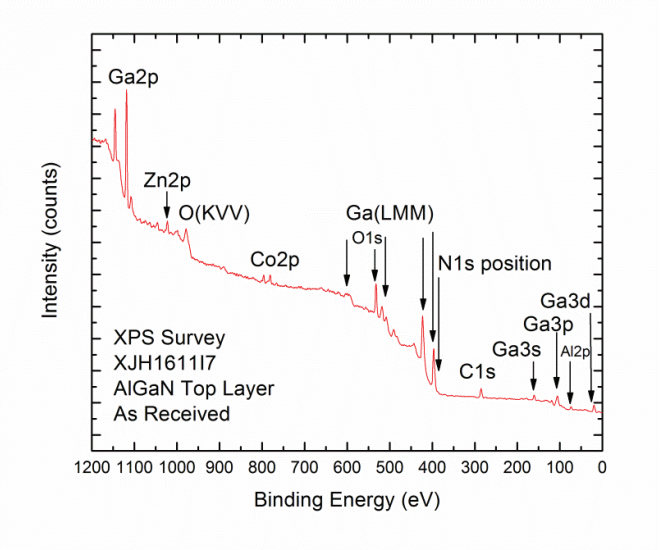

XPS Surface Elemental Composition (at %)						
Element	**Ga**	**Al**	**C**	**O**	**Co**	**Zn**
	3.6	26.6	37.5	28.9	2.4	1.0

b

Figure: *XPS spectra of (b) AlGaN top layer AlGaN/GaN HEMTs heterostructures. The table below the graphs show the percentage of elemental composition on this sample.*

Appendix D

Scanning Electron Microscope (SEM) Measurements

Scanning electron microscopy (SEM) uses methods based on the injection of charge carriers by the electron beam in the SEM to measure properties of semiconductors, such as carrier lifetime or diffusion length, or to study surface topography by imaging methods. [11] By using SEM we aimed to observe defects and differences in their distributions in samples that were chosen from different locations in the AlGaN/GaN wafers. Unfortunately, the collected images were too similar to identify the defects. We were not able to identify the defects.

The cross-sectional SEM micrograph for samples were taken from the center (a) and edge (b) piece of 6″ AlGaN/GaN HEMTs heterostructure grown on Si substrate. The presence of different interfaces can be clearly seen from the cross sectional view in the figure.

Nonetheless, it is hard to tell which layers corresponds to which layer since we cannot observe the entire layer that we have in our structures. It seems like the layer close to the Si substrate (AlN in our structures) has trapezoid shaped islands which results in the rough morphology of this layer. Similar shapes of islands in AlGaN/GaN heterostructures have been observed by other researchers.[12] The other layers grown on this layer look smoother. Ishikawa *et al*.[12] attributed the presence of the trapezoid-shaped islands to the coalescence of the AlGaN crystals does not occur perfectly in the AlGaN growth stage. In our case the coalescence of crystals might exists in AlN layers. According to these images, it appears that the crystal quality is gradually improved from the AlN bottom layer to the GaN top layer.

In conclusion, SEM images of the samples that were used in the DR-UV-SPIV measurements were taken to investigate the defects. Unfortunately, we were not able to identify defects and their locations by SEM image. We observed that towards the surface crystal quality of the growth increased.

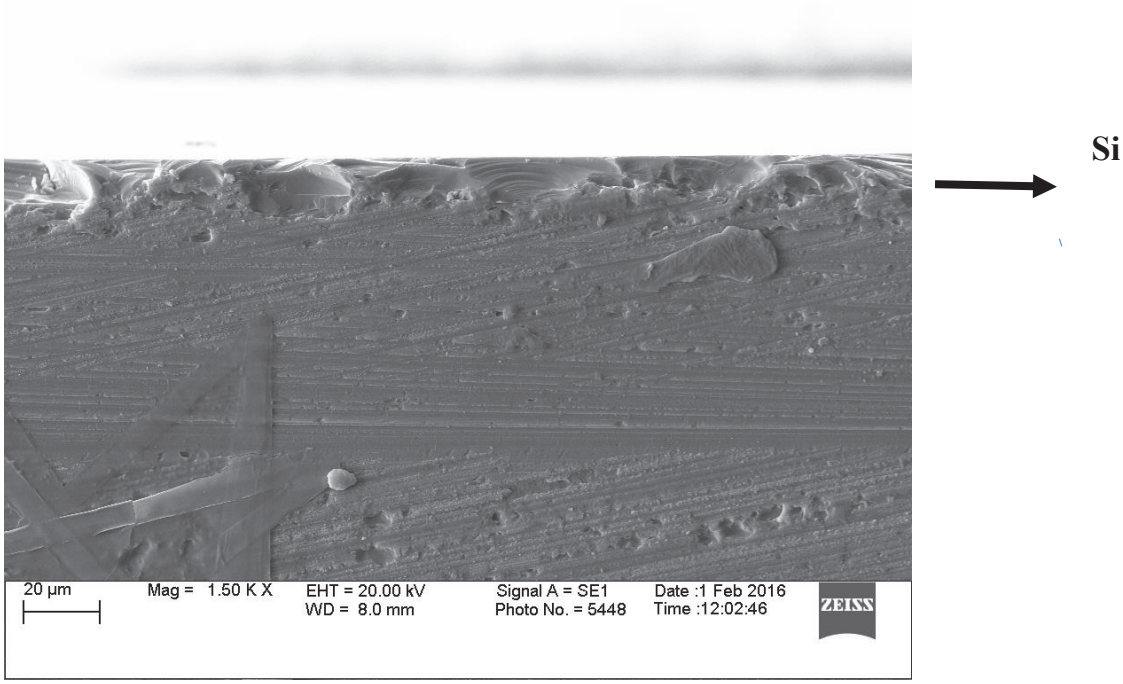

a

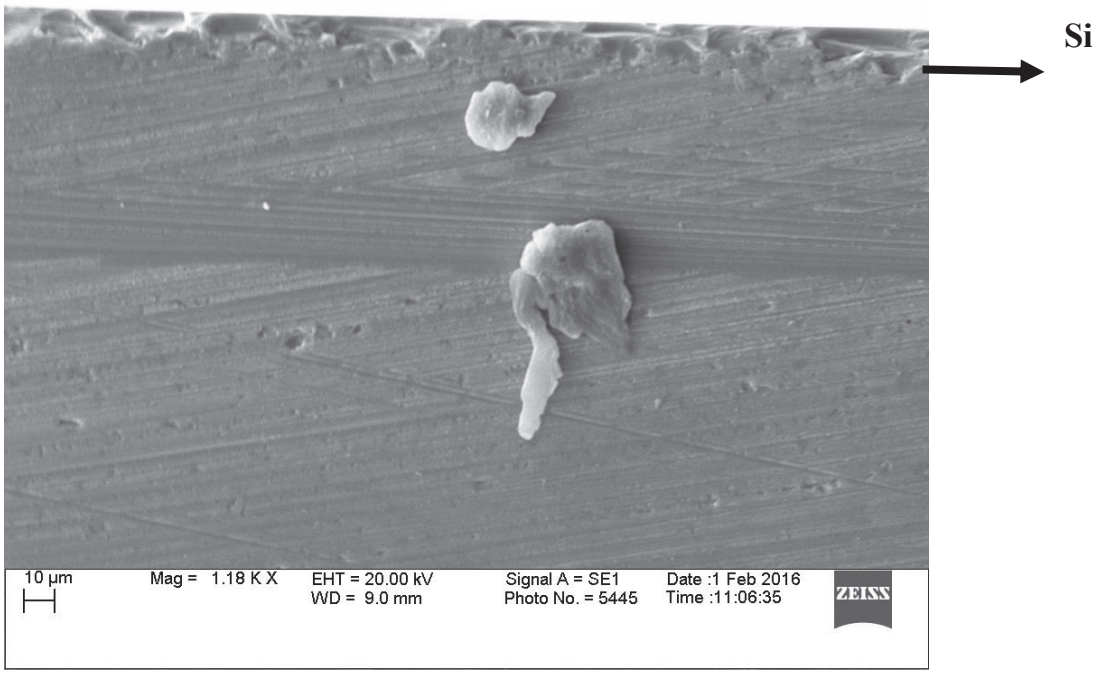

b

Figure: *SEM image of AlGaN/GaN HEMTs heterostructure chosen from the (a) center and (b) edge of 6″ wafer.*

References

1 Z. Li, J. Y. Lin, H. X. Jiang, M. Asif Khan, and Q. Chen, "Persistent photoconductivity in a two-dimensional electron gas system formed by an AlGaN/GaN heterostructure", J. Appl. Phys. **82**, 1227 (1997).

2 E. Monroy, F. Calle, E. Muñoz, and F. Omnès, "AlGaN metal–semiconductor–metal photodiodes", Appl. Phys. Lett. **74**, 3401 (1999).

3 S. K. Zhang, W. B. Wang, and I. Shtau, "Back illuminated GaN/AlGaN heterojunction ultraviolet photodetector with high internal gain", Appl. Phys. Lett. **81**, 4862 (2002).

4 L. Rigutti, M. Tchernycheva, A. De Luna Bugallo, G. Jacopin, F. H. Julien, L. F. Zagonel, K. March, O. Stephan, M. Kociak, and R. Songmuang, "Ultraviolet photodetector based on GaN/AlN quantum disks in a single nanowire", Nano Lett. **10**, 2939 (2010).

5 M. Mello, A. Scarascia, S. De Guido, D. Altamura, V. Tasco, M. De Vittorio, and A. Passaseo, "High responsivity AlGaN-based UV sensors for operation in harsh conditions", IEEE Sensors 2008 Conference, Lecce, 1588 (2008).

6 J. M. Wu and W. E. Chan, "Ultrahigh responsivity and external quantum efficiency of an ultraviolet-light photodetector based on a single VO2 microwire", Appl. Matter. Interfaces **6**, 14286 (2014).

7 G. W. F. Drake "Handbook of Atomic, Molecular, and Optical Physics, Springer Science Business Media (2006).

8 S. K. Hong, K. H. Shim, and J. W. Yang, "Reduced gate leakage current in AlGaN/GaN HEMT by oxygen passivation of AlGaN surface", Electron. Lett. **44**, 18 (2008).

9 J. Sun, K. A. Richert, J. M. Redwing, A. B. Ellis, F. J. Himpel, and T. F. Kuech "p-GaN surface treatments for metal contacts", Appl Phys Lett. **76** 415 (2000).

10 J. S. Jang and T. Y. Seong "Mechanism for the reduction of the Schottky barrier height of high-quality nonalloyed Pt contacts on surface-treated p-GaN", J. Appl. Phys. **88**, 3064 (2000).

11 D. B. Holt and D. C. Joy, "Techniques of physics: 12: SEM microcharacterization of semiconductors", Academic Press, San Diego, (1989).

12 H. Ishikawa, G. –Y. Zhao, N. Nakada, T. Egawa, T. Jimbo, and M. Umeno, "GaN on Si Substrate with AlGaN/AlN Intermediate Layer", Jpn. J. Appl. Phys. **38**, L492 (1999).